

Mechanical Properties of Multi-Year Sea Ice

Progress Report 1

1 March 1981

by

G.F.N. Cox; M. Mellor; and W.F. Weeks

US Army Cold Regions Research and
Engineering Laboratory

prepared for

Shell Development Company

United States Geological Survey

Introduction

This progress report describes the work performed in the Mechanical Properties of Multi-Year Sea Ice Study from 1 December 1980 to 28 February 1981. During this period, work concentrated on preparing for the field ice sampling program and the development of equipment and testing techniques for the ice strength tests. Automated petrographic analyses of sea ice thin sections and tritium dating of multi-year sea ice were also briefly investigated at the request of Shell.

Field Sampling Program

The field sampling program has been scheduled for the month of April. Originally it was planned to go into the field on 15 March; however, it was later felt that the ice samples would be best obtained during April when air temperatures were slightly warmer. The higher air temperatures would minimize possible thermal cracking of the ice cores when removed from the pressure ridge.

The field program will be staged out of NANA Camp in Deadhorse as considerable amounts of multi-year ice have been reported in the Prudhoe Bay area near the coast and barrier islands. Arrangements have been made with NANA for room and board, two unheated storage huts, and a truck. The storage huts will serve as a field office and lab. Transportation to the multi-year ice will be provided by a Bell 205 helicopter chartered from ERA Helicopters. In the event poor weather conditions do not allow us to fly offshore, the truck will be used to drive to Prudhoe Bay to obtain first-year sheet ice samples for study.

All field equipment have been procured, tested, and packed for shipment to Deadhorse. It is planned to ship the equipment during the second week of March.

The equipment and procedures for the field sampling program have been briefly described in the study proposal. Details of the sampling program will be given in the next progress report after the field trip and in the final report. However, it is appropriate at this time to discuss the 4½-inch diameter auger developed and fabricated at CRREL and our plans to ship the ice from Prudhoe to Hanover.

Ice Augers

In order to obtain a suitable sample size/crystal size ratio of ten, it was necessary to develop and fabricate an ice auger that was slightly larger than the conventional CRREL or SIPRE ice auger. A core diameter of 4-inches was required for testing and only 3-inch diameter core could be obtained with the CRREL auger.

Three constraints were placed on the design of this auger. They were: first, the core diameter was to be over 4-inches, second, the drill was to be as light as possible and finally, the maximum depth to be drilled in the pressure ridges was expected to be around 40 feet.

The design of the auger was completed in early December. It was decided to design the auger to obtain 4½-inch diameter core, so that the core could be machined to obtain a final diameter of 4 inches for testing. Because of the weight limitations and the ease of which the auger was to be handled, the auger barrel was designed around the use of a fiberglass reinforced epoxy pipe. The shop drawing and mechanical specifications for the fiberglass pipe are given in the Appendix.

The total weight of the auger, extension adapter, and cutters is 8 pounds. This is significantly less than the smaller CRREL auger.

Materials for the auger were received by the end of December. At this time, one auger has been completed; the second will be ready in one week.

Initial tests conducted on the first auger in fresh water ice were very successful. Problems with the core wafering were eliminated by reducing the core diameter about 0.06 in, from 4.250 in. to 4.190 in. Once this was accomplished excellent core was obtained. An ½" electric drill, hand held, was used to power the auger. The drill speed was reduced to approximately 200 rpm using a variable resistor. Penetration rates during the short runs were typically over 24 inch per min. It should be noted that the CRREL auger is not used in fresh water ice because of core wafering. Generally samples are obtained with a chain saw. It appears that we have developed an auger superior to the existing CRREL auger. The auger should work very well in less brittle sea ice.

A 12-inch diameter auger will also be developed, fabricated, and tested at CRREL. The purpose of this auger is to obtain large diameter core from which horizontal ice samples could be obtained.

The 12-inch ice coring auger has developed some procurement delays and will not be ready for shipment to the field this year. It was hoped that if the auger were ready, it could be tested in the field this winter for subsequent use. The major delay is procurement of the 12-inch fiberglass pipe for the auger barrel. This tubing has been selected over conventional aluminum and steel tubing because of its tremendous weight advantage. A comparison of weights for the four foot length required for the drill is 24 lbs for the fiberglass, 72 lbs for aluminum and 216 lbs for steel tubing.

Ice Storing and Shipping

If seasonal temperature prevail, the ice will be transported from the field collection sites to Deadhorse without refrigeration. If it is unseasonably warm, dry ice will be utilized to cool the samples directly at the field site. Once processing is completed and several shipping containers are filled with samples at Deadhorse, a small amount of dry ice will be added and the containers will be placed on a Wien flight for shipment to Anchorage. When a shipment is ready to leave, Emery Air Freight will be contacted and they will meet the aircraft and take the shipment to Ten and M Lockers. Ultimately our complete

shipment will be located at Ten and M. At the completion of the field season we will make one shipment via Northwest Airlines. Each box will be charged with dry ice and the boxes will be containerized in two large containers. The NW freighter leaves Anchorage daily at 0030 and proceeds on to Seattle, there the shipment will be changed to another NW flight proceeding directly to Boston arriving at 1730 on the same day. We will meet the shipment with a truck and transport the ice directly to the CRREL cold rooms.

Development of Testing Equipment and Techniques

Work to date has concentrated on developing the appropriate test equipment and techniques for performing unconfined compression and direct tension tests. Multi-axial testing will be addressed once the unconfined compression testing program has been started in Task 2. In Task 2, the variation of multi-year sea ice strength will be investigated by conducting a large number of unconfined compression tests at given ice temperatures and strain rates.

Uniaxial Compression Tests: Core samples are expected to be 4.20 inches in diameter after drilling, and there may be some surface irregularities. The broad aim is to turn the specimens down to a diameter of 4.000 ± 0.001 inches. The finished length will be 10 inches resulting in a L/D ratio of 2.5.

Two possibilities for shape were considered: (1) a simple right circular cylinder, (2) a cylinder with slight flaring of the ends. Alternative (2) would involve use of a form tool when turning the specimen down from 4.2 in to 4.0 in. diameter, forming fillets of large radius and leaving the end planes at 4.2 in. diameter. The resulting gain of area at the end planes (to combat stress concentrations) is somewhat exiguous (10%) with these dimensions, and for the time being the dumbbell shape will not be used for compression.

To form a right cylinder, the end planes will be cut square to the axis of the core, forming a cylinder approximately 12 in. long. This will then be mounted in the lathe, using special caps to hold the cylinder between the chuck and the tailstock center. The core will be turned down to 4.0 in., and finally the ends will be cut to give a finished length of 10 in. The end planes will be cut flat and square to the axis by face milling, with the cylinder held in a double vice-block. Lapping has been considered, and it will remain an option, but there is a potential for problems if the specimen is not rotated about its axis while on the lapping wheel.

All machining will be done at an ambient temperature of -20°C , and precautions will be taken to avoid chemical contamination. Dimensional tolerance for machining are expected to be ± 0.001 in.

The cylindrical specimens for uniaxial compression tests will be machined to tolerances that are within the acceptable range for high precision tests on rock and other brittle solids. Theoretically, it should be possible to achieve

good results with direct contact between the ice and ground-flat steel platens. However, because ice surfaces are rather unstable at typical test temperatures, it is expected that a "crushable" platen cushion may be interposed between the ice and the steel. A cutter has been made for forming discs of thin uniform card (manila file folder stock).

The desirability of using a ball seat to compensate for possible lack of parallelism has been considered, but no definite conclusions have yet been reached. If a ball seat is used, it will be one that is specially designed to avoid "racking" displacements, and it will be lubricated with very light oil to ensure that it locks under load.

As an alternative to use of "frictional" platens, which impose radial restraint on the end planes of the specimen, consideration is being given to use of compliant platens. Compliant platens have been developed earlier by CRREL for field testing, and their merits were validated by critical experiments. They were not recommended for precise laboratory testing because they represent a compliant element in an otherwise stiff system. However, for present purposes their merits may outweigh their disadvantages. At the relatively low strain rates that are to be used, the main CRREL MTS machine should easily be able to compensate for variations in the deformation rate of the compliant platens. Some notes on compliant platens for this project are given below.

The objective of using compliant platens is to subject the specimen end plane to uniform pressure while permitting radial expansion equal to that in the specimen mid-plane. This may be achieved by several possible approaches: application of hydrostatic pressure; using a confined plug of a low-modulus elastic solid; or the combination of a low-modulus elastic plug and elastic ring.

Application of hydrostatic pressure: To do this we have to make the specimen a "piston" which has a short length of its end inserted into a cylinder filled with fluid. The wall of the cylinder has an O-ring seal. This approach, requires close tolerances and it is fairly complicated to introduce fluid into the cylinder and bleed out air. When all this has been done, there is still radial restraint from the O-ring and the annulus of pressurized fluid above it.

Confined plug of low-modulus elastic solid: The "compliant platen" developed earlier consisted of a plug of low modulus urethane ($E = 5.5 \times 10^3 \text{ lbf/in}^2$) confined in a thick-wall aluminum cylinder (0.25" wall thickness). The inside diameter of the cylinder allowed for a generous oversize tolerance on specimen diameter, and also for radial expansion of the specimen under load. All indications were that the device worked well, in spite of the tendency for bulging of urethane in the clearance annulus.

Combination of low modulus elastic plug and an elastic ring: In principle, a low modulus elastic plug can be confined within a metal ring that is designed to expand under axial loading to the same extent as the specimen. This eliminates the need for a clearance annulus wider than about 0.002". However, in order to design the platen it is necessary to pre-compute the radial strain.

To analyze the plug-ring combination we assume the following properties:

<u>Aluminum</u>	$E_{al} = 10 \times 10^6$	lb/in^2	$\nu_{al} = 0.33$
<u>Urethane</u>	$E_u = 5.5 \times 10^3$	lb/in^2	$\nu_u = 0.30$
<u>Ice</u>	$E_i = 1.23 \times 10^6$	lb/in^2	$\nu_i = 0.33$

The aluminum confining ring is assumed to be filled with urethane over its complete length, and to be pressurized by a radial pressure p . When the plug of urethane is loaded axially by an ice cylinder of the same diameter, the axial stress in both ice and urethane is σ_c . Thus the radial pressure p is

$$p = \frac{\nu_u}{1 - \nu_u} \sigma_c = 0.43 \sigma_c$$

The radial displacement of the aluminum ring, ΔR , is

$$\Delta R = \frac{p R^2}{E_{al} t} \left(1 - \frac{\nu_{al}}{2} \right)$$

where R and t are the radius and wall thickness of the ring respectively.

The radial strain of the ice in its mid-plane depends on the loading rate, i.e. on the relative magnitudes of elastic and viscous components of strain. For loading at very high rates, the pure elastic radial strain ϵ_{re} is

$$\epsilon_{re} = \frac{\Delta R}{R} = \nu_i \frac{\sigma_c}{E_i} = 2.68 \times 10^{-7} \sigma_c$$

For this case, equality of radial strain in the ice and the ring is given by

$$2.68 \times 10^{-7} \sigma_c = \frac{0.43 \sigma_c}{10 \times 10^6} \cdot \frac{R}{t} \cdot 0.835$$

With $R = 2''$, this gives $t = 0.268''$.

For practical purposes it is unrealistic to assume purely elastic strain in the ice. In polycrystalline freshwater ice, the axial strain at failure is typically of order 10^{-2} with mixed-mode rupture at strain rates less than 10^{-4} s^{-1} . Since there is some constant volume flow and some dilatation prior to final failure, we can take $\nu_i \approx 0.5$ for want of a better value. Thus, taking the radial failure strain as 5×10^{-3} , the required wall thickness for the aluminum cylinder is

$$5 \times 10^{-3} = \frac{0.43 \sigma_c}{10 \times 10^6} \cdot \frac{R}{t} \cdot 0.835$$

$$t/R = 7.18 \times 10^{-6} \sigma_c$$

Taking $\sigma_c \approx 1000 \text{ lb/in}^2$ and $R = 2''$, this gives $t = 0.0144''$. This is about $1/64''$ and probably too small for the simple machining we propose to employ. The strain in the aluminum is also too high for comfort in 60-61 T6 aluminum.

An "exact" design can be achieved for ice that fails at small strains, provided that results of pilot tests are available for guidance. Using a simple elastic ring around a low-modulus plug, it does not seem practical or feasible to have full radial compliance for very high strains. Taking into account the well-documented success of a very simple thick-wall device, we therefore propose to accept a design compromise along the following lines: (a) Design the aluminum ring to expand to somewhere near its elastic limit; (b) Rely on a small radial clearance plus the low shear modulus of the urethane to accommodate further expansion of the ice.

If we use 60-61 T6 aluminum, the elastic limit of strain can be taken as about 3.5×10^{-3} , and this value could perhaps be doubled using high-strength aircraft alloy (70-75). Taking the lower value:

$$3.5 \times 10^{-3} = \frac{0.43 \sigma_c}{10 \times 10^6} \cdot \frac{R}{t} \cdot 0.835$$

$$t/R = 1.03 \times 10^{-5} \sigma_c$$

Taking $\sigma_c = 1000 \text{ lbf/in}^2$ and $R = 2"$, $t = 0.0205"$. This might constitute a very good compromise when we can afford special machining.

At present, the machine shop foreman would prefer not to take the wall thickness below $1/16"$. This would allow the platen to strain to

$$\Delta R = \frac{0.43 \sigma_c}{10 \times 10^6} \cdot \frac{2}{0.0625} \cdot 0.835 = 1.14 \times 10^{-6} \sigma_c$$

With $\sigma_c = 1000 \text{ lbf/in}^2$, this is a radial strain of 1.14×10^{-3} . For low-rate tests, the radial clearance has to allow for an additional radial strain of about 4×10^{-5} , i.e. an annular clearance width of $0.008"$. As a practical matter, we need a clearance on the diameter of about $0.004"$, so this annulus is hardly a matter of great concern.

Thickness of the urethane plug: On the earlier design the urethane plug had a thickness that was 40% of the diameter. For the new platen we would like to limit the plug thickness so as to minimize the compliance, but at the same time the plug has to be thick enough to effectively pressurize the aluminum ring, and any slight bulging into the clearance annulus has to represent only a small fraction of the total volume. The plugs now on order are to be 0.75 in. thick, i.e. 19% of the diameter.

Differential thermal strain: In these calculations, no allowance has been made for differential thermal strain between the urethane and the aluminum, although we believe that the expansion coefficient for the urethane exceeds that for aluminum. At a later stage, differential thermal strain can perhaps be utilized to refine the design.

Uniaxial Tension Tests: The original intention was to pull simple cylindrical specimens, identical to those used for compression. However, present indications are that stress concentrations near the bonded interface will produce failure near the end planes, even when the bond itself remains intact. The selected alternative is to use a dumbbell specimen with bonded synthane end caps.

End caps will probably be made to match the diameter of the core as it comes from the drill, with slight "undersize" allowance. The ends of the core will be trimmed square to the correct length (≈ 12 in.), and the end caps will be bonded on, square to the axis, in a jig. The caps will then be used to mount the specimen in the lathe, where it will be turned using a form tool. If the starting diameter is 4.2 in., it will probably be necessary to make the neck diameter less than 4.0 in., say 3.75 in. With these diameters, the area of the end plane will be 1.25 times the area of the neck. The radius of the fillets will be twice the diameter of the neck. Judging from previous two-dimensional photoelastic studies, this should bring the stress concentration at the outer radius of the end planes to about 3%. Specimens will be checked for eccentricity by a comparator.

The cylindrical end caps will be made from linen-base Synthane, with a thickness approximately half the diameter. They will be drilled and tapped to take a 1" x 14 stud for "stiff" connection to the MTS machines. If necessary, steel studs will be cemented in after careful centering in the lathe. The preparation of the faces for bonding is a special technique that has been evolved over the past year or two, with only a brief description in the literature. The notes below therefore describe the procedure in detail.

Preparation of Synthane end caps for uniaxial tensile tests on ice: The cylindrical Synthane end cap is first machined to the required dimensions, with smooth surface finish. The face of the end cap that will be bonded to the ice is then prepared according to the following steps.

Step 1. The end cap is chucked accurately in the lathe, and the lathe is set up for a spindle speed of 125 rev/min, and a feed speed of approximately 4.7 in/min. A special sharp tool with 0° rake, 30° clearance, and 15° top angle is set in the tool post with its point parallel to the spindle axis and its cutting tip adjusted vertically to be on center. The tool is set to give an axial cutting depth of 0.010 in. at the center of the cap, the feed is engaged, and the tool makes a spiral traverse across the face of the cap. This produces a "hairy" surface that is incised to a depth of 0.010 in.

Step 2. The next step is to cut a set of circular grooves into the face, using the same special tool. The grooves are spaced 0.100 in. apart, i.e. 200 divisions advance on the perpendicular feed knob of the lathe. The depth of each groove is 0.050 in., i.e. the in-line travel of the toolpost is 0.50 in. from the setting used for the spiral scuffing of Step 1.

Step 3. A wire brush is applied lightly to the face of the cap while it is rotating, so as to remove long shreds of cut material. However, the fine "hairs" should not be removed, as these help in the bonding process.

Care should be taken throughout to ensure that the face of the cap is not touched by oil, oily tools, or oily hands.

Application of load to tension specimens: Load will be transferred to the tensile specimens through the bonded Synthane end caps, and the problem of the triaxial stress state produced by radial restraint will be dealt with by a faired transition in the dumbbell specimen. The end caps will be connected to the testing machine by 1" x 14 threaded steel rod. Above the specimen will be a tensile ball seat that was designed and built for this project.

A design has also been developed to permit load cycling between tension and compression, with zero backlash. The general idea is to attach the specimen to the machine rigidly at one end by a threaded rod, and to clamp it at the other end by peripheral dogs. Present plans do not call for alternation of tension and compression.

Measurement of force and displacement: Consideration has also been given to measuring the axial force and axial and radial displacement of the specimen during testing.

Measurements of axial force: External load cells will be attached to the testing machines. These will be of the electrical resistance strain gauge type, and their readings will be recorded in analogue form.

Measurements of axial displacement: Two options have been considered for measurement of axial displacement, both of them involving use of DCDT's. The preferred method is to attach a pair of DCDT's and their core rods directly to the cylindrical surface of the specimen. The two transducers will be set at opposite ends of a diameter and averaged electrically. Since the specimen will be constrained to displace axially, without tilting, bending or racking, it is not considered necessary to use three transducers, or to record the individual signals. The main unanswered question is whether the attachments will be stable. The carrying frames for the transducers are light, but the DCDT's themselves are quite heavy.

If the direct attachment is unstable because of creep at the suspension points, the DCDT's will rest on the lower platen of the machine, and only the core rods will be attached to the specimen. With this arrangement, twice as many transducers will be needed to give the differential displacement that yields strain over the mid-section of the specimen.

Measurements of radial displacement: Present plans are based on an assumed requirement for separate measurement of radial strain across two mutually perpendicular diameters. Two broad options have been considered. One involves direct attachment of measuring yokes, with displacement measured by DCDT's; the other involves non-contact proximity sensors (Kaman MULTI-VIT's).

The simplest arrangement is to sense radial displacement by measuring the change of diameter with a caliper of some kind. The first yoke built for the purpose was too heavy, and the yoke was modified to reduce its weight. The new yoke is to be suspended from the upper platen by a trapeze, and it is balanced so that only negligible vertical force is transmitted to the specimen. Contact with the specimen is made by conical points at the tips of 2-56 set screws, with penetration limited by steel ears on the yoke. As the specimen deforms axially, the yoke has to pivot on the contact points because the suspension does not change its length.

If the DCDT yoke proves unsatisfactory, the probable alternative will be use of Kaman MULTI-VIT's. Foil targets will be frozen to the ice, and proximity transducers will be supported on the lower platen at each end of each monitored diameter. Disadvantages are that two transducers and associated circuits are needed for each measurement of radial strain, and the targets move down relative to the transducer pickups as the specimen deforms axially.

Verification of Test Equipment and Procedures: It was originally planned to verify the test equipment and procedures described above prior to the field sampling program, so that we would be ready for testing immediately when we returned from the field. This has not been possible due to delays in procurement of the lathe and milling machine required for preparing the test specimens. As of 1 March the lathe has been obtained and we have been notified that the milling machine will be shipped to CRREL by 7 March 1981. Once the field program is completed, development of test equipment and procedures will continue.

Additional Work

At the request of Shell Development Company the feasibility of dating sea ice and performing automated thin section petrographic analyses were also briefly investigated.

Shell learned from Michel Metge, Consultant, that it may be possible to determine the age of multi-year sea ice by tritium dating. Metge indicated that additional information could be obtained from Dr. Gote Ostlund of the Tritium Laboratory at the University of Miami. Telecons with Dr. Ostlund revealed that by using tritium analysis it would be possible to determine whether the ice had formed prior to, or after 1962 when numerous thermonuclear tests were conducted. The testing released large quantities of tritium in the atmosphere and oceans. Prior to 1962, the ice would contain little tritium, and after that date, large quantities of tritium. The possibility of dating sea ice after 1962 was also discussed. Tritium has a half-life of 12.3 years. Given an estimate of the initial tritium content of the ice at the time of formation, and the amount of tritium remaining in the ice, it may be possible to determine the ice age. However, the problem is complicated by brine drainage, and flushing of melted freshwater through the ice. Dr. Ostlund indicated that the degree of contamination may be estimated by measuring the deuterium content of the ice. He said that he would be interested in working on the problem and would provide special containers for obtaining sea ice samples in the field for dating.

Shell is also interested in developing an automated petrographic thin section analysis technique. Rapid thin section analyses (grain size and orientation) would facilitate determining the effects of ice structure on ice strength. Through conversations with other CRREL staff, it was learned that Dr. Robert C. Lile of the University of Melbourne had developed a photometric method of crystallographic analysis. Copies of Lile's papers on the subject were sent to Shell. CRREL will also provide Shell photographs of sea ice thin sections in polarized light, in various orientations for further analysis.

Costs to Date

An estimate of the labor and materials costs to date are given below.

LABOR

Direct	26,419
Indirect	11,096

OTHER DIRECT

Materials	23,202
Travel	3,480
G and A and Overhead	27,848
Surcharge on Non-Gov't Contracts (15%)	<u>13,807</u>
Total Cost to Date	105,852

In addition, \$5,926 was spent by Shell to procure the lathe and milling machine. Cost to 1 March 1981 in the original proposal was estimated at \$175,841. We are therefore \$64,027 under budget.

Photo 1a Components for compliant platen mold.
Photo 1b

Photo 2 Bearing for rotating mold.

Photo 3 Pouring the freshly-mixed flexane

Photo 4a Centrifuging the Flexane to remove bubbles.
Photo 4b

Photo 5 Synthane end cap for uniaxial compression tests.

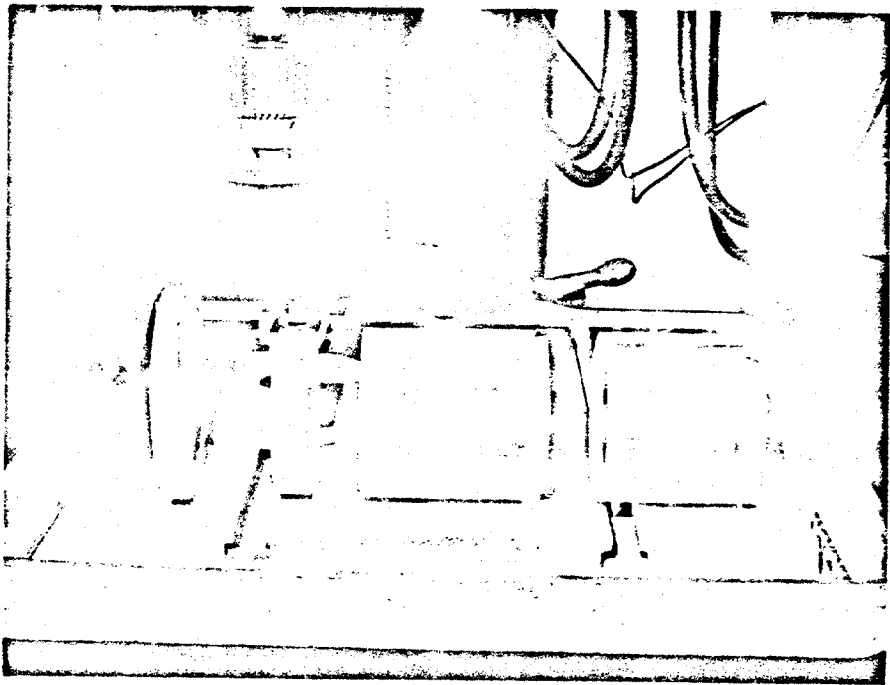
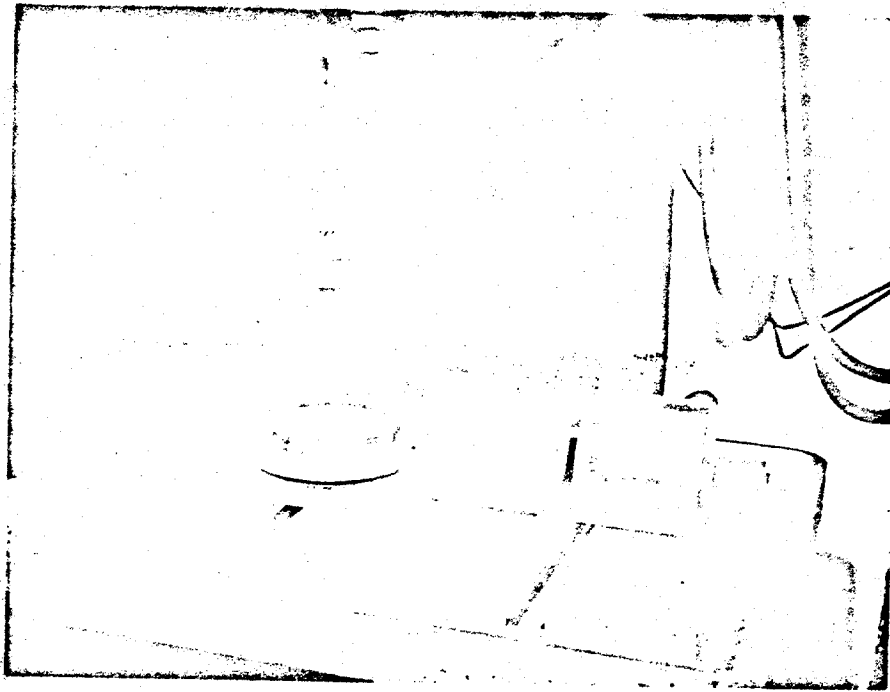


Photo 1a and 1b. Components for compliant platen mold.

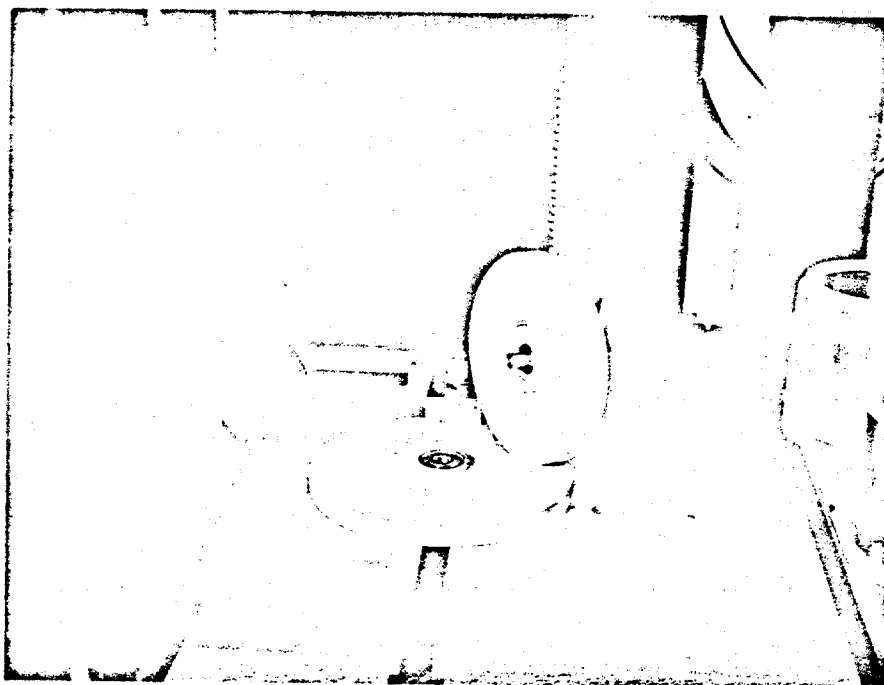


Photo 2. Bearing for rotating mold.

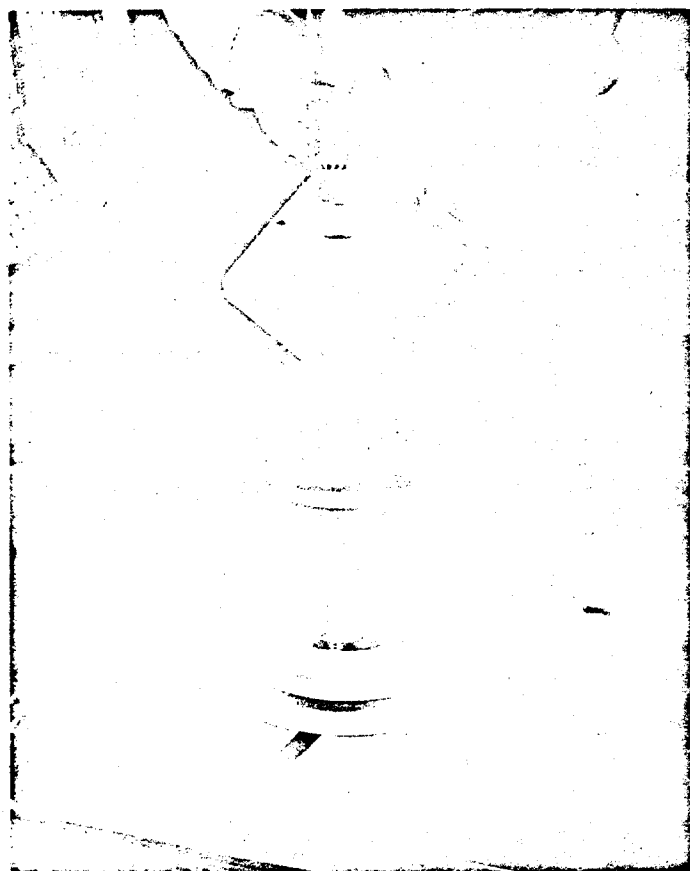


Photo 3. Pouring the freshly-mixed flexane

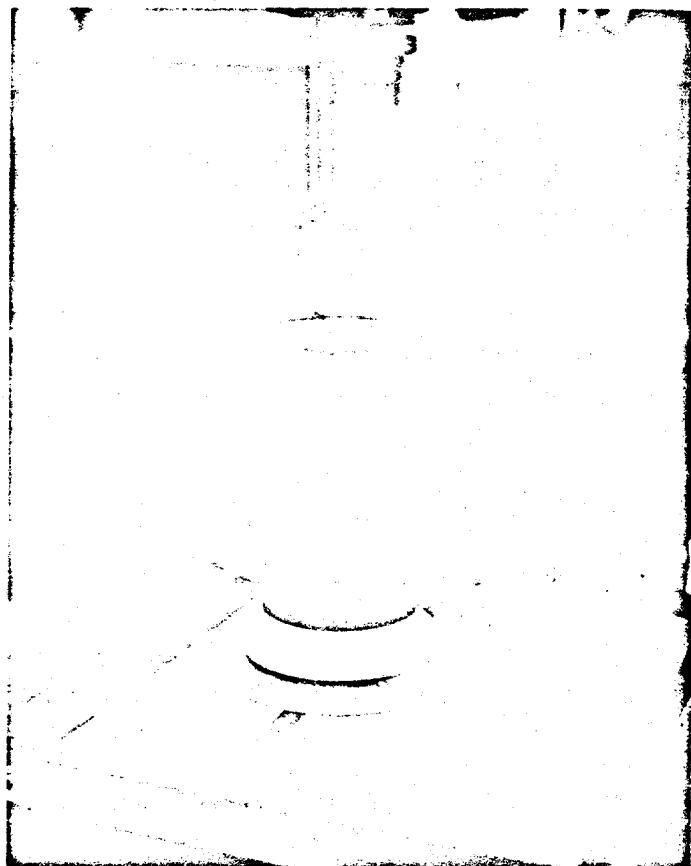
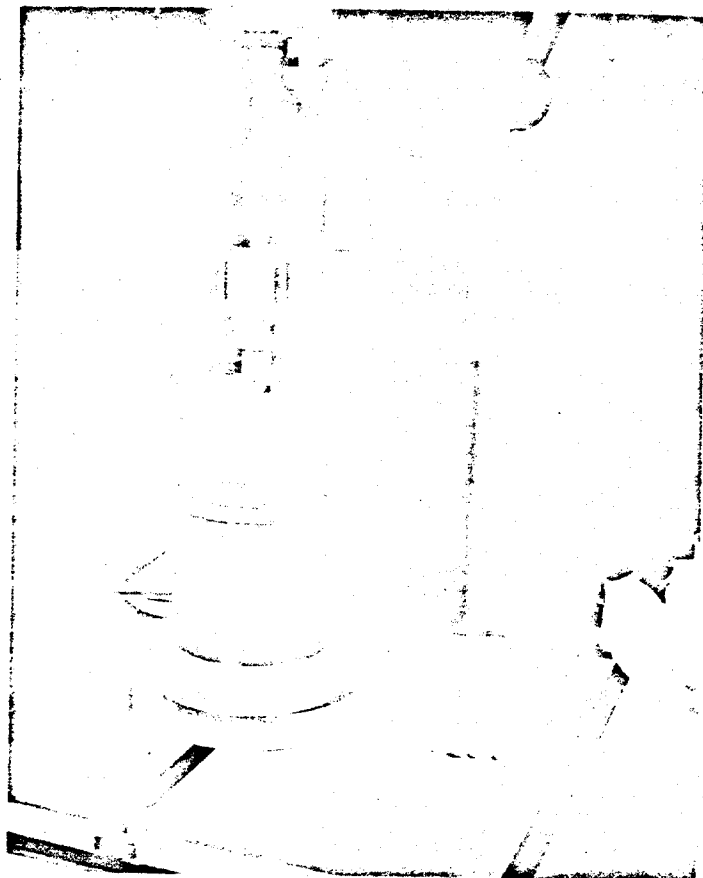


Photo 4a and b. Centrifuging
the Flexane to remove
bubbles.

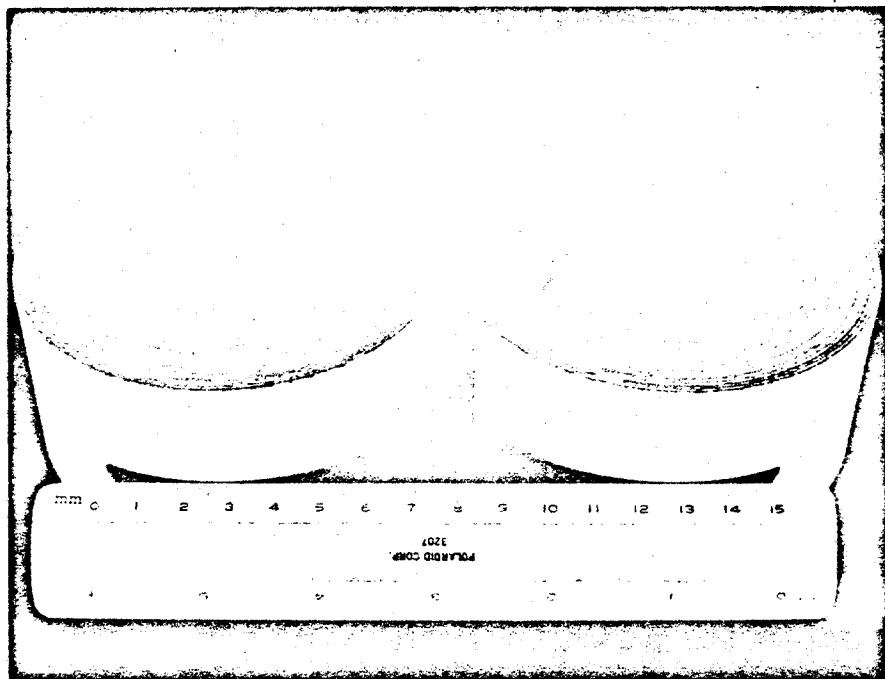


Photo 5. Synthane end cap for uniaxial compression tests.



DEPARTMENT OF THE ARMY JUN 23 1981
COLD REGIONS RESEARCH AND ENGINEERING LABORATORY, CORPS OF ENGINEERS
HANOVER, NEW HAMPSHIRE 03755

CRREL-EA

17 June 1981

SUBJECT: Mechanical Properties of Multi-Year Sea Ice

Gentlemen:

Enclosed for your information and files is a copy of the second progress report for the subject study. We look forward to discussing these and other results with you at the 30 June Participants Meeting in Hanover.

Sincerely,

Gordon F. N. Cox

1 Encl.
as

GORDON F. N. COX
Geophysicist
Applied Research Branch

Mechanical Properties of Multi-Year Sea Ice

Progress Report 2

1 June 1981

by

G.F.N. Cox; M. Mellor; and W.F. Weeks

US Army Cold Regions Research and
Engineering Laboratory

prepared for

Shell Development Company

United States Geological Survey

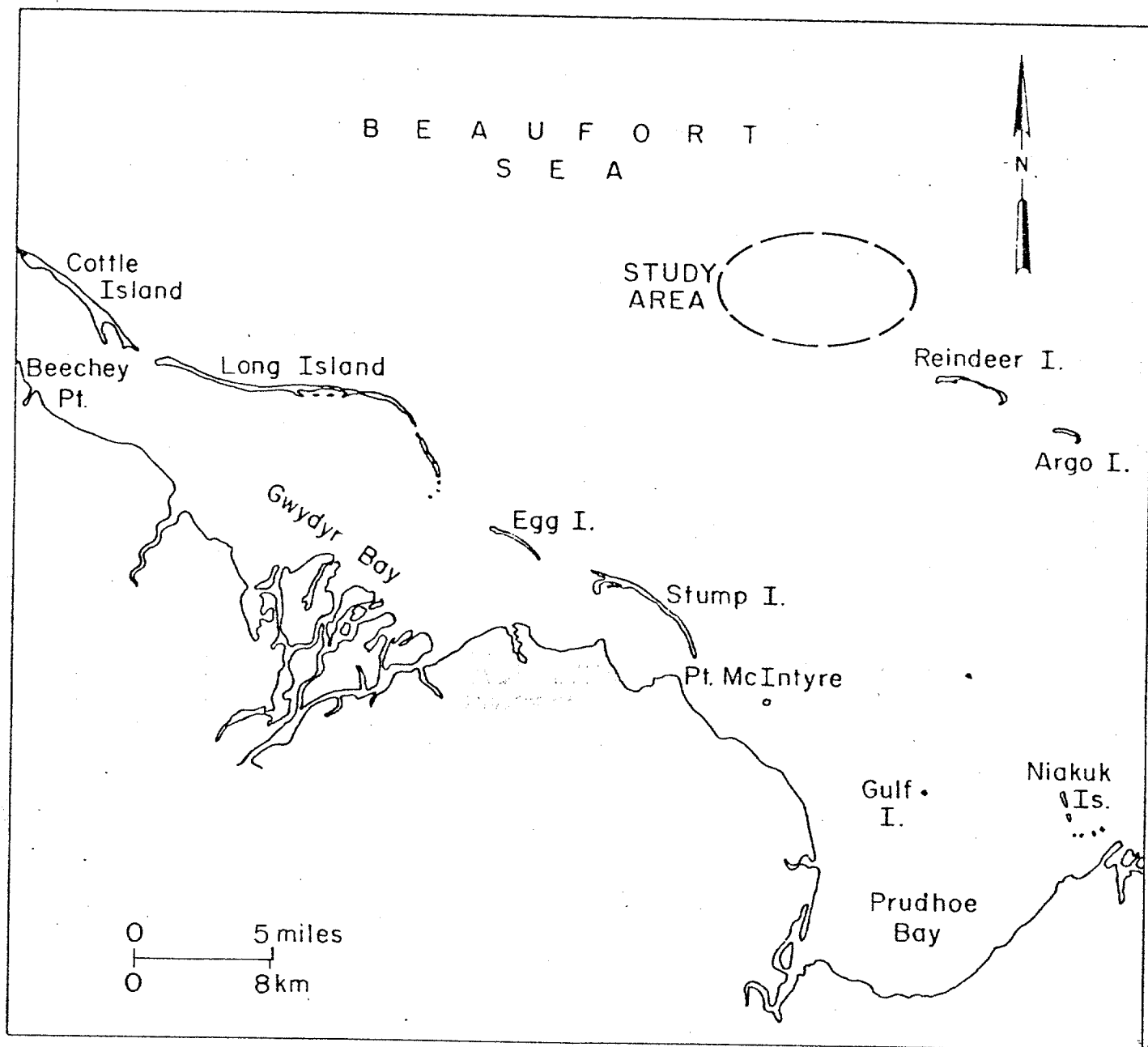


Figure 1: Map of Prudhoe Bay showing area where multi-year sea ice samples were obtained.

Introduction

This progress report describes the work performed in the Mechanical Properties of Multi-Year Sea Ice study from 1 March to 1 June 1981. During this period, the field ice sampling program was conducted offshore of Prudhoe Bay and work continued on the development of suitable testing techniques for studying the mechanical properties of sea ice.

Field Sampling Program

The field sampling program was performed during the first two weeks of April. NANA's facility in Deadhorse was used as a base camp and a Bell 205 was chartered from ERA Helicopters to get on the ice. On 1 to 2 April reconnaissance flights were flown to observe the distribution of multi-year ice in the Prudhoe Bay area. The area north and west of Reindeer Island was selected as the study area since it contained a wide variety of multi-year floes and was convenient to Deadhorse. The study area is shown in Figure 1. Coring and sampling operations began on 3 April and continued to 15 April. Weather during this period was excellent, -15°C and clear, and since there were no serious equipment problems, the field ice sampling program was completed one week earlier than expected. After coring and logging over 1000 feet of ice, the field party was ready to be carried back to Hanover.

Ten multi-year ridges and an area of presumably undeformed multi-year ice were sampled during the field program. Continuous core were also obtained from a ridge and undeformed area for detailed structural analyses. Horizontal and vertical cores were taken at two sites. In all, 329 meters of ice were cored, 223 meters were shipped to Hanover, resulting in 590 potential test specimens. Only 304 test samples were needed to perform Tasks 2 and 3.

Ten multi-year ridges were sampled at sites located on several multi-year floes located north and west of Reindeer Island. No attempt was made to obtain the exact position of the different ridges as there is no reason to believe that there should be any relation between position and ridge characteristics. The ridges and floes did not appear to be grounded. All the ridges studies were part of the fast ice belt at the time they were sampled. However, at sometime during the previous month there had been some limited lead development between the sample sites and the mainland with lateral motions of several hundred meters. The multi-year floes were generally rounded and quite varied in size. Some of the larger floes had lateral dimensions of 500 m to a kilometer. Figures 2 and 3 give general aircraft views of some of these floes. Figure 3 is in fact a view of the floe which contained Ridges 1 and 2. The structure visible in the picture is a one room building installed on this floe by Vaudrey and Associates.

In selecting specific ridges, an attempt was made to include both large and small multi-year ridges. In all cases the ridges sampled were well defined linear features that were readily discernable from the air. On each ridge, 4 cores were obtained, a pair of cores from each of two sites. A distance of 17 to 63 cm separated the cores in each pair at a given site. Figure 4 shows the pair A and B on Ridge 2 that are separated by 33 cm. Sites AB and CD are separated by larger distances varying from 14 to 46 m. A summary of the A-B, C-D and AB-CD distances are given in Table 1 which also gives the elevation of the drill sites above the mean level of undeformed ice in the near vicinity. The idea behind this sampling scheme was to sample two different locations on 10 ridges with a sample distance large enough so that the specimens are clearly from different areas of the same ridge and at each of these locations obtain 2 replicate cores

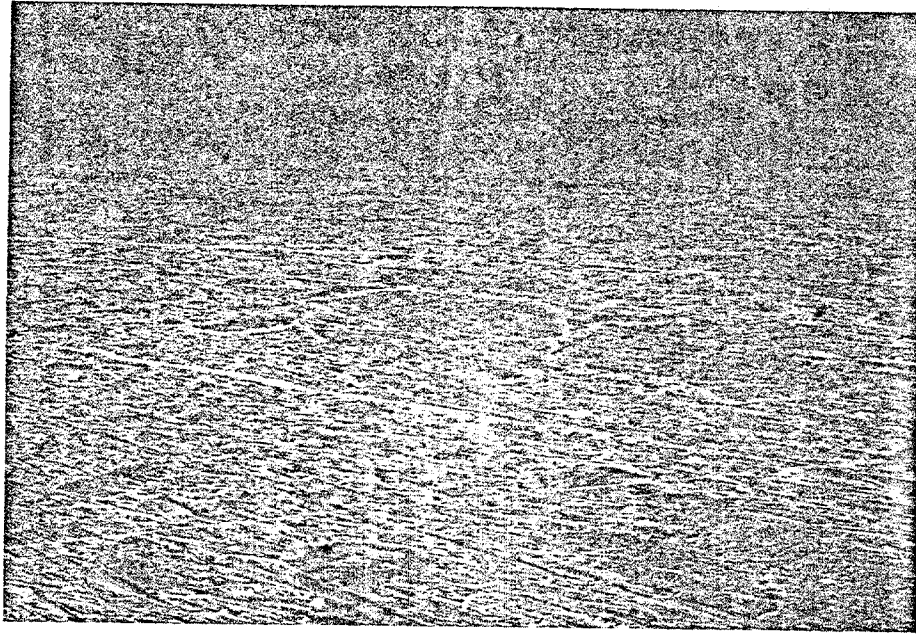


Figure 2: Areal view of study area.

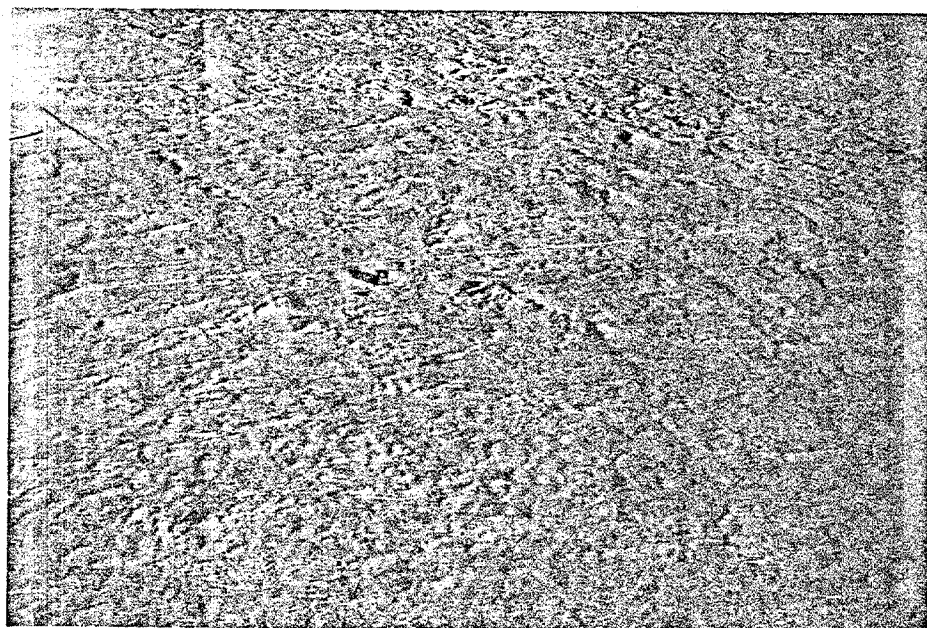


Figure 3: Areal view of multi-year floe which contained Ridges 1 and 2. Floe also studied by Vaudrey and Associates.

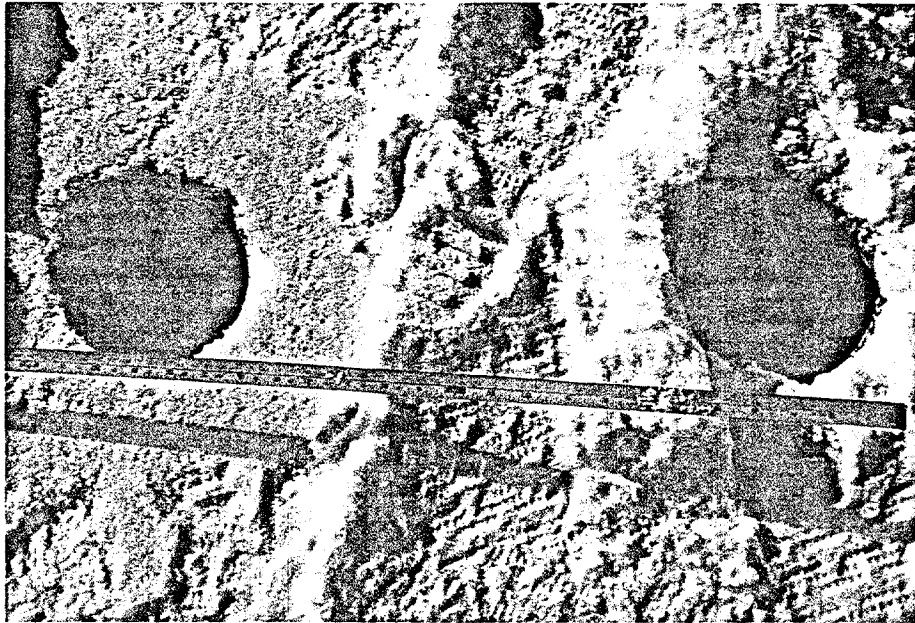


Figure 4: Core holes A and B on Ridge 2.



Figure 5: Surface view of floe containing Ridges 1 and 2.

RIDGE MEASUREMENTS

Ridge	HT A & B	HT C & D	Dist A to B	Dist C to D	Dist AB to CD
1	2.1 m	1.7 m	45 cm	47 cm	20 m
2	2.7 m	1.7 m	33 cm	41 cm	25 m
3	2.1 m	1.8 m	40 cm	43 cm	30 m
4	4 m	3.7 m	63 cm	47 cm	15 m
5	2.1 m	1.7 m	21 cm	24 cm	20 m
6	5.2 m (A1)	1.8 m (A2)	-----	-----	18 m
7	1.5 m	.6 m	17 cm	21 cm	36 m
8	1.8 m	3.7 m	17 cm	20 cm	27 m
9	3.7 m	1.8 m	21 cm	37 cm	46 m
10	2.7 m	2.1 m	26 cm	22 cm	14 m

Ridge	HT A & B	HT C & D	Dist A to B	Dist C to D	Dist AB to CD
1	7 ft	5.5 ft	17.7 in	18.5 in	65 ft
2	9 ft	5.5 ft	13 in	16.1 in	82 ft
3	7 ft	6 ft	15.7 in	16.9 in	98 ft
4	13 ft	12 ft	24.8 in	18.5 in	49 ft
5	7 ft	5.5 ft	8.3 in	9.4 in	65 ft
6	17 ft	6 ft	-----	-----	59 ft
7	5 ft	2 ft	6.7 in	8.3 in	118 ft
8	6 ft	12 ft	6.7 in	7.9 in	89 ft
9	12 ft	6 ft	8.3 in	14.6 in	150 ft
10	9 ft	7 ft	10.2 in	18.7 in	45 ft

Table 1: Hight and distance between ridge sample sites

as close to each other as reasonable without developing drilling difficulties. The exact spacings were controlled by the geometries of the various ridges. A brief summary of the general characteristics of the different ridges follows.

Ridges 1 and 2 were located on a large floe that was studied extensively by Vaudrey and his group. Figures 3 and 5 show general air and surface views of this floe. The Ridge 1 sites were also located on the same ridge where the first set of vertical and horizontal cores were collected. Figures 6 and 7 show surface views of this ridge. It might be remarked that in general the surface expressions of all the ridges sampled are similar. All show rounded outlines indicating that they have undergone surface melt. In general, the surface is covered with a thin snow cover. The ridge height varies in an irregular pattern as one moves along the ridge. Figures 8 and 9 show two surface views of Ridge 2 and Figure 10 shows an aerial view. Figure 11 shows an aerial view of Ridge 3, note figures for scale. The portion of the ridge studied is located near the boxes in the right center of the picture. Ridge 4 was high with the drill sites located 4 and 3.7 m above the surrounding floe (Figures 12 and 13). This ridge also showed a split exposing its internal structure (Figure 14). Ridge 5 was a lower ridge located in the near vicinity of Ridge 4 (Figure 15). Ridge 6 was the highest ridge sampled with a drill site 5.2 m above the surrounding ice. Surface views of this ridge are shown in Figures 16 and 17. The blocky nature of portions of this ridge suggest that it is composed of second-year ice. This conclusion was also supported by the observation that a number of voids were present in the core. In fact, the general condition of ice in this ridge was so poor that coring was terminated after drilling only one hole at each site. Ridge 7 was a low ridge that did not possess any particularly distinguishing features. It is shown in Figures 18 and

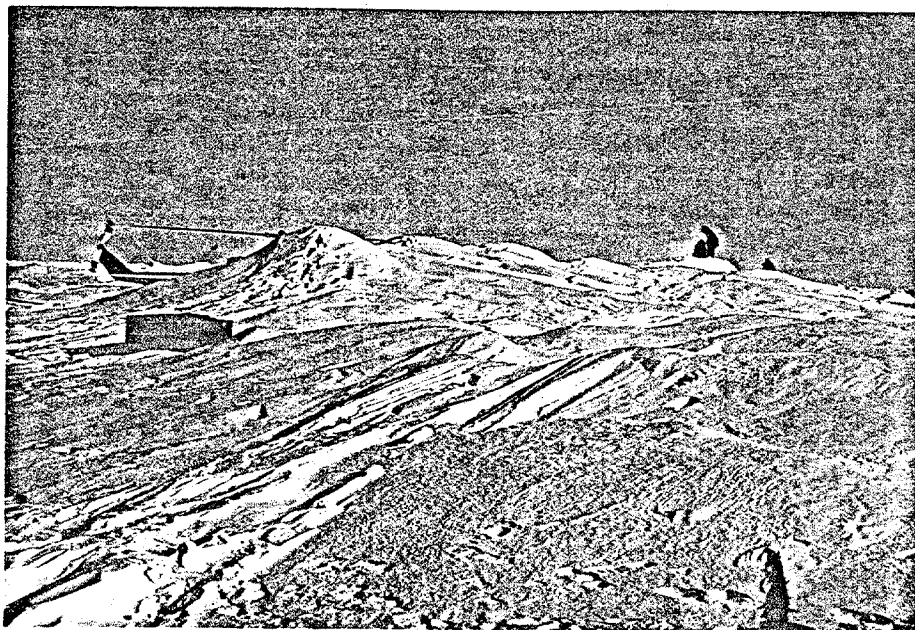


Figure 6: Photograph of Ridge 1. of Ridge

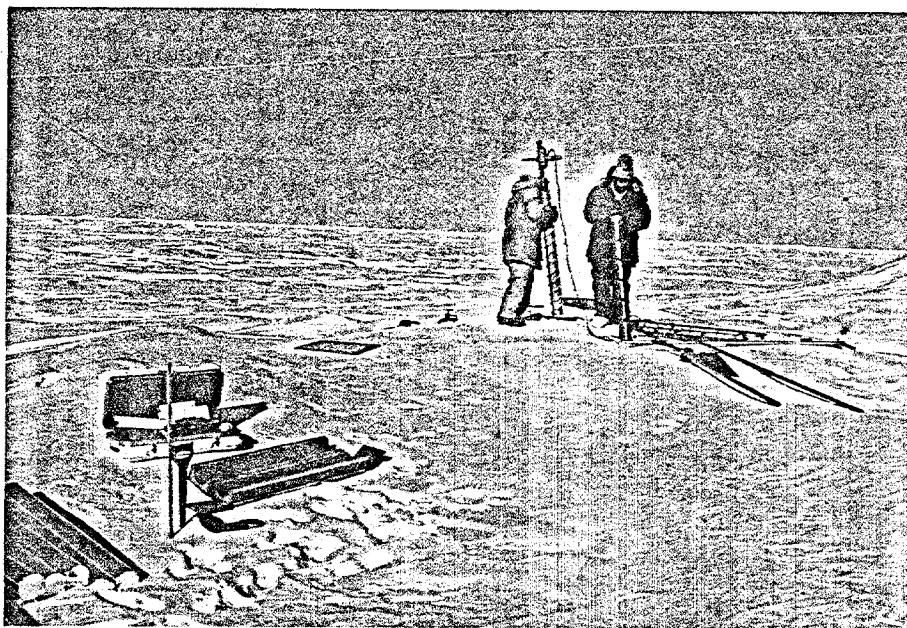


Figure 7: Photograph of Ridge 1.

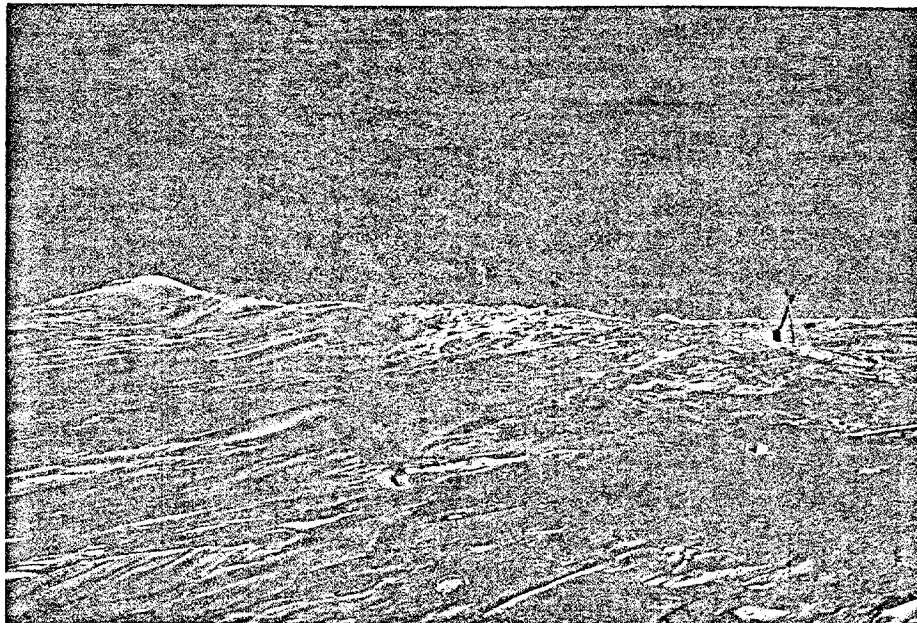


Figure 8: Photograph of Ridge 2.



Figure 9: Photograph of Ridge 2.

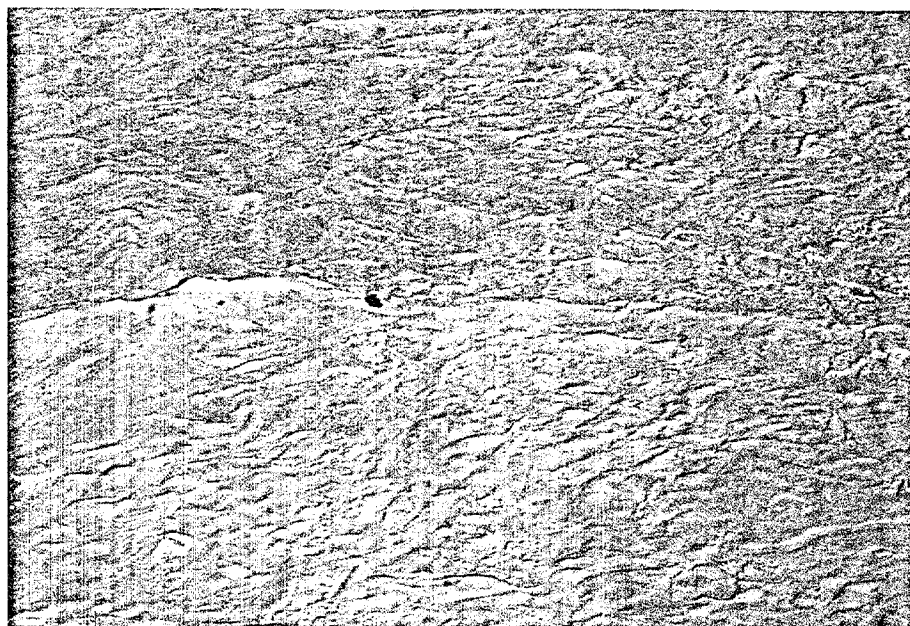


Figure 10: Areal view of Ridge 2.

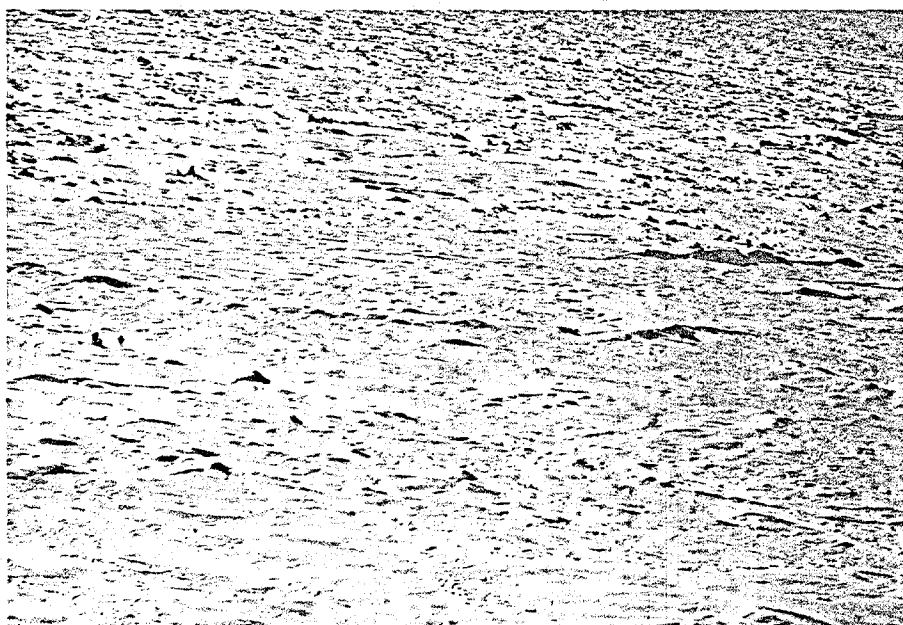


Figure 11: Areal view of Ridge 3.

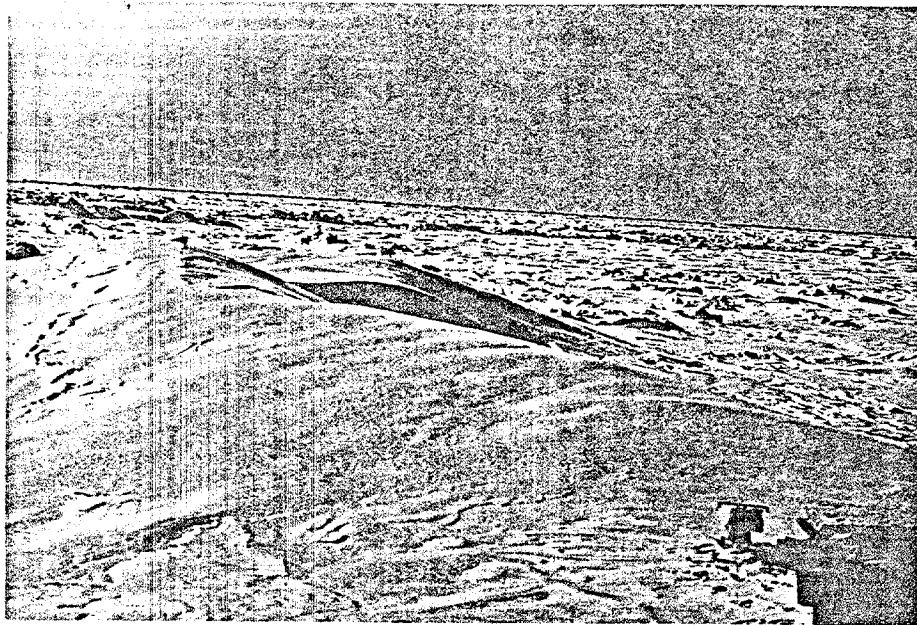


Figure 12: Photograph of Ridge 4.

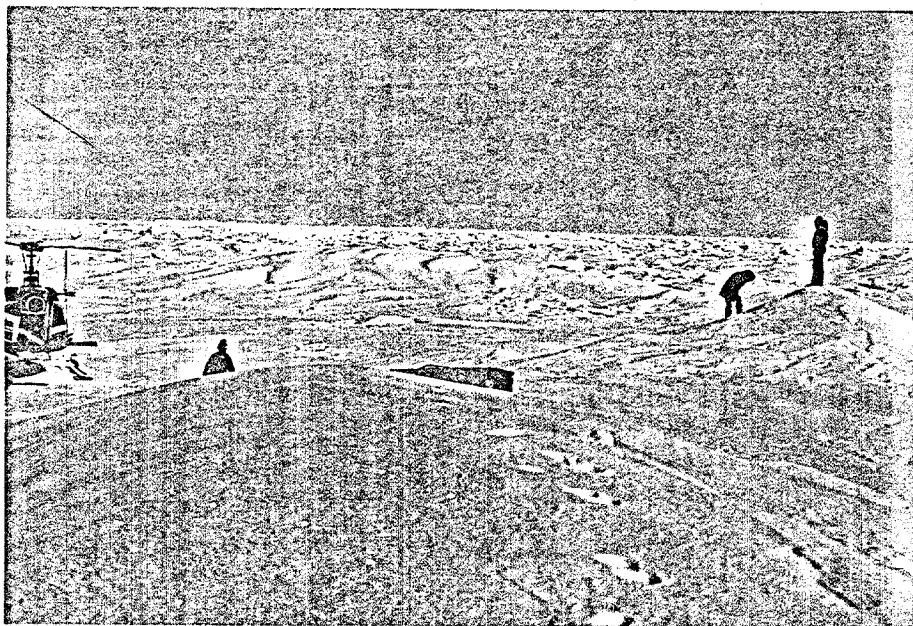


Figure 13: Photograph of Ridge 4.

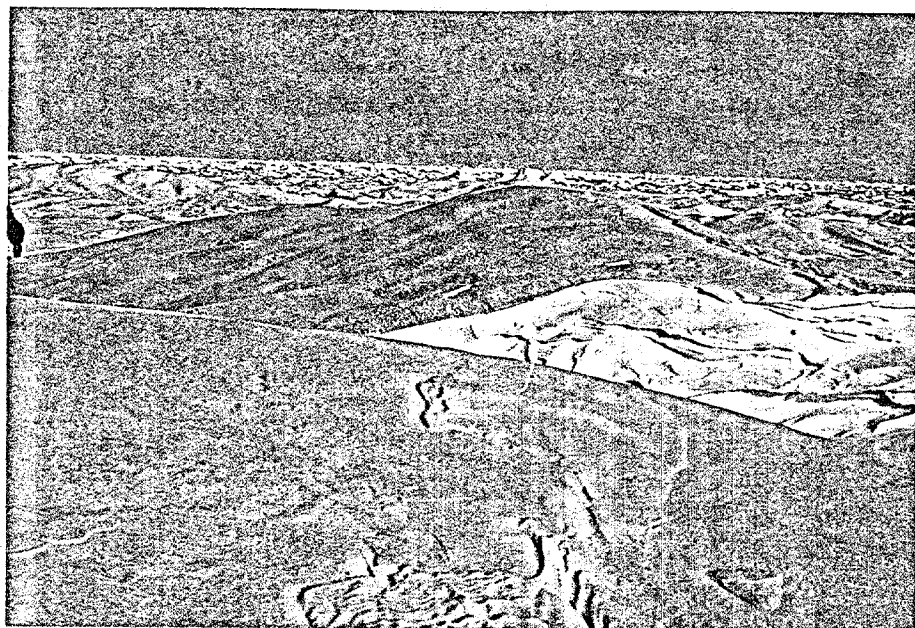


Figure 14: Split portion of Ridge 4.

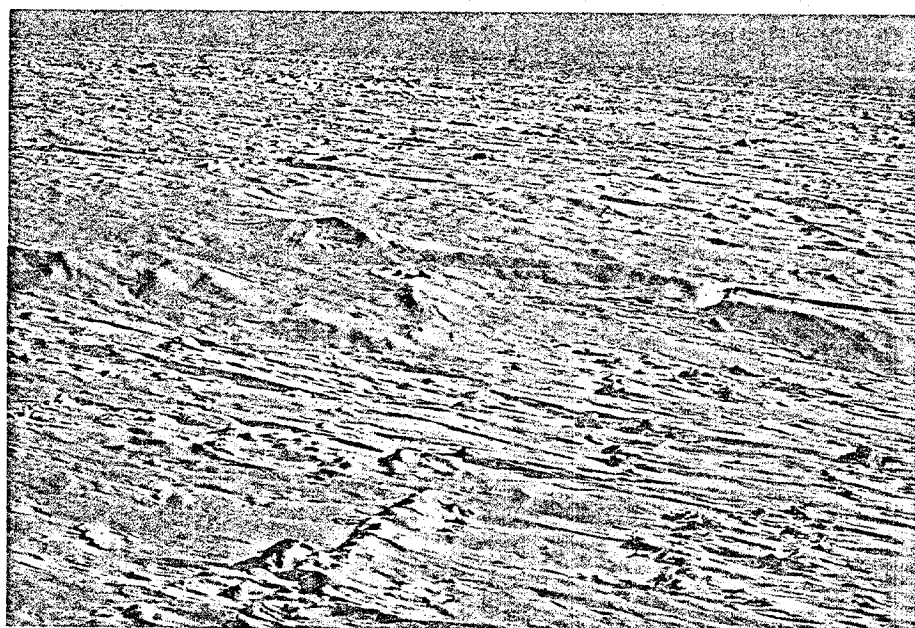


Figure 15: Areal view of Ridges 4 and 5.

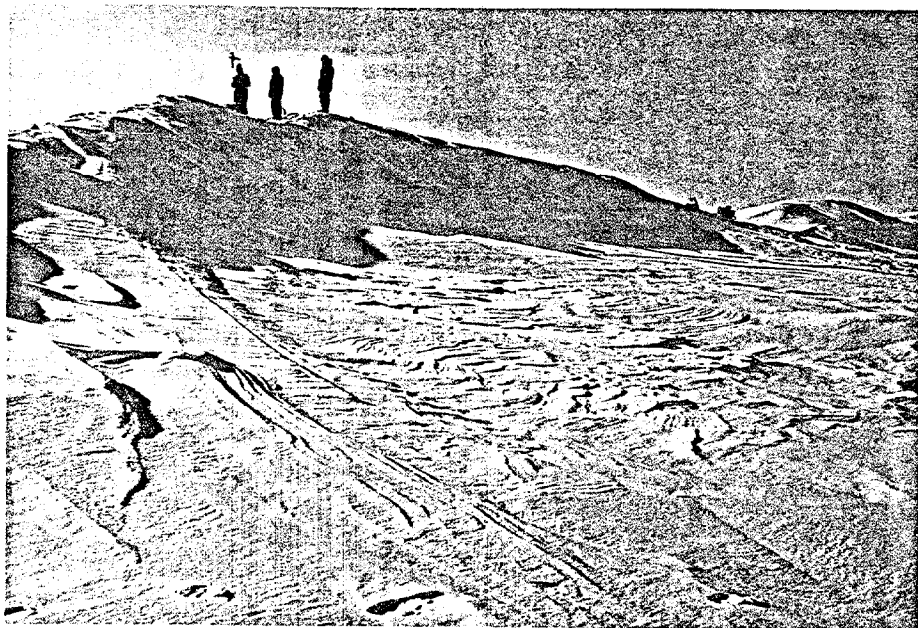


Figure 16: Photograph of Ridge 6.



Figure 17: Photograph of Ridge 6.

19. Figure 20 shows an aerial view of Ridge 8 which was a long distinctive feature. Ridges 9 and 10 were both located on the same large floe. Figures 21 and 22 show views of Ridge 9. An aerial view of Ridge 10 is given in Figure 23.

The undeformed multi-year ice that was cored was obtained at a location near the Vaudrey's hut near Ridges 1 and 2. The first set of "matching" horizontal and vertical cores were also obtained from the same general location; on Ridge 1 from an area where Vaudrey's group had quarried ice for test beams. Figure 24 shows this location during the time horizontal coring was proceeding. It should also be noted that the continuous core collection from a multi-year pressure ridge was also obtained near here at a location where Vaudrey had installed a thermistor string. Finally, the second set of matching horizontal and vertical cores were collected from a large ridge that has split cross-wise thereby allowing horizontal coring. A view of this site is shown in Figure 25.

Tables 2, 3, and 4 present data on the length of hole drilled, the estimated number of specimens obtained, and the amount of core that was shipped to CRREL. A total of 467 samples are available from the various multi-year pressure ridges that were sampled. It was hoped to be able to collect at least 6 samples from each drill site (there were 4 drill sites on each ridge). The actual number of samples obtained at one site varied from 8 to 16. It was also planned to collect 2 samples from above sea level and 4 samples from below at each site. This requirement was met and usually exceeded at all sites except at 7C and D where a low freeboard resulted in only one sample above sea level at each site and at 4A and B where a high freeboard resulted in only 2 samples below sea level at each site. About 123 samples were collected of undeformed multi-year ice.



Figure 18: Photograph of Ridge 7.

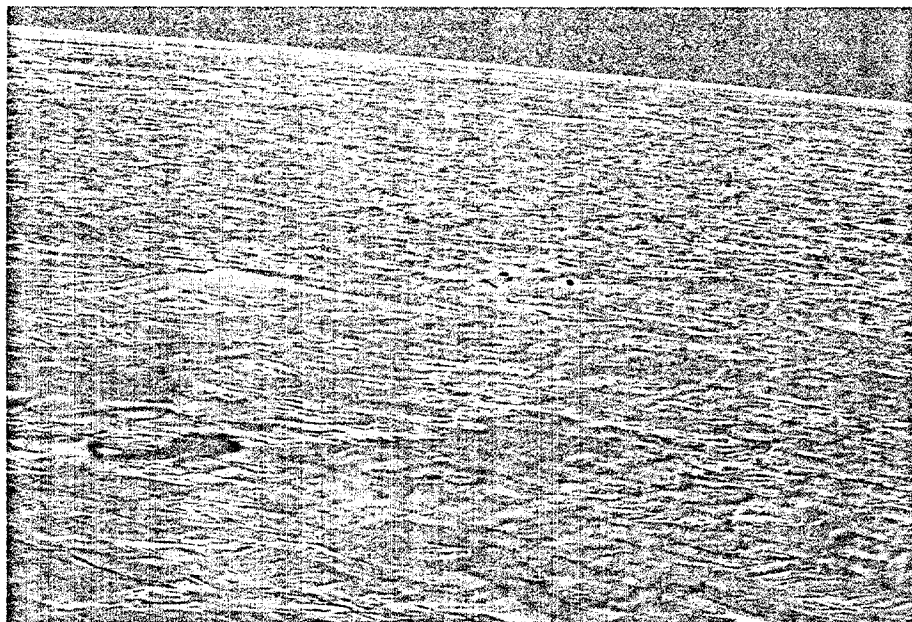


Figure 19; Areal view of Ridge 7.



Figure 20: Areal view of Ridge 8.

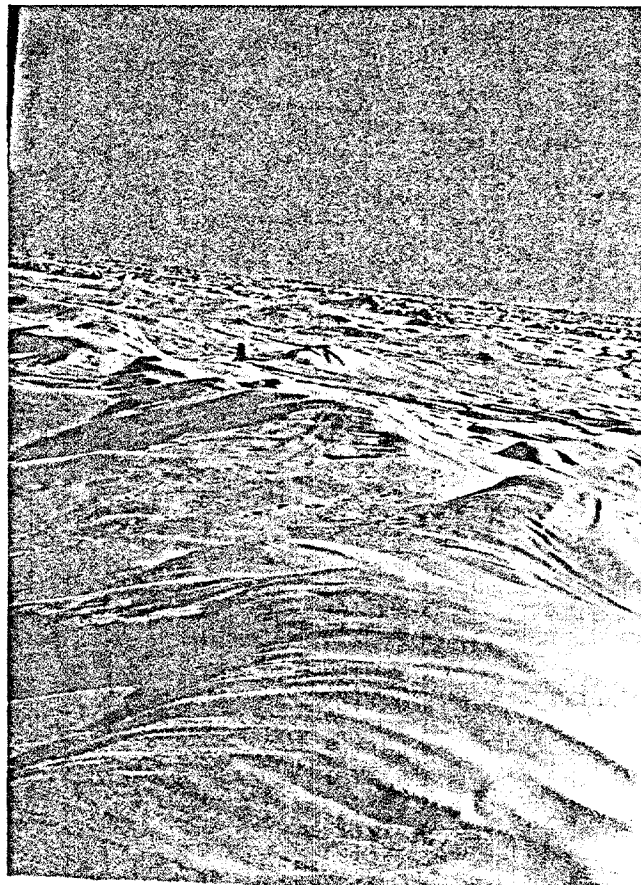


Figure 21: Photograph of Ridge 9.



Figure 22: Areal view of Ridge 9.



Figure 23: Areal view of Ridge 10.

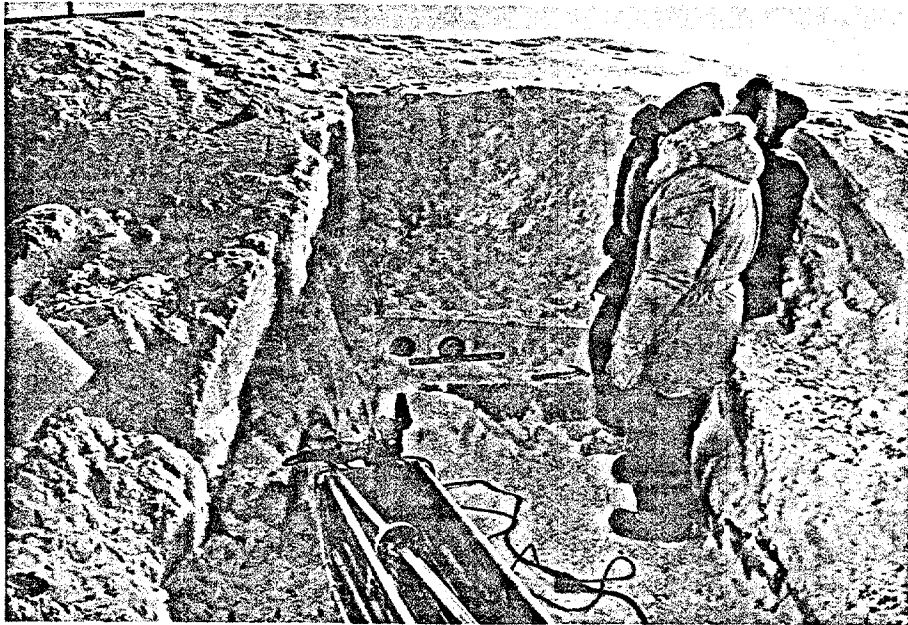


Figure 24: Horizontal core being obtained at Vaudrey's ice quetry.

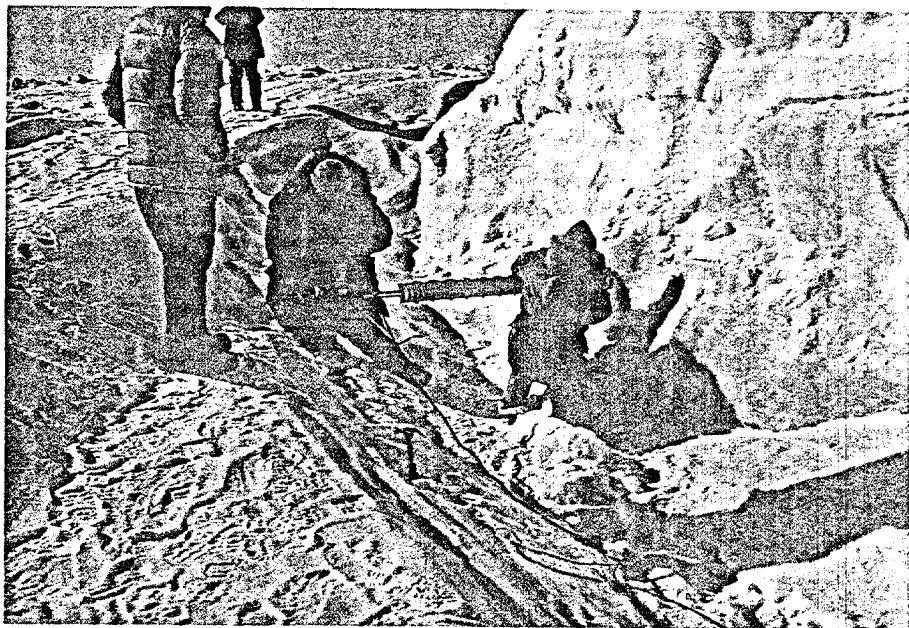


Figure 25: Horizontal coring in split ridge.

Ridge No	Site	Ridge Height (m)	Depth of Penetration (m)	Approximate No. of Samples			Core Length Retained
				Above Sea-Level	Below Sea-Level	Total	
1	A	2.1	4.75	6	6	12	4.70
	B	2.1	5.65	4	10	14	5.19
	C	1.7	4.30	3	6	9	3.73
	D	1.7	4.22	3	6	9	3.48
2	A	2.7	4.53	6	5	11	3.77
	B	2.7	5.09	6	6	12	4.82
	C	1.7	5.14	3	8	11	4.44
	D	1.7	5.37	4	5	9	3.61
3	A	2.1	5.47	3	8	11	3.99
	B	2.1	4.07	5	4	9	3.76
	C	1.8	4.46	4	6	10	3.76
	D	1.8	3.99	4	5	9	3.57
4	A	4.0	4.68	9	2	11	4.63
	B	4.0	4.78	10	2	12	4.78
	C	3.7	5.82	7	5	12	4.31
	D	3.7	5.63	9	5	14	5.63
5	A	2.1	5.38	7	8	15	5.28
	B	2.1	4.30	6	5	11	4.30
	C	1.7	5.92	4	10	14	5.47
	D	1.7	5.88	3	10	13	5.29
6	A1	5.2	7.29	7	6	13	4.60
	A2	1.8	6.29	5	9	14	5.14
7	A	1.5	5.92	4	9	13	4.81
	B	1.5	6.93	3	13	16	6.30
	C	0.6	6.07	1	8	9	3.01
	D	0.6	5.76	1	9	10	3.30
8	A	1.8	4.68	4	5	9	3.23
	B	1.8	5.45	4	8	12	4.16
	C	3.7	6.25	6	5	11	3.86
	D	3.7	7.00	4	6	10	3.27

Table 2: Data on the coring of multi-year pressure ridges. The symbols H and V indicate paired sets of Horizontal and Vertical cores from such ridges.

Ridge No	Site	Ridge Height (m)	Depth of Penetration (m)	Approximate No. of Samples			Core Length Retained
				Above Sea-Level	Below Sea-Level	Total	
9	A	3.7	5.70	7	4	11	3.63
	B	3.7	5.12	7	3	10	3.28
	C	1.8	5.45	4	7	11	3.63
	D	1.8	4.98	4	5	9	2.97
10	A	2.7	5.81	3	6	9	2.94
	B	2.7	4.99	4	4	8	2.64
	C	2.1	5.73	3	8	11	3.63
	D	2.1	5.99	3	7	10	3.63
Total			204.84			424	156.54
H	1		4.06			7	2.31
	2		3.02			5	1.66
V	1		2.18			4	1.32
	2		2.30			3	1.02
	3		2.31			2	.66
	4		2.11			3	1.34
H	1		3.26			5	1.65
	2		3.27			3	.99
V	1		3.30			2	.66
	2		3.21			1	.33
	3		2.30			3	.99
	4		3.18			5	1.65
Total			34.50			43	14.58
Thin-Section and Salinity Core			8.18				8.02
Grand Total			247.52			467	179.14

Site	Depth of Penetration (m)	Total No. of Samples	Core Length Retained (m)
C1	3.35	2	.66
C2	3.56	7	2.31
C3	3.31	7	2.31
C4	3.35	6	1.98
C5	3.17	6	1.98
C6	3.32	5	1.65
C7	3.31	5	1.65
C8	3.14	5	1.65
C9	3.31	6	1.98
C10	3.27	6	1.98
C11	3.00	6	1.98
C12	3.29	5	1.65
C13	3.20	5	1.65
C14	3.28	4	1.35
C15	3.13	5	1.65
C16	3.35	6	1.98
C17	3.10	4	1.35
C18	3.34	5	1.65
C19	3.34	5	1.65
C20	3.23	4	1.35
C21	3.17	7	2.31
C22	3.30	5	1.65
C23	3.13	4	1.35
C24	<u>3.14</u>	<u>5</u>	<u>1.65</u>
Total	78.09	123	40.74
Salinity and Temp.	3.18		3.18

Table 3: Data on coring of undeformed multi-year ice.

Ice Cored	Length Cored (m)	Length Retained (m)	Percentage Retained	Approx. No. of Test Specimens
Multiyear pressure ridges				
(1) Vertical holes	204.84	156.54	76	424
(2) Paired vertical and horizontal cores	34.50	14.58	42	43
(3) Thin section and salinity core	8.18	8.02	87	---
Undeformed multiyear ice				
(4) Temperature and salinity core	3.18	3.18	100	---
(5) Vertical holes	78.09	40.74	52	123
Totals	328.79	223.06		590

Table 4: Summary of core and sample recovery information.

There are large variations in the percentage of ice collected to that which was actually retained (see Table 4). These variations are readily explainable. Two cores were taken strictly to provide ice for the determination of ice temperature, salinity, and internal structure. In this case, all the ice cored was retained (except for a small, badly shattered segment that was judged unusable even for these purposes). The ice from the multi-pressure ridges was collected first during a time when only one person was available to log core. As core logging was the slowest part of the sampling procedure, time was not available to trim all samples to size. Therefore, an appreciable amount of extra ice was loaded in order to provide ice for thin sections and additional salinities. Later when undeformed multi-year ice was being collected, two persons were logging core, samples were trimmed to 33 cm lengths, and it was not necessary to collect additional ice for thin sections and salinities. A recovery rate of 60% is probably a reasonable figure to use in planning future programs involving vertical coring. The low recovery rate (42%) from the two sites where paired vertical and horizontal cores were collected was caused by the fact that general quality of the ice at these locations was poor.

Ice Sampling Procedures

Drilling: Four and one-quarter inch diameter ice cores were obtained with a fiberglass coring auger specifically designed and fabricated for this study (see Progress Report 1). The auger was driven by a 3/4-inch, 3/4 HP electric drill (Figure 26). Power was supplied by a 1700 watt generator. Core was obtained at depth by attaching CRREL auger extension rods to the core barrel. To prevent vibration of the extension rods and core barrel down the hole, spacers having an outside diameter of 4 1/4-inches were attached around the extension rods. The new large diameter auger produced high quality ice core up to 120



Figure 26: Coring equipment.

inches in length.

Some problems were encountered in breaking the core, coring in unsound ice, and on the last day in the field, the upper portion of one of the flights on the auger barrel failed. Efforts to break off the core by engaging the core dogs in the head proved to be unsuccessful. In fact, on many occasions, the core dogs scored the lower portion of the core sample while attempting to lift the unbroken core up the hole. To break the base of the core from the surrounding ice, a tee-bar was attached to the core barrel or upper extension rod and pounded with a hammer. The hammer blows generally caused the ice to break at or near the base of the core. This method of core removal worked, but is certainly unsatisfactory and must be improved. The core dogs also resulted in other problems. Frequently, in ice containing large voids, the core would be turned down by the core dogs. One or both of the spring loaded dogs would fall into a void, and as the core barrel rotated, the core dogs would mill down the core. Again the use of core dogs in core retrieval needs to be reviewed.

On the last day of the field program, the upper portion of one of the flights on the core barrel failed. During coring, cuttings would accumulate above the core barrel. When the barrel was lifted, the cuttings compacted and exerted stress on the top of the auger flights. It is therefore necessary to reinforce the auger flights near the top of the barrel. At this time, the entire length of flight is only epoxied to the fiberglass tube. It should be noted that another core barrel was available to obtain 4 1/4-inch diameter core.

Core Measurements: Immediately after the core was retrieved from the ice, a temperature reading would be taken in the bottom of the core. This was accomplished by drilling a hole into the center of the core with a portable electric hand drill and inserting a thermistor probe into the ice (Figure 27). While the

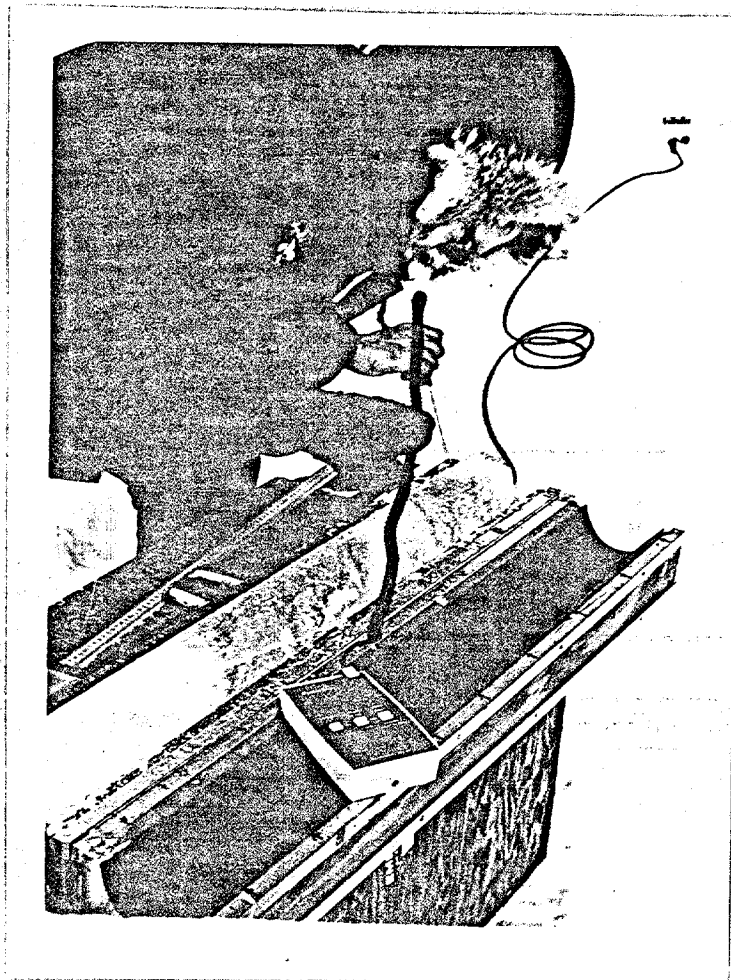


Figure 27: Taking ice temperature measurements.

temperature equilibrated, the length of core was measured and the ice was examined for suitable strength test samples (Figure 28). Generally, one to three, 33 cm long test samples were obtained from each barrel of ice. The samples were cut to length with a coarse tooth pruning saw. The lower 5 cm of core, from which the ice temperature was obtained, was also usually saved for an ice salinity measurement. This ice was placed in a numbered one-quarter freezer container. Pieces less than 33 cm long were measured and discarded. It was reasoned that a 33 cm long sample would be needed for easy machining to final test specimen dimensions. Both discarded and test ice were cataloged for length and depth. The position of the temperature and salinity sample were also noted so that temperature and salinity profiles could be plotted. The test ice was then placed in numbered core tubes taking note of the core tube number and position of the test ice in the tube (Figure 29). The core tubes were packed in wooden boxes lined with insulation for shipment back to Deadhorse.

In Deadhorse, the core tubes were transferred to insulated boxes for shipment back to Hanover. Details on ice shipping are given below. The ice salinity samples were melted and salinities were determined with a conductivity bridge (Figure 30).

Shipping and Storage of Ice Samples

Shipping and storage of the core samples was an important part of the ice sampling program. Samples were temporarily stored in Deadhorse and Anchorage and shipped from Deadhorse to Anchorage and on to Hanover.

During the ice sampling program, air temperatures in the Prudhoe Bay area remained below -15°C . Since ambient temperatures were close to the $\text{NaCl}\cdot 2\text{H}_2\text{O}$ eutectic, -21°C , and because the multi-year ice had a low salinity, usually less than 4 ‰ (parts per thousand), no special measures were taken to refrigerate



Figure 28: Examining core for suitable test samples and logging ice.



Figure 29: Logging site. Note core tubes and salinity containers.

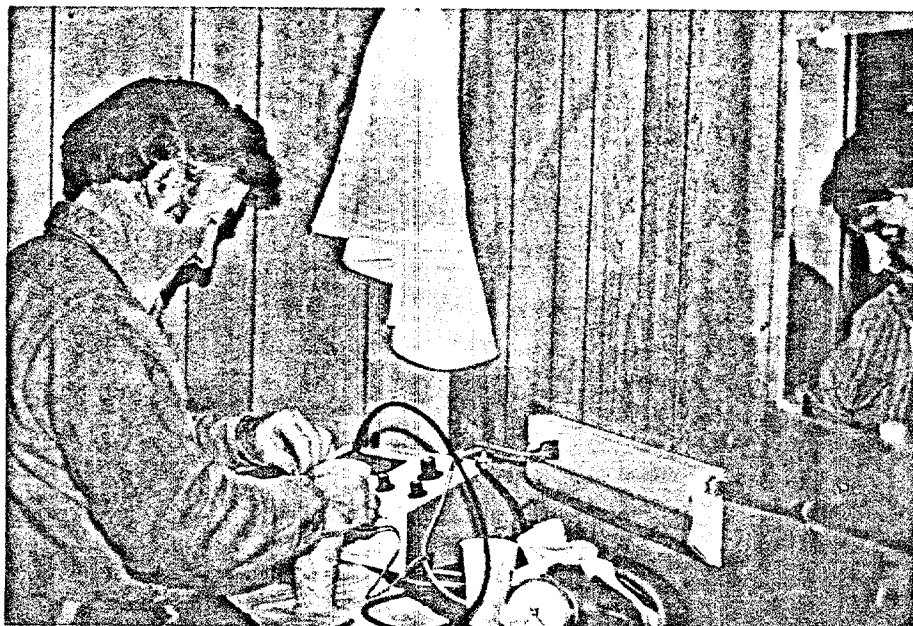


Figure 30: Taking salinity measurements.

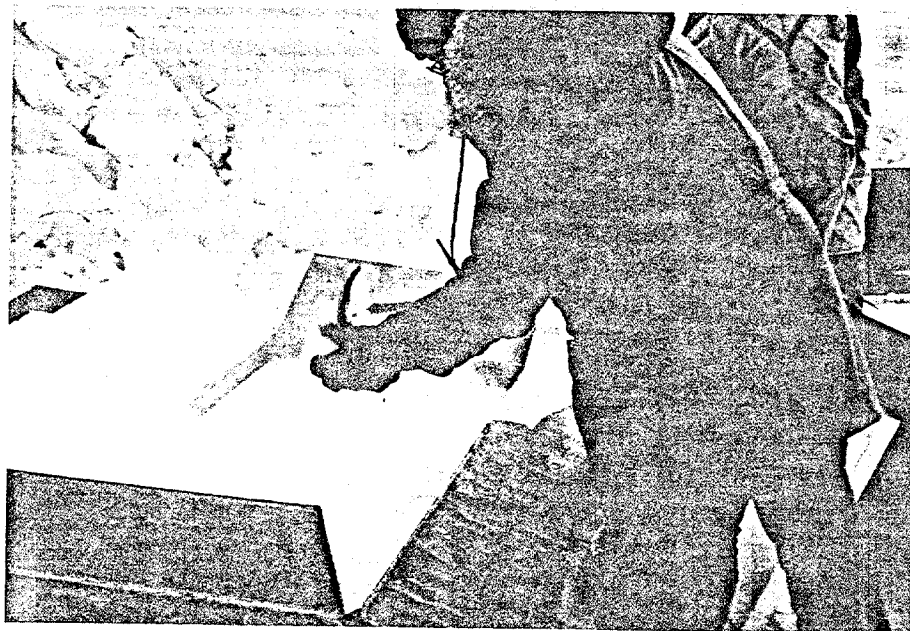


Figure 31: Crushing dry ice to refrigerate ice samples.

the samples on the ice or while in Deadhorse. No brine drainage was observed from the core samples. Had it been unseasonably warm, the core would have been packed in dry ice immediately after removal from the ice.

Upon removal from the ice, ice cores were cut to length, cataloged, and packed in core tubes. In Deadhorse, gaps in the core tubes were packed with paper to protect the core ends from damage due to excessive motion during shipment. The core tubes were then placed in insulated shipping boxes. The core shipping boxes were constructed of heavy-weight, wax-coated cardboard with three-inch thick styrafoam on the bottom, sides, and top of the container. Each box could accommodate six, meter-long core tubes, snow, and dry ice.

When ten or more shipping boxes were filled with core samples, a shipment of dry ice was ordered from Alaska Gourmet in Anchorage. To avoid problems of having the dry ice delayed in shipment, the ice was shipped to Deadhorse by Alaska International Air Cargo (AIA). When the dry ice arrived in Deadhorse, the ice core boxes were taken to AIA for shipment to Anchorage and packed with snow and dry ice. Two to three inches of snow were first packed on top of the core tubes to prevent thermal cracking of the core caused by direct contact with the dry ice. After the snow was in place, two blocks of dry ice were crushed and spread over the top of the snow in each box (Figure 31). Originally, each block of dry ice weighed 25 pounds. About 8 pounds of this were lost in shipment to Deadhorse due to sublimation. Thus, each shipping box was sent to Anchorage with about 35 pounds of dry ice.

To minimize shipping damage and facilitate handling, the boxes were strapped to wooden pallets (Figure 32). Two boxes were placed on each pallet. Instructions were given to AIA not to stack the pallets more than two pallets high. FREEZE stickers were also placed on the boxes by CRREL personnel to alert shippers that



Figure 32: Strapping ice shipping boxes on to pallets.

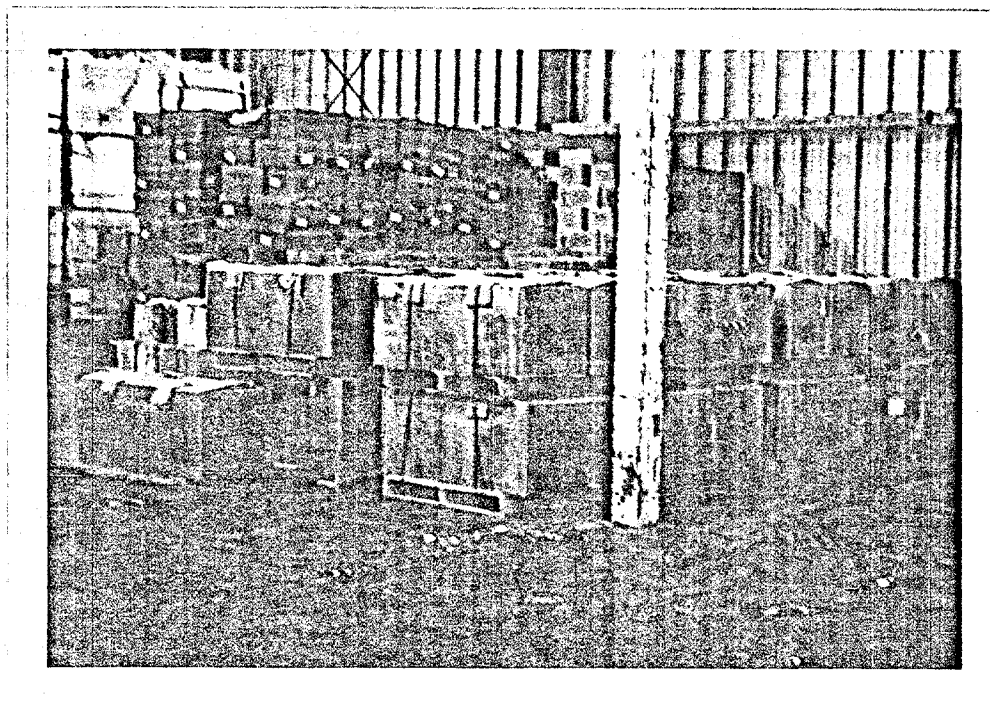


Figure 33: Ice shipment at Whitney-Fidalgo.

the boxes should be refrigerated if delayed while in shipment. AIA provided us with shovels, hammers, pallets, and the banding equipment. They were most helpful in assisting us with shipping the ice samples. It should also be mentioned that they have freezer facilities in Deadhorse, Fairbanks, and Anchorage. To prevent the ice from being delayed in Deadhorse, or bumped in Fairbanks, the ice was usually sent priority air freight to Anchorage. Three separate ice shipments were made from Deadhorse to Anchorage. Airport Drayage, an expediting firm in Anchorage, was alerted prior to each ice shipment to Anchorage. They were provided with shipping information such as air bill number, number of boxes, etc. Airport Drayage met each shipment as it arrived in Anchorage, inspected the condition of the dry ice, and moved the ice to our Anchorage storage facility at Whitney-Fidalgo Seafoods (Figure 33). Storage temperatures were maintained at -20°F. Airport Drayage also delivered a large shipment of dry ice from Alaska Gourmet to Whitney-Fidalgo, just prior to shipping the ice south.

All the shipping boxes still contained dry ice when they arrived in Anchorage. About half the dry ice in each box was lost after sitting in Deadhorse for 36 hours and the 3 hour flight to Anchorage (stopped in Fairbanks).

At the completion of the field sampling program, two CRREL personnel went to Anchorage to prepare and arrange shipment of the ice samples to Hanover. Each of the 41 ice shipping boxes were opened at Whitney-Fidalgo and repacked with dry ice. About 75 pounds of dry ice were packed in each box. After charging the boxes with dry ice, the boxes were rebanded to the pallets. This took about 9 hours.

The next day Airport Drayage took the boxes to Flying Tigers for shipment to Boston. Prior arrangements were made with Flying Tigers to have the ice shipped from Anchorage to New York and then transferred to a cargo flight to Boston.

The boxes were to leave Anchorage at 10:00 am and arrive in Boston at 8:30 am the next morning (about 18 hours after leaving the cold storage facility). Unfortunately, there was insufficient room on the 747 aircraft when it arrived in Anchorage. Since our boxes were already packed with dry ice, the shipment was split. Thirty-four boxes were removed from their pallets to save space and shipped as previously arranged. The remaining 7 boxes were shipped later that day to Seattle, Chicago, and then on to Boston. They arrived in Boston the next evening, about 28 hours after leaving Whitney-Fidalgo.

Each shipment was met in Boston by CRREL personnel. The ice was taken to Hanover in a reefer truck at a temperature of -20°F . When the ice arrived at CRREL the ice was moved to CRREL's core storage room at -30°C . This cold room has a back-up refrigeration system. All the boxes arrived in Hanover in good condition containing large amounts of dry ice.

Other than having the ice shipment split, only two problems were encountered during this portion of the program. Twice, dry ice shipments to Deadhorse were delayed. The first time our shipment was confused with a shipment for Exxon. On another occasion, the dry ice manufacturing plant broke down. The other problem was discovered in Anchorage. The storage facility at Whitney-Fidalgo was colder than temperatures in Prudhoe Bay and most of the arctic clothing was already shipped south. This certainly was our coldest day in Alaska.

Development of Equipment and Testing Techniques

Just prior to and after the field program, work concentrated on preparing adequate samples for testing. Desirable tolerances are given in Table 5. To prepare samples to these tolerance a lathe and milling machine were purchased by Shell and sent to CRREL. After the equipment arrived, they were wired in a cold room, degreased, and cleaned. Special jigs were also designed and fabricated to

hold the samples on the lathe and milling machine. Presently, it is planned to turn down the field samples to 4 inch diameter test specimens on the lathe. Both the lathe and milling machine are being considered to cut the samples to length and prepare the ends. Using the lathe to face off the specimen ends insures end squareness; however, this requires two steps and two special set-ups on the lathe. On the milling machine the ends can be prepared by either vertical or horizontal milling. Preliminary trials on the milling machine show that vertical milling tends to round off the corners of the test specimen. Horizontal milling or slabbing may prove to be better. At this time, we are familiarizing ourselves with the operation of the equipment and getting a handle on optimum rotational and traverse speeds and depths of cut to produce high tolerance test specimens.

Small modifications have been made to the radial strain measurement devices to ease placement of the gauges on the sample. In addition, a special jig has been made to position both the axial and radial strain measurement devices on the devices test specimens. Other jigs have been designed and fabricated to center the test specimen and platens on the MTS machine. A cold plate was also made to minimize heat transfer through the lower actuator on the testing machine.

CRREL has borrowed a 7 channel analog Ampex recorder from Shell. The MTS technician is now familiarizing himself with its operation and means to interface the recorder to our test system.

SAMPLE PREPARATION TOLERANCES

Diameter, D	D > 10•(grain size) Preferably D > 20•(grain size)
Length, L	L/D > 2.0 Preferably L/D = 2.5
End Flatness	Better than 0.0005 in.
End Parallelism	Within 0.001 D or 0.004 inches 0.004 inches
End Squareness	Square to the sample axis to within 0.06° or 0.004 inches
Straightness of Cylinder Surface	Straight to within 0.001 inches
Diameter Uniformity	D should not vary more than 0.001 inches over the length of the sample

Table 5: Desirable sample tolerances

Introduction

This progress report describes work performed in the Mechanical Properties of Multi-year Sea Ice study from 1 June to 1 October 1981. During this period a series of uniaxial compression tests were performed to evaluate the platens and axial strain measurement devices described in Progress Report 1. As the test results were unsatisfactory, sample preparation methods, platens, and strain measurement devices were re-evaluated. This resulted in new testing techniques and procedures for uniaxial compression. The revised methods and a summary of the test results are presented in this report.

We are now ready to perform a production run of high-quality uniaxial compression tests at a constant strain-rate of 10^{-5} /sec at -20 and -5°C . Tests at a strain-rate of 10^{-3} /sec require more work.

During the field sampling program a core of presumably undeformed multi-year sea ice was obtained and shipped to CRREL for salinity and petrographic analysis. The salinity and a preliminary discussion of the structure of the core are presented. It is interesting to note that the core contained columnar ice and fine-grained crystals which appear to be frazil.

Equations have also been derived to calculate the air volume of sea ice given the ice salinity, temperature, and density. Unlike previous investigators, the presence of solid salts is considered. As the salinity of multi-year sea ice is much lower than that of first-year sea ice, brine volume effects on ice strength may be over-shadowed by the effect of the air volume or total porosity of the ice.

Development of Testing Equipment and Techniques

We have continued to refine the techniques to be used in uniaxial compression testing and have given tension and triaxial testings further consideration. Various types of platens have been evaluated and we have gone through several iterations on measuring axial strain.

Platens: Three types of platens have been considered for use in this study: steel, compliant flexane, and bonded synthane. Originally, it was planned to use the compliant platens described in Progress Report 1 (Figure 1) for compression testing. It was reasoned that at low strain-rates the closed-loop machine response would be able to compensate for the softness of the platen. At high strain-rates another type of platen might have to be considered. The bonded synthane end caps (Figure 2) also described in Progress Report 1, were to be used in tension tests.

In a number of tests to evaluate axial strain measurement techniques on right circular cylinders the compliant platens consistently resulted in sample failure near the end planes of the specimen, not in the central portion of the sample. Initially, it was believed that the ice was weaker near the specimen ends as the samples were not homogeneous. However, after several end failures, this explanation was rejected. The objective of using compliant platens was to subject the specimen ends to uniform pressure while permitting radial expansion of the ice due to the Poisson effect. However, relative to the central position of the specimen, the expansion at the ends was excessive. Figures 3 and 4 show test specimens after tests at a displacement rate of 10^{-4} in/sec. Similar results were obtained using steel platens and this type of platen was also rejected. It should be noted that specimen ends were square and parallel to within 0.003 inches. Sample preparation was not regarded as being the problem.

It was later learned that Exxon Production Research uses steel platens in uniaxial compression testing of ice. To prevent excessive radial expansion at the

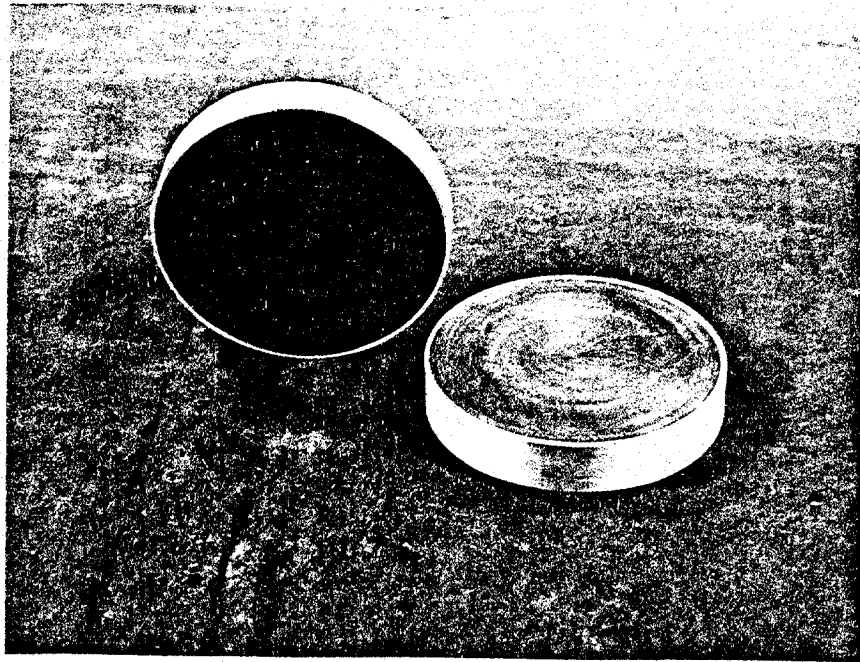


Figure 1: Compliant flexane platens

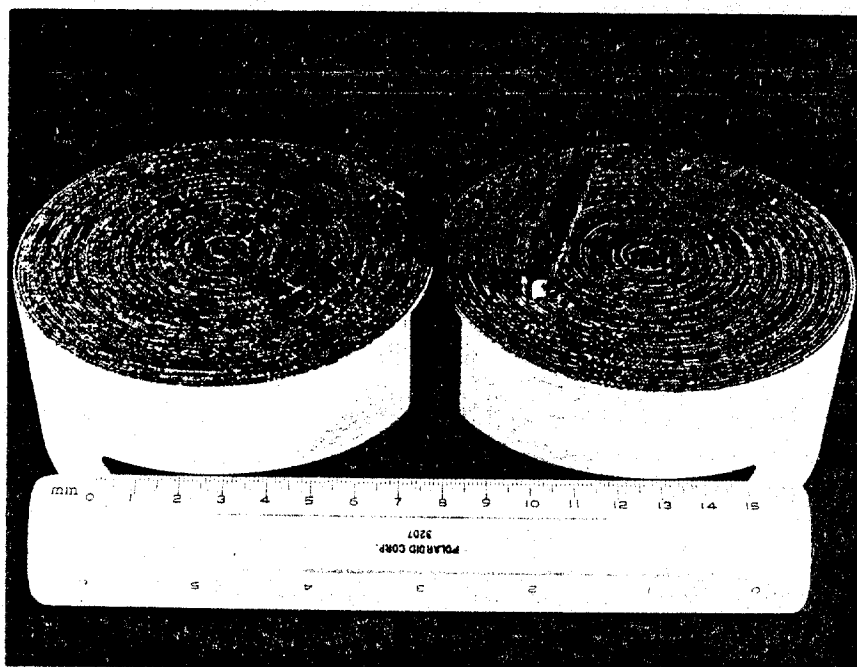


Figure 2: Synthane end caps

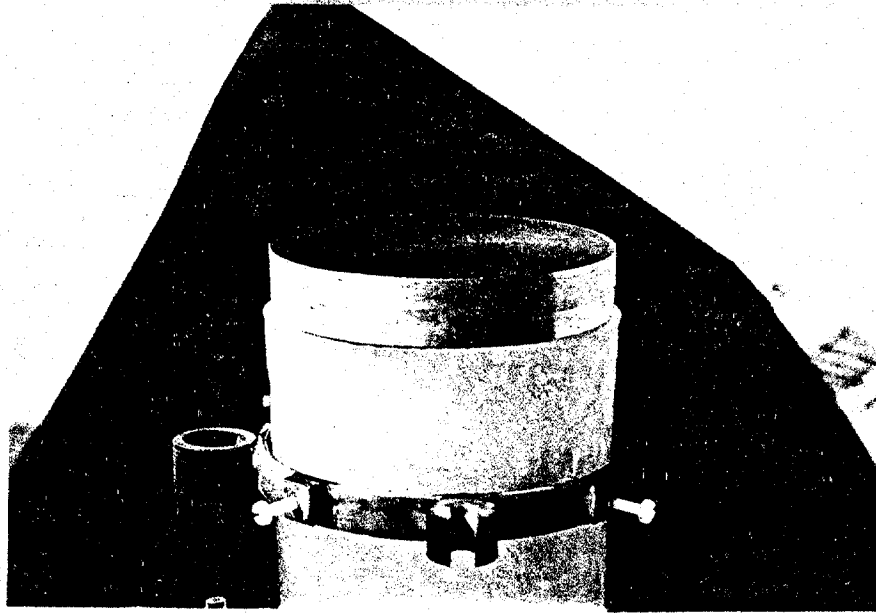


Figure 3: End failure using compliant platens

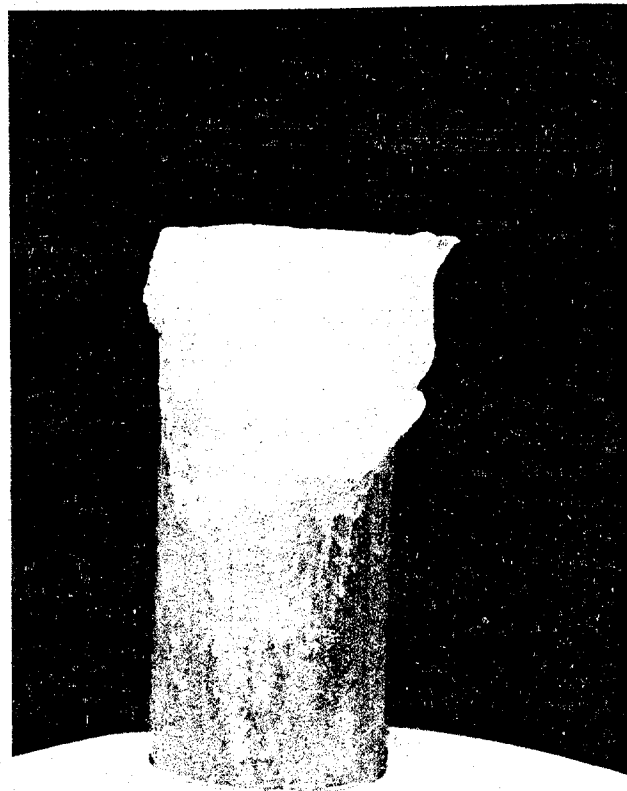


Figure 4: End failure using compliant platens

specimen ends, circular grooves are machined on the platen surface.

In order to minimize failure in the end planes of the specimen it was decided to use bonded synthane end caps on the compression specimens. In addition, it was also decided to use slightly dumbelled samples. Rather than using right circular cylinders having a diameter of 4-inches, dumbell's with 4.2 inch diameter ends and a 4-inch diameter reduced center section will be used in the compression tests. The radius of curvature of the fillet at the ends of the specimen was chosen to be 8 inches. Previous photo-elastic studies by Mellor have shown that fillets having a radius of curvature of 2 diameters minimize stress concentrations near the ends. Without the fillets, there appears to be a tendency for the ice to chip at the ends of the specimen. The use of bonded synthane end caps also standardizes our sample preparation procedures as these end caps will be used in both tension and compression tests.

Sample Preparation: The samples for compression tests are now prepared in the following manner. The core is first cut to about 10 1/4-inches in length with a pruning saw in the ice machine shop at 5°F (-15°C). It is then placed in a horizontal jig on the milling machine where the ends are milled square to the specimen axis. A 10-inch long right circular cylinder is produced having a diameter of 4.2 inches. The sample is then weighed and measured with a dial caliper to determine its density.

During this time, the end caps are being prepared for bonding in another cold room at 32°F (0°C). Prior to freezing the end caps to the sample, the hairy surface of the end caps are saturated with fresh water at 32°F (0°C). Once saturated, the bottom end cap is placed, hairy surface up, in a jig, a 13-inch long split mold having an inner diameter of 4.206 inches. The inner diameter of the jig is equal to the outer diameter of the end caps at 32°F (0°C). The mold is then bolted together and a 1/8-inch layer of ice water is placed on the hairy surface of the end cap. At this point the cold sample is brought into the room and inserted into the

jig until it comes into contact with the end cap. Five minutes is then allowed for the sample to freeze to the end cap. After the end cap is bonded, the mold is taken apart. The above procedure is then repeated to bond the top end cap to the sample.

Once the end caps are bonded to the sample, the sample is returned to the ice machine shop where it is turned down on the lathe. An 8-inch radius cutting tool is used to turn the sample down to 4 inches in diameter and produce the slight fillets at each end.

It should be noted that as the mold is 13 inches long, and the end cap-sample-end cap is 14 inches long, use of the mold results in precise alignment of the upper and lower end caps. Since the end caps are square, the ends of the capped sample are square and parallel. Typically, the capped ends are parallel to within 0.008 inches. The high side of the sample is determined on a comparitor and marked. Later, when the sample is placed in the MTS machine, steel shim stock is used to take up the slack on the low side of the sample.

Axial Strain Measurements: We have gone through several iterations to measure the axial strain on the gauge length or center portion of the sample. All methods involved the use of DCDTs on opposite sides of the specimen.

The first jig used to measure axial strain is shown in Figure 5. Spring loaded pins were used to hold the upper and lower frames on the sample. The frames were positioned with a split mold (Figure 6). At the time we were not using bonded end caps on the sample. A fully instrumented specimen is shown in Figure 7. This figure also shows two radial strain measurement devices on the sample which are discussed later. The frames used to hold the axial DCDTs proved to be unstable. They were easily disturbed by handling and movement of the DCDT wires during testing. Furthermore, at large strains the ice deforms in an irregular manner. This caused the DCDT core rods to bind in the transducer cores. The frames were discarded.

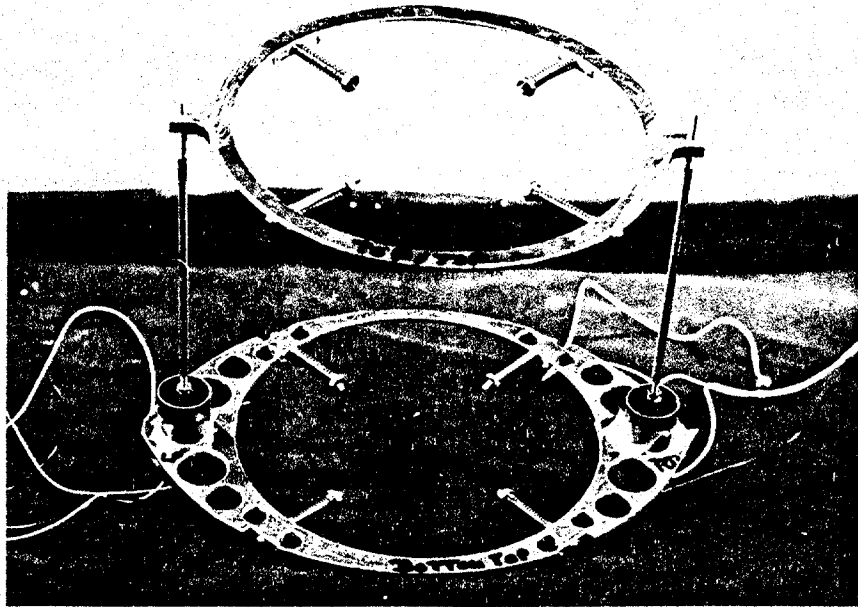


Figure 5: First jig used to measure axial strain on test sample.

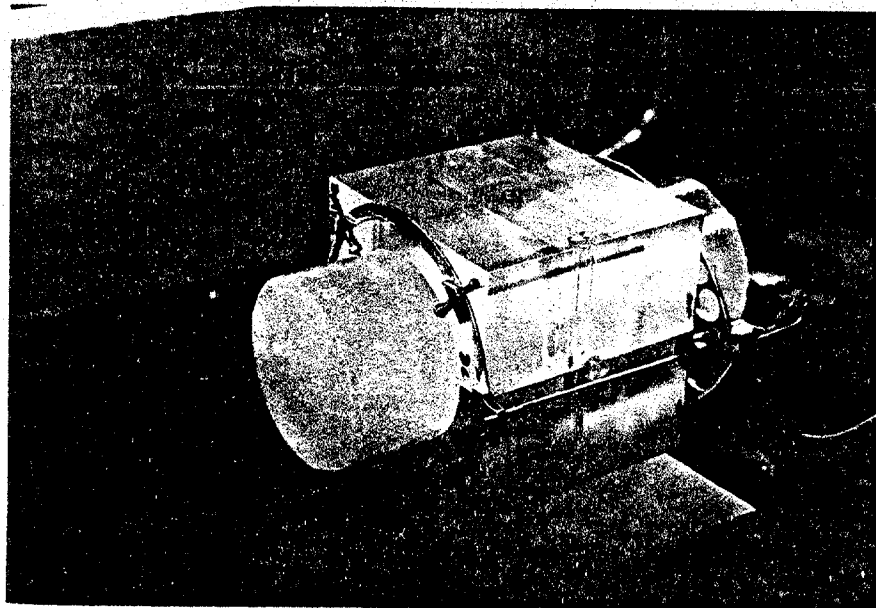


Figure 6: Split mold used to position DCDT frames on sample.

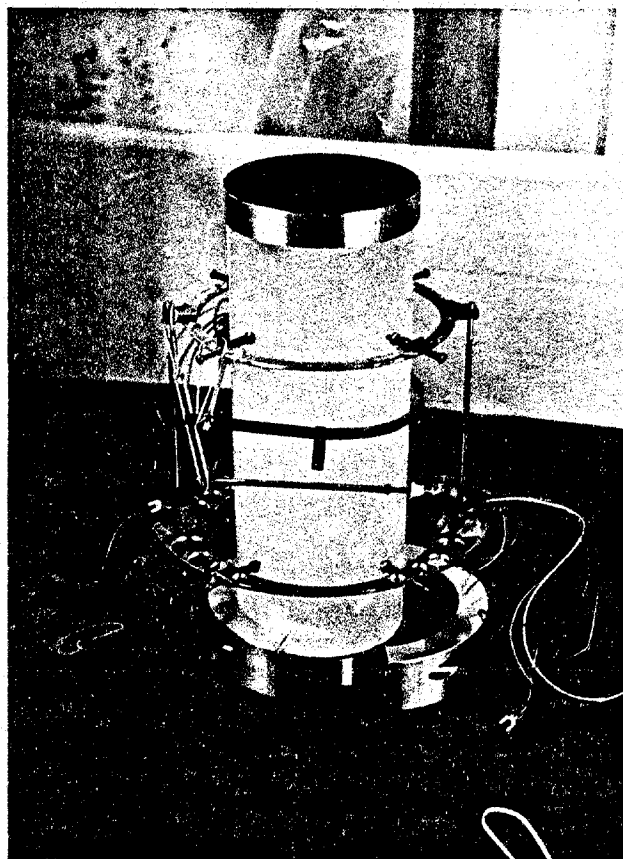


Figure 7: Fully instrumented specimen using first generation strain measurement devices.

The next attempt to measure large axial strains on the sample is shown in Figure 8. The upper and lower frames were made of thin-walled fiberglass tubing which were held in position with teflon screws. As the ice expanded during compression the frame would deform. Unlike the previous set-up the DCDT core rods were not directly attached to the core rod holder frame. Instead, the DCDT cores were attached to the upper frame and the core rods rested on pedestals which were attached to the lower frame. Without a rigid connection between the core rods and frame, the core rods did not bind at large strains. Hardware for positioning and aligning the frames on the sample is also shown in Figure 8.

This method of attaching the DCDTs to the sample was also rejected. As it turned out the fiberglass tubing was too stiff and after large strains the teflon screws dug into the sample. In addition, the deformed sample would come into contact with the frame (Figure 9). Increasing the diameter of the frame or decreasing its wall thickness would probably result in an unstable set-up as in the previous attempt. Fortunately, the concept of resting the DCDTs on pedestals proved to be successful and was included in the next trial.

The method that was finally adopted to measure axial strain on the sample is shown in Figure 10. Again the DCDT core rod rests on a pedestal which is attached to the lower portion of the sample. Both the DCDT core and the pedestal are supported by teflon feet which are attached to the sample by o-rings. Details on the teflon feet and method to attach the axial strain gauge to the sample will be given in the next progress report when photographs of the procedure are available.

In this technique two axial strain gauges are attached to opposite sides of the sample. The use of o-rings to support the teflon feet allow each of the gauges to function independently. This is desirable in that preliminary tests have shown that the sample deformation at large strains is quite irregular. Classic barreling of the sample is the exception rather than the rule. At large strains the

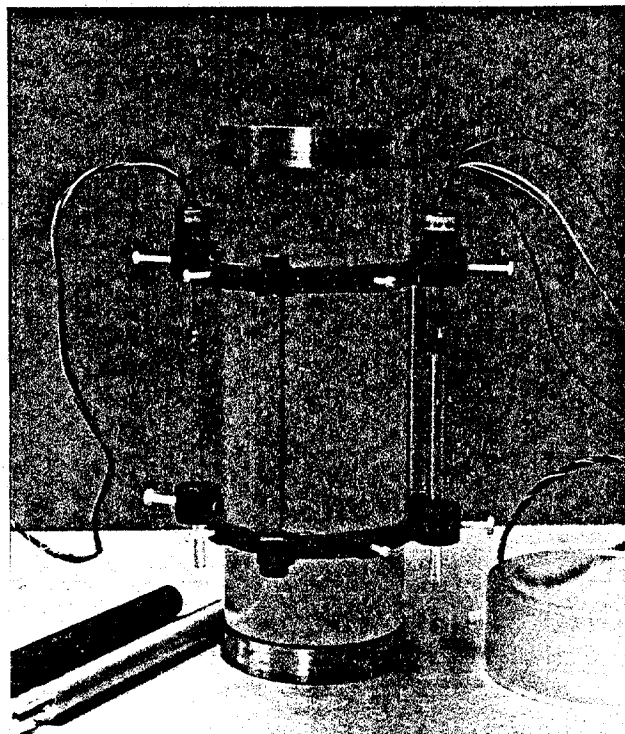


Figure 8: Second attempt at measuring axial strains.

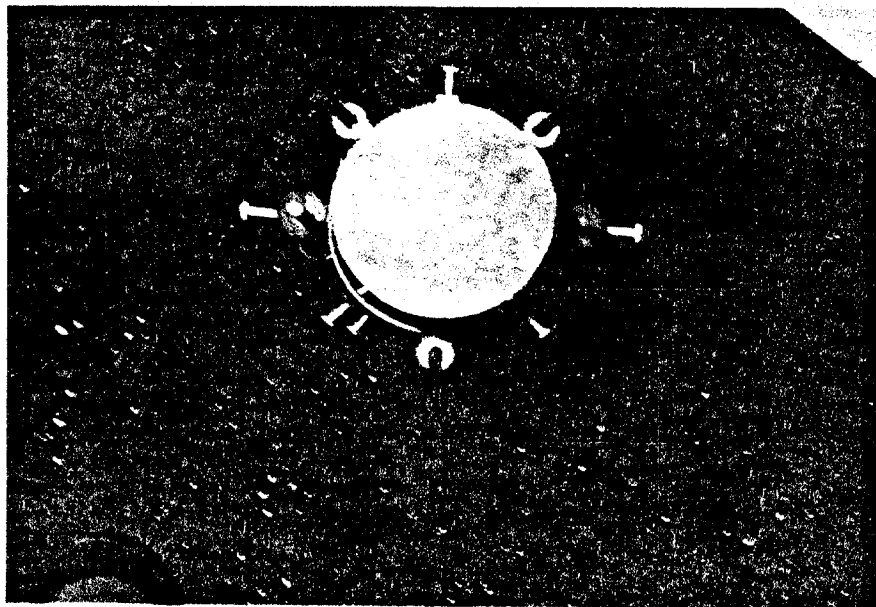


Figure 9: Failed sample using second generation axial strain measurement device.

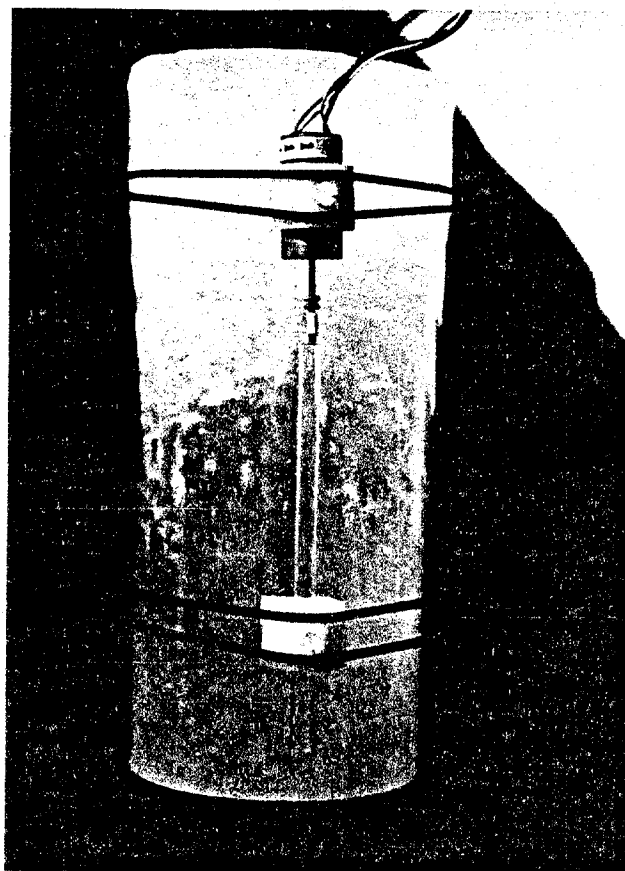


Figure 10: Method finally adopted to measure axial strain.

DCDT core rods usually fall off the pedestals. However, at this point in the test the strain of the sample is probably best represented by the strain measured between the end caps on the specimen. This strain is measured by an extensometer mounted between the end caps whose output is used to control the strain rate of the test in the closed-loop system.

Radial Strain Measurements: The radial strain transducer shown on an ice sample in Figure 7 was our first and last attempt to measure radial displacements across the diameter of the test specimen. As in our first attempt to measure axial strains, the DCDT core rods tended to bind in the DCDT cores. Since measurement of radial displacements were of secondary importance, little progress was made to improve this technique.

During the evaluation of the bonded end caps and axial strain transducers, it became apparent that measurement of diametrical expansion of the sample may be misleading after initial yielding of the sample. Radial deformation of the test samples at large strains varied considerably both along the axis of the sample and in a given cross-section. It was decided that measuring the circumferential strain at one or more positions in the middle portion of the sample would be more meaningful. We have ordered a circumferential strain measurement kit from MTS for testing and evaluation.

Strain-Rate Control: A technique has been developed to perform constant strain-rate tests. Basically an MTS extensometer is connected between the end caps on the sample and the output is used to control the full sample deformation rate. Since a photograph or sketch of the set-up is not available at this time, the technique will be described in detail in the next progress report. Preliminary tests have shown that a uniform constant strain-rate can be obtained at 10^{-5} /sec. At higher rates the strain rate is cyclic and not constant. This may be due to the instrumentation or tuning of the MTS machine. An MTS service representative has been scheduled to check out the MTS system.

Structure and Salinity of Multi-year Sea Ice

Previous Work: Little is known about the structure of multi-year sea ice. The limited work that has been performed on multi-year ice has largely focused on the horizontal layers that are produced by the summer melt cycle. The reason for this interest is that the annual layering allows one to establish a minimum age for thick floes of pack ice. Previous to these studies, age estimates were based upon subjective criteria such as the amount of pressuring and the detailed morphology of the ice surface. Age estimates have also been made from the ice thickness and from the locations of the maxima and minima in the salinity profiles (Savel'ev, 1958). Although there is a general tendency to form a low salinity layer on the underside of the ice during the summer melt period, this salinity distribution is rapidly modified by brine migration and is difficult to use in estimating ice age except in extremely simple cases.

The first study of a horizontal "translucent-longitudinal" section of a thick (291 cm) thick ice floe was by Shumskii (1955) when in July of 1954 he made a brief visit to the drifting station SP-3. As a result of above-freezing temperatures during the period of field work, very few detailed observations were made. The ice was divided into 2 main types, infiltrated (0-38 cm) and normal sea ice (38-291 cm). The infiltrated ice layer was described as resembling the firn of arctic glaciers and contained 4 distinguishable layers which were interpreted as annual. The normal sea ice was also classified into 2 types. The upper part (38 to 150 cm) contained lens-like irregular strata that were believed to be the result of thaw cycles. These strata were absent in the lower portion (150 to 291 cm) of the ice. Shumskii reasoned that the lower portion of the sea ice (141 cm thick) was formed after the end of the thaw period while the 4-years accumulation of infiltrated ice was forming at the surface of the ice sheet. The

upper 112 cm of the sea ice was believed to be older. The total age of the floe was estimated at not less than 6 to 7 years. Shumskii also suggested that the presence of infiltrated ice indicates that the snow line in the central arctic is presently at sea level.

Following this preliminary study, detailed investigations of the horizontal layering in pack ice were made on SP-4 (Cherepanov, 1957) and Station Alpha (Schwarzacher, 1959). It was found that the annual layering is readily observable in the lower part of the ice sheet and less clearly defined nearer the upper surface where the effects of the summer melt are more pronounced. Cherepanov found 10 recognizable annual layers in a 335 cm thick floe (Figure 11) while Schwarzacher found either 7 or 8 layers in a 345 thick floe. The boundaries between the annual layers were of 2 different types. The most common is a thin (2-5 mm) layer of milky white ice with a sharp upper and an irregular lower boundary. The details of the formation of this layer are not known but it apparently develops during the period when the ice growth has stopped. The milky color of the layer may, in some way, be connected with the biological activity beneath the ice surface during the summer months. The formation of the milky layer is apparently not associated with either the recrystallization or the nucleation of new grains since when ice growth starts in the fall in most cases the crystals of the previous winter take up growth again with the same crystallographic orientation (Schwarzacher, 1959).

The other type of summer layer is considerably thicker (1 to 10 cm) and shows a sharp decrease in grain size relative to the overlying winter ice. The grain shapes on this layer have been described as slightly elongated in the vertical direction. The c-axes orientations are in general horizontal but they show deviations up to 30 degrees (Schwarzacher, 1957). In the ice studied by

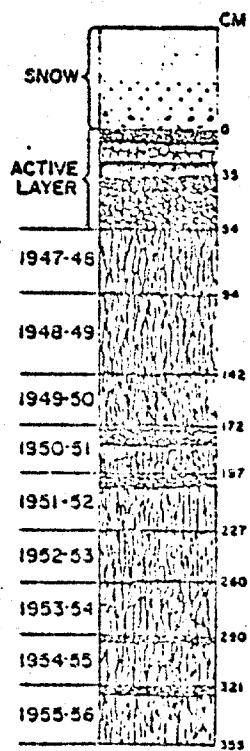


Figure 11: Cross-section of a multi-year floe (from Cherepanov, 1957).

Cherepanov the crystals were equi-axed and the orientation was random. This ice does not show the platy substructure so characteristic of sea ice and has a much lower salinity (1 to 1.5‰) than the surrounding ice. The formation of this type of annual layer is believed to be the result of the formation of a stable layer of fresh melt water between the lower surface of the ice and the underlying dense sea water during the summer. This process has been known for some time (Malmgren, 1972) and has been described in considerable detail on Station Alpha by Untersteiner and Badgley (1958). They found that many of the fresh water melt ponds that developed during the summer drained through core holes forming an irregular layer of fresh water between the ice and the sea water. At the interface between the fresh (0°C) and salt water (-1.6°C), ice crystals formed and floated upward until the fresh water layer was filled with a mesh of fragile crystals. When the crystals forming at the fresh-salt water boundary could no longer rise, the formation of a solid layer of fresh water ice began. The formation of such a layer is to be expected under any floe occupied by a scientific station because the large number of core holes drilled in the floe for technical studies facilitate the rapid transfer of melt water to the underside of the ice. On an unoccupied floe early in the melt period, melt water will either be channeled into open leads where wave action will favor mixing with the sea water or it will form large melt pools toward the interior of the floe. Only later in the melt period when deterioration is far advanced do drainage holes form in all areas of the floe (Bennington, 1959). Even during this period, the lower density of the fresh melt water inhibits it from percolating completely through the floe. When a fresh water layer does form, it is usually localized under the thinner portions of the ice floe and is particularly prevalent near open leads. This layer, if preserved by freezing, is very useful as a marker; Cherepanov found that 4 out of the 9

annual boundaries in the NP-4 floe were marked by "fresh" ice layers (Figure 11). On the other hand, Schwarzacher (1959) has noted from examination of a large number of cores in the vicinity of Station Alpha that the "fresh" ice layers do not contribute significantly to the total ice growth.

Schwarzacher (1959) observed that the top 50 cm of the floes he examined contained ice which formed at or near the upper surface of the floe. This ice was predominantly the result of the freezing of melt-water pools that form during the summer and was characterized by c-axes vertical orientations. A fine grained granular ice may also be formed by snow falling in the melt water pools producing a slush and subsequent freezing of this mixture. This melting and refreezing associated with the upper ice surface tends to obliterate the annual layering in the upper part of the ice sheet and makes the accurate estimation of the age of the ice in a floe difficult if only one cross-section is examined. For example of the 150 cores collected by Schwarzacher in the summer of 1958 from areas that did not show signs of old pressure ridges, only 25 percent consisted of undisturbed ice and only 2 percent were sufficiently unaltered to show an annual layering throughout the complete thickness of the floe (8 layers to 1950). Inasmuch as neither Schwarzacher, Cherepanov, or Bennington observed any annual stratification or superimposed firn, this casts considerable doubt on Shumskii's suggestion that the snow line in the central arctic is presently at sea level. Both Cherepanov and Schwarzacher have noted that the formation of infiltrated ice is strictly local and is highly dependent upon the details of the surface relief. If infiltrated ice forms at all it will form in small depressed areas where old heavy snow drifts are present. In most areas on both NP-4 and Alpha both the snow cover and 20 to 30 cm of ice thawed during the summer (Untersteiner, 1961). It therefore seems quite likely that the ice identified by Schumskii as superimposed firn was actually ice formed by melting and refreezing in the upper part of the ice sheet. If this

is the case, the SP-3 floe would be a minimum of 9 years old instead of 6 or 7 as suggested by Shumskii.

One interesting aspect of the freezing of the fresh water layers that can form beneath multi-year ice floes is that the heat transfer rates are 5 to 10 times those calculated assuming that all heat transfer is by thermal diffusion (Martin and Kauffman, 1974). What appears to happen is as follows. When the surface melt flows off the pack into the ocean, and ultimately beneath the ice, we have an ice layer at its melting point ($\sim 0^{\circ}\text{C}$) underlain by a nearly fresh-water layer at its freezing point ($\sim 0^{\circ}\text{C}$), in turn underlain by sea water at its freezing point (-1.8°C). At the boundary between the fresh and the sea water a zone of water forms which, because of the rapid diffusion of heat relative to salt and the fact that the density of water with a salinity of $<24.7\text{‰}$ decreases on cooling, is both supercooled and less dense than the overlying water. The density distribution is unstable with a Rayleigh number of 10^3 to 10^4 and free convection results. When this supercooled water rises, it is nucleated by the overlying ice layer and forms a mesh of thin vertical interlocking ice crystals that ultimately grow down to the fresh water-sea water interface. At this time the presence of ice crystals throughout the complete thickness of the fresh water layer eliminates supercooling, constrains both temperature and salinity to lie on the freezing curve and permits them to diffuse in the vertical direction until both quantities become horizontally uniform. The combination of these processes results in the lateral growth of the ice crystals which continues until a horizontal ice sheet forms. Excellent photographs showing the growth of ice crystals during a laboratory simulation of this process can be found in Martin and Kauffman (1974).

The only detailed petrographic analysis of multi-year sea ice are those performed by Gow et al (1981) in Antarctica. A total of 66 floes were sampled in

the Weddell Sea pack ice, 12 of which are believed to be multiyear. In addition to columnar or congelation ice, the floes contained significant amounts of frazil ice. Congelation ice is formed by the direct freezing of sea water on the bottom of the existing ice sheet, whereas frazil ice is derived from small crystals nucleated in the water column. Two multi-year floes in excess of 4 m in thickness contained more than 60% frazil ice. Generally, the frazil crystals varied in size from 0.4 to 4 mm and were sometimes layered indicating several episodes of frazil formation. The congelation ice also frequently exhibited a preferred c-axis orientation in the plane of the sheet as observed in Arctic sea ice.

Salinity data for multi-year sea ice are scattered throughout the literature. The most comprehensive studies are those of Schwarzacher (1959) and Cox and Weeks (1974). Average salinity profiles from both these studies are presented in Figure 12. Schwarzacher's average profile, Curve C, is based on the salinity profiles of 40 cores. This mean profile is commonly quoted in the literature and has served as a basis for a variety of calculations in which the salinity profile of multi-year sea ice are important.

Unfortunately, Schwarzacher (1959) did not consider the effects of the surface topography on the ice salinity profile. Cox and Weeks (1974) later showed that the salinity profiles from cores collected from areas beneath surface hummocks were characteristically different than those collected from areas beneath surface depressions. In Figure 12, Curve A is an average hummock salinity profile based on 7 cores and Curve B is an average depression salinity profile based on 10 cores.

The low salt content of the upper portions of the hummocks is probably due to brine drainage by flushing. Flushing is similar to gravity drainage in that the brine moves through interconnected tubes and cavities. The force to overcome capillary retention is the hydrostatic head produced when snow or ice melts on

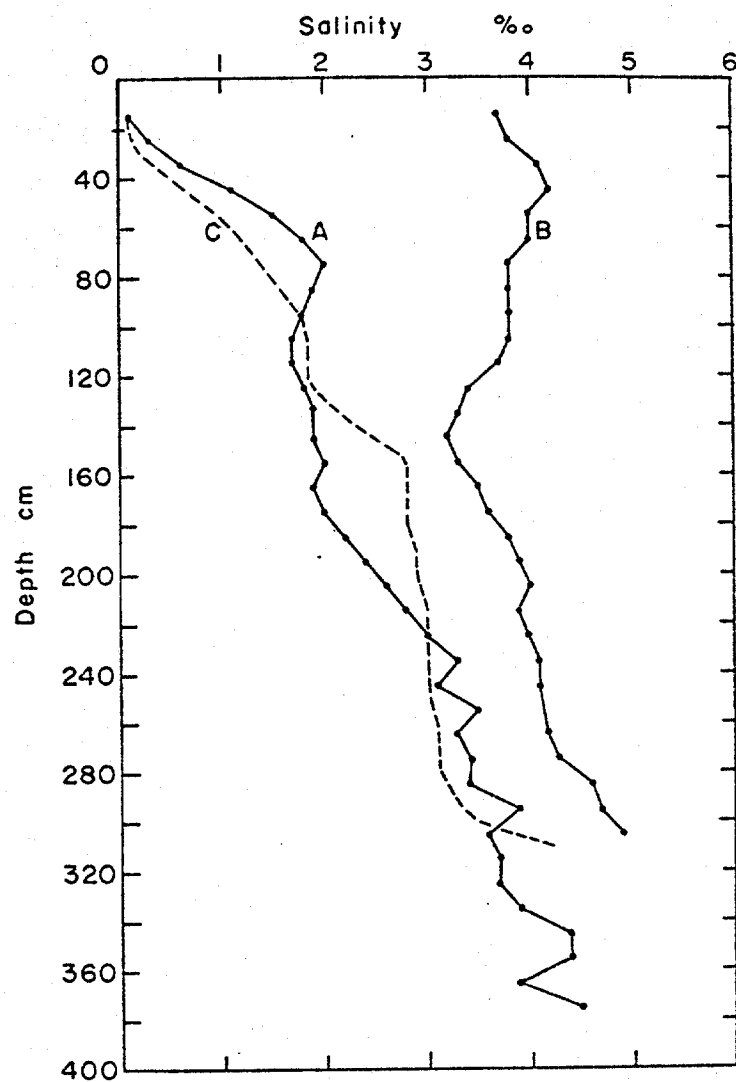


Figure 12 Average salinity profiles. Curves A and B are the average hummock and melt pond salinity profiles respectively. Curve C is the multi-year ice average salinity profile determined by Schwarzacher (1959).

the surface. Cox and Weeks (1974) observed that the average salinity of the upper meter of the ice decreased with increasing freeboard of the ice sheet.

The high salinity of the upper portion of the depression profiles is not understood. It is possible that the depressions were once melt holes in the floe and consisted of first-year sea ice. However, observations in the general area of the sampling site the previous summer suggested that this was not the case.

Salinity and Structure Core: During the ice sampling program in this project continuous cores were obtained from the upper portion of the ice sheet from a multi-year ridge and from an area of presumably undeformed multi-year sea ice. These cores were obtained for detailed salinity and structure analyses. A preliminary analysis of the undeformed multi-year sea ice core has been completed. Photographs of both horizontal and vertical thin sections in crossed polarized light from this core are presented in Figures 13 through 19. The upper 9 cm of the core consists of fine-grained slush or snow ice underlain by randomly oriented congelation ice. From 45 to 170 cm the columnar ice exhibits a preferred, nearly horizontal c-axis alignment. Crystals are about 0.5 cm in diameter. As the crystals are not exactly vertical, the ice sheet was probably deflected by the nearby pressure ridge. At 170 cm we encounter a thin frazil layer followed by a thin layer of congelation ice. Beneath 190 cm the remaining core consists of frazil ice of varying grain size. The salinity profile for the core and a schematic structural profile are presented in Figure 20.

Surprisingly, about 45% of the core is composed of frazil ice. We believe that the upper 190 cm of the core are the remains of the first year growth. The underlying frazil was probably formed the following fall. There doesn't appear to be any correlation between the ice type and salinity.

Based on the observations of Gow et al. (1981) and the results of this core analysis, frazil ice may be more wide-spread than originally believed. This is

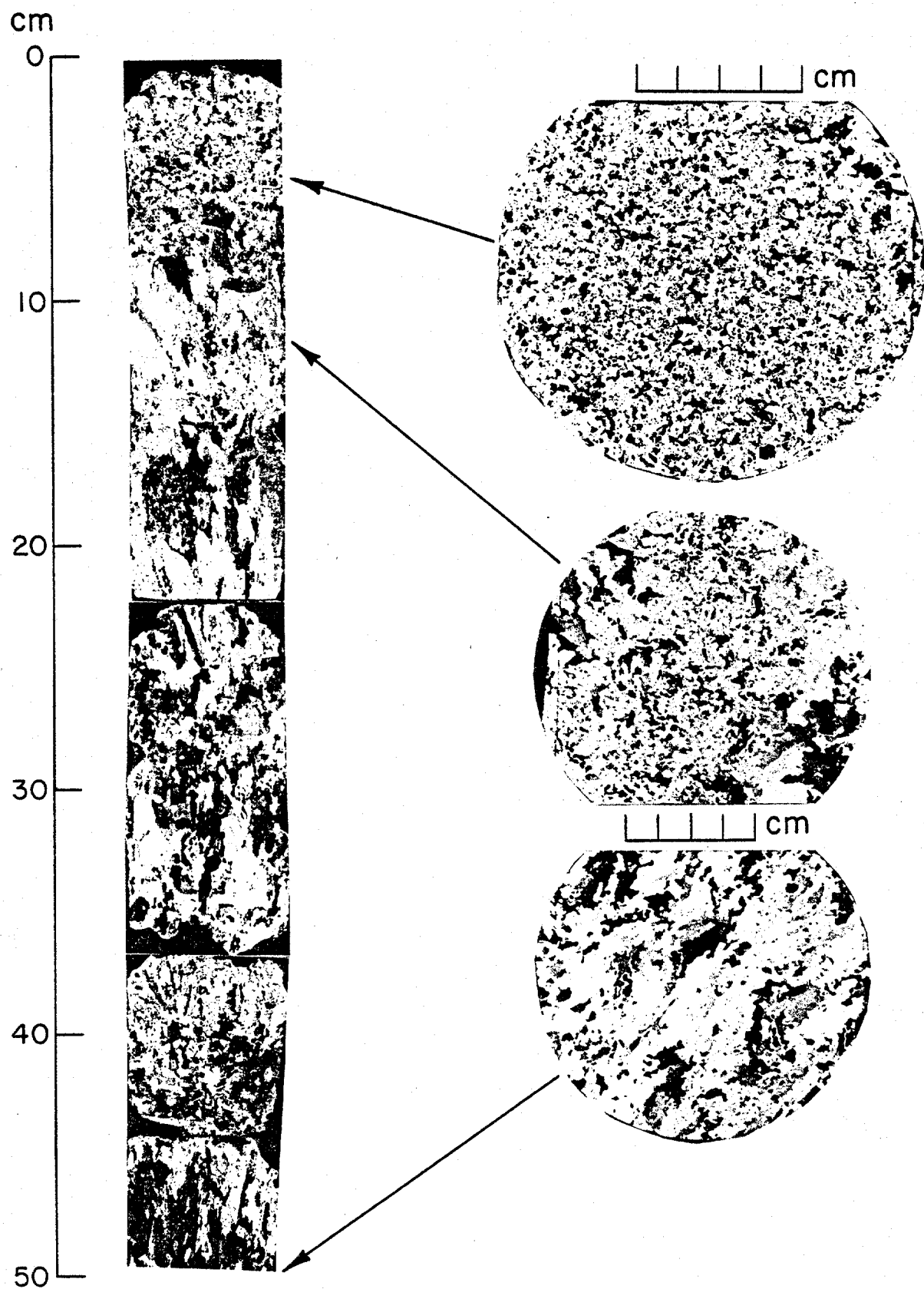


Figure 13: Structure of core of undeformed multi-year sea ice.

the surface. Cox and Weeks (1974) observed that the average salinity of the upper meter of the ice decreased with increasing freeboard of the ice sheet.

The high salinity of the upper portion of the depression profiles is not understood. It is possible that the depressions were once melt holes in the floe and consisted of first-year sea ice. However, observations in the general area of the sampling site the previous summer suggested that this was not the case.

Salinity and Structure Core: During the ice sampling program in this project continuous cores were obtained from the upper portion of the ice sheet from a multi-year ridge and from an area of presumably undeformed multi-year sea ice. These cores were obtained for detailed salinity and structure analyses. A preliminary analysis of the undeformed multi-year sea ice core has been completed. Photographs of both horizontal and vertical thin sections in crossed polarized light from this core are presented in Figures 13 through 19. The upper 9 cm of the core consists of fine-grained slush or snow ice underlain by randomly oriented congelation ice. From 45 to 170 cm the columnar ice exhibits a preferred, nearly horizontal c-axis alignment. Crystals are about 0.5 cm in diameter. As the crystals are not exactly vertical, the ice sheet was probably deflected by the nearby pressure ridge. At 170 cm we encounter a thin frazil layer followed by a thin layer of congelation ice. Beneath 190 cm the remaining core consists of frazil ice of varying grain size. The salinity profile for the core and a schematic structural profile are presented in Figure 20.

Surprisingly, about 45% of the core is composed of frazil ice. We believe that the upper 190 cm of the core are the remains of the first year growth. The underlying frazil was probably formed the following fall. There doesn't appear to be any correlation between the ice type and salinity.

Based on the observations of Gow et al. (1981) and the results of this core analysis, frazil ice may be more wide-spread than originally believed. This is

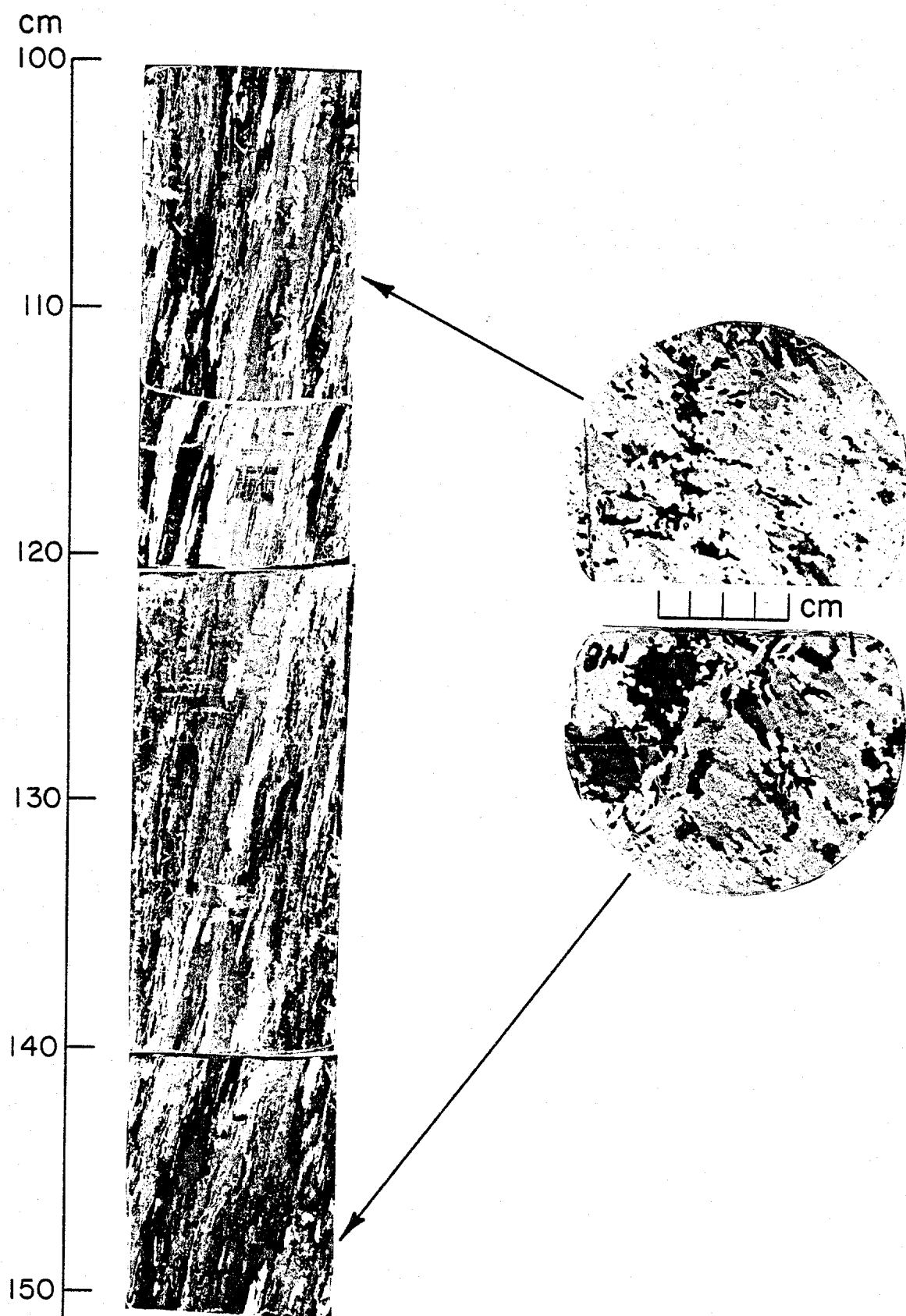


Figure 14: Structure of core of undeformed multi-year sea ice.

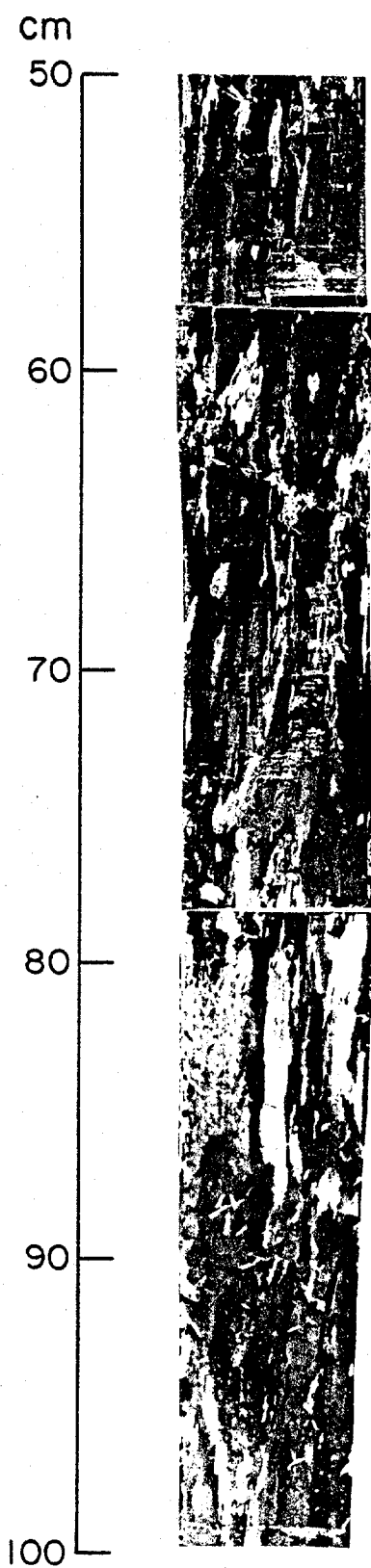


Figure 15: Structure of core of undeformed multi-year sea ice.

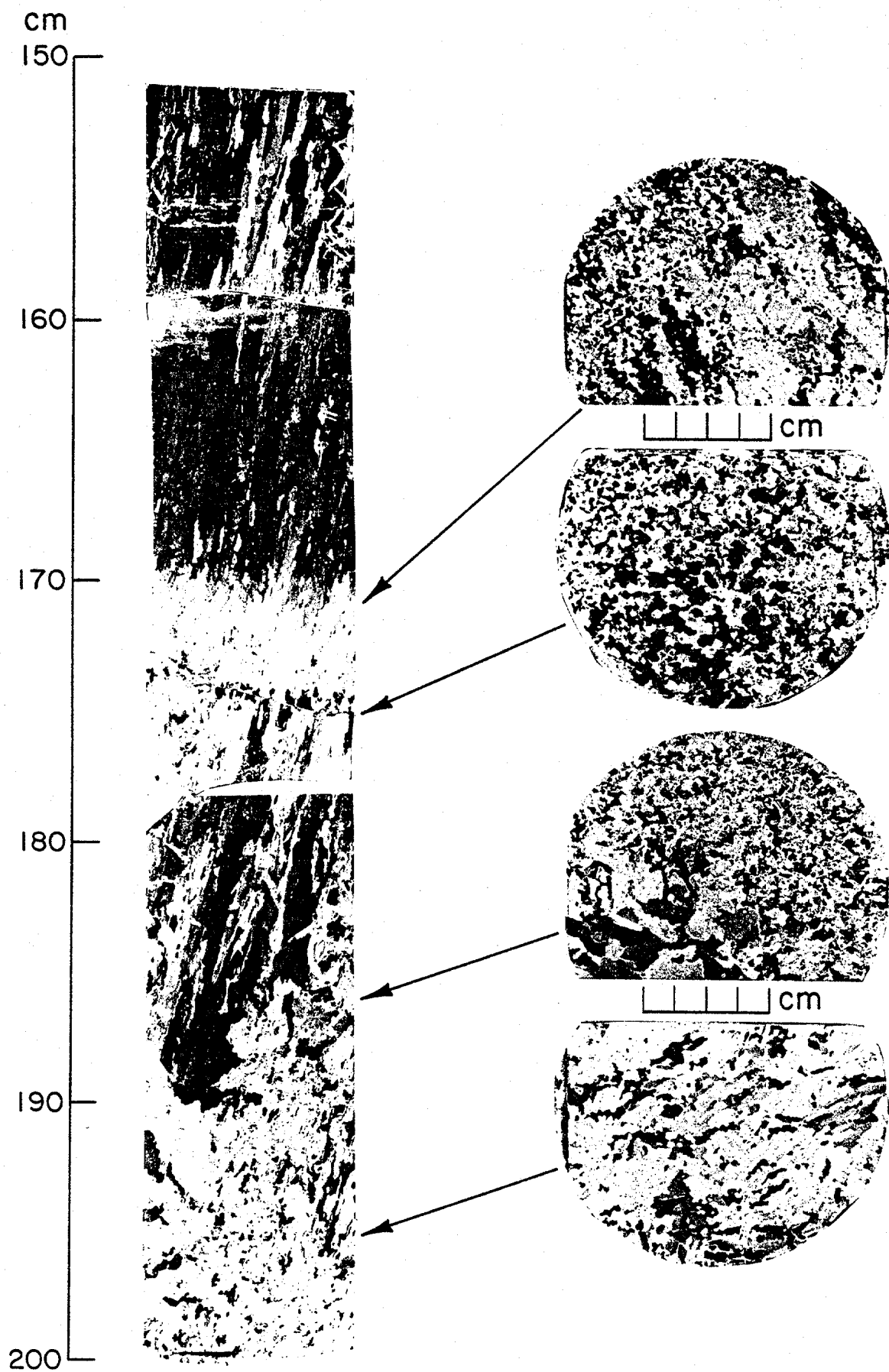


Figure 16: Structure of core of undeformed multi-year sea ice.

Figure 17: Structure of core of undeformed multi-year sea ice.

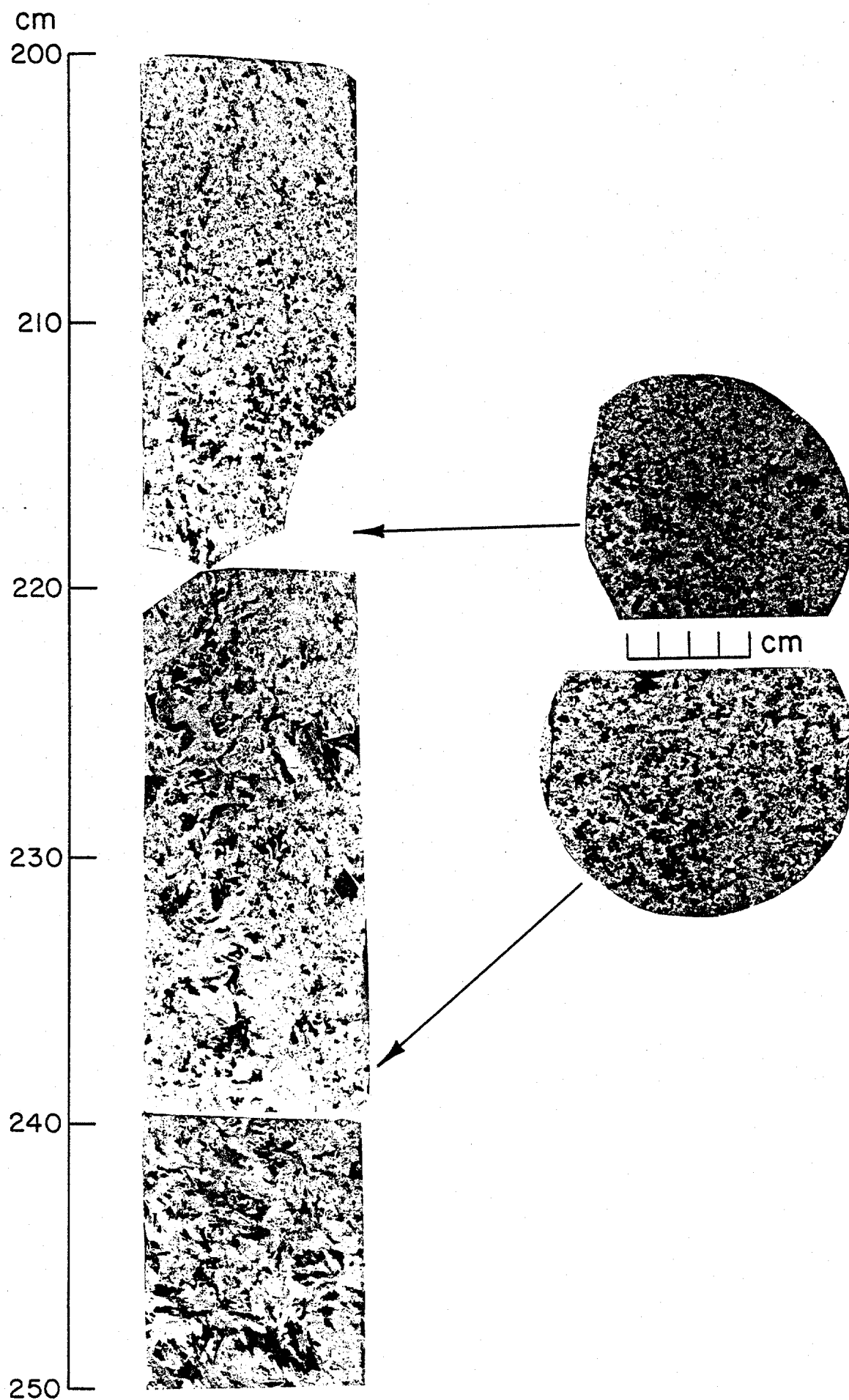
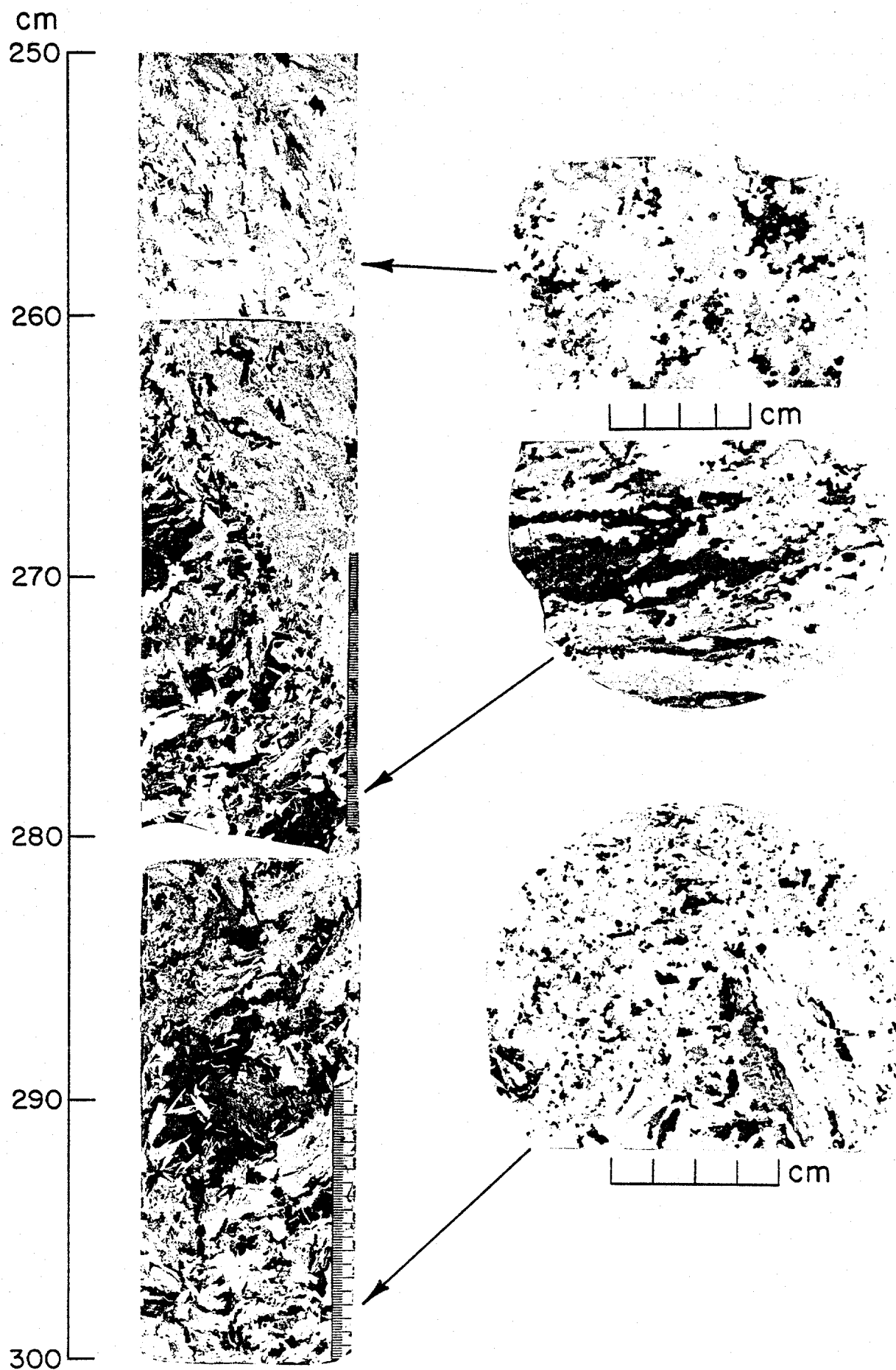


Figure 18: Structure of core of undeformed multi-year sea ice.



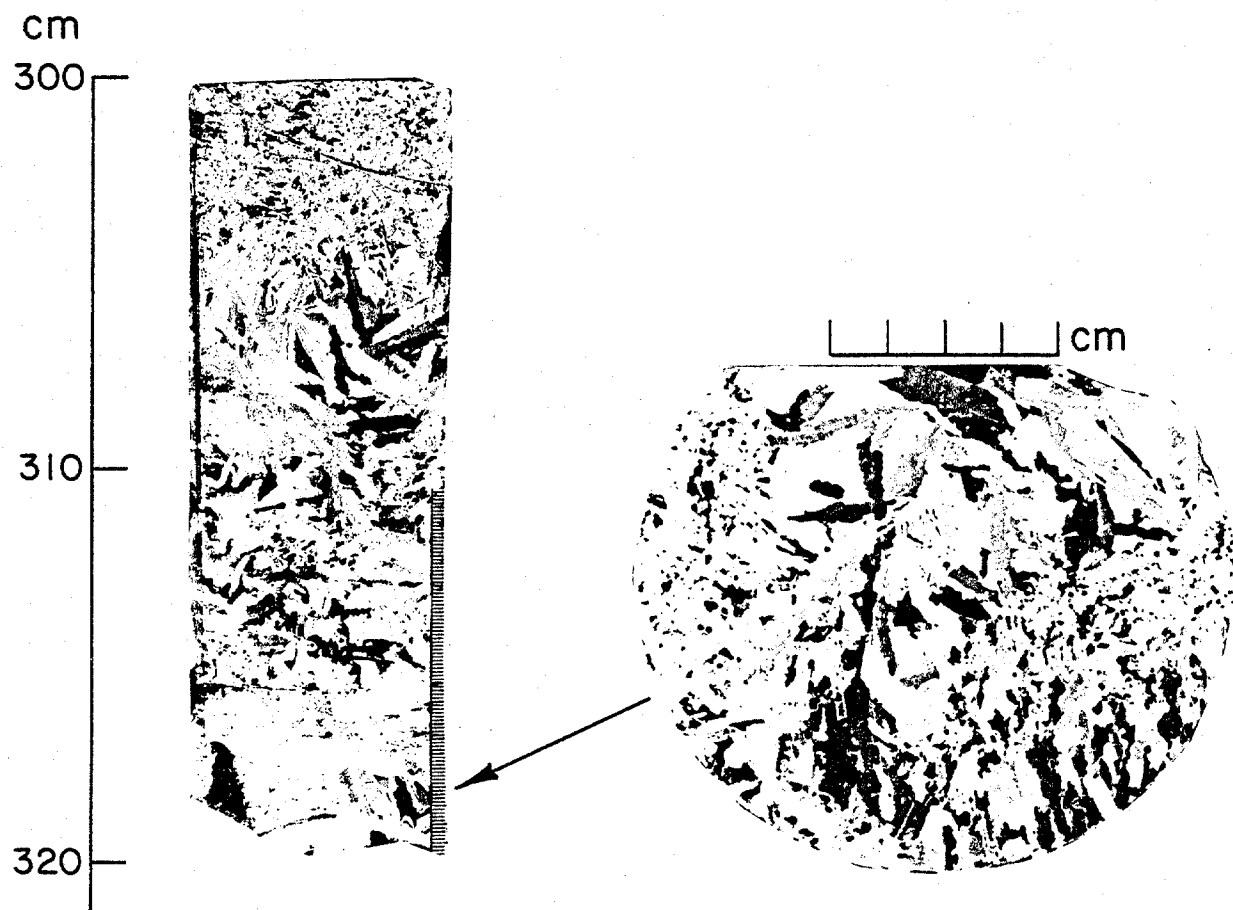
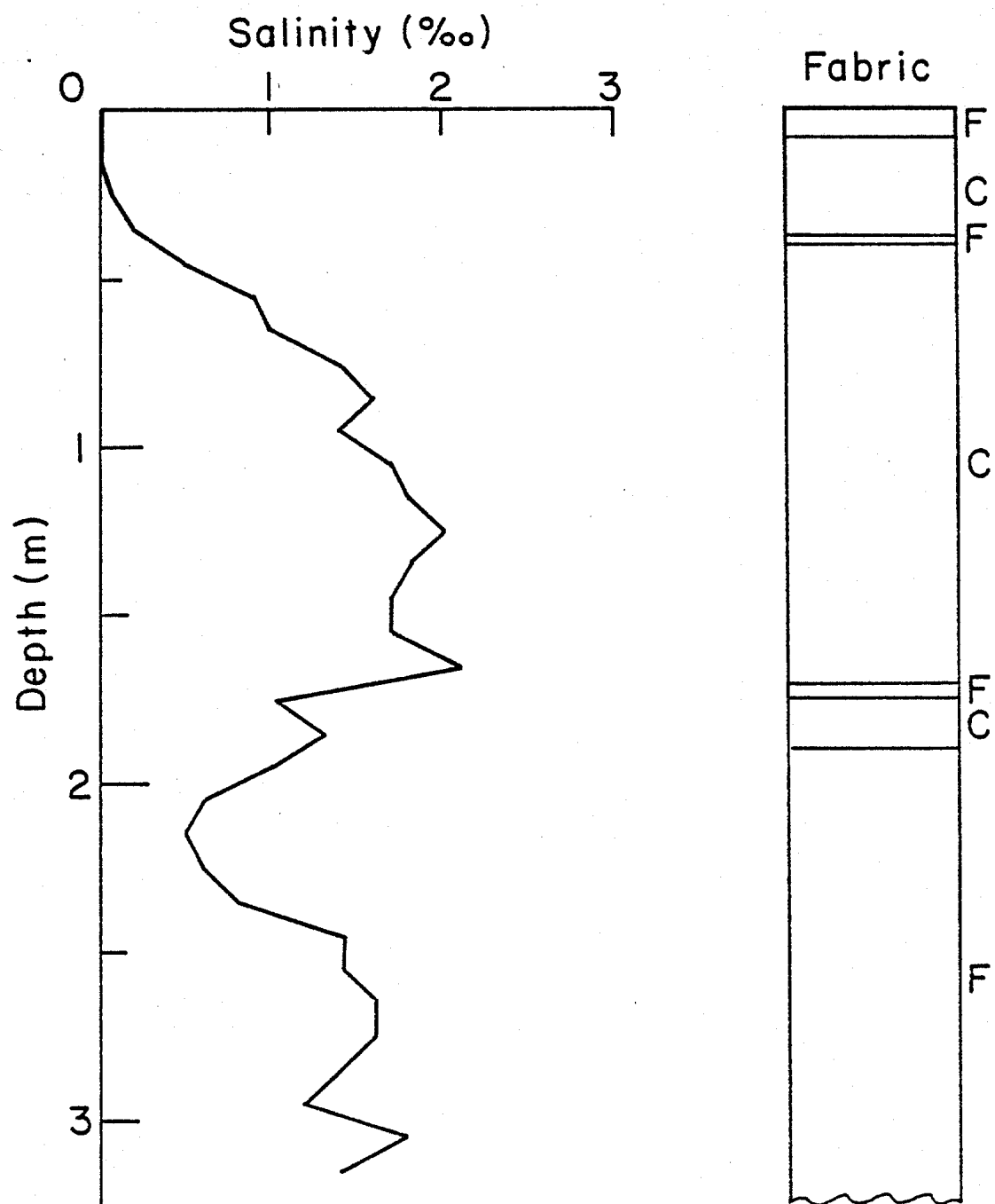


Figure 19: Structure of core of undeformed multi-year sea ice.

Figure 20: Salinity and structure of undeformed multi-year sea ice core.



significant in that ice thicknesses may be greater than those predicted by normal congelation growth and Wang (1979) has shown that fine-grained, granular sea ice is stronger than columnar ice.

Prior to these observations, frazil ice was thought to account for only the top 5% or so of the ice cover, with congelation or columnar ice providing the vast majority of the structural type (95%) of most sea ice. This condition has been found in fast ice regimes in the Arctic Basin (Weeks and Gow, 1978, 1980), in the Labrador Sea (Weeks and Lee, 1958) and more recently in the fast ice region of Antarctica near McMurdo Sound (Gow et al., 1981).

In ice edge regions and in large polynyas where substantial open water can be maintained, Martin and others described frazil ice plumes and features such as pancakes, that could conceivably result in frazil ice thicknesses of up to a meter prior to the onset and domination of congelation structure (columnar ice crystals).

Work in the Weddell Sea has, however, indicated even greater potential for frazil growth. A serious revision of the importance and distribution of frazil ice structure, at least for the Antarctic pack ice regions, appears to be in order. If frazil ice is more widespread than once believed, mechanisms for ice-ocean interaction must also be modified.

Mechanisms of Frazil Generation in Oceans: To generate fine grained ice structure in freezing from the melt, the observations from rivers, lakes, and oceans settle on one necessary condition, namely turbulence. Frazil generation originates as a result of large-scale (>cm scale) mixing of waters and has been likened to a blizzard (an upside down one) in the water column in its development. Some basic differences exist, both in the momentum and heat flow characteristics of rivers and oceans that need distinction however. In rivers, the turbulence is nearly always purely mechanically derived from accelerations in the flow by increasing

discharge, varying bed geometry (falls and rapids) or the like. Although the literature is not clear on this point it appears that a threshold velocity of 0.6 m/sec is necessary under freezing conditions to allow the onset of frazil formation (Ashton, pers. comm.). The constraint is primarily a mechanical one; while frazil generation requires efficient heat transfer between the cold atmosphere and the water, sufficient mechanical shear is necessary to mix the flow and carry the newly formed ice crystals away before a complete skim of ice can form. In the ocean, these mechanical influences are much less pronounced leading to a search for different sources of the turbulence. In oceans we speculate four possible sources of turbulence that can affect freezing conditions leading to frazil formation. The first three of these are essentially localized processes:

(1) Wind and wave induced turbulence. This effect can only account for limited frazil production in wide leads, polynyas and near ice edges due to the extreme damping of these effects when a significant percentage of ice covers the surface.

(2) Water which is at a depressed freezing point due to pressure at depth and is suddenly adiabatically brought to the surface (Foldvik and Kvinge 1974). Water of this type typically exists under large ice shelves and the ascent occurs near the front. If this were the only mechanism to make frazil one might expect the frequency of frazil structured floes to increase as the ice shelves are approached. No correlation of this type was observed in the Weddell Sea or the Arctic. Furthermore, the amount of ice production available by this mechanism (since freezing point depression is only a few tenths of a degree) does not seem compatible with the amount of frazil structure observed (~50% of the observed structure).

(3) Contact between two water masses of significantly different salinity, but both at their freezing point. We discuss this point further in relation to multi-

year ice structure since one source of this type of ice forms in Arctic under-ice melt ponds (of primarily fresh water) which drains into the ocean from melting surface ice and is stratified due to density differences. Freezing then occurs due to double diffusion (transfer of heat at a faster rate than salt) from the cold ($<-1^{\circ}\text{C}$) sea water and the fresh water on top of it (Martin 1974). Another region appears to be in river or glacier drainage regions where fresh water intrudes in contact with colder sea water which is below the fresh water freezing point. Again these effects are local in the regions they affect.

A process of sufficient generality and occurring over a broad enough region to account for much of the observed production is: (4) thermohaline convection initiated by surface cooling and freezing. Figure 21 indicates some differences between Arctic and Antarctic water column structure that indicates some potential for the observed structure. In general, the mixed layer in the Antarctic is considerably deeper than in the Arctic and totally at its local freezing point. Martin (1974), in a study of ice stalactites, indicated that the heat loss of a descending brine plume in their tanks could be as much as 50% accounted for by frazil production when the water was at its freezing point. As the temperature of the brine plume is closer to the freezing point of the surrounding water, there is less tendency for stalactite forms to occur implying all the heat loss could be taken out by frazil ice formation. We note however that in Martin and Kaufmann's study they indicated the frazil crystals appeared to be entrained downward with the descending plume. More likely is the frazil crystals are generated in waters adjacent to the descending plume for two reasons. One effect is buoyancy, that is the energy necessary to force an ice crystal downward with a density defect approaching 10% compared to surrounding waters is considerable and much larger than the relative density

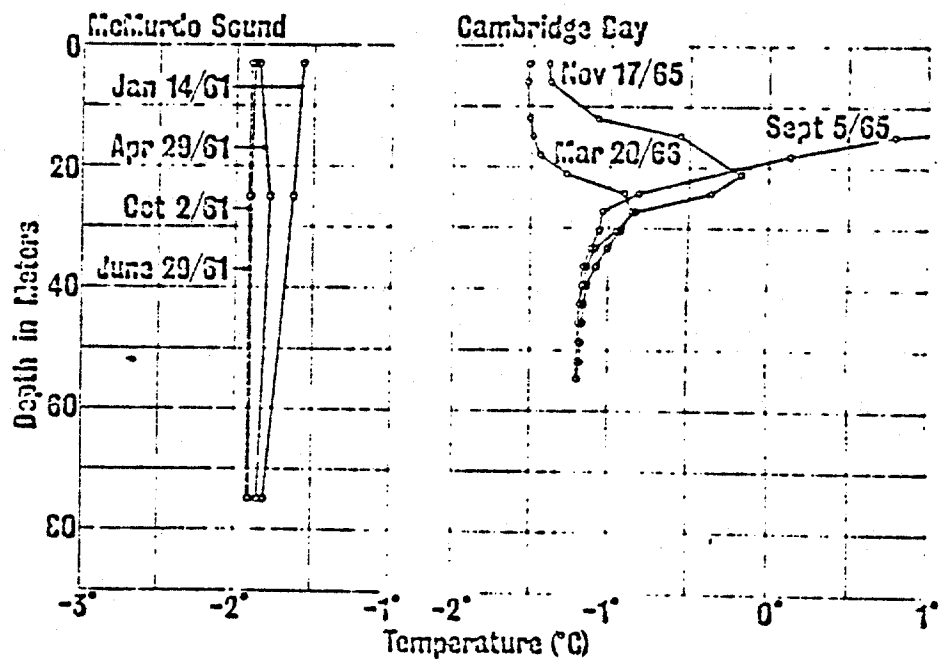


Figure 21: Seasonal changes of temperature depth profiles in the water column typical of the Antarctic (McMurdo Sound) and the Arctic (Cambridge Bay). The Antarctic near surface waters remain closer to the freezing point at greater depths than seen in the Arctic.

differences that can lead to water column overturning. Secondly, if the waters of a descending cold brine plume are entraining surrounding waters then the mixture will also be in equilibrium at its freezing point, that is there should not be any ice production, merely a more saline mixture at a temperature intermediate between the cold brine plume and the surrounding water. A simpler mechanism that preserves the buoyant characteristic of the ice crystals and still allows ice production at depth is to maintain the integrity of the descending brine plume and allow it to gain heat at a different rate than salt. This is known as double diffusion and has been observed in several other contexts in the ocean (e.g. Turner, 1974). In this mechanism, the descending brine plume gains heat but diffuses salt at a much lower rate thereby cooling adjacent waters to temperatures below their freezing point (at their given salinity). An ice crystal is then nucleated, rises due to buoyancy and the remaining water also descends at a new equilibrium freezing temperature and salinity. While the process appears to be diffusion limited by the ability to extract heat from the brine plume, the convection is continuously strengthened by the ice formation so the effect is a convection cascade which should quite effectively use the heat sink of the brine plume and establish a circulation boosting the convective process at each stage. Based on the observed structures of frazil ice in the Weddell Sea, we also see that frazil forms under thicker ice. Advecting surface generated frazil downward underneath this thicker ice is again a problem of overcoming strong buoyancy forces in the upward direction. A generation mechanism whereby ice crystals are formed at depth due to thermohaline convection is not constrained in this way. Descending brine plumes in leads and polynyas will set up a local circulation that could bring the ascending arm (containing some of the frazil) underneath adjoining ice. Also, substantial shear usually exists between the ice and the water column due to wind action on the ice so motion of the ice cover would tend to bring a different

piece (possibly thicker) into position over the ascending frazil crystals, if they are formed at depths greater than a few meters.

None of the above mentioned mechanisms have been detailed to any substantial degree. Whether they do indeed account for the observed frazil ice structures and whether frazil structures are more wide spread than previously thought or are only an anomaly of the Weddell Region and our multi-year sea ice sampling area remain the subjects for future theoretical and field work.

Uniaxial Compression Tests

A series of constant displacement rate, uniaxial compression tests were performed to evaluate the bonded synthane end caps and the "teflon feet" axial strain measurement device. The tests were conducted at a temperature of 20 to 21°F (-6.0 to -6.5°C) at constant displacement rates of 10^{-4} , 10^{-3} , and 10^{-2} in./sec. Considering that the samples were 10 inches in length and that the tests were performed on a stiff machine (250,000 pounds capacity), the displacement rates approximate full sample strain-rates of 10^{-5} , 10^{-4} , and 10^{-3} /sec, respectively.

In general, the bonded synthane end caps and axial strain measurement device functioned properly. The ice usually failed away from the sample end planes and the axial strain measurement device provided good data up to, and beyond yielding of the sample. Only at large strains did the core rod fall off the pedestal.

A partial summary of the test results are given in Table 1. More detailed information is presented in Appendix A. σ_{\max} is the peak stress during the test and ϵ_{\max} and t_{\max} are the strain and time of failure, respectively. S_i is the ice salinity, ρ the density, and n the total porosity (air and brine). Some comments on the ice structure are also given. An analysis of the elastic moduli and several petrographic analyses still need to be performed.

Typical force-displacement curves are given in Figures 22 through 24. The displacements are those measured on the sample gauge length (5.5 inches) by the DCDTs. The peak stress for each of the tests are plotted against displacement rate in Figure 25.

In general, the failure strength increases with displacement or strain-rate. As the ice salinity, temperature, and porosity are similar for all the samples, the variation in strength at a given displacement rate is best explained by the ice structure. Samples consisting of columnar crystals having a near horizontal and aligned c-axes are the strongest. Samples containing fine to medium grained frazil or granular crystals are weaker. These trends are consistent with those reported

SAMPLE NO. core-depth, cm	DISPL. RATE in/sec	TEMP. OF	σ_{max} psi	ϵ_{max} %	t_{max} sec	S_i %	ρ lb/ft ³	n %	Columnar %	STRUCTURE* Orientation	Size
C3-228/254	10 ⁻⁴	21	338	0.38	576	0.9	56.6	21.6	40	random	f to m
C2-315/341	10 ⁻⁴	20	154	0.23	438	2.0	-	-	80	random	f to m
C4-177/203	10 ⁻⁴	21	445	0.30	408	1.7	57.0	21.6	100	horiz. & align.	m
C2-168/194	10 ⁻⁴	20	680	0.16	414	1.9	57.2	18.6	97	horiz. & align.	m
C2-282/308	10 ⁻⁴	20	383	0.32	402	1.7	-	-	25	random	f to m
C3-161/187	10 ⁻³	21	585	0.30	52	1.8	56.9	24.9	80	horiz.	c
C3-261/287	10 ⁻³	21	706	0.13	34	1.6	57.1	18.7	95	horiz. & align.	m
C3-079/105	10 ⁻³	20	1532	0.70	70	1.9	-	-	100	horiz. & align.	m
C4-090/116	10 ⁻²	21	1265	0.13	3	1.5	57.0	20.0	100	horiz. & align.	m
C3-128/154	10 ⁻²	20	1243	0.10	4	1.5	-	-	100	horiz. & align.	m
C3-136/061	10 ⁻²	20	1683	0.27	5	1.1	-	-	100	horiz.	m

* Orientation - c-axes - alignment in several tests need to be confirmed by petrographic analysis

Size - grain size - f - fine <2 mm

m - medium 2 to 6 mm

c - coarse >6 mm

Table 1: Summary of constant displacement rate, uniaxial compression tests.

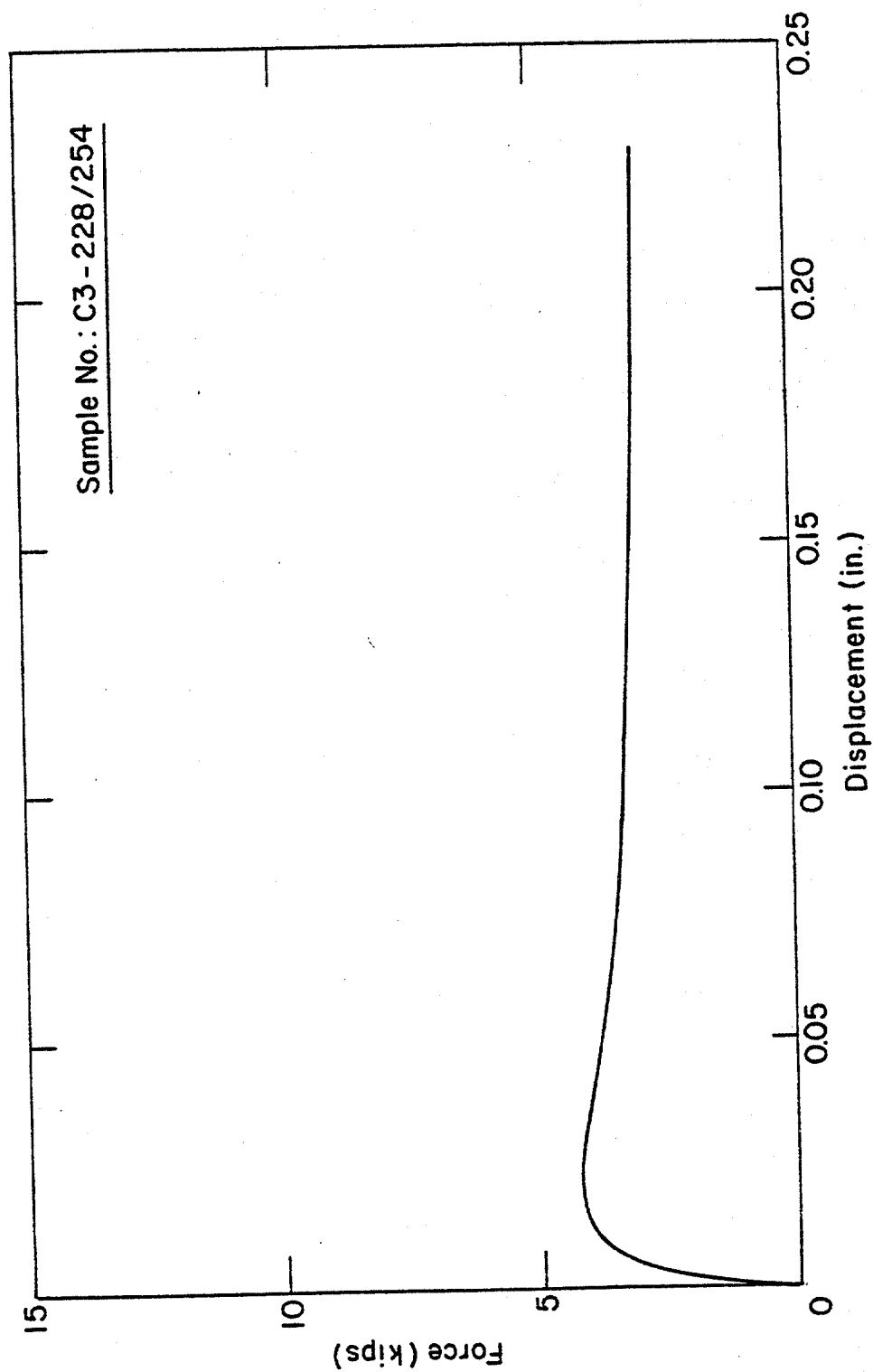


Figure 22: Force-displacement curve for constant displacement rate test at 10^{-4} in/sec.

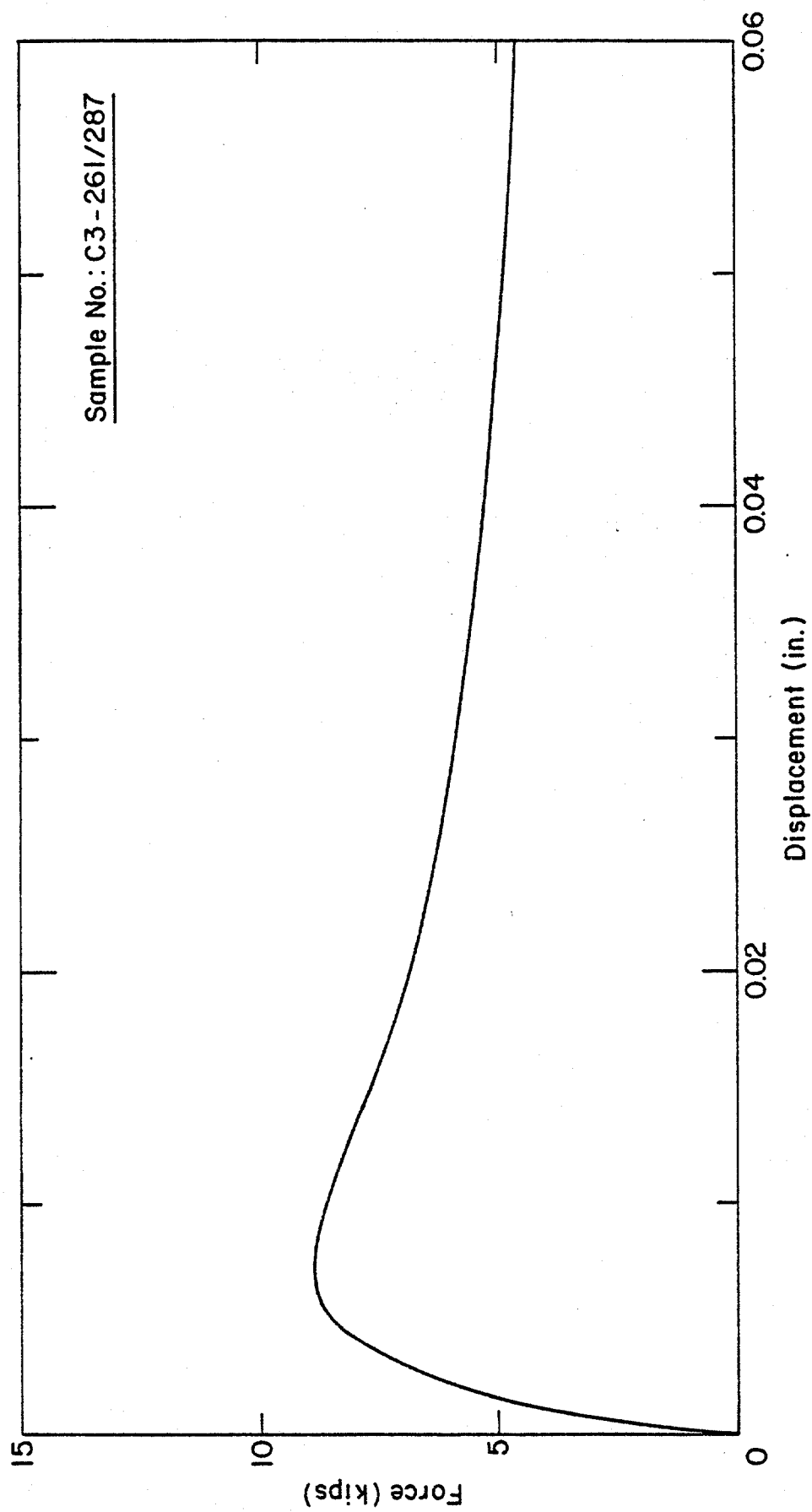


Figure 23: Force-displacement curve for constant displacement rate test at 10^{-3} in/sec.

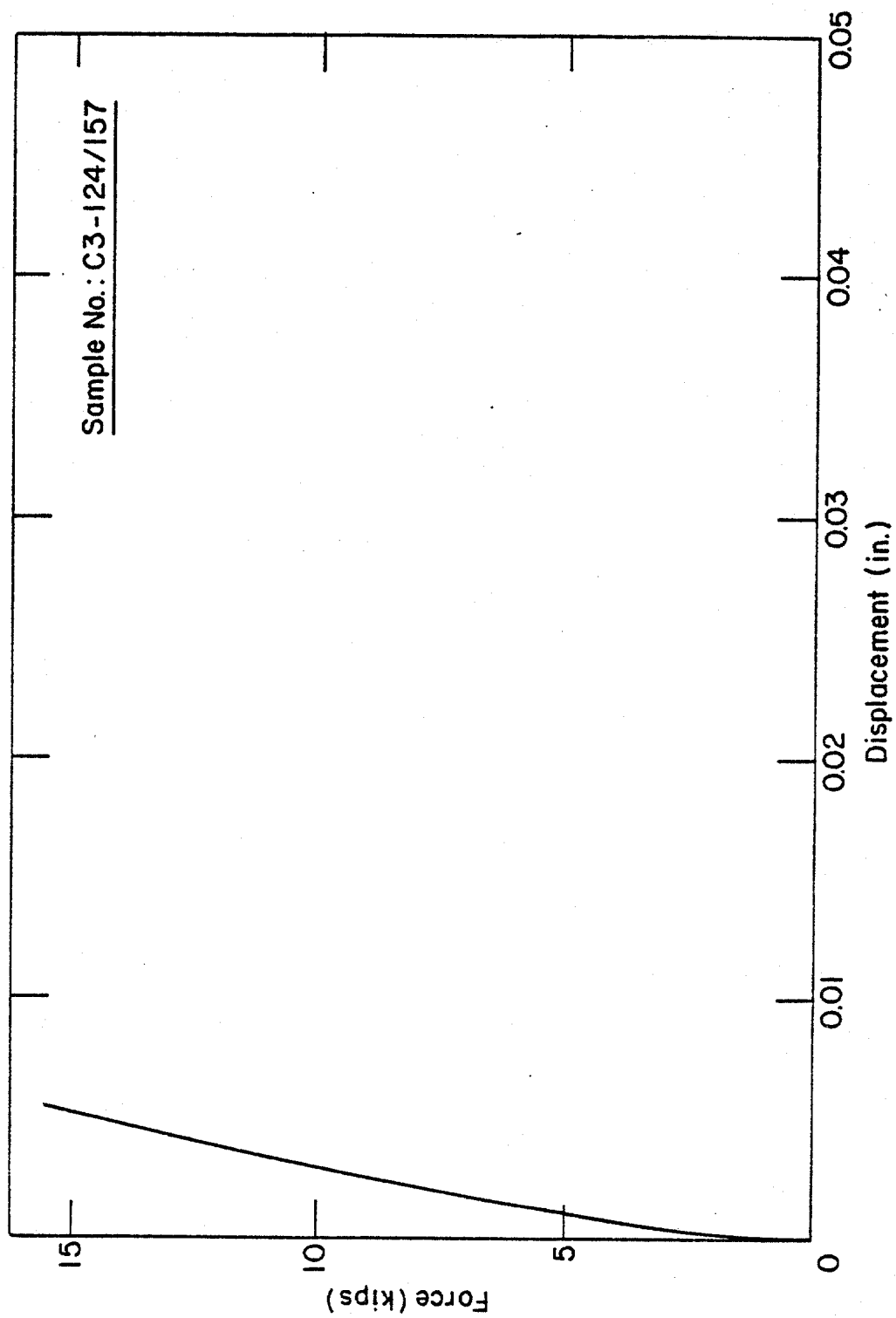


Figure 24: Force-displacement curve for constant displacement rate test at 10^{-2} in/sec.

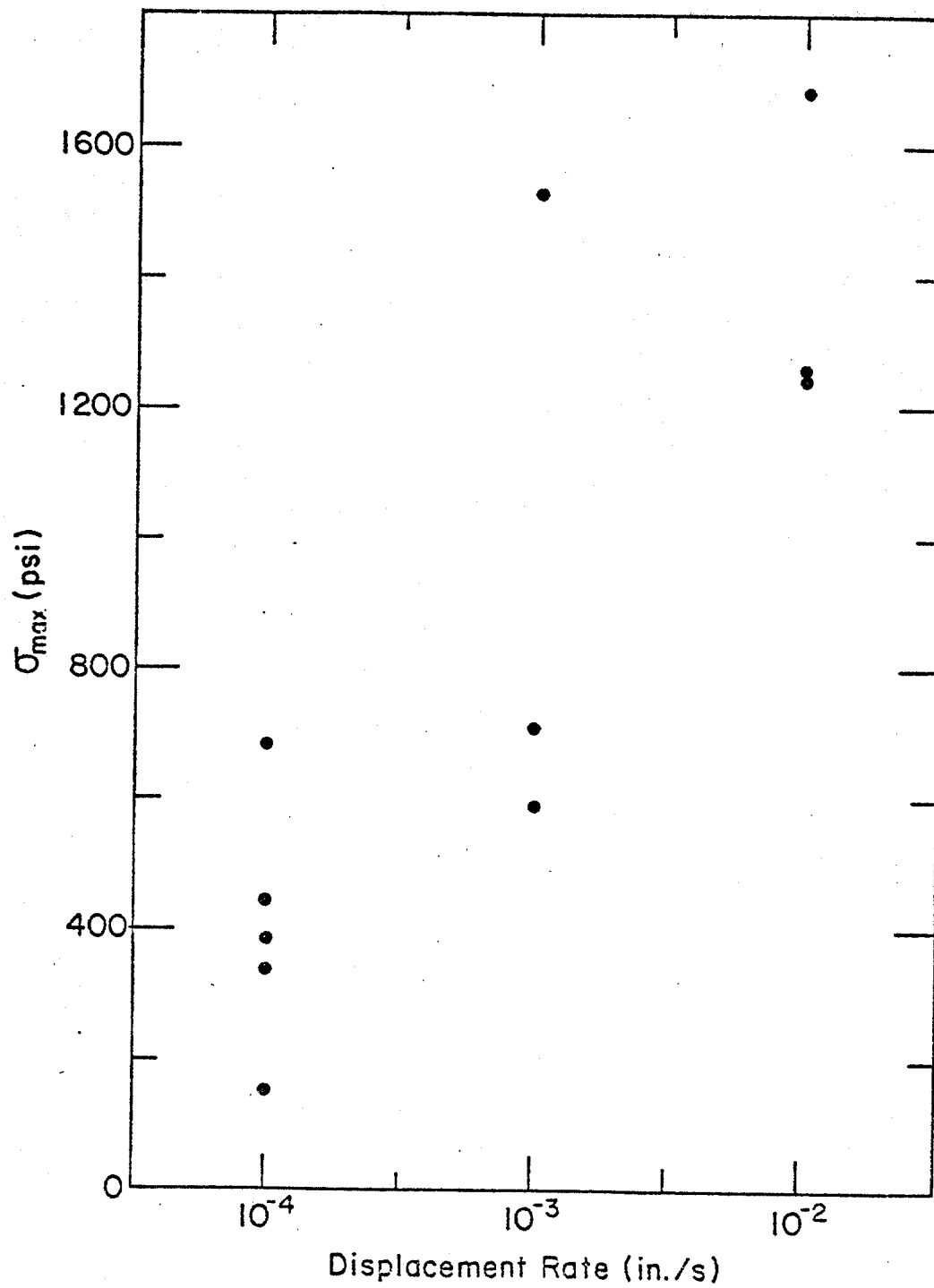


Figure 25: Peak stress versus displacement rate for undeformed multi-year sea ice in uniaxial compression.

by Wang (1979) for first-year sea ice and comparison of the results to Wang's data indicates that, indeed, multi-year ice is stronger. This is contrary to the data recently presented by Timco and Frederking (1980). We are not surprised that the multi-year ice is stronger in that the salinity and porosity of multi-year sea ice are lower.

Equations for Determining Air Volume

Equations are presented in Appendix B to calculate the air and brine volume of sea ice given the ice salinity, temperature, and density. The presence of solid salts in the ice is considered in the air volume equations. In addition, equations are also given to recalculate the air and brine volumes if the ice sample temperature is changed. The air volume equations are more precise and cover a wider temperature range than that given by Schwerdtfeger (1963) and eliminate the lengthy arithmetic calculations if Assur's (1960) phase table is used.

REFERENCES

- Bennington, K.O. (1959) Preliminary report on sea ice crystal fabrics on Station Charlie. In "Semi-Annual Report 1 December 1959, Drifting Station Charlie," Project Husky Nonr. 477(24) T.O. 307-252.
- Cherepanov, N.V. (1957) Using the methods of crystal optics for determining the age of drift ice (in Russian). Problemy Arktiki, 2:179-84.
- Cox, G.F.N. and W.F. Weeks (1974) Salinity variations in sea ice. Journal of Glaciology, 13(67), 109-20.
- Foldvik, A. and T. Kvinge (1974) Conditional instability of sea water at the freezing point, Deep Sea Research, Vol. 21, pp. 169-74.
- Gow, A.J., S.F. Ackley, W.F. Weeks, and J.W. Govoni (1981) Physical and structural characteristics of Antarctic sea ice. Third Int. Symp. Antarct. Glaciol., Ohio State Univ. Annals of Glaciology.
- Malmgren, F. (1927) On the properties of sea ice. Sci. Res. Norwegian North Pole Exped. with the "Maud", 1918-1925, Vol. 1, No. 5, 67 pp.
- Martin, S. (1974) Ice stalactites: comparison of a laminar flow theory with experiment. Journal of Fluid Mechanics, 63(1), 51-79.
- Martin, S. and P. Kauffman (1974) The evolution of under-ice melt ponds, or double diffusion at the freezing point. Journal of Fluid Mechanics, 64(3), 507-527.
- Savel'ev, B.A. (1963) Structure, composition, and properties of the ice cover of sea and fresh waters (in Russian), Izd. Moskovskogo Univ. 541 pp.
- Schwarzacher, W. (1959) Pack-ice studies in the Arctic Ocean. Journal of Geophysical Research, 64, 2357-2367.
- Shumskii, P.A. (1955) K izucheniiu l'dov Severnogo Ledovitogo okeana (A study of ice in the Arctic Ocean). Vestnik Akademii Nauk SSSR, 25, No. 2, 33-38.
- Timco, G.W. and Frederking, R.M.W. (1980) Compressive strength of multi-year ridge ice. Workshop on Sea Ice Ridges, Calgary, Alberta, 22-24, October, 1980.
- Turner, J.S. (1973) Buoyancy Effects in Fluids, Cambridge Press, 367 pp.
- Untersteiner, N. (1961) On the mass and heat budget of arctic sea ice. Arch. Meteorol. Geophys. Biok. 12, 151-182.
- Wang, Y.S. (1979) Crystallographic studies and strength tests of field ice in the Alaskan Beaufort Sea. In POAC '79 Proceedings, p. 651-665. Trondheim, Norway.

Weeks, W.F. and A.J. Gow (1978) Preferred crystal orientations along the margins of the Arctic Ocean. Journal of Geophysical Research 84(C10), p. 5105-21.

Weeks, W.F. and A.J. Gow (1980) Crystal alignments in the fast ice of arctic Alaska. Journal of Geophysical Research 85 (C2), p. 1137-46.

Weeks, W.F. and O.S. Lee (1958) Observations on the physical properties of sea ice at Hopedale, Labrador. Arctic 11, 134-155.

APPENDIX A

Uniaxial Compression Test Data*

* Data available at time of progress report. Not complete.

C3-228/254

Uniaxial Compression

Displacement rate: 10^{-4} in/sec.

Temperature: 21°F (-6.1°C)

Salinity: 0.9‰

Density: 0.906 g/cm³ (56.6 lbs/ft³)

Brine Volume: 7.4‰

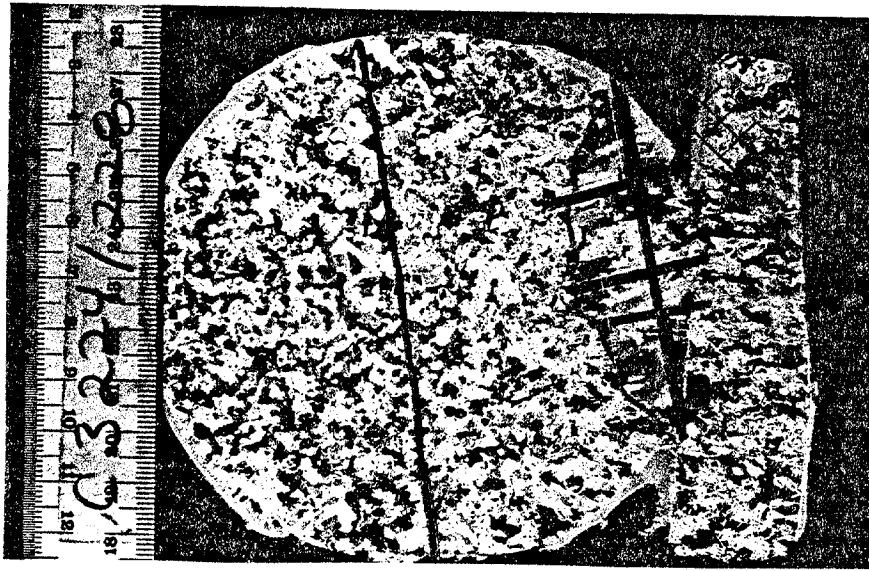
Air Volume: 14.2‰

Porosity: 21.6‰

Structure: ~60% granular
~40% columnar in center portion of sample.
grain size variable, see photos

$$\frac{\sigma_{\max} = 338 \text{ psi}}{t_{\max} = 576 \text{ sec}} \quad \epsilon_{\max} = 0.38\%$$

C3-228/254: PRE-TEST



TOP

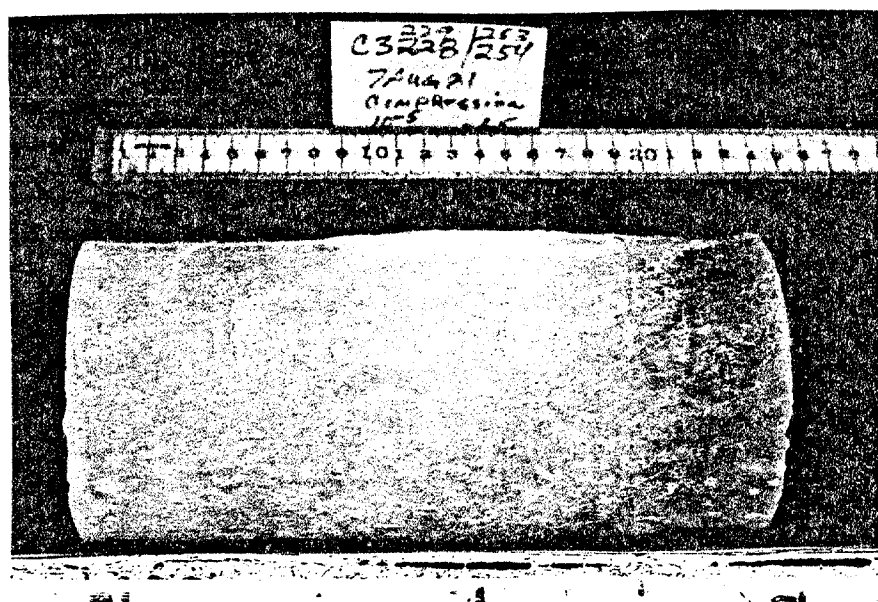
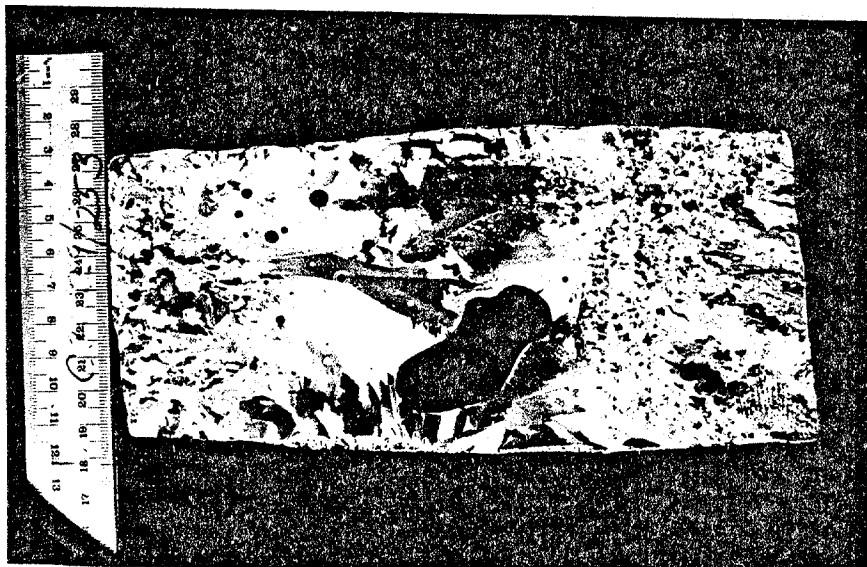
LARGE GRAINS: $\bar{L} = 4.1 \text{ mm}$; $\bar{W} = 2.6 \text{ mm}$
SMALL GRAINS: $L = 2.0 \text{ mm}$



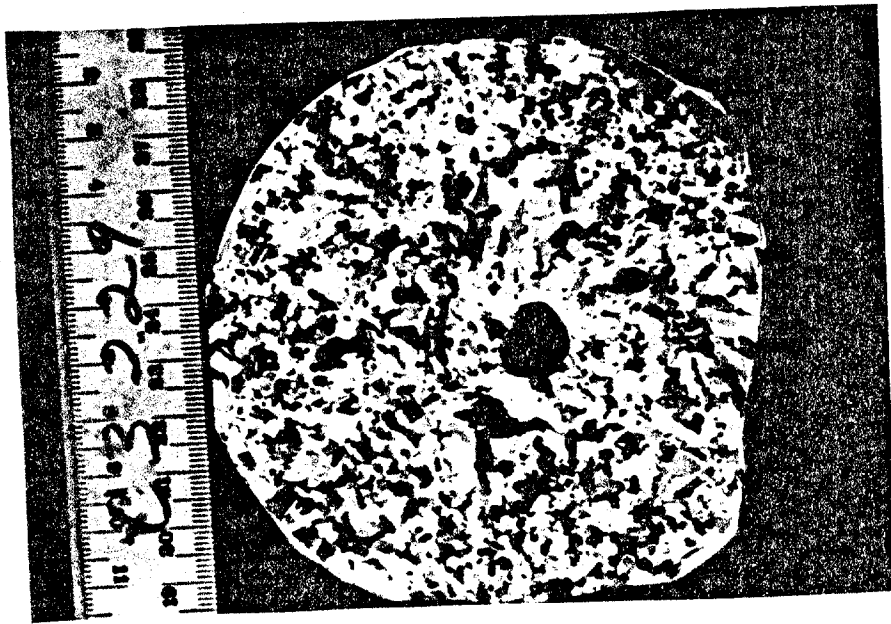
BOTTOM

$\bar{L} = 4.7 \text{ mm}$; $\bar{W} = 4.0 \text{ mm}$

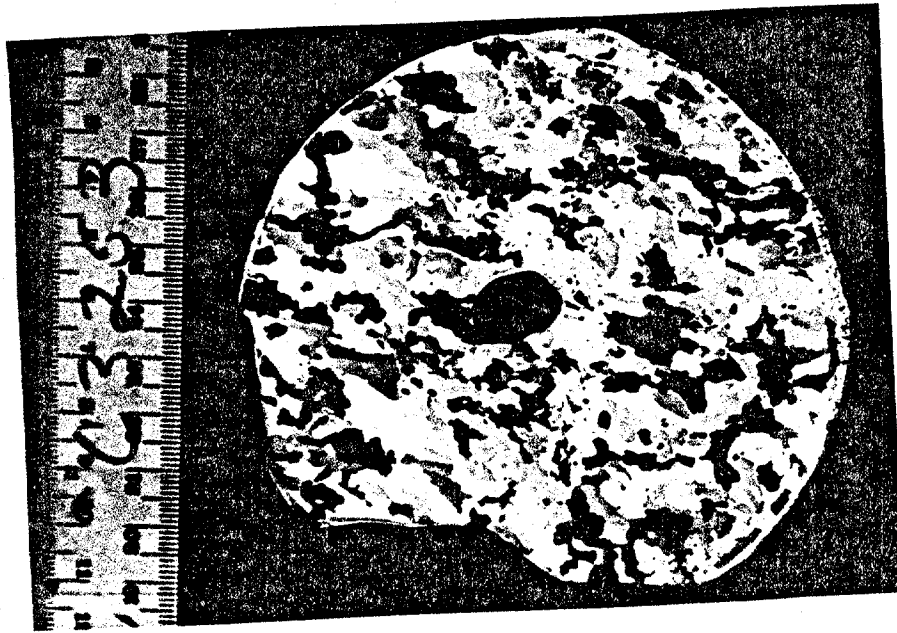
C3 - 228/254: POST-TEST



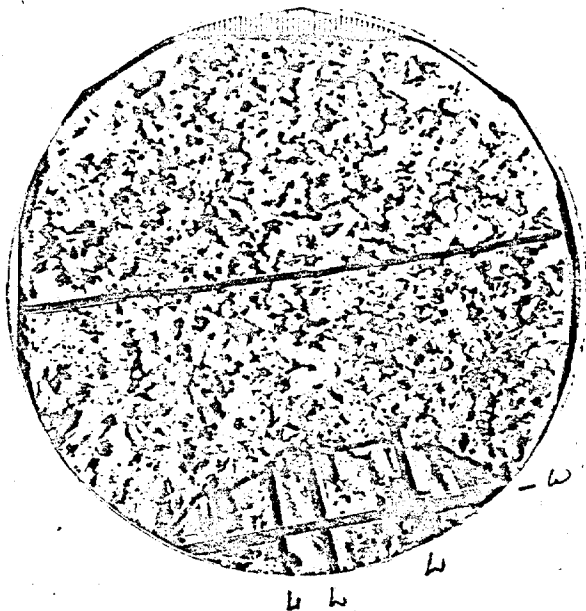
C3-228/254 : POST-TEST



TOP



BOTTOM



SAMPLE NO. C3-228/254
@ C3-228

GRAIN DESCRIPTION: _____

Colony size 10 % SAMPLE

GRAIN LENGTH: 4.1 mm

A) TOTAL LENGTH OF TEST LINE: _____ mm

B) TOTAL NO. OF INTERSECTIONS: _____

$$\begin{aligned} \text{LENGTH OF GRAIN} &= \frac{A}{B} \\ &= \underline{2.88} \text{ mm (READING)} \\ &= \underline{4.11} \text{ mm (ACTUAL)} \end{aligned}$$

$$\begin{array}{r} 4 \quad 15 \\ 8 \quad 12 \\ 5 \quad 16 \\ \hline 17 \quad 43 \end{array}$$

GRAIN WIDTH: 2.6 mm

A) TOTAL LENGTH OF TEST LINE: 46 mm

B) TOTAL NO. OF INTERSECTIONS: 25

$$\begin{aligned} \text{WIDTH OF GRAIN} &= \frac{A}{B} \\ &= \underline{1.84} \text{ mm (READING)} \\ &= \underline{2.63} \text{ mm (ACTUAL)} \end{aligned}$$

SAMPLE NO. C3-228/254
@ C3-228

GRAIN DESCRIPTION: _____

Fine Grain 90 % SAMPLE

GRAIN SIZE: 2.0 mm

A) TOTAL LENGTH OF TEST LINE: 72 mm

B) TOTAL NO. OF INTERSECTIONS: 51

$$\begin{aligned}\text{GRAIN SIZE} &= \frac{A}{B} \\ &= \frac{1.41}{} \text{ mm (READING)} \\ &= \frac{2.01}{} \text{ mm (ACTUAL)}\end{aligned}$$

GRAIN DESCRIPTION: _____

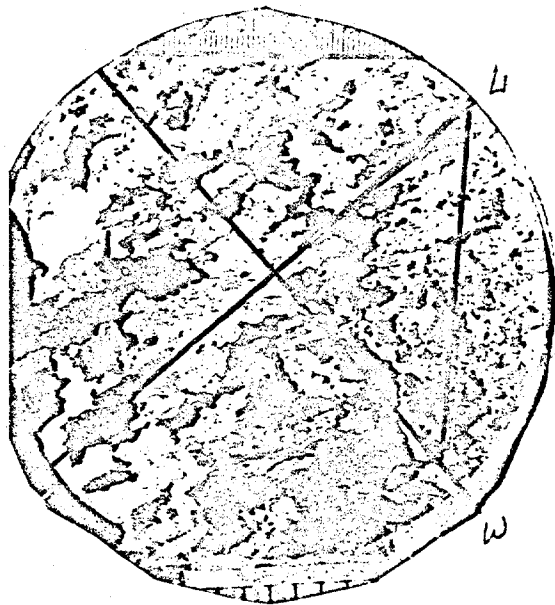
% SAMPLE

GRAIN SIZE: _____ mm

A) TOTAL LENGTH OF TEST LINE: _____ mm

B) TOTAL NO. OF INTERSECTIONS: _____

$$\begin{aligned}\text{GRAIN SIZE} &= \frac{A}{B} \\ &= \frac{}{} \text{ mm (READING)} \\ &= \frac{}{} \text{ mm (ACTUAL)}\end{aligned}$$



SAMPLE NO. C3-228/254
@ C3-254

GRAIN DESCRIPTION: _____

Columellar 75% 70 SAMPLE

GRAIN LENGTH: 4.7 mm

A) TOTAL LENGTH OF TEST LINE: 73 mm

B) TOTAL NO. OF INTERSECTIONS: 32

$$\begin{aligned} \text{LENGTH OF GRAIN} &= \frac{A}{B} \\ &= \frac{3.32}{} \text{ mm (READING)} \\ &= \frac{4.74}{} \text{ mm (ACTUAL)} \end{aligned}$$

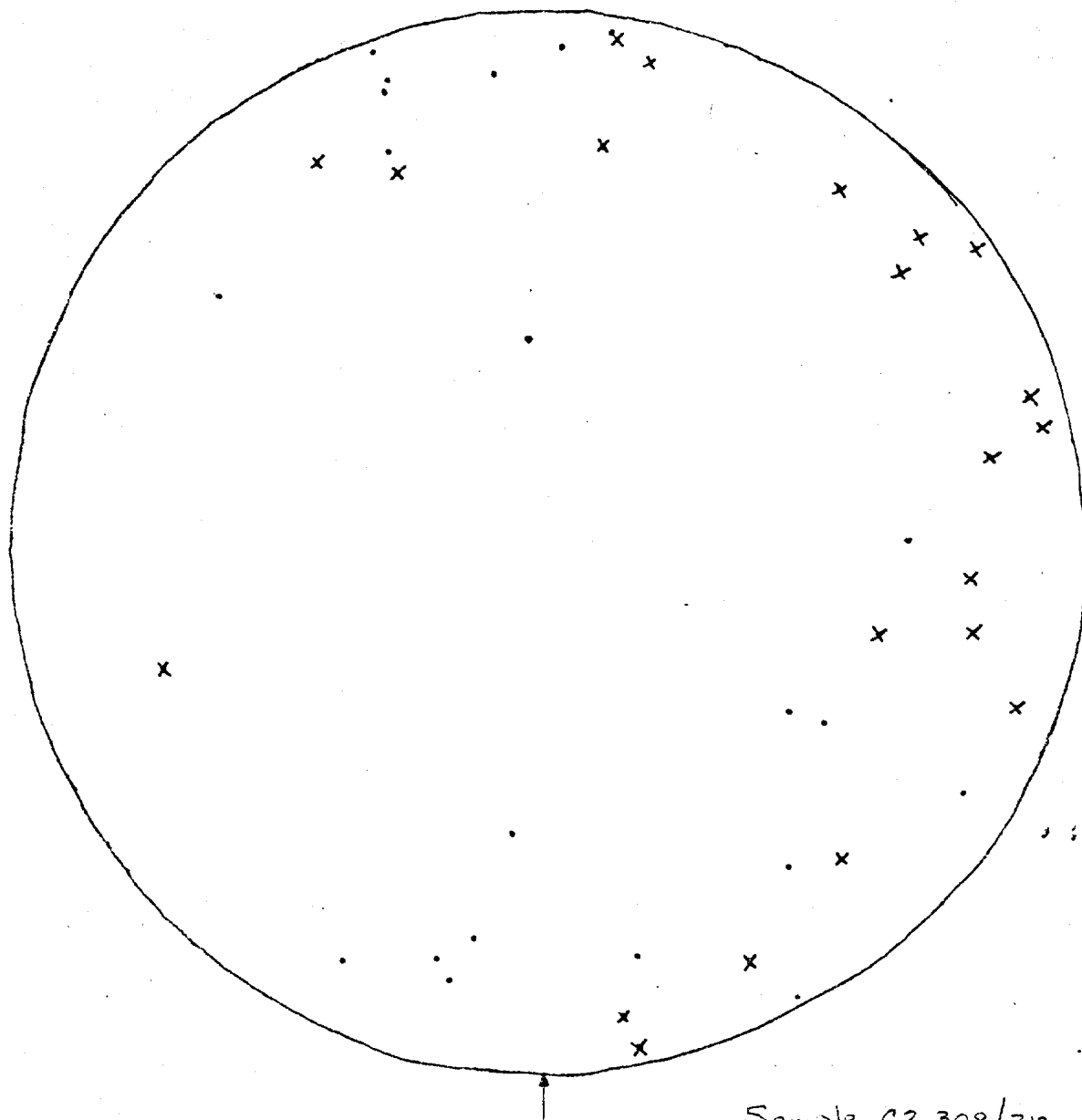
GRAIN WIDTH: 4.0 mm

A) TOTAL LENGTH OF TEST LINE: 73 mm

B) TOTAL NO. OF INTERSECTIONS: 26

$$\begin{aligned} \text{WIDTH OF GRAIN} &= \frac{A}{B} \\ &= \frac{2.81}{} \text{ mm (READING)} \\ &= \frac{4.01}{} \text{ mm (ACTUAL)} \end{aligned}$$

C2-282/308 : BOTTOM



Sample C2 308/312

C2-315/341

Uniaxial compression

Displacement rate: 10^{-4} in/sec.

Temperature: 20°F (-6.5°)

Salinity: 2.0‰

Density: ---

Brine Volume: ~15.6‰

Air Volume: ---

Porosity: ---

Structure: Mostly medium grained columnar crystals with
random orientation. $\bar{L} = 4.4$ mm; $\bar{W} = 2.7$ mm
some granular ice, $\bar{L} = 1.9$ mm.

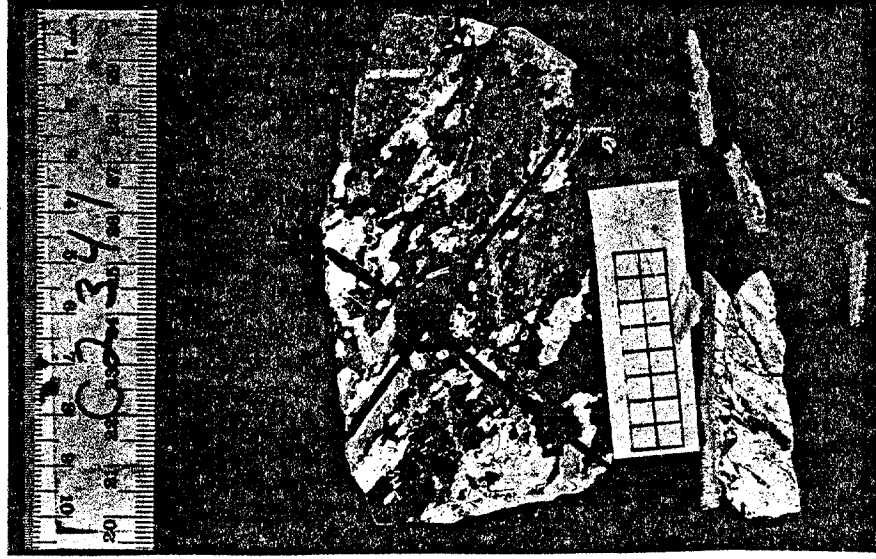
$$\frac{\sigma_{\max} = 154 \text{ psi}}{t_{\max} = 438 \text{ sec}} \quad \epsilon_{\max} = 0.23\%$$

C2-315/341 : PRE-TEST



TOP

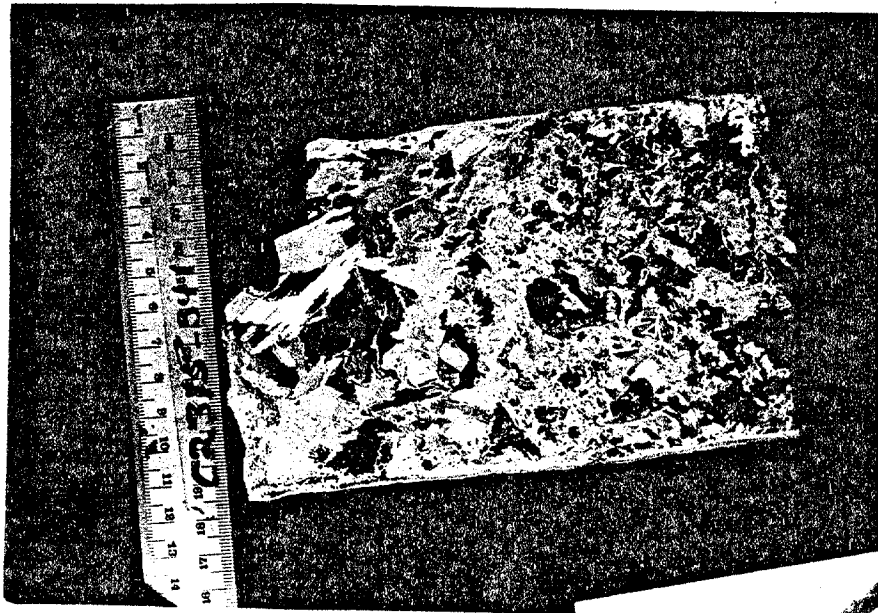
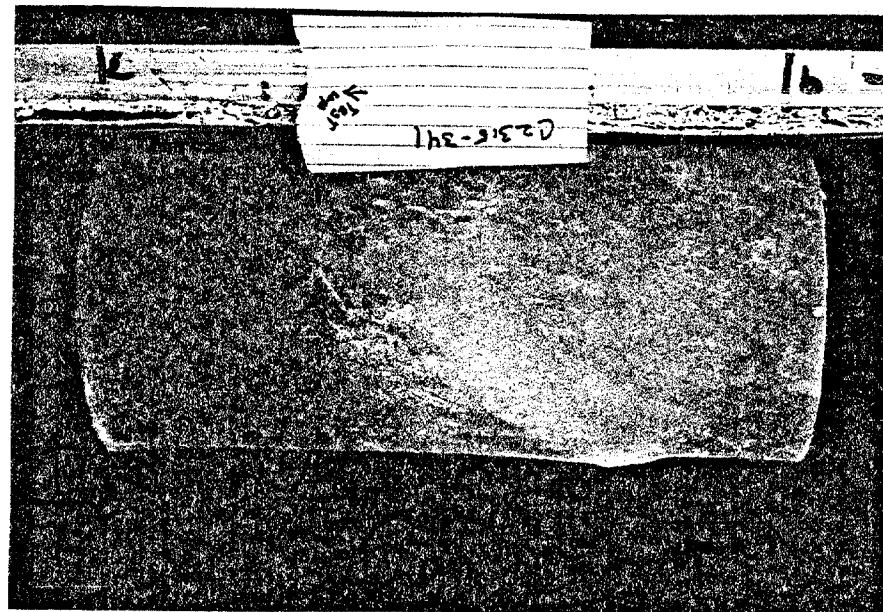
LARGE GRAINS: $\bar{L} = 4.4 \text{ mm}$; $\bar{W} = 2.7 \text{ mm}$
 MED. GRAINS: $\bar{L} = 3.7 \text{ mm}$; $\bar{W} = 2.9 \text{ mm}$
 SMALL GRAINS: $\bar{L} = 1.9 \text{ mm}$



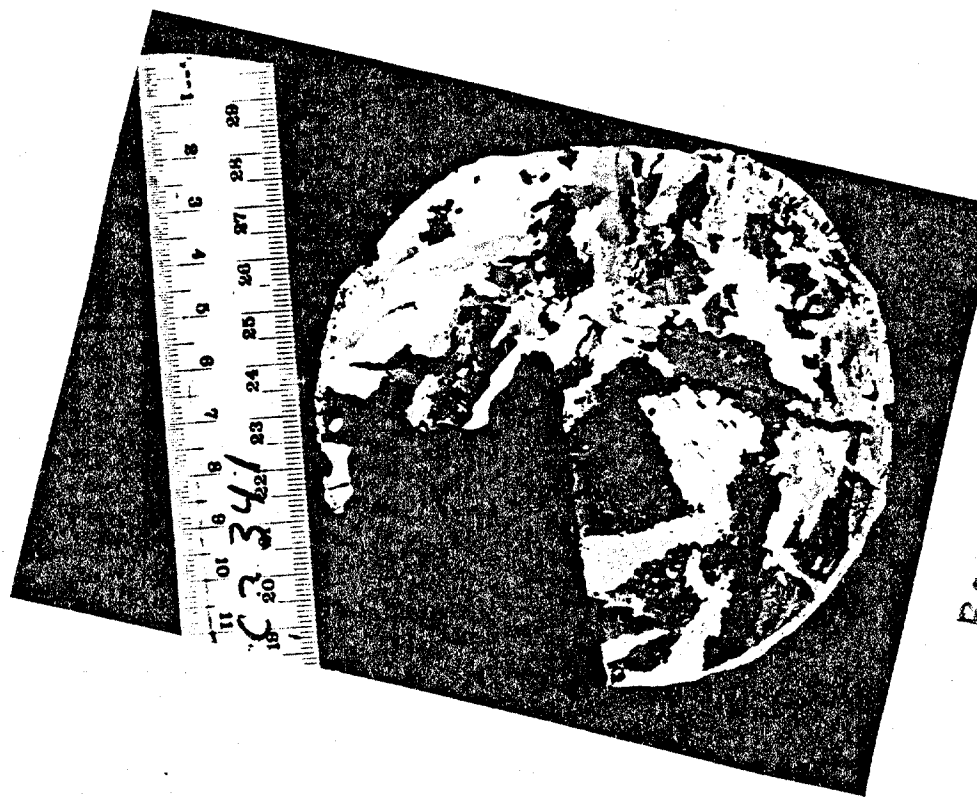
BOTTOM

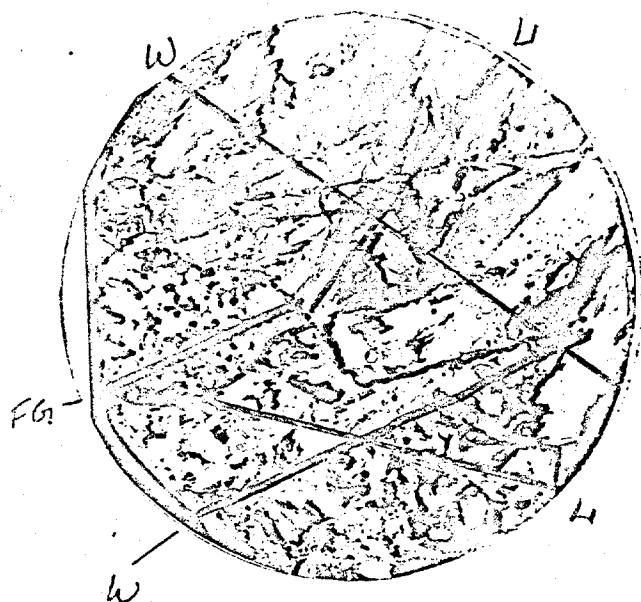
$\bar{L} = 4.4 \text{ mm}$; $\bar{W} = 2.7 \text{ mm}$

C2-315/341 : POST-TEST



C2-315/341 : POST-TEST





SAMPLE NO. C2-315/341
@ C2-315

GRAIN DESCRIPTION: _____

COLUMNAR 60 % SAMPLE

GRAIN LENGTH: 4.4 mm

A) TOTAL LENGTH OF TEST LINE: 46 mm

B) TOTAL NO. OF INTERSECTIONS: 15

$$\text{LENGTH OF GRAIN} = \frac{A}{B}$$

$$= \underline{3.1} \text{ mm (READING)}$$

$$= \underline{4.4} \text{ mm (ACTUAL)}$$

GRAIN WIDTH: 2.7 mm

A) TOTAL LENGTH OF TEST LINE: 72 mm

B) TOTAL NO. OF INTERSECTIONS: 37.5

$$\text{WIDTH OF GRAIN} = \frac{A}{B}$$

$$= \underline{1.9} \text{ mm (READING)}$$

$$= \underline{2.7} \text{ mm (ACTUAL)}$$

SAMPLE NO. C2-315/341
@ C2-315

GRAIN DESCRIPTION: _____

Med grain 30 % SAMPLE

GRAIN LENGTH: 3.7 mm

A) TOTAL LENGTH OF TEST LINE: 51 mm

B) TOTAL NO. OF INTERSECTIONS: 19

$$\begin{aligned}\text{LENGTH OF GRAIN} &= \frac{A}{B} \\ &= \frac{2.6}{1} \text{ mm (READING)} \\ &= \frac{3.7}{1} \text{ mm (ACTUAL)}\end{aligned}$$

GRAIN WIDTH: 2.9 mm

A) TOTAL LENGTH OF TEST LINE: 53 mm

B) TOTAL NO. OF INTERSECTIONS: 27

$$\begin{aligned}\text{LENGTH OF GRAIN} &= \frac{A}{B} \\ &= \frac{2.0}{1} \text{ mm (READING)} \\ &= \frac{2.9}{1} \text{ mm (ACTUAL)}\end{aligned}$$

GRAIN DESCRIPTION: _____

% SAMPLE

GRAIN LENGTH: _____ mm

A) TOTAL LENGTH OF TEST LINE: _____ mm

B) TOTAL NO. OF INTERSECTIONS: _____

$$\begin{aligned}\text{LENGTH OF GRAIN} &= \frac{A}{B} \\ &= \text{_____ mm (READING)} \\ &= \text{_____ mm (ACTUAL)}\end{aligned}$$

GRAIN WIDTH: _____ mm

A) TOTAL LENGTH OF TEST LINE: _____ mm

B) TOTAL NO. OF INTERSECTIONS: _____

$$\begin{aligned}\text{LENGTH OF GRAIN} &= \frac{A}{B} \\ &= \text{_____ mm (READING)} \\ &= \text{_____ mm (ACTUAL)}\end{aligned}$$

SAMPLE NO. C2-315/341
@ C2-315

GRAIN DESCRIPTION: _____

Fine grain 10 % SAMPLE

GRAIN SIZE: _____ mm

A) TOTAL LENGTH OF TEST LINE: 25 mm

B) TOTAL NO. OF INTERSECTIONS: 19

$$\text{GRAIN SIZE} = \frac{A}{B}$$

$$= \frac{1.3}{1.9} \text{ mm (READING)}$$

$$= \frac{1.9}{1.3} \text{ mm (ACTUAL)}$$

GRAIN DESCRIPTION: _____

% SAMPLE

GRAIN SIZE: _____ mm

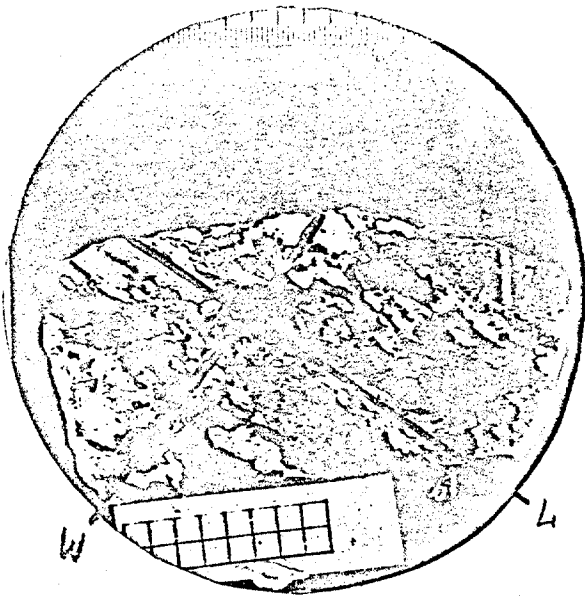
A) TOTAL LENGTH OF TEST LINE: _____ mm

B) TOTAL NO. OF INTERSECTIONS: _____

$$\text{GRAIN SIZE} = \frac{A}{B}$$

$$= \text{_____ mm (READING)}$$

$$= \text{_____ mm (ACTUAL)}$$



SAMPLE NO. C 2-315/341
@ C 2341

GRAIN DESCRIPTION: COLUMNAR 100% SAMPLE

GRAIN LENGTH: 4.6 mm

A) TOTAL LENGTH OF TEST LINE: 50 mm

B) TOTAL NO. OF INTERSECTIONS: 15.5

$$\begin{aligned} \text{LENGTH OF GRAIN} &= \frac{A}{B} \\ &= \underline{3.22} \text{ mm (READING)} \\ &= \underline{4.60} \text{ mm (ACTUAL)} \end{aligned}$$

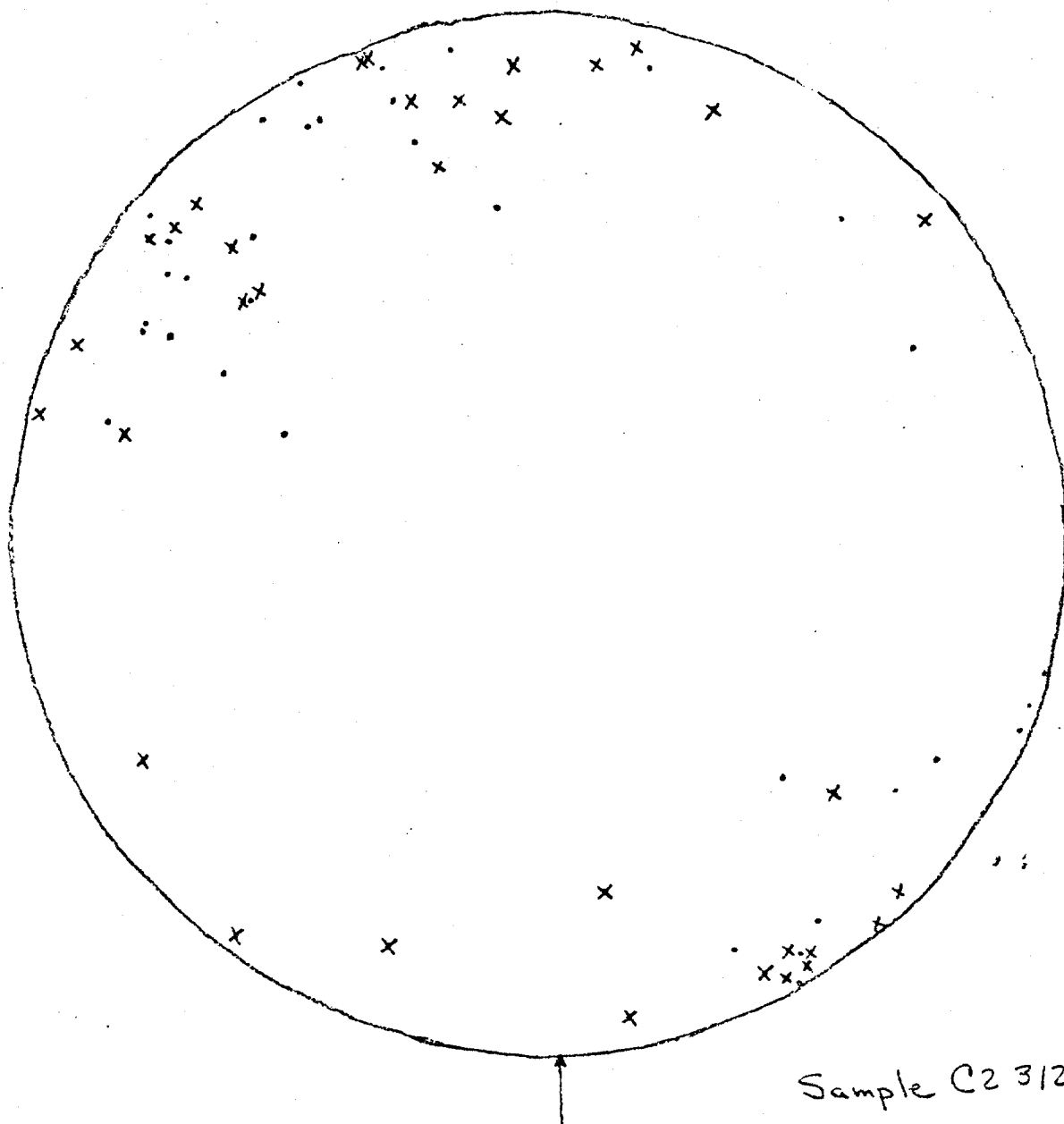
GRAIN WIDTH: 3.9 mm

A) TOTAL LENGTH OF TEST LINE: 41 mm

B) TOTAL NO. OF INTERSECTIONS: 15

$$\begin{aligned} \text{WIDTH OF GRAIN} &= \frac{A}{B} \\ &= \underline{2.73} \text{ mm (READING)} \\ &= \underline{3.9} \text{ mm (ACTUAL)} \end{aligned}$$

C2- 315/341 : BOTTOM



Sample C2 312/315

C4-177/203

Uniaxial compression

Displacement rate: 10^{-4} in/sec

Temperature: 21°F (-6.2°C)

Salinity: $1.7^{\circ}/_{\text{oo}}$

Density: 0.913 g/cm^3 (57.0 lbs/ft^3)

Brine Volume: $13.8^{\circ}/_{\text{oo}}$

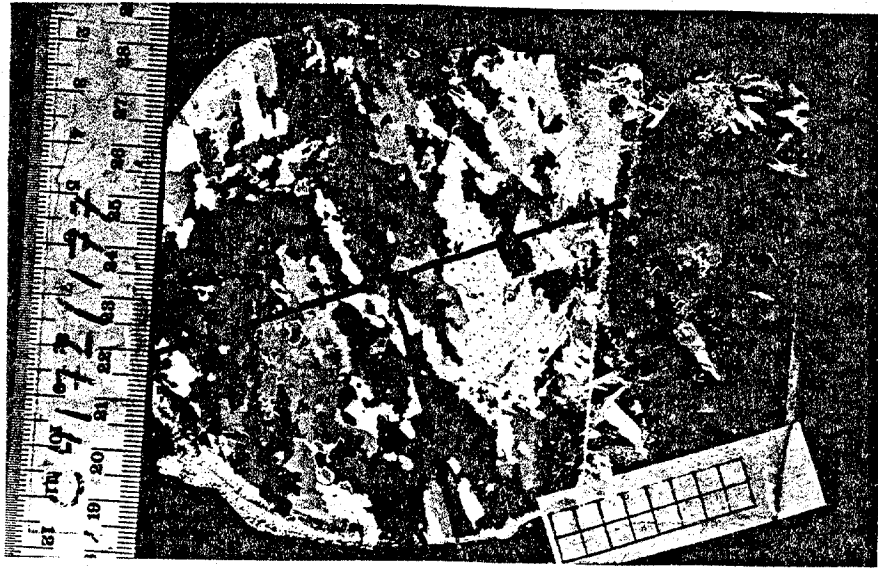
Air Volume: $7.8^{\circ}/_{\text{oo}}$

Porosity: $21.6^{\circ}/_{\text{oo}}$

Structure: 100% columnar (congelation)
C-axes $\sim 85^{\circ}$ from vertical
alignment $\sim 80^{\circ}$
 $\bar{L} = 6.7 \text{ mm}$ $\bar{W} = 3.9 \text{ mm}$

$$\frac{\sigma_{\text{max}} = 445 \text{ psi}}{t_{\text{max}} = 408 \text{ sec}} \quad \epsilon_{\text{max}} = 0.30\%$$

C4-177/203: PRE-TEST



TOP

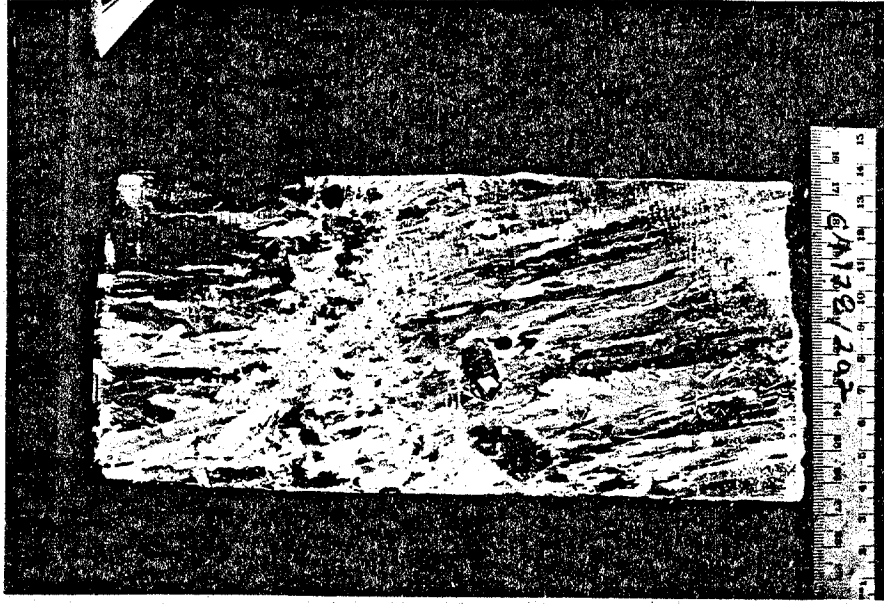
$\bar{L} = 6.7 \text{ mm}$; $\bar{W} = 3.9 \text{ mm}$



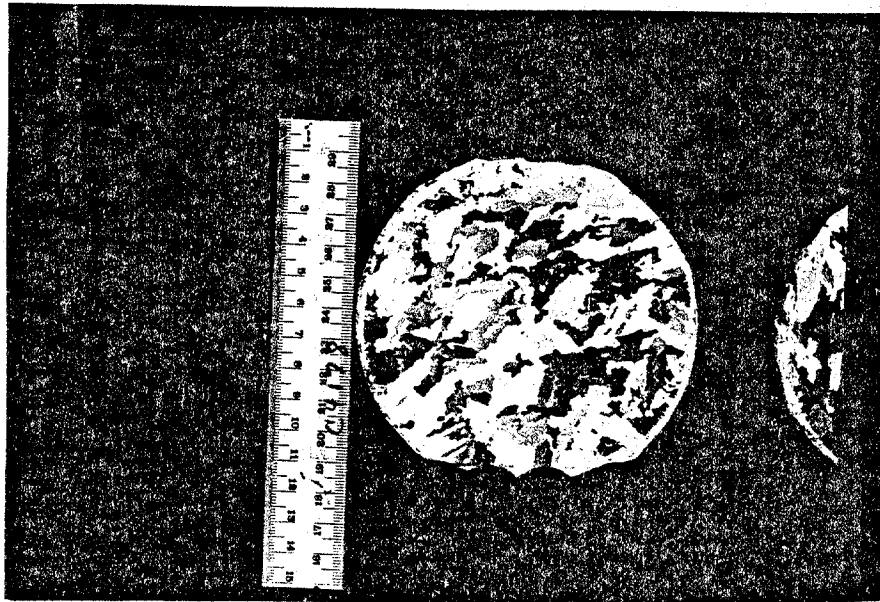
BOTTOM

$\bar{L} = 6.4 \text{ mm}$ $\bar{W} = 3.1 \text{ mm}$

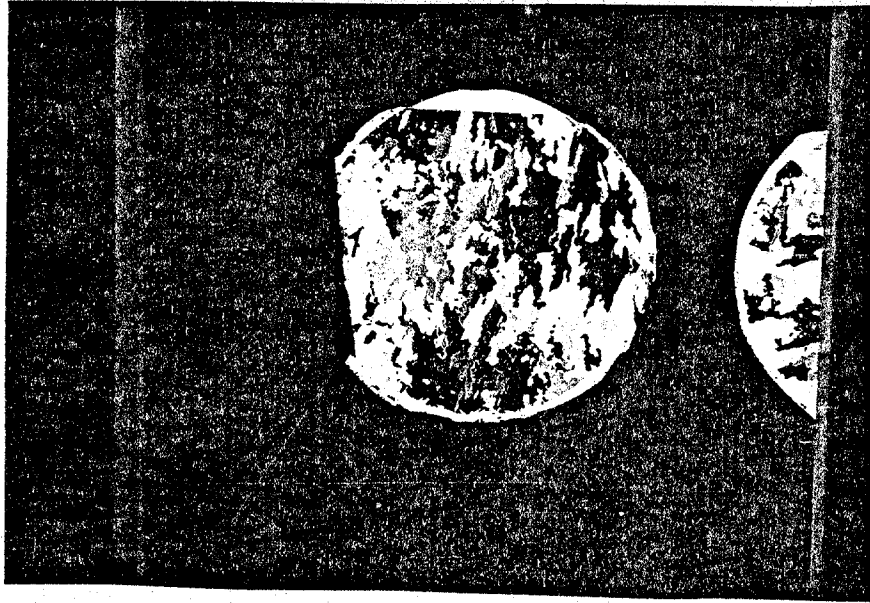
CA-177/203 : POST - TEST



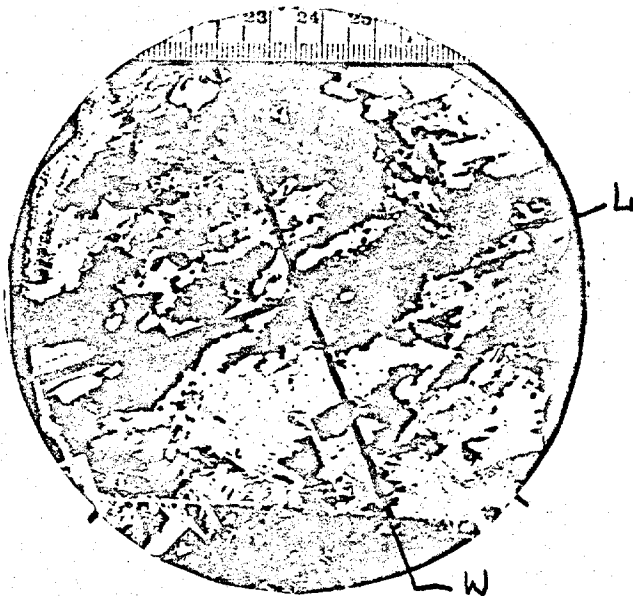
C4-177/203 : POST-TEST



TOP



BOTTOM



SAMPLE NO. C4-177/203
@ C4-177

GRAIN DESCRIPTION: _____
17 F/100 = 1.7 100 % SAMPLE

GRAIN LENGTH: 6.4 mm

A) TOTAL LENGTH OF TEST LINE: 72 mm

B) TOTAL NO. OF INTERSECTIONS: 16

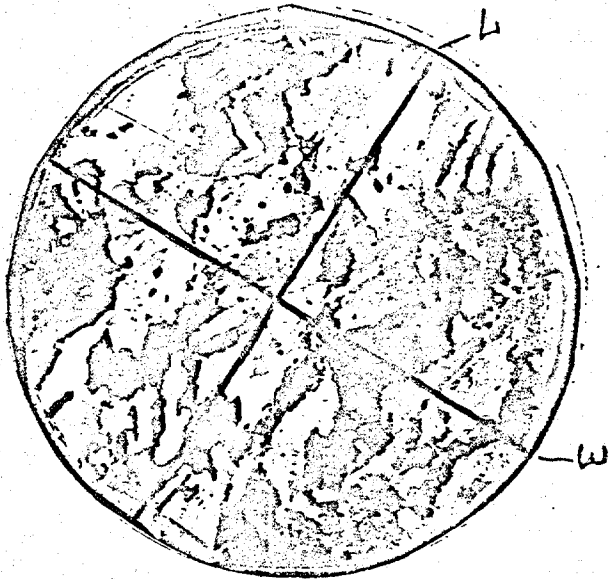
$$\begin{aligned} \text{LENGTH OF GRAIN} &= \frac{A}{B} \\ &= \frac{72}{16} \text{ mm (READING)} \\ &= \underline{4.5} \text{ mm (READING)} \\ &= \underline{6.43} \text{ mm (ACTUAL)} \end{aligned}$$

GRAIN WIDTH: 3.1 mm

A) TOTAL LENGTH OF TEST LINE: 65 mm

B) TOTAL NO. OF INTERSECTIONS: 21

$$\begin{aligned} \text{WIDTH OF GRAIN} &= \frac{A}{B} \\ &= \frac{65}{21} \text{ mm (READING)} \\ &= \underline{3.1} \text{ mm (READING)} \\ &= \underline{3.09} \text{ mm (ACTUAL)} \end{aligned}$$



SAMPLE NO. C4-177/203
@ C4-203

GRAIN DESCRIPTION: _____

COLUMNAR 100% SAMPLE

GRAIN LENGTH: 6.7 mm

A) TOTAL LENGTH OF TEST LINE: 70 mm

B) TOTAL NO. OF INTERSECTIONS: 15

$$\text{LENGTH OF GRAIN} = \frac{A}{B}$$

$$= \frac{4.66}{\text{mm}} \text{ (READING)}$$

$$= \frac{6.65}{\text{mm}} \text{ (ACTUAL)}$$

GRAIN WIDTH: 3.9 mm

A) TOTAL LENGTH OF TEST LINE: 73 mm

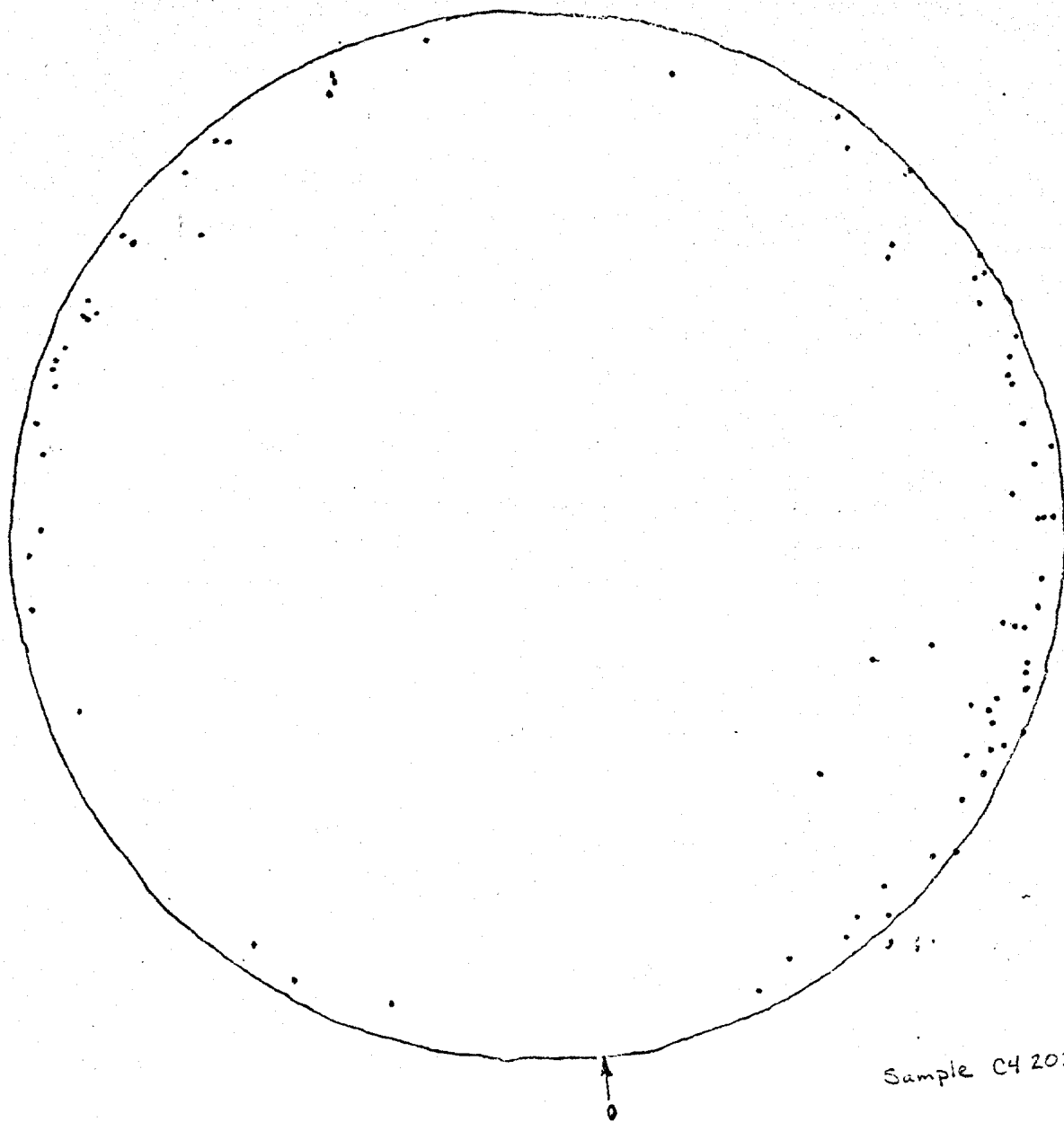
B) TOTAL NO. OF INTERSECTIONS: 27

$$\text{WIDTH OF GRAIN} = \frac{A}{B}$$

$$= \frac{2.70}{\text{mm}} \text{ (READING)}$$

$$= \frac{3.86}{\text{mm}} \text{ (ACTUAL)}$$

C4-177/203 ; BOTTOM



Sample C4 203/208

C2-168-194

Uniaxial compression

Displacement rate: 10^{-4} in/sec.

Temperature: 20°F (-6.5°C)

Salinity: $1.9^{\circ}/\text{oo}$

Density: 0.917 g/cm^3 (57.2 lbs/ft^3)

Brine Volume: $14.9^{\circ}/\text{oo}$

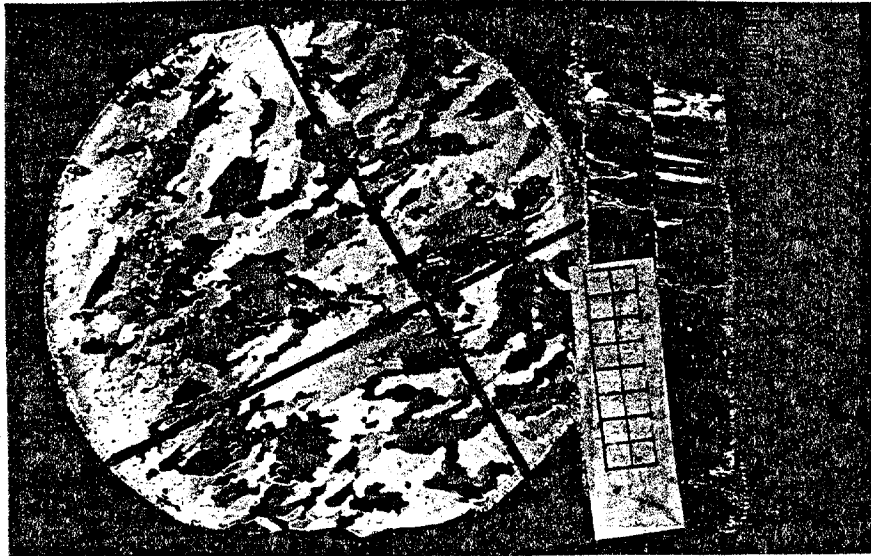
Air Volume: $3.7^{\circ}/\text{oo}$

Porosity: $18.6^{\circ}/\text{oo}$

Structure: $\sim 97\%$ columnar (congelation)
C-axes $\sim 70\%$ from vertical
alignment $\sim 30^{\circ}$
 $\bar{L} = 5.1 \text{ mm}$ $\bar{W} = 2.4 \text{ mm}$.

$$\begin{array}{l} \sigma_{\text{max}} = 680 \text{ psi} \quad \epsilon_{\text{max}} = 0.16\% \\ \underline{\sigma_{\text{max}}} \\ t_{\text{max}} = 414 \text{ sec} \end{array}$$

C2-168/194: PRE-TEST



TOP

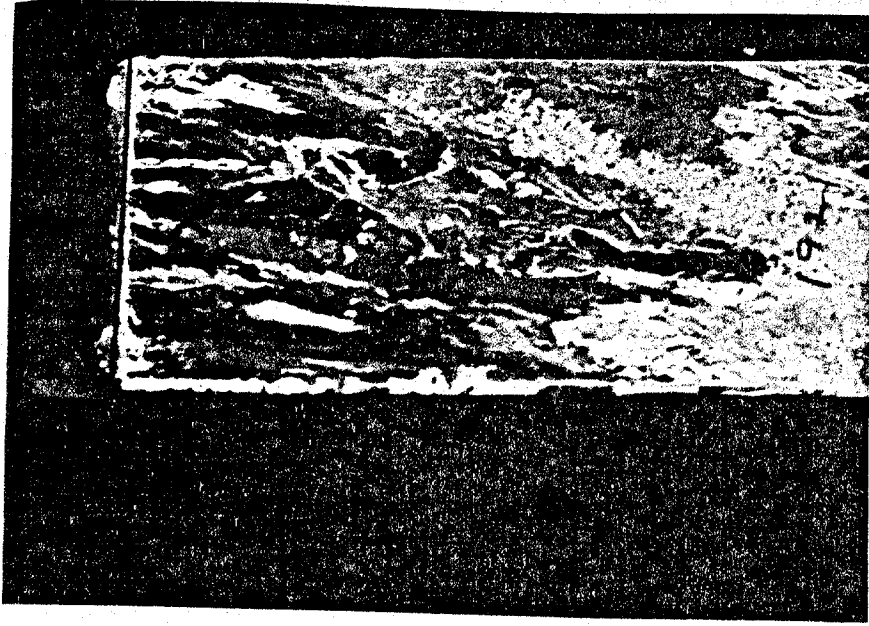
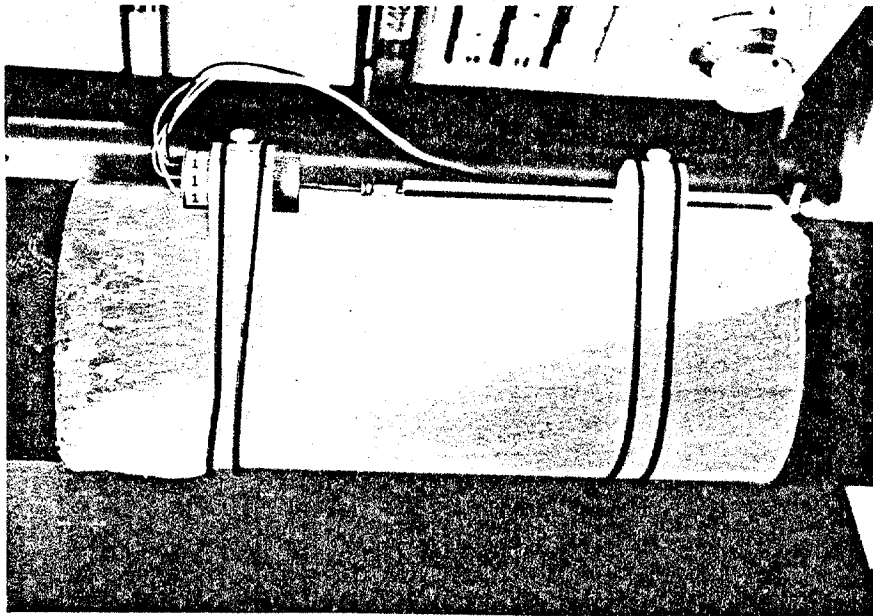
$\bar{L} = 4.9 \text{ mm}$
 $\bar{W} = 2.6 \text{ mm}$



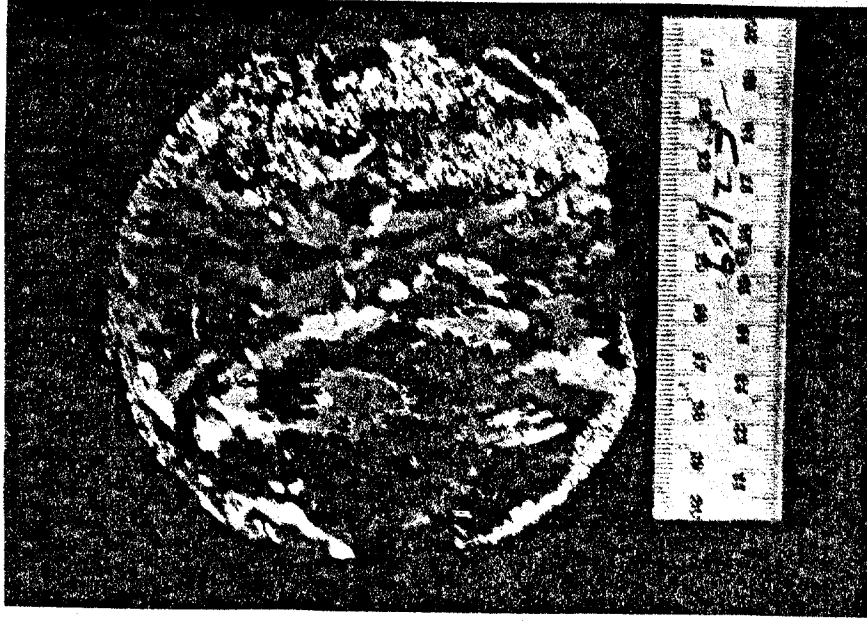
BOTTOM

$\bar{L} = 5.3 \text{ mm}$
 $\bar{W} = 2.2 \text{ mm}$

C2-168/194: POST-TEST



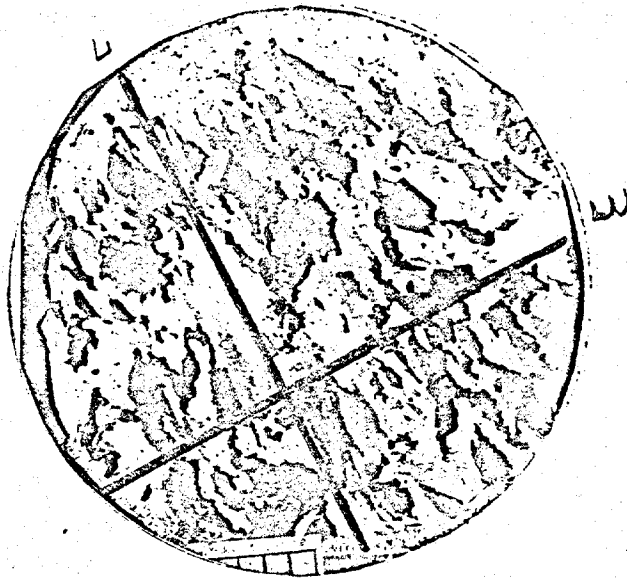
C2-168/194 : POST-TEST



Top



Bottom



SAMPLE NO. C2-168/194
@ C2-165

GRAIN DESCRIPTION: _____
_____ COLUMNAR 100 % SAMPLE

GRAIN LENGTH: 5.3 mm

A) TOTAL LENGTH OF TEST LINE: 69 mm

B) TOTAL NO. OF INTERSECTIONS: 18.5

$$\text{LENGTH OF GRAIN} = \frac{A}{B}$$

$$= \underline{3.73} \text{ mm (READING)}$$

$$= \underline{5.3} \text{ mm (ACTUAL)}$$

..

GRAIN WIDTH: 2.2 mm

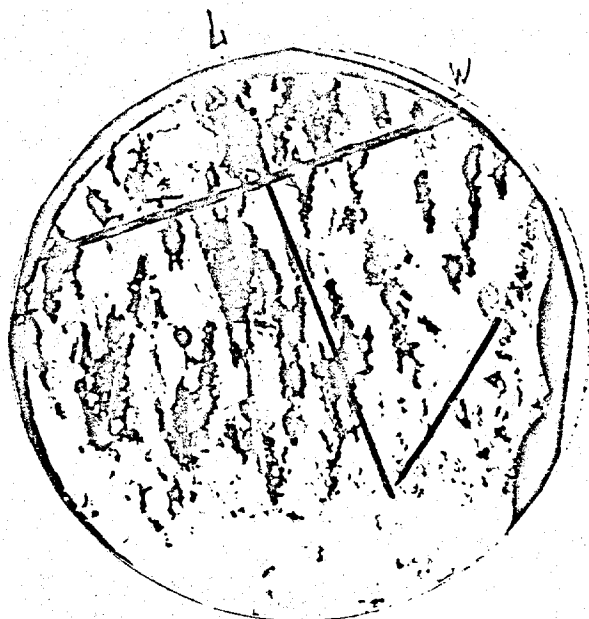
A) TOTAL LENGTH OF TEST LINE: 71 mm

B) TOTAL NO. OF INTERSECTIONS: 46

$$\text{WIDTH OF GRAIN} = \frac{A}{B}$$

$$= \underline{1.5} \text{ mm (READING)}$$

$$= \underline{2.2} \text{ mm (ACTUAL)}$$



SAMPLE NO. C2-168/194
@ C2-197

GRAIN DESCRIPTION: _____

COLUMNAR 6.2 TO SAMPLE

GRAIN LENGTH: 4.9 mm

A) TOTAL LENGTH OF TEST LINE: 51 mm

B) TOTAL NO. OF INTERSECTIONS: 15

$$\begin{aligned} \text{LENGTH OF GRAIN} &= \frac{A}{B} \\ &= \underline{3.4} \text{ mm (READING)} \\ &= \underline{4.9} \text{ mm (ACTUAL)} \end{aligned}$$

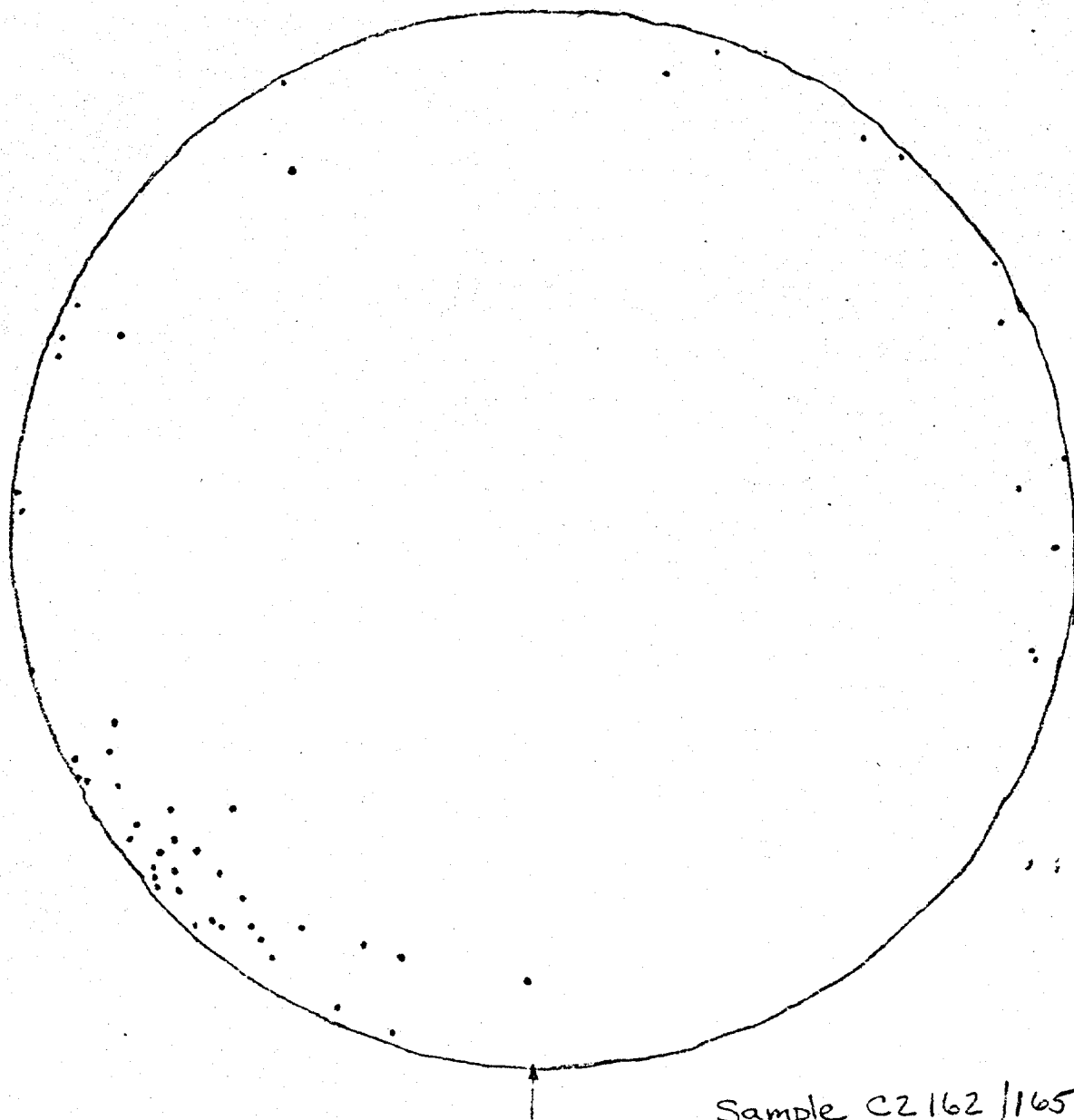
GRAIN WIDTH: 2.6 mm

A) TOTAL LENGTH OF TEST LINE: 61 mm

B) TOTAL NO. OF INTERSECTIONS: 33.5

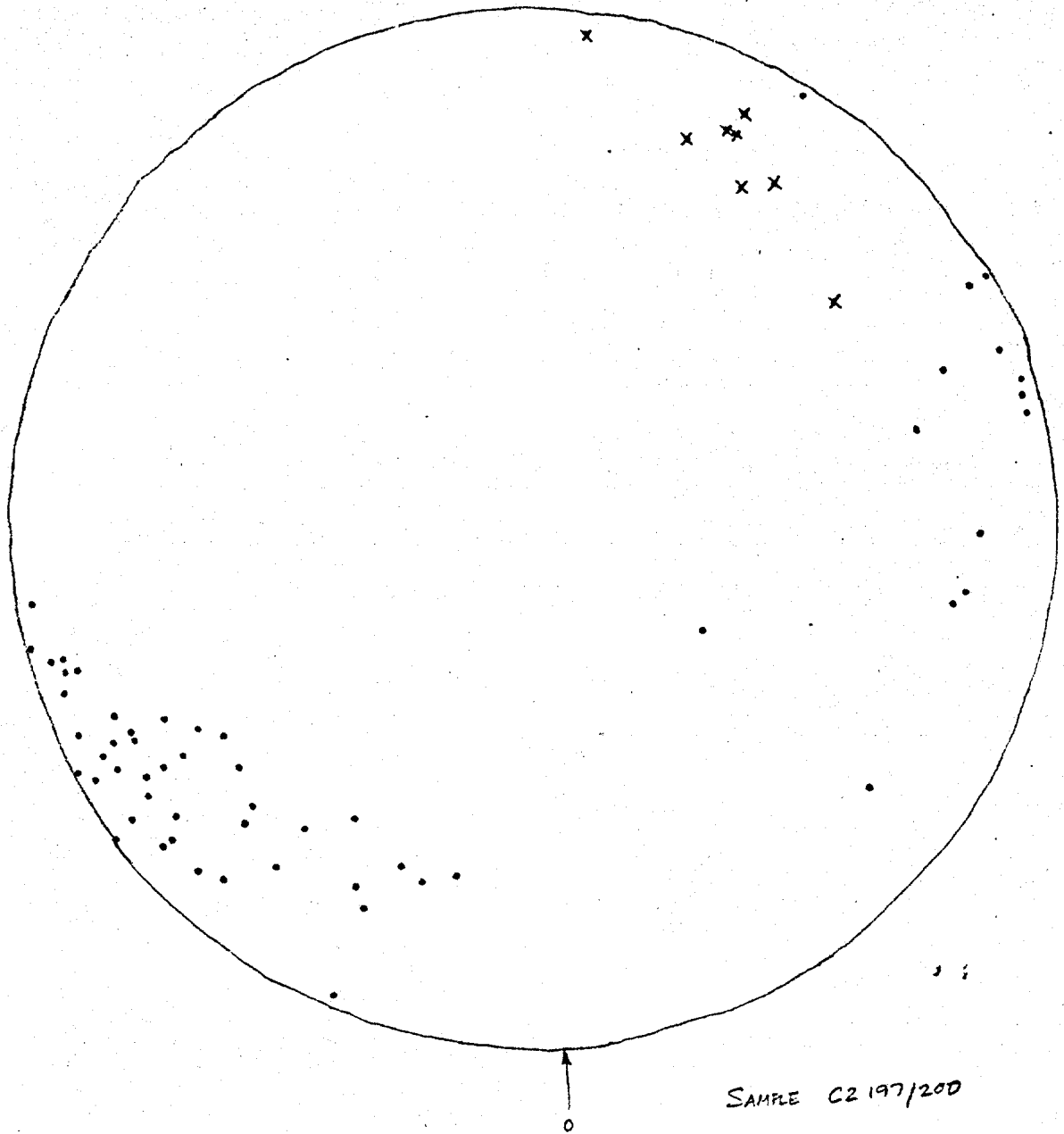
$$\begin{aligned} \text{WIDTH OF GRAIN} &= \frac{A}{B} \\ &= \underline{1.8} \text{ mm (READING)} \\ &= \underline{2.6} \text{ mm (ACTUAL)} \end{aligned}$$

C2-168/194: TOP



Sample C2162/165

8/194 : BOTTOM



C2-282/308

Uniaxial compression

Displacement rate: 10^{-4} in/sec

Temperature: 20°F (-6.5°C)

Salinity: $1.7^{\circ}/\text{oo}$

Density: --

Brine Volume: $\sim 13.3^{\circ}/\text{oo}$

Air Volume: ---

Porosity: ---

Structure: $\sim 25\%$ columnar (lrg. frazil plates?)

no strong preferred orientation

$\bar{L} = 10$ mm, $\bar{W} = 2.9$ mm

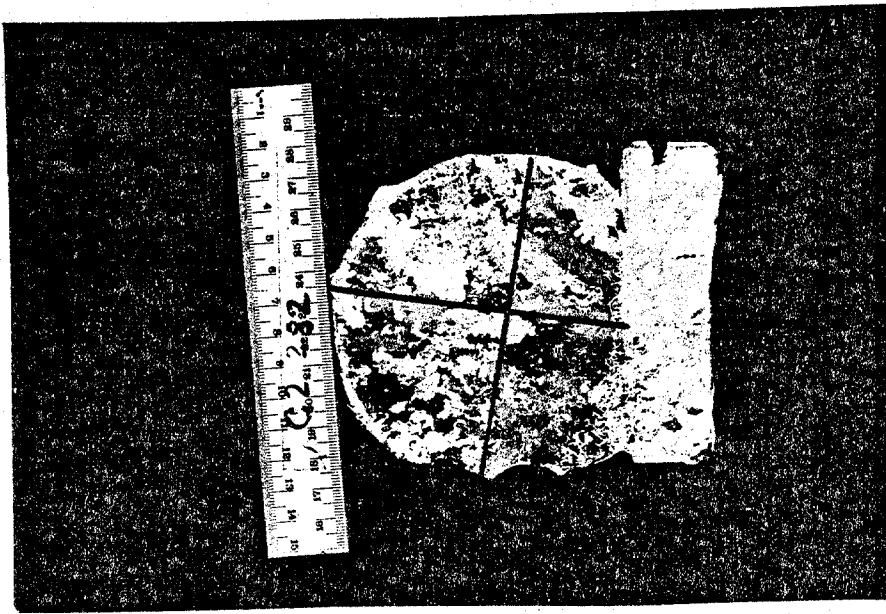
$\sim 75\%$ granular - coarse

$\bar{L} = 3.4$ mm, $\bar{W} = 2.8$ mm

$\sigma_{\text{max}} = 383$ psi $\epsilon_{\text{max}} = 0.32\%$

$t_{\text{max}} = 402$ sec

C2-282/308 : PRE-TEST



TOP

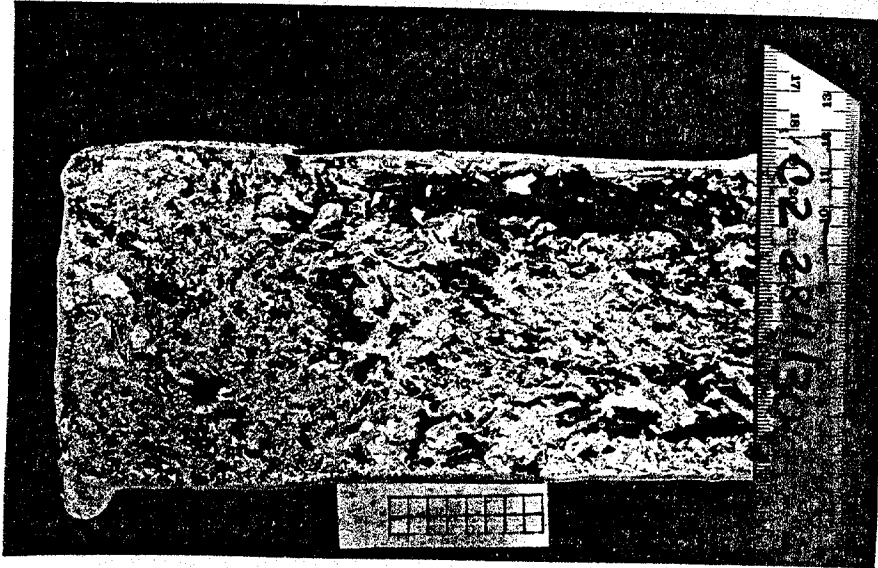
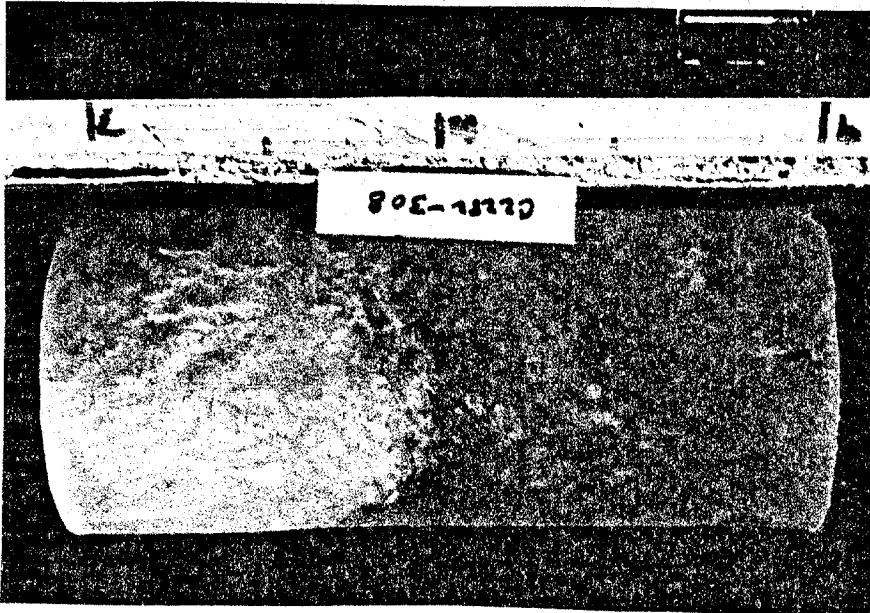
$\bar{L} = 4.0 \text{ mm}$
 $\bar{W} = 3.1 \text{ mm}$



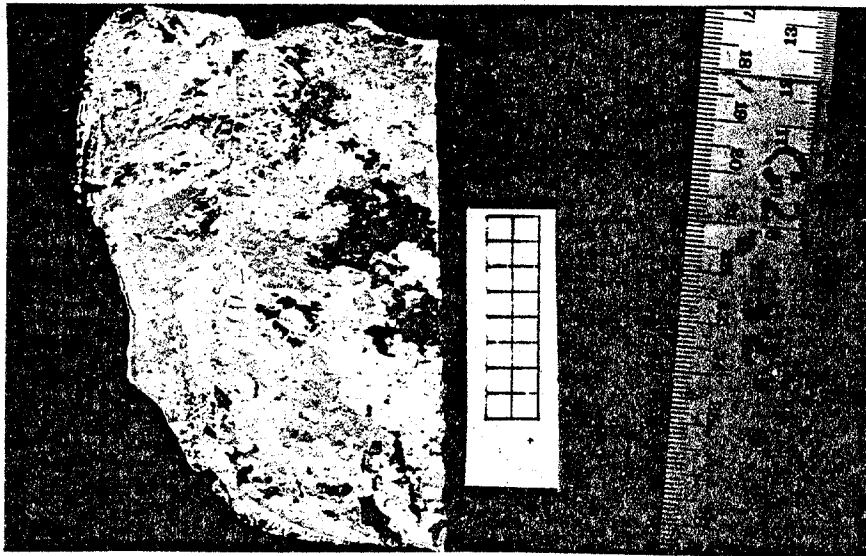
BOTTOM

LARGE GRAINS : $\bar{L} = 10 \text{ mm}$; $\bar{W} = 2.9 \text{ mm}$
SMALL GRAINS : $\bar{L} = 3.4 \text{ mm}$; $\bar{W} = 2.8 \text{ mm}$

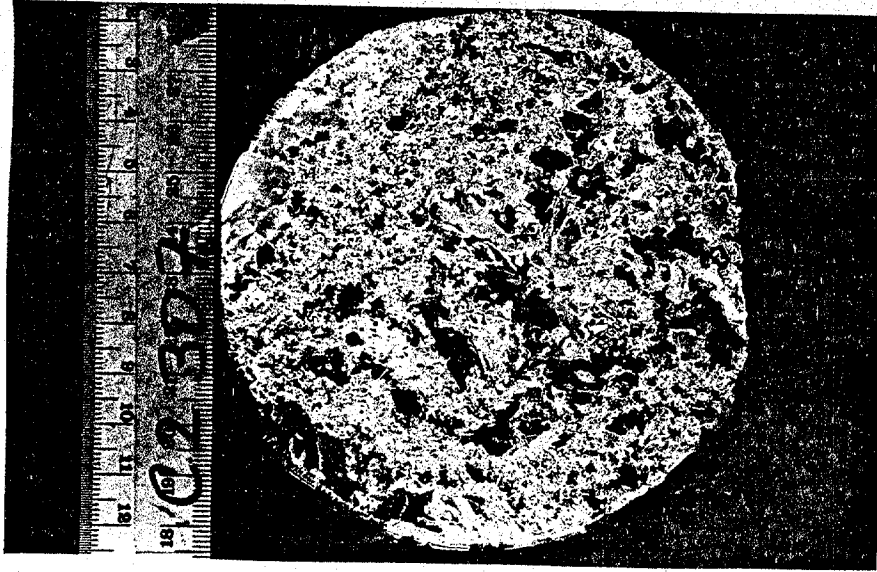
C2-282/308: POST-TEST



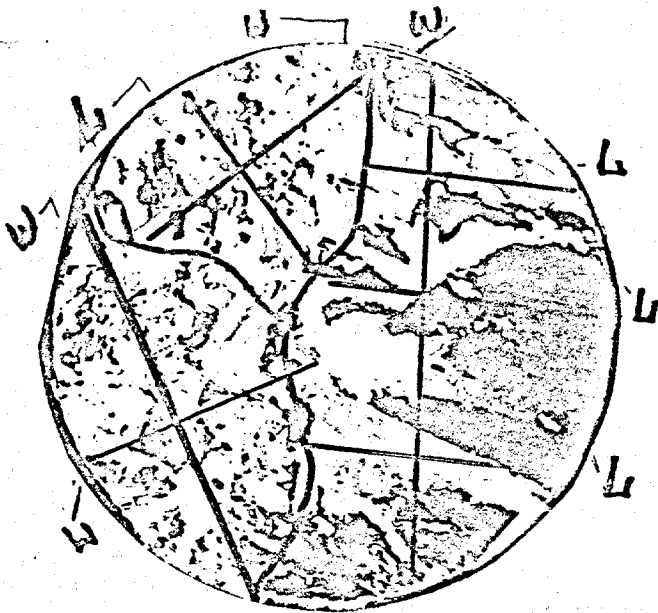
C2-282/308 : POST-TEST



TOP



BOTTOM



SAMPLE NO. C2-282/308
@ C2-308

3

GRAIN DESCRIPTION: _____
_____ Columnar 50 % SAMPLE _____

GRAIN LENGTH: 10 mm

GRAIN WIDTH: 4.5 mm

A) TOTAL LENGTH OF TEST LINE: 112.5 mm

A) TOTAL LENGTH OF TEST LINE: 70 mm

B) TOTAL NO. OF INTERSECTIONS: 16

B) TOTAL NO. OF INTERSECTIONS: 22

$$\text{LENGTH OF GRAIN} = \frac{A}{B}$$

$$\text{WIDTH OF GRAIN} = \frac{A}{B}$$

$$= \frac{7.0}{0.7} \text{ mm (READING)}$$

$$= \frac{3.2}{0.7} \text{ mm (READING)}$$

$$37.5 \quad 3.5 \quad = \frac{10}{1} \text{ mm (ACTUAL)}$$

$$= \frac{4.6}{1} \text{ mm (ACTUAL)}$$

$$42 \quad 6.5$$

$$33 \quad 7$$

SAMPLE NO. C2-282/305

@ C2-308

GRAIN DESCRIPTION: _____

Med gr 20 % SAMPLE

GRAIN LENGTH: 4.3 mm

A) TOTAL LENGTH OF TEST LINE: 30 mm

B) TOTAL NO. OF INTERSECTIONS: 10

$$\begin{aligned}\text{LENGTH OF GRAIN} &= \frac{A}{B} \\ &= \frac{30}{7} \text{ mm (READING)} \\ &= \underline{4.3} \text{ mm (ACTUAL)}\end{aligned}$$

GRAIN WIDTH: 2.9 mm

A) TOTAL LENGTH OF TEST LINE: 42 mm

B) TOTAL NO. OF INTERSECTIONS: 21

$$\begin{aligned}\text{LENGTH OF GRAIN} &= \frac{A}{B} \\ &= \frac{42}{15} \text{ mm (READING)} \\ &= \underline{2.9} \text{ mm (ACTUAL)}\end{aligned}$$

GRAIN DESCRIPTION: _____

Med gr 30 % SAMPLE

GRAIN LENGTH: 2.9 mm

A) TOTAL LENGTH OF TEST LINE: 32 mm

B) TOTAL NO. OF INTERSECTIONS: 16

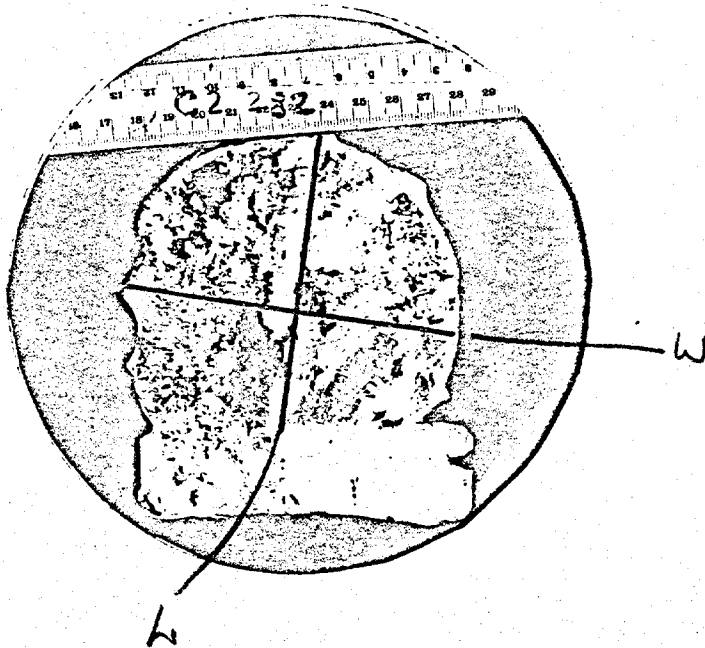
$$\begin{aligned}\text{LENGTH OF GRAIN} &= \frac{A}{B} \\ &= \frac{32}{11} \text{ mm (READING)} \\ &= \underline{2.9} \text{ mm (ACTUAL)}\end{aligned}$$

GRAIN WIDTH: 2.7 mm

A) TOTAL LENGTH OF TEST LINE: 56 mm

B) TOTAL NO. OF INTERSECTIONS: 30

$$\begin{aligned}\text{LENGTH OF GRAIN} &= \frac{A}{B} \\ &= \frac{56}{20} \text{ mm (READING)} \\ &= \underline{2.7} \text{ mm (ACTUAL)}\end{aligned}$$



SAMPLE NO. C2-282-308

@ C2-282

GRAIN DESCRIPTION: _____

Columbian 75% SAMPLE

GRAIN LENGTH: 4.0 mm

A) TOTAL LENGTH OF TEST LINE: 38 mm

B) TOTAL NO. OF INTERSECTIONS: 23

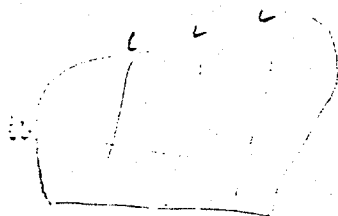
$$\begin{aligned} \text{LENGTH OF GRAIN} &= \frac{A}{B} \\ &= \frac{1.7}{} \text{ mm (READING)} \\ &= \frac{4.0}{} \text{ mm (ACTUAL)} \end{aligned}$$

GRAIN WIDTH: 3.1 mm

A) TOTAL LENGTH OF TEST LINE: 44 mm

B) TOTAL NO. OF INTERSECTIONS: 34

$$\begin{aligned} \text{WIDTH OF GRAIN} &= \frac{A}{B} \\ &= \frac{1.3}{} \text{ mm (READING)} \\ &= \frac{3.1}{} \text{ mm (ACTUAL)} \end{aligned}$$



$$\begin{array}{r} 28 \ 28 \ 30 \ - \ 86 \\ 13 \ 7 \ 12 \ - \ 32 \\ \hline L. \\ 2.7 \\ 3.9 \end{array}$$

$$\begin{array}{r} W \\ 69 \\ \hline 32 \\ 2.2 \\ 3.1 \end{array}$$

C3-161/187

Uniaxial compression

Displacement rate: 10^{-3} in/sec

Temperature: 21°F (-6.1°C)

Salinity: $1.8^{\circ}/\text{oo}$

Density: 0.911 g/cm^3 (56.9 lbs/ft^3)

Brine Volume: $14.8^{\circ}/\text{oo}$

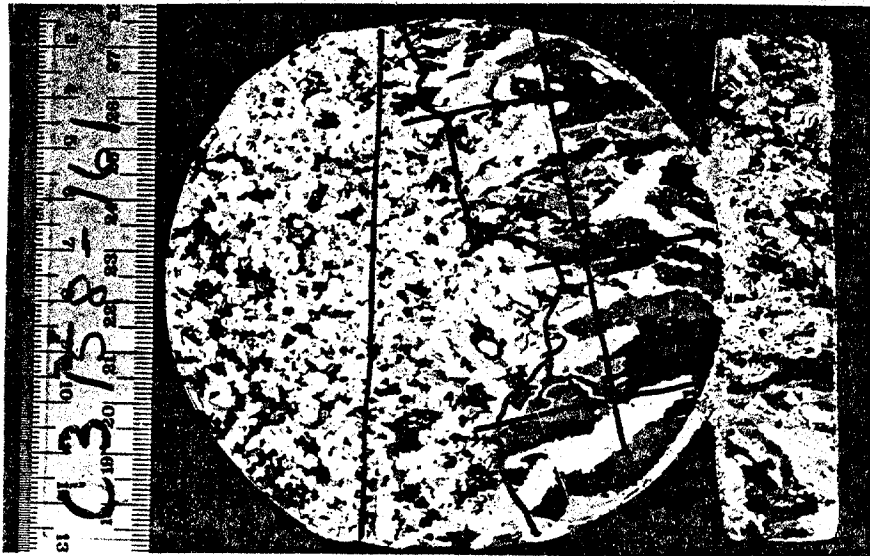
Air Volume: $10.1^{\circ}/\text{oo}$

Porosity: $24.9^{\circ}/\text{oo}$

Structure: largely columnar
c-axes horizontal with no
preferred orientation
 $\bar{L} = 8.2 \text{ mm}$, $\bar{W} = 5.9 \text{ mm}$

$\sigma_{\text{max}} = 585 \text{ psi}$ $\epsilon_{\text{max}} = 0.30\%$
 $t_{\text{max}} = 52 \text{ sec}$

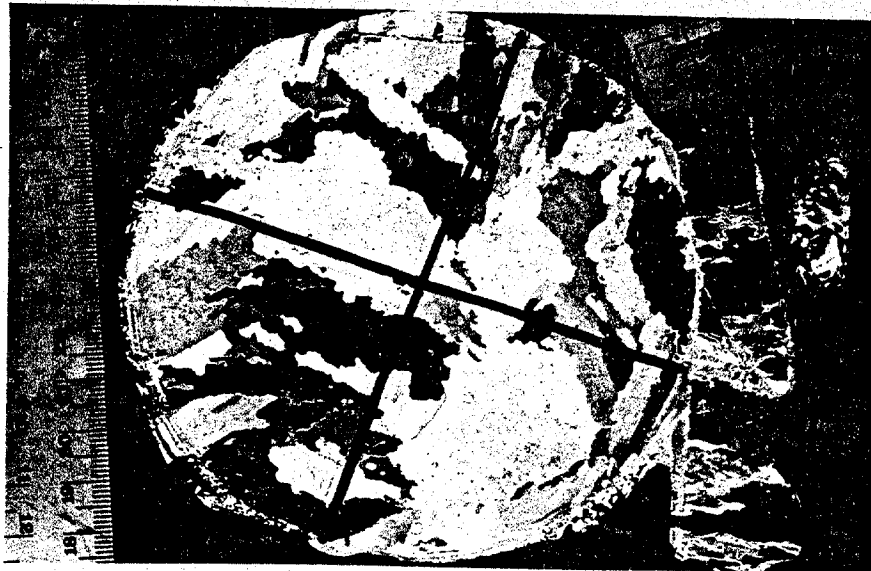
C3-161/187 : PRE-TEST



TOP

SMALL GRAINS : $\bar{L} = 1.8 \text{ mm}$

LARGE GRAINS : $\bar{L} = 4.3 \text{ mm}$; $\bar{W} = 3.4 \text{ mm}$

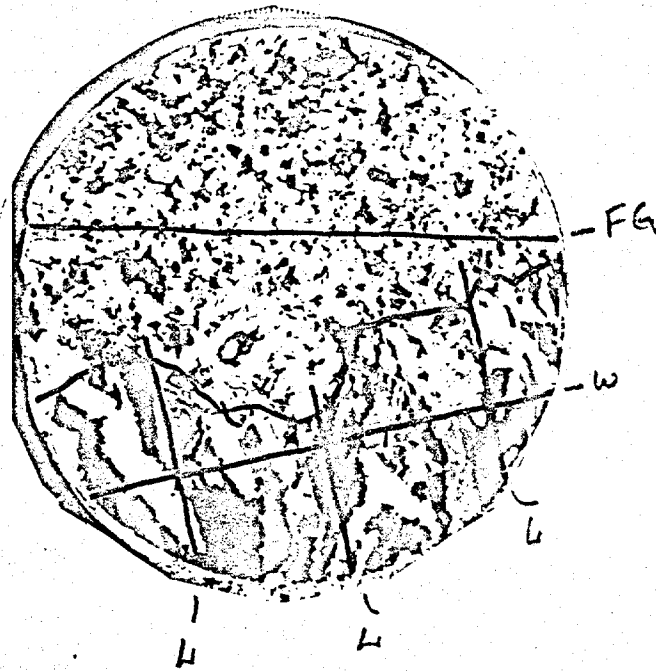


BOTTOM

$\bar{L} = 8.2 \text{ mm}$; $\bar{W} = 5.9 \text{ mm}$

C3-161/187 : POST-TEST





SAMPLE NO. C3-161/187
@ C3-161

GRAIN DESCRIPTION: _____

Columbar 40 No SAMPLE

GRAIN LENGTH: 4.3 mm

A) TOTAL LENGTH OF TEST LINE: 87 mm

B) TOTAL NO. OF INTERSECTIONS: 29

$$\text{LENGTH OF GRAIN} = \frac{A}{B}$$

$$= \frac{3.0}{\text{mm (READING)}}$$

$$= \frac{4.29}{\text{mm (ACTUAL)}}$$

$$\begin{array}{r} 7 \quad 30 \\ 10 \quad 26 \\ 12 \quad 31 \\ \hline 29 \quad 87 \end{array}$$

GRAIN WIDTH: 3.4 mm

A) TOTAL LENGTH OF TEST LINE: 65 mm

B) TOTAL NO. OF INTERSECTIONS: 27

$$\text{WIDTH OF GRAIN} = \frac{A}{B}$$

$$= \frac{2.41}{\text{mm (READING)}}$$

$$= \frac{3.44}{\text{mm (ACTUAL)}}$$

SAMPLE NO. C3-111/187
@ C3-163

GRAIN DESCRIPTION: _____

FINE GRAIN 60 % SAMPLE

GRAIN SIZE: 1.8 mm

A) TOTAL LENGTH OF TEST LINE: 71 mm

B) TOTAL NO. OF INTERSECTIONS: 56

$$\begin{aligned}\text{GRAIN SIZE} &= \frac{A}{B} \\ &= \frac{1.27}{} \text{ mm (READING)} \\ &= \frac{1.81}{} \text{ mm (ACTUAL)}\end{aligned}$$

GRAIN DESCRIPTION: _____

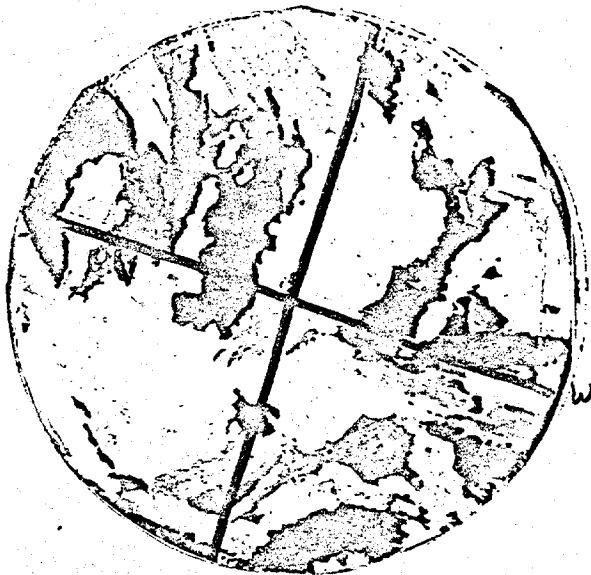
% SAMPLE

GRAIN SIZE: _____ mm

A) TOTAL LENGTH OF TEST LINE: _____ mm

B) TOTAL NO. OF INTERSECTIONS: _____

$$\begin{aligned}\text{GRAIN SIZE} &= \frac{A}{B} \\ &= \frac{}{} \text{ mm (READING)} \\ &= \frac{}{} \text{ mm (ACTUAL)}\end{aligned}$$



SAMPLE NO. C3-161/187
@ C3-188

GRAIN DESCRIPTION: _____

Column - 100% SAMPLE

GRAIN LENGTH: 8.2 mm

A) TOTAL LENGTH OF TEST LINE: 75 mm

B) TOTAL NO. OF INTERSECTIONS: 13

$$\text{LENGTH OF GRAIN} = \frac{A}{B}$$

$$= \underline{5.77} \text{ mm (READING)}$$

$$= \underline{8.24} \text{ mm (ACTUAL)}$$

GRAIN WIDTH: 5.9 mm

A) TOTAL LENGTH OF TEST LINE: 74 mm

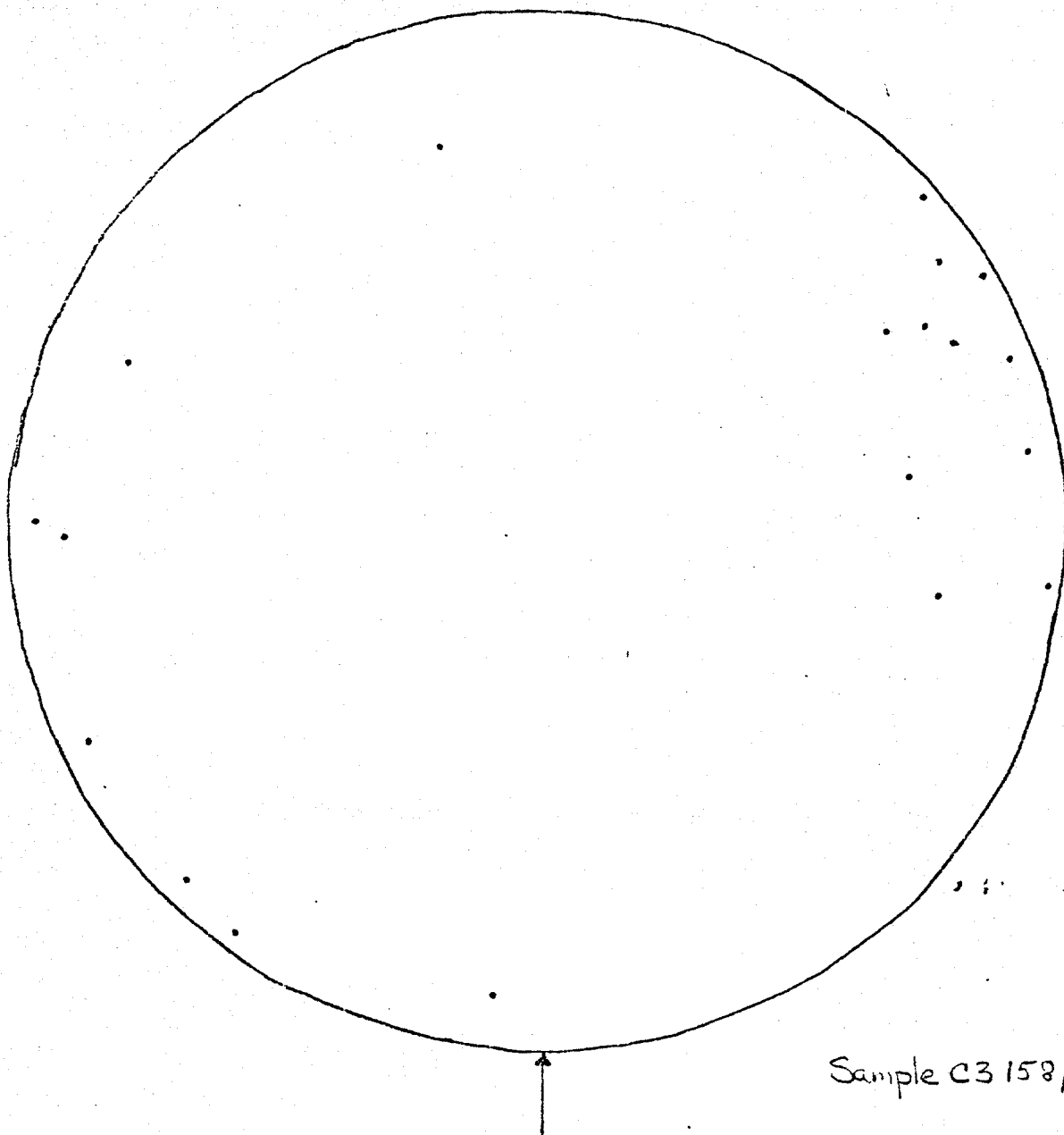
B) TOTAL NO. OF INTERSECTIONS: 18

$$\text{WIDTH OF GRAIN} = \frac{A}{B}$$

$$= \underline{4.11} \text{ mm (READING)}$$

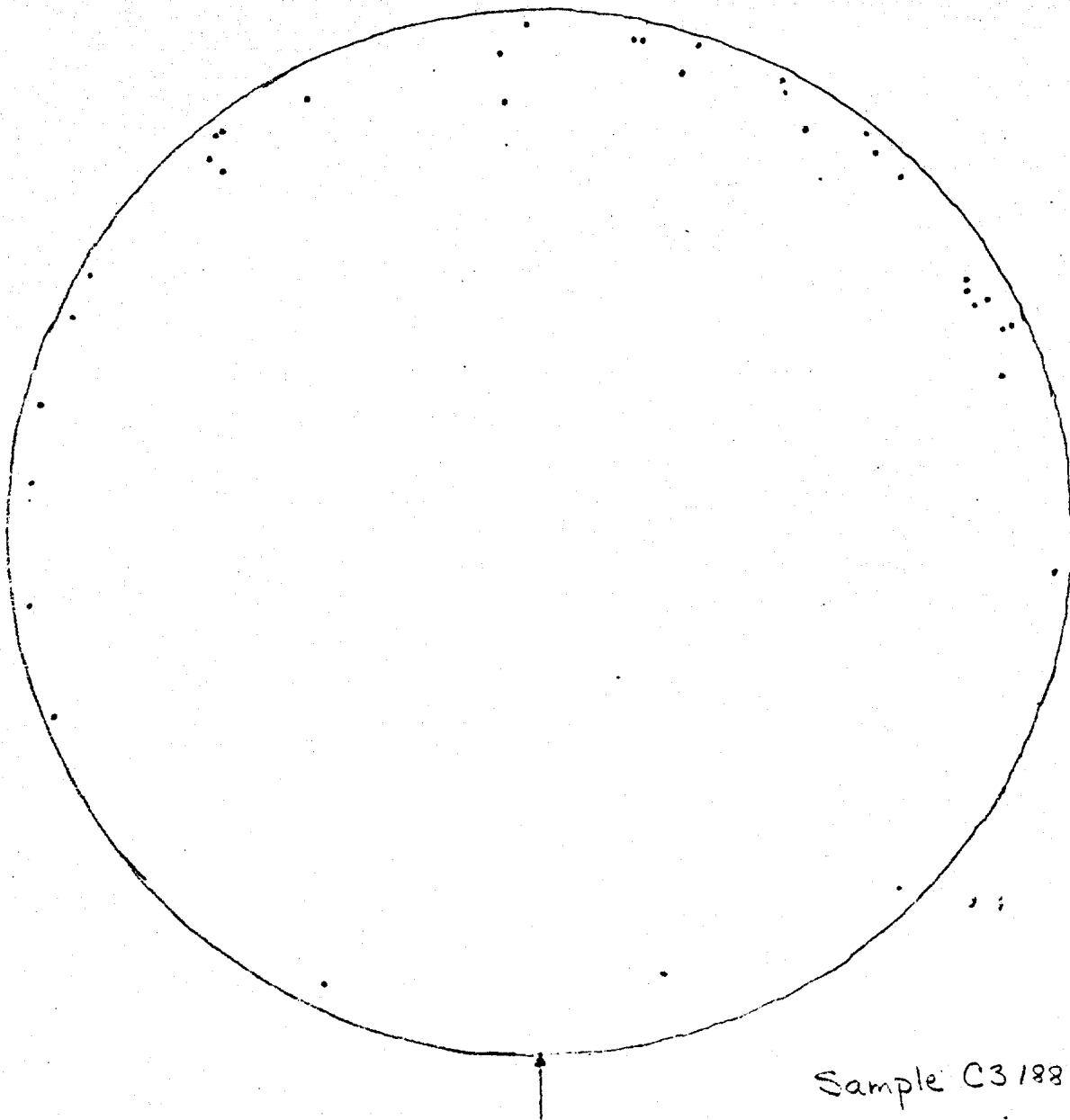
$$= \underline{5.87} \text{ mm (ACTUAL)}$$

C3-161/187: TOP



Sample C3 158/161

C3-101/187 : BOTTOM



Sample C3188/191

C3-261/287

Uniaxial Compression

Displacement rate: 10^{-3} in/sec

Temperature: 21°F (-6.1°C)

Salinity: $1.6^{\circ}/\text{oo}$

Density: 0.915 g/cm^3 (57.1 lbs/ft^3)

Brine Volume: $13.2^{\circ}/\text{oo}$

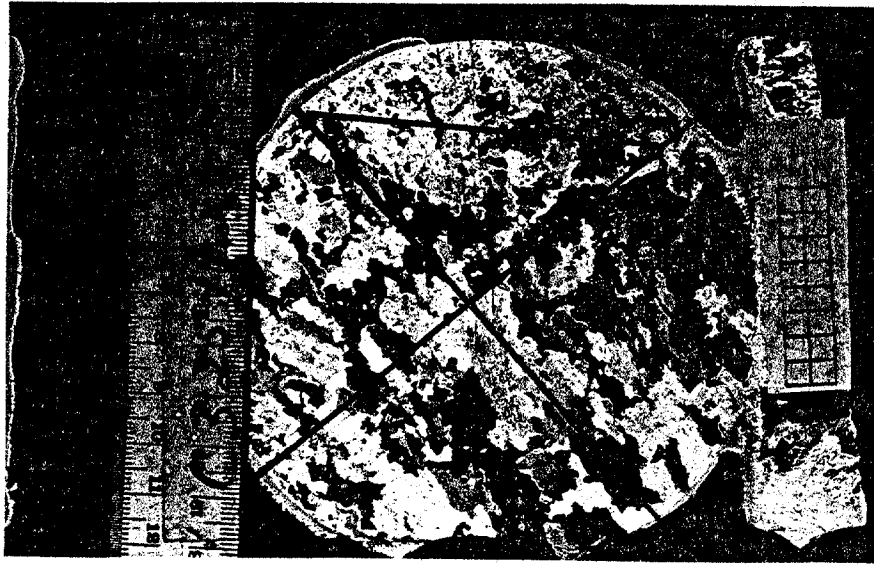
Air Volume: $5.5^{\circ}/\text{oo}$

Porosity: $18.7^{\circ}/\text{oo}$

Structure: Largely columnar
 $\bar{L} = 6.2 \text{ mm}$, $\bar{W} = 3.9 \text{ mm}$

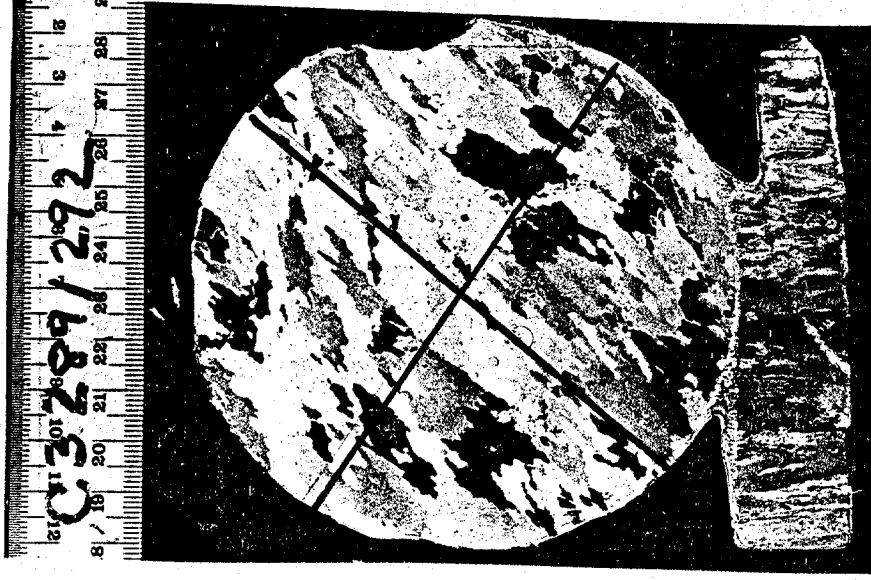
$$\frac{\sigma_{\text{max}} = 706 \text{ psi}}{t_{\text{max}} = 34 \text{ sec}} \quad \epsilon_{\text{max}} = 0.13\%$$

C3-261/287: PRE-TEST



TOP

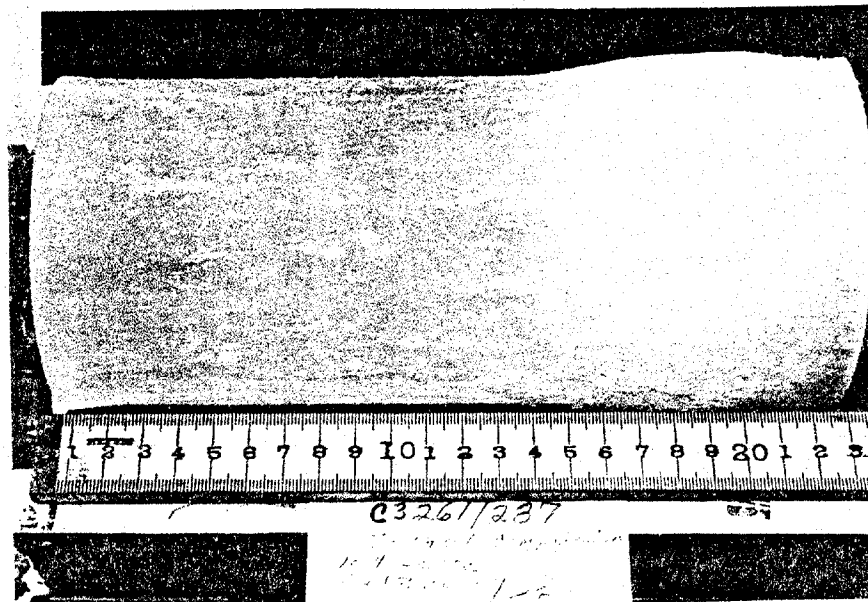
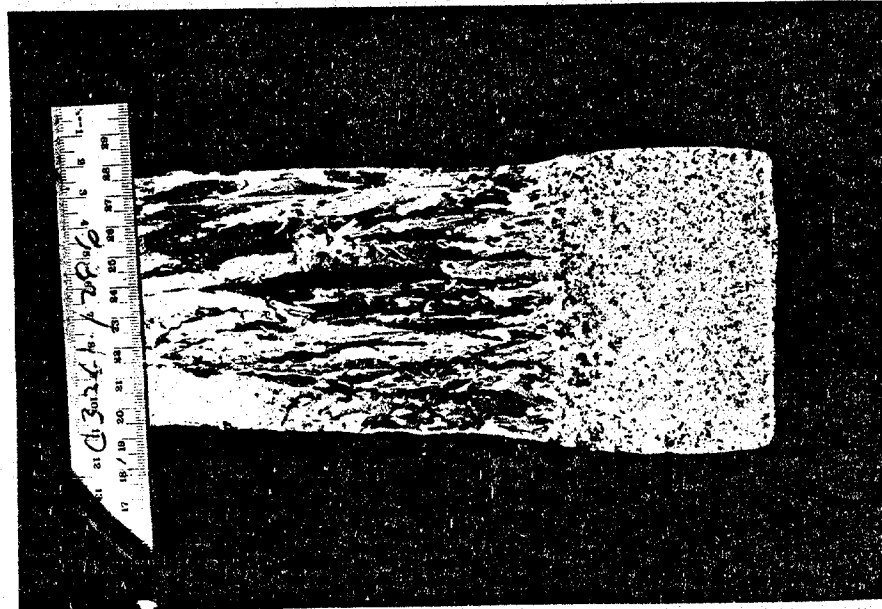
LARGE GRAINS: $\bar{L} = 4.7 \text{ mm}$, $\bar{W} = 4.0 \text{ mm}$
SMALL GRAINS: $\bar{L} = 1.7 \text{ mm}$

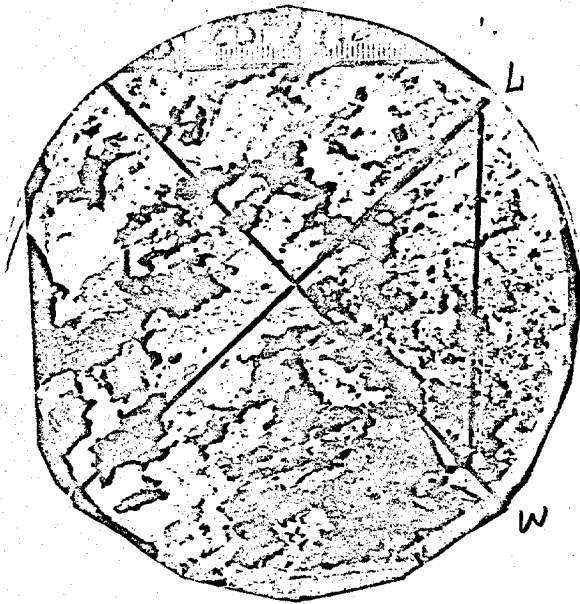


BOTTOM

$\bar{L} = 6.2 \text{ mm}$; $\bar{W} = 3.9 \text{ mm}$

C3-261/287: POST-TEST





SAMPLE NO. C3-261/287
@ C3-261

GRAIN DESCRIPTION: _____

Columnar 75% SAMPLE

GRAIN LENGTH: 4.7 mm

A) TOTAL LENGTH OF TEST LINE: 73 mm

B) TOTAL NO. OF INTERSECTIONS: 32

$$\begin{aligned} \text{LENGTH OF GRAIN} &= \frac{A}{B} \\ &= \underline{3.32} \text{ mm (READING)} \\ &= \underline{4.74} \text{ mm (ACTUAL)} \end{aligned}$$

GRAIN WIDTH: 4.0 mm

A) TOTAL LENGTH OF TEST LINE: 73 mm

B) TOTAL NO. OF INTERSECTIONS: 26

$$\begin{aligned} \text{WIDTH OF GRAIN} &= \frac{A}{B} \\ &= \underline{2.81} \text{ mm (READING)} \\ &= \underline{4.01} \text{ mm (ACTUAL)} \end{aligned}$$

SAMPLE NO. C3-211/287

@ C3-261

GRAIN DESCRIPTION: _____

?? Filazil ??

25% SAMPLE

GRAIN SIZE: 1.7 mm

A) TOTAL LENGTH OF TEST LINE: 47 mm

B) TOTAL NO. OF INTERSECTIONS : 39

$$\text{GRAIN SIZE} = \frac{A}{B}$$

$$= \frac{1.21}{\quad} \text{ mm (READING)}$$

$$= \underline{1.73} \text{ mm (ACTUAL)}$$

GRAIN DESCRIPTION: _____

570 SAMPLE

GRAIN SIZE: _____ mm

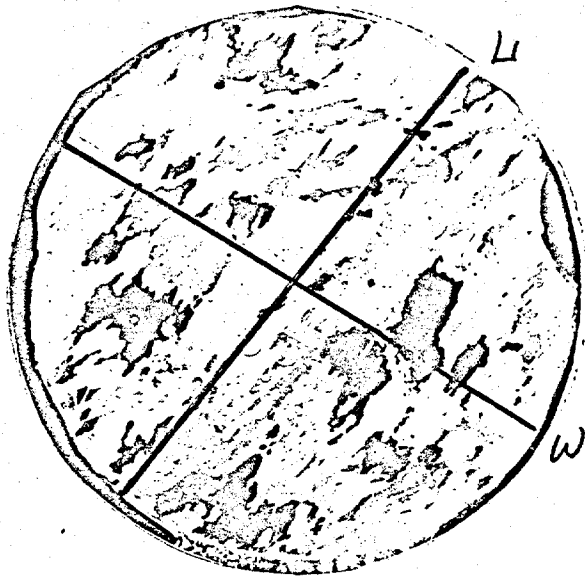
A) TOTAL LENGTH OF TEST LINE: _____ mm

B) TOTAL NO. OF INTERSECTIONS : _____

$$\text{GRAIN SIZE} = \frac{A}{B}$$

= _____ mm (READING)

= _____ mm (ACTUAL)



SAMPLE NO. C3-261/287
@ C3-289

GRAIN DESCRIPTION: _____
Columbite 100 % SAMPLE

GRAIN LENGTH: 6.2 mm

- A) TOTAL LENGTH OF TEST LINE: 74 mm
B) TOTAL NO. OF INTERSECTIONS: 17

$$\begin{aligned} \text{LENGTH OF GRAIN} &= \frac{A}{B} \\ &= \underline{4.35} \text{ mm (READING)} \\ &= \underline{6.21} \text{ mm (ACTUAL)} \end{aligned}$$

GRAIN WIDTH: 3.9 mm

- A) TOTAL LENGTH OF TEST LINE: 73 mm
B) TOTAL NO. OF INTERSECTIONS: 27

$$\begin{aligned} \text{WIDTH OF GRAIN} &= \frac{A}{B} \\ &= \underline{2.70} \text{ mm (READING)} \\ &= \underline{3.86} \text{ mm (ACTUAL)} \end{aligned}$$

C3-79/105

Uniaxial compression

Displacement rate: 10^{-3} in/sec

Temperature: 20°F (-6.5°C)

Salinity: 1.9‰

Density: ---

Brine Volume: ~14.8‰

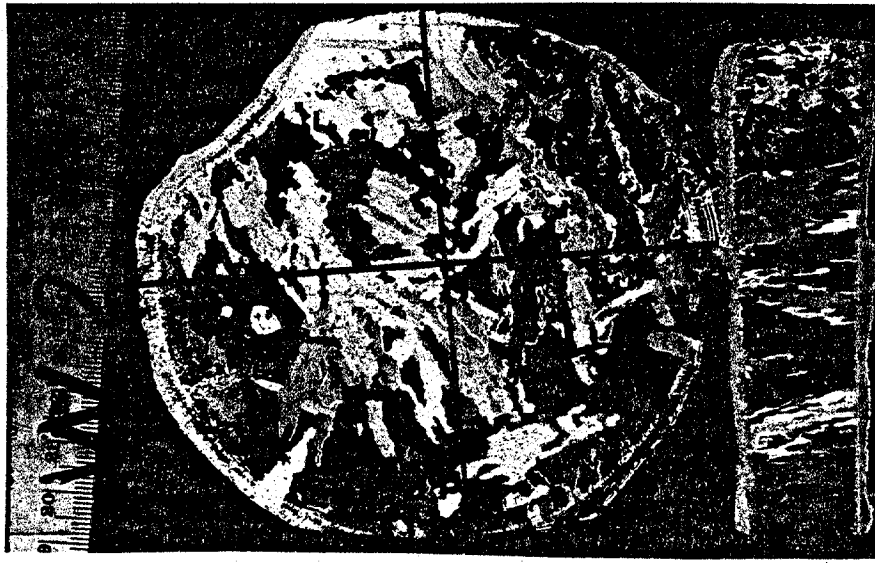
Air Volume: ---

Porosity: ---

Structure: 100% columnar (congelation)

$$\frac{\sigma_{\max} = 1532 \text{ psi}}{t_{\max} = 70 \text{ sec}} \quad \epsilon_{\max} = 0.70\%$$

C3-79/105 : PRE-TEST



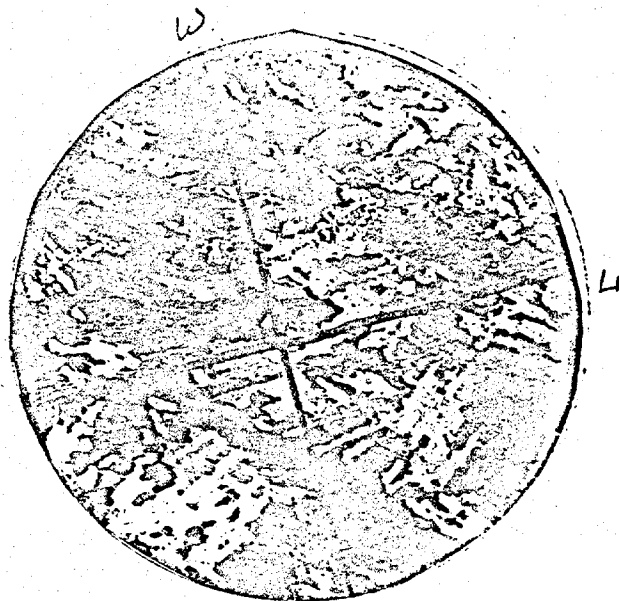
TOP

$\bar{L} = 4.9 \text{ mm} ; \bar{W} = 4.2 \text{ mm}$



BOTTOM

$\bar{L} = 4.9 \text{ mm} , \bar{W} = 4.0 \text{ mm}$



SAMPLE NO. C3-79/105
@ C3 105

GRAIN DESCRIPTION: _____
COLUMNAR 100% SAMPLE

GRAIN LENGTH: 4.9 mm

A) TOTAL LENGTH OF TEST LINE: 72 mm

B) TOTAL NO. OF INTERSECTIONS: 21

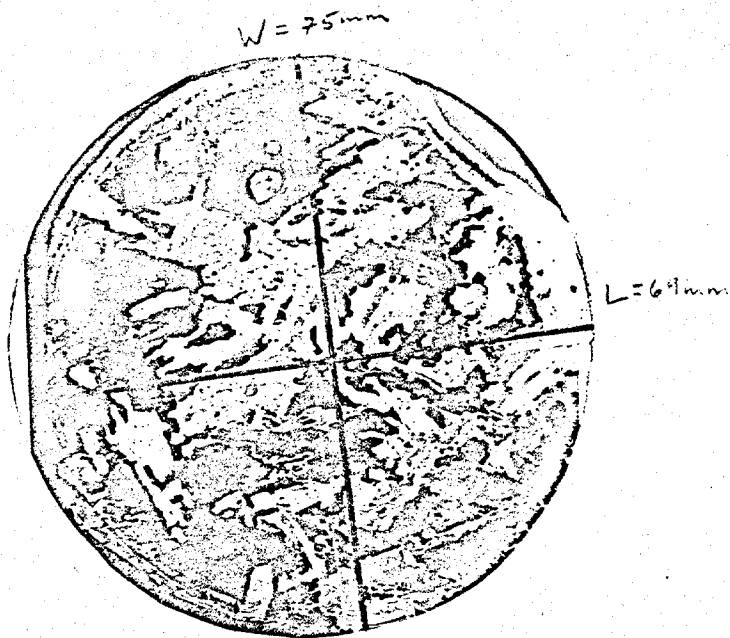
$$\begin{aligned} \text{LENGTH OF GRAIN} &= \frac{A}{B} \\ &= \underline{3.43} \text{ mm (READING)} \\ &= \underline{4.9} \text{ mm (ACTUAL)} \end{aligned}$$

GRAIN WIDTH: 4.0 mm

A) TOTAL LENGTH OF TEST LINE: 72 mm

B) TOTAL NO. OF INTERSECTIONS: 26

$$\begin{aligned} \text{WIDTH OF GRAIN} &= \frac{A}{B} \\ &= \underline{2.77} \text{ mm (READING)} \\ &= \underline{3.95} \text{ mm (ACTUAL)} \end{aligned}$$



SAMPLE NO. C3 79/105
 @ C3 76/79

GRAIN DESCRIPTION: Columnar
100 % SAMPLE

GRAIN LENGTH: 4.9 mm

A) TOTAL LENGTH OF TEST LINE: 69 mm

B) TOTAL NO. OF INTERSECTIONS: 20

$$\text{LENGTH OF GRAIN} = \frac{A}{B}$$

$$= \underline{3.45} \text{ mm (READING)}$$

$$= \underline{4.9} \text{ mm (ACTUAL)}$$

GRAIN WIDTH: 4.2 mm

A) TOTAL LENGTH OF TEST LINE: 75 mm

B) TOTAL NO. OF INTERSECTIONS: 25.5

$$\text{WIDTH OF GRAIN} = \frac{A}{B}$$

$$= \underline{2.94} \text{ mm (READING)}$$

$$= \underline{4.2} \text{ mm (ACTUAL)}$$

C4-909/116

Uniaxial Compression

Displacement rate: 10^{-2} in/sec

Temperature: 21°F (-6.0°C)

Salinity: $1.5^{\circ}/\text{oo}$

Density: 0.913 g/cm^3 (57.0 lbs/ft^3)

Brine Volume: $12.5^{\circ}/\text{oo}$

Air Volume: $7.5^{\circ}/\text{oo}$

Porosity: $20.0^{\circ}/\text{oo}$

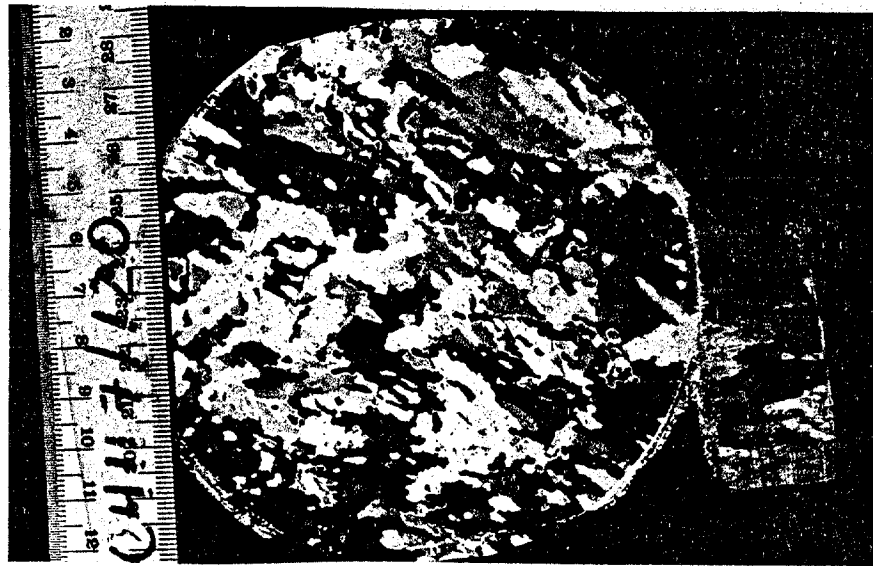
Structure: 100% columnar
c-axes horizontal
alignment $\sim 40^{\circ}$ (top)
 $\bar{L} = 7.6 \text{ mm}$, $\bar{W} = 2.6 \text{ mm}$

$$\frac{\sigma_{\max} = 1265 \text{ psi}}{t_{\max} = 3 \text{ sec}} \quad \epsilon_{\max} = 0.13\%$$

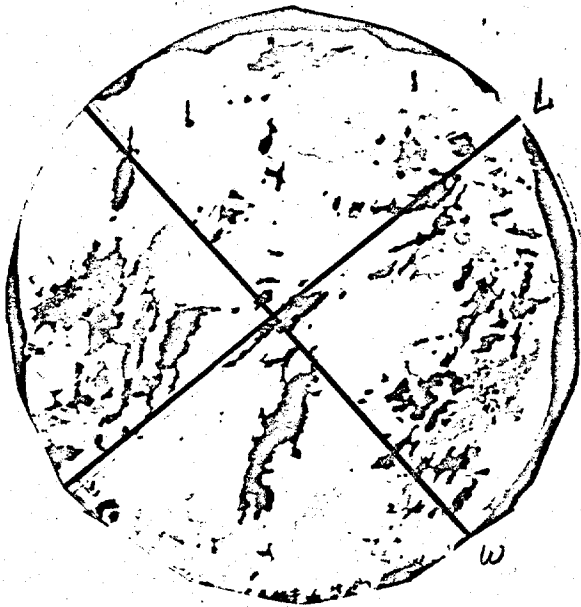
C4-090/116 : PRE-TEST



TOP
 $\bar{L} = 7.6 \text{ mm}, \bar{W} = 2.6 \text{ mm}$



BOTTOM
 $\bar{L} = 4.7 \text{ mm}, \bar{W} = 3.1 \text{ mm}$



SAMPLE NO. C4-98/116.
@ C4-90

GRAIN DESCRIPTION: _____

COLUMNAR 100% SAMPLE

GRAIN LENGTH: 7.6 mm

A) TOTAL LENGTH OF TEST LINE: 75 mm

B) TOTAL NO. OF INTERSECTIONS: 14

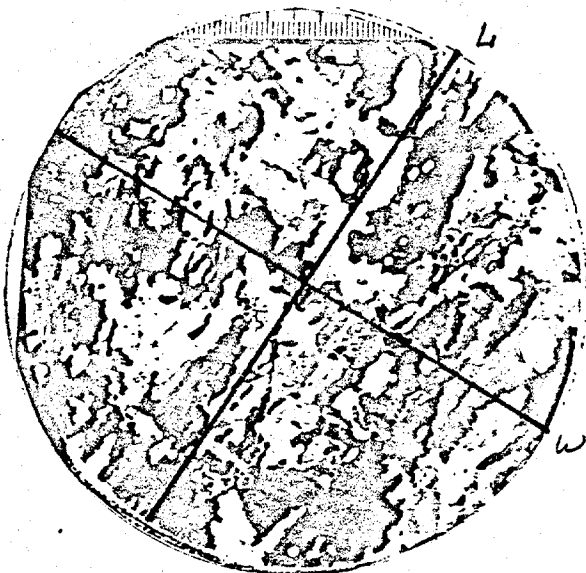
$$\begin{aligned}\text{LENGTH OF GRAIN} &= \frac{A}{B} \\ &= \underline{5.36} \text{ mm (READING)} \\ &= \underline{7.57} \text{ mm (ACTUAL)}\end{aligned}$$

GRAIN WIDTH: 2.6 mm

A) TOTAL LENGTH OF TEST LINE: 75 mm

B) TOTAL NO. OF INTERSECTIONS: 41

$$\begin{aligned}\text{WIDTH OF GRAIN} &= \frac{A}{B} \\ &= \underline{1.83} \text{ mm (READING)} \\ &= \underline{2.61} \text{ mm (ACTUAL)}\end{aligned}$$



SAMPLE NO. C4-90/116
@ C4-117

GRAIN DESCRIPTION: _____
COLUMNAR 100% SAMPLE

GRAIN LENGTH: 4.7 mm

A) TOTAL LENGTH OF TEST LINE: 75 mm

B) TOTAL NO. OF INTERSECTIONS: 23

$$\begin{aligned} \text{LENGTH OF GRAIN} &= \frac{A}{B} \\ &= \frac{3.26}{\text{mm}} \text{ (READING)} \\ &= \frac{4.66}{\text{mm}} \text{ (ACTUAL)} \end{aligned}$$

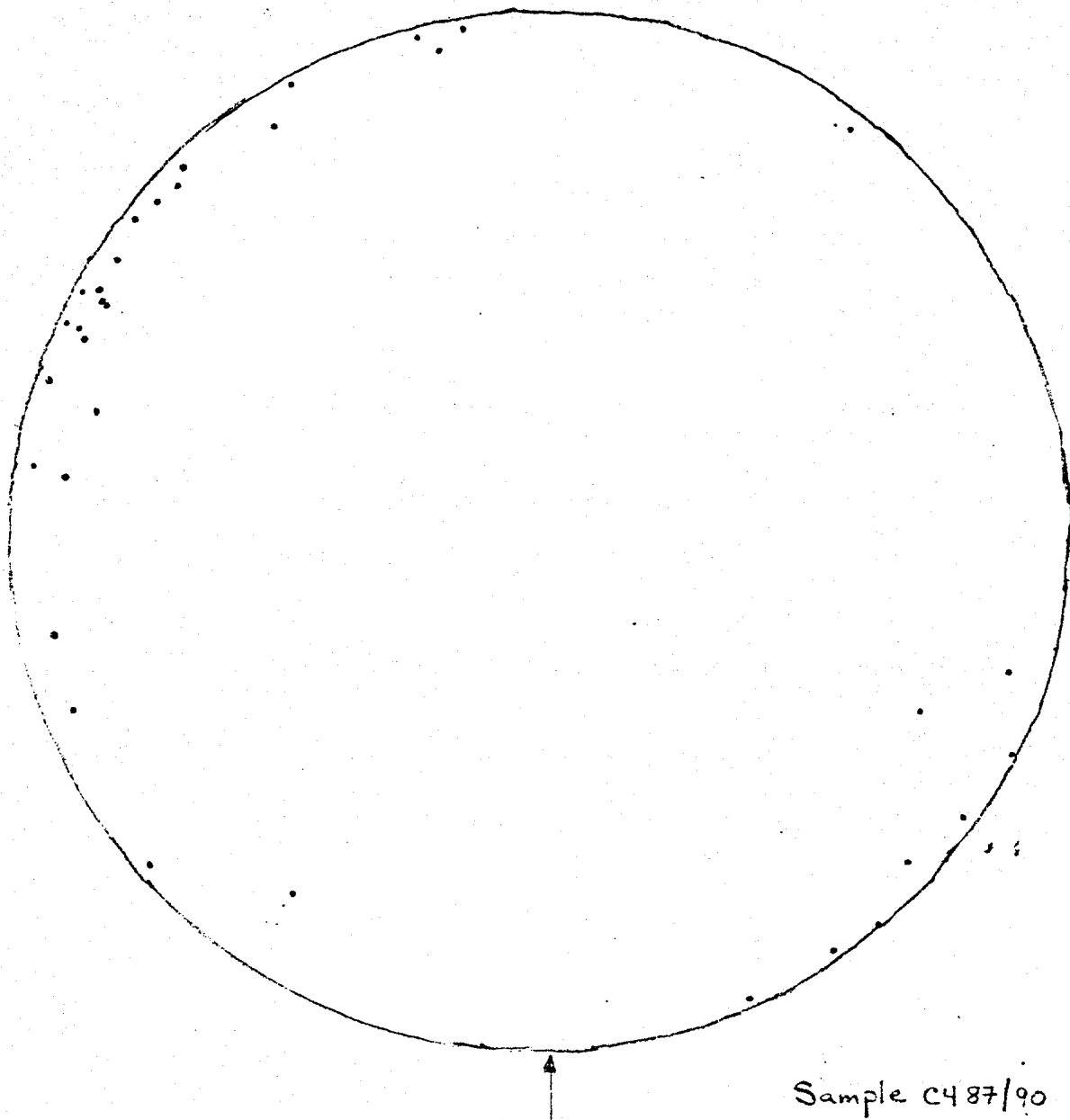
GRAIN WIDTH: 3.1 mm

A) TOTAL LENGTH OF TEST LINE: 74 mm

B) TOTAL NO. OF INTERSECTIONS: 34

$$\begin{aligned} \text{WIDTH OF GRAIN} &= \frac{A}{B} \\ &= \frac{2.18}{\text{mm}} \text{ (READING)} \\ &= \frac{3.11}{\text{mm}} \text{ (ACTUAL)} \end{aligned}$$

C4-090/110 : TOP



Sample C487/90

C3-128/154

Uniaxial Compression

Displacement rate: 10^{-2} in/sec

Temperature: 20°F (-6.5°C)

Salinity: 1.5‰

Density: ---

Brine Volume: ~11.7‰

Air Volume: ---

Porosity: ---

Structure: 100% columnar

$$\begin{array}{l} \sigma_{\max} = 1243 \text{ psi} \quad \epsilon_{\max} = 0.10\% \\ \quad \quad \quad t_{\max} = 4 \text{ sec} \end{array}$$

C3-128/154 : PRE-TEST



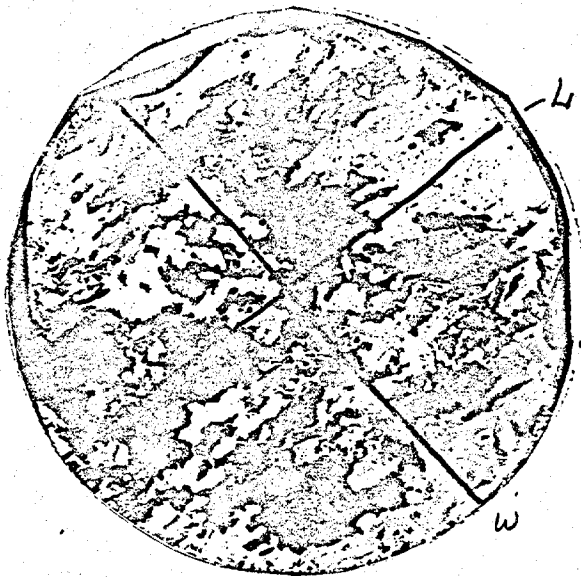
TOP

$\bar{L} = 4.9 \text{ mm}; \bar{W} = 3.5 \text{ mm}$



BOTTOM

$\bar{L} = 5.6 \text{ mm}; \bar{W} = 4.0 \text{ mm}$



SAMPLE NO. C3-128/154
@ C3-128

GRAIN DESCRIPTION: _____
Columnar 100% SAMPLE

GRAIN LENGTH: 4.9 mm

A) TOTAL LENGTH OF TEST LINE: 75 mm

B) TOTAL NO. OF INTERSECTIONS: 22

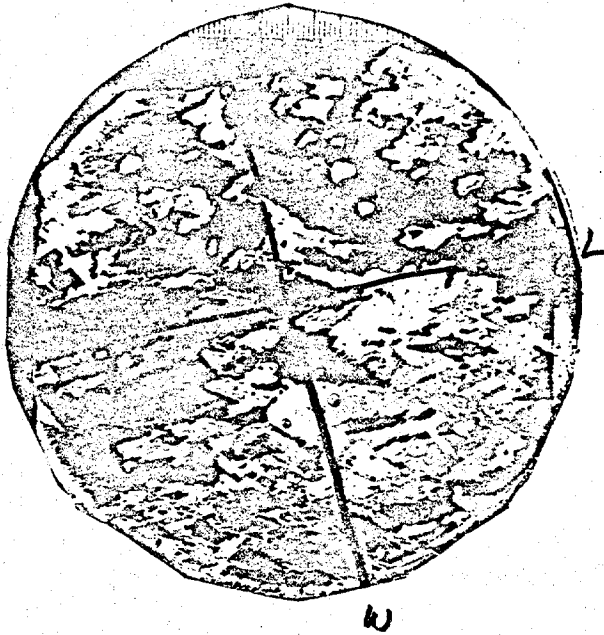
$$\begin{aligned} \text{LENGTH OF GRAIN} &= \frac{A}{B} \\ &= \underline{3.41} \text{ mm (READING)} \\ &= \underline{4.87} \text{ mm (ACTUAL)} \end{aligned}$$

GRAIN WIDTH: 3.5 mm

A) TOTAL LENGTH OF TEST LINE: 72 mm

B) TOTAL NO. OF INTERSECTIONS: 29

$$\begin{aligned} \text{WIDTH OF GRAIN} &= \frac{A}{B} \\ &= \underline{2.48} \text{ mm (READING)} \\ &= \underline{3.54} \text{ mm (ACTUAL)} \end{aligned}$$



SAMPLE NO. C3-128/154
@ C3-154

GRAIN DESCRIPTION: _____
Co/Al AL-100 % SAMPLE

GRAIN LENGTH: 5.6 mm

- A) TOTAL LENGTH OF TEST LINE: 70 mm
B) TOTAL NO. OF INTERSECTIONS: 18

$$\begin{aligned} \text{LENGTH OF GRAIN} &= \frac{A}{B} \\ &= \frac{3.89}{\text{mm}} \text{ (READING)} \\ &= \frac{5.56}{\text{mm}} \text{ (ACTUAL)} \end{aligned}$$

GRAIN WIDTH: 4.0 mm

- A) TOTAL LENGTH OF TEST LINE: 70 mm
B) TOTAL NO. OF INTERSECTIONS: 25

$$\begin{aligned} \text{WIDTH OF GRAIN} &= \frac{A}{B} \\ &= \frac{2.8}{\text{mm}} \text{ (READING)} \\ &= \frac{4.0}{\text{mm}} \text{ (ACTUAL)} \end{aligned}$$

C3-36/61

Uniaxial Compression

Displacement rate: 10^{-2} in/sec

Temperature: 20°F (-6.5°C)

Salinity: 1.1‰

Density: ---

Brine Volume: ~8.6‰

Air Volume: ---

Porosity: ---

Structure: largely columnar

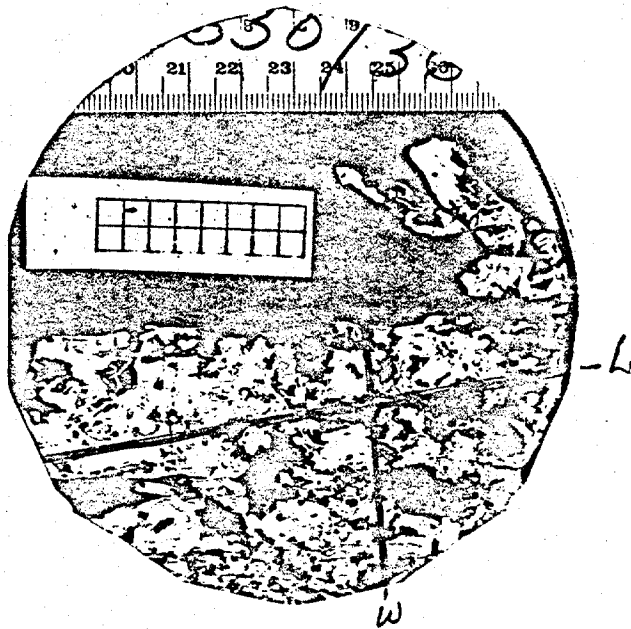
$$\begin{array}{l} \sigma_{\max} = 1683 \text{ psi} \quad \epsilon_{\max} = 0.27\% \\ \hline t_{\max} = 5 \text{ sec} \end{array}$$

C3-36/61 : PRE-TEST



TOP

$\bar{L} = 3.6 \text{ mm} ; \bar{W} = 2.5 \text{ mm}$



SAMPLE NO. C3-36/61
@ C3-36

GRAIN DESCRIPTION: _____

?? FINE L?? 100% 70 SAMPLE

GRAIN LENGTH: 3.6 mm

A) TOTAL LENGTH OF TEST LINE: 68 mm

B) TOTAL NO. OF INTERSECTIONS: 27

$$\text{LENGTH OF GRAIN} = \frac{A}{B}$$

$$= \frac{2.52}{1} \text{ mm (READING)}$$

$$= \frac{3.6}{1} \text{ mm (ACTUAL)}$$

GRAIN WIDTH: 2.5 mm

A) TOTAL LENGTH OF TEST LINE: 37 mm

B) TOTAL NO. OF INTERSECTIONS: 21

$$\text{WIDTH OF GRAIN} = \frac{A}{B}$$

$$= \frac{1.76}{1} \text{ mm (READING)}$$

$$= \frac{2.51}{1} \text{ mm (ACTUAL)}$$

APPENDIX B

Equations for Determining the Air Volume and Brine Volume of Sea Ice

INTRODUCTION

A knowledge of the total porosity of sea ice is important in interpreting its physical properties. It has been shown, both theoretically and experimentally, that the mechanical properties of sea ice vary with the ice brine volume (Weeks and Assur, 1969). However, not only is the ice brine volume important, but also its air or gas volume. This is particularly true for low salinity sea ice, that is, where the ice air volume may make up a considerable portion of its total porosity.

The air volume of sea ice can be calculated given the ice density, salinity, and temperature. Generally, Assur's (1960) phase diagram table (Table III, p. 31) is used to perform such calculations. This table gives the relative masses of the different components in standard sea ice at two degree temperature intervals. From the density of the various components, the theoretical, or air-free density is calculated and compared to the measured density to determine the air volume. However, since the table is based on an ice salinity of 34.325 ‰, it is first necessary to reduce the data to the appropriate ice salinity. This is done by dividing all the components, except pure ice, by $S_i/34.325$ where S_i is the ice salinity in parts per thousand. The mass of pure ice is then 1000g minus the total mass of brine and precipitated salts. Even though these calculations are straightforward, they are time consuming and prone to arithmetic errors.

Schwerdtfeger (1963) presents an equation to calculate the air volume of sea ice above -8.2°C , the $\text{Na}_2\text{SO}_4 \cdot 10\text{H}_2\text{O}$ eutectic. He neglects the presence of solid salts and assumes that the volume of brine is equal to that of pure water. For warm sea ice these are reasonable assumptions, and Schwerdtfeger's equation gives a difference of only 2 to 3 ‰ when compared to the method presented in this paper. However, in sea ice having very low air volumes, these differences are significant.

It should also be noted that Assur's (1960) brine volume table and the brine volume equations based on this table derived by Frankenstein and Garner (1967) assume an ice density of 0.926g/cm^3 . Consequently, these reports should be used with caution in air volume calculations. The brine volume obtained from these

sources should be multiplied by $\rho/0.926$, where ρ is the measured ice density in g/cm^3 , to determine the brine volume for a given sea ice density.

Equations are derived and presented in this report from which the air volume and brine volume can be directly calculated given the ice salinity, temperature, and density. The equations cover the temperature range from -2°C to -30°C and consider the presence of solid salts. Equations are also given to calculate sea ice density and the variation of air and brine volume of a sea ice sample, if the temperature of the sample is changed from the temperature at which the ice density was obtained.

DERIVATION OF EQUATIONS

A sample of sea ice is composed of pure ice, brine, solid salts, and air. In determining the air volume of sea ice we are interested in the relative masses and volumes of the different components at a given ice salinity, temperature, and bulk density.

In the derivations to follow, m_ℓ , ρ_ℓ and V_ℓ are the mass, density, and volume of component ℓ where the subscripts a, b, i, s, and ss denote the component air, brine, pure ice, salt, and solid salts, respectively. M is the bulk mass and ρ the bulk density. The terms m_s^b and m_s^{ss} denote the mass of salt in the brine and mass of salt in the solid salts, respectively.

Brine Volume

The salinity of the ice, S_i , is defined as:

$$S_i = \frac{m_s}{M} = \frac{m_s^b + m_s^{ss}}{m_b + m_{ss} + m_i} \quad (1)$$

The mass of air in the ice is negligible. The salinity of the brine, S_b , is defined as:

$$S_b = \frac{m_s^b}{m_b} \quad (2)$$

From these two relations we can derive an equation for the brine volume of sea ice. It should be noted that the brine salinity and relative amounts of salt in the brine and solid salts are unique functions of ice temperature via phase relations.

From Equation (1)

$$MS_i = m_S^{ss} + m_S^b$$

and

$$m_S^b = MS_i - m_S^{ss}$$

or

$$m_S^b = MS_i - km_S^b$$

where

$$k = \frac{m_S^{ss}}{m_S^b}$$

Solving for m_S^b and noting from Equation (2) that

$$m_S^b = \rho_b V_b S_b$$

we obtain

$$\frac{V_b}{V} = \frac{\rho S_i}{\rho_b S_b} \left(\frac{1}{1+k} \right) \quad (3)$$

where V_b/V is the relative brine volume. If we neglect the salts in the solid salts, $k=0$, Equation (3) reduces to

$$\frac{V_b}{V} = \frac{\rho S_i}{\rho_b S_b}$$

as derived by Weeks (1968).

Since the brine density can be approximated by (Zubov, 1945; and Cox and Weeks, 1975):

$$\rho_b = 1 + 0.0008 S_b$$

where S_b is in ‰, and because S_b and k are unique functions of temperature, the relative brine volume can be expressed as

$$\frac{V_b}{V} = \frac{\rho S_i}{F_1(T)} \quad (4)$$

where S_i is in ‰, ρ is in g/cm³, and

$$F_1(T) = \rho_b S_b (1+k) \quad (5)$$

Values for $F_1(T)$ are given in Table 1 and plotted against temperature in Figure 1. The lines through the data in Figure 1 are least-squares curves of the form

$$F_1(T) = \alpha_1 + \alpha_2 T + \alpha_3 T^2 + \alpha_4 T^3 \quad (6)$$

where T is the ice temperature (°C).

Coefficients for the curves are given in Table 2.

Solid Salts Volume

Also, via phase relations, the mass of solid salts is proportional to the mass of brine at a given temperature, that is

$$m_{ss} = C m_b. \quad (7)$$

The relative volume of solid salts, V_{ss}/V , is then equal to

$$\frac{V_{ss}}{V} = C \frac{\rho_b}{\rho_{ss}} \frac{V_b}{V} \quad (8)$$

where ρ_{ss} is the average solid salt density assumed to be constant at 1.5 g/cm³.

Pure Ice Volume

The mass of pure ice is equal to

$$m_i = M - m_b - m_{ss}$$

or from Equation (7)

$$m_i = M - (1+C)m_b$$

Since

$$m_i = \rho_i V_i$$

$$M = \rho V$$

$$m_b = \rho_b V_b$$

T	S_b	$k \times 10^3$	$C \times 10^3$	$F_1(T)$	$F_2(T)$
(°C)	(°/°°)			(g/cm ³)	
- 2	37.6	0	0	38.731	0.123
- 4	70.6	0.554	0.148	74.662	0.151
- 6	99.8	1.050	0.387	107.876	0.177
- 8	126.5	1.400	0.660	139.441	0.199
-10	142.8	55.277	18.256	167.865	0.222
-12	157.6	84.141	30.493	192.378	0.240
-14	171.5	97.627	38.421	214.143	0.256
-16	184.4	106.330	44.952	234.033	0.271
-18	197.0	112.570	50.808	253.588	0.284
-20	209.9	118.078	56.851	274.074	0.298
-22	222.6	123.090	63.015	294.496	0.312
-24	230.5	509.787	217.168	412.236	0.394
-26	232.7	1312.694	537.697	638.433	0.556
-28	234.1	2065.827	842.341	852.171	0.708
-30	235.6	2685.708	1098.887	1032.102	0.836

Table 1: Values for S_b , k , C , $F_1(T)$, and $F_2(T)$ at different temperatures.

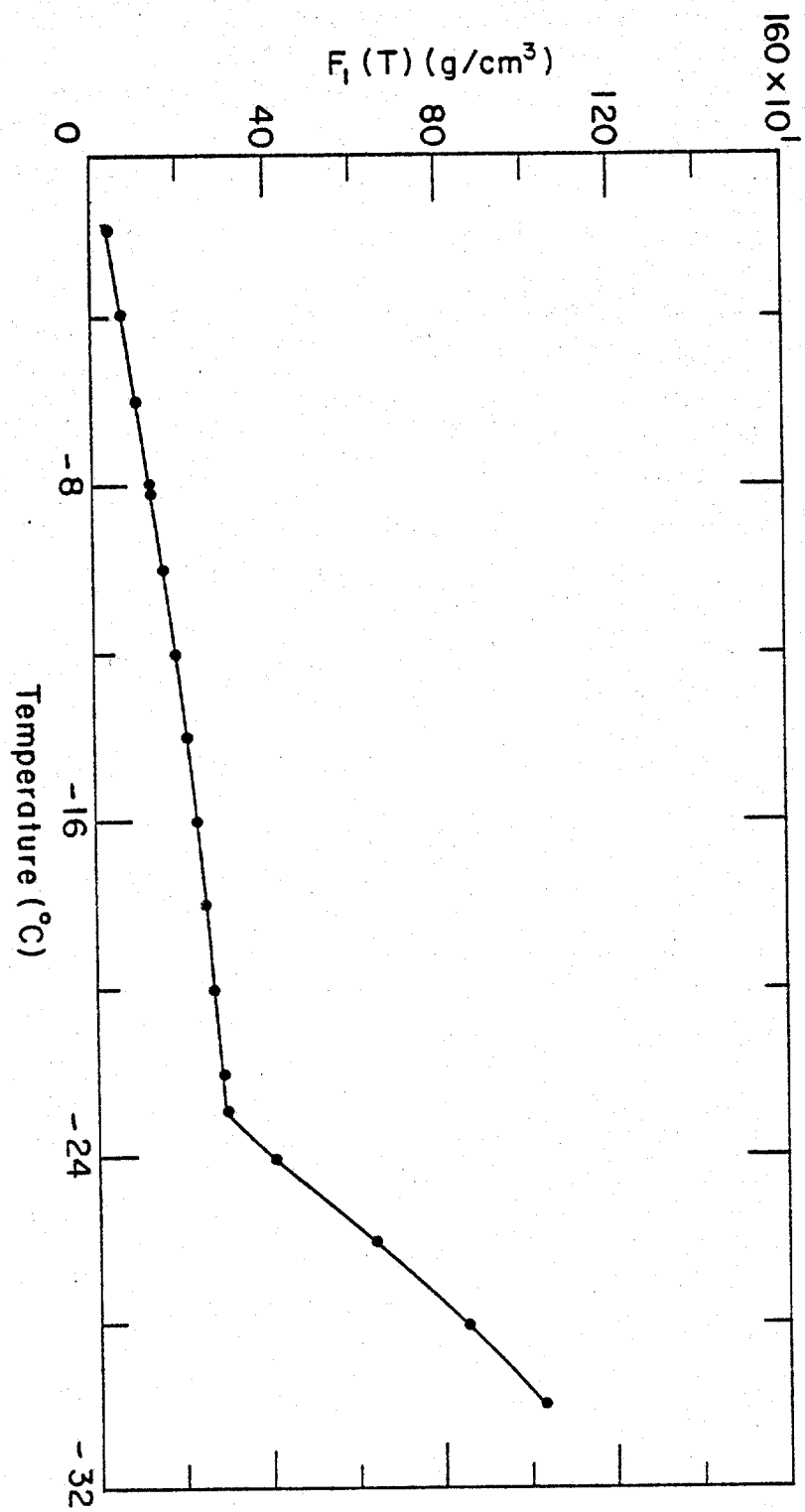


Figure 1. Function $F_1(T)$ versus temperature. Curve determined by method of least-squares.

F₁(T)

<u>T(°C)</u>	<u>α₁</u>	<u>α₂</u>	<u>α₃</u>	<u>α₄</u>	<u>Correlation Coefficient</u>	<u>Standard Error</u>
-22.9	-4.732	-2.245 x 10 ¹	-6.397 x 10 ⁻¹	-1.074 x 10 ⁻²	0.9999	1.0389
-22.9 to -30	9.899 x 10 ³	1.309 x 10 ³	5.527 x 10 ¹	7.160 x 10 ⁻¹	0.9999	3.438

F₂(T)

-22.9	8.903 x 10 ⁻²	-1.763 x 10 ⁻²	-5.330 x 10 ⁻⁴	-8.801 x 10 ⁻⁶	0.9999	0.001
-22.9 to -30	8.547	1.089	4.518 x 10 ⁻²	5.819 x 10 ⁻⁴	0.9999	0.004

Table 2: Coefficients for functions F₁(T) and F₂(T) determined by method of least-squares.

we have

$$\rho_i V_i = \rho V - (1+C) \rho_b V_b$$

Solving for the relative pure ice volume, V_i/V , we obtain:

$$\frac{V_i}{V} = \frac{\rho}{\rho_i} - (1+C) \frac{\rho_b}{\rho_i} \frac{V_b}{V} \quad (9)$$

Air Volume

The relative air volume, V_a/V , is equal to

$$\frac{V_a}{V} = 1 - \frac{V_b}{V} - \frac{V_i}{V} - \frac{V_{ss}}{V} \quad (10)$$

Substituting Equations (4), (8), and (9) into Equation (10) we obtain

$$\frac{V_a}{V} = 1 - \frac{\rho}{\rho_i} + \frac{V_b}{V} \left((1+C) \frac{\rho_b}{\rho_i} - \frac{C \rho_b}{\rho_{ss}} - 1 \right) \quad (11)$$

Since ρ_{ss} is assumed to be constant and C , ρ_b , and ρ_i are functions of temperature, Equation (11) can be simplified to

$$\frac{V_a}{V} = 1 - \frac{\rho}{\rho_i} + \rho_{ss} \frac{F_2(T)}{F_1(T)} \quad (12)$$

where

$$F_2(T) = (1+C) \frac{\rho_b}{\rho_i} - C \frac{\rho_b}{\rho_{ss}} - 1 \quad (13)$$

Values for $F_2(T)$ are given in Table 1 and plotted against temperature in Figure 2. The lines through the data in Figure 2 are also least-squares curves of the form

$$F_2(T) = \alpha_1 + \alpha_2 T + \alpha_3 T^2 + \alpha_4 T^3 \quad (14)$$

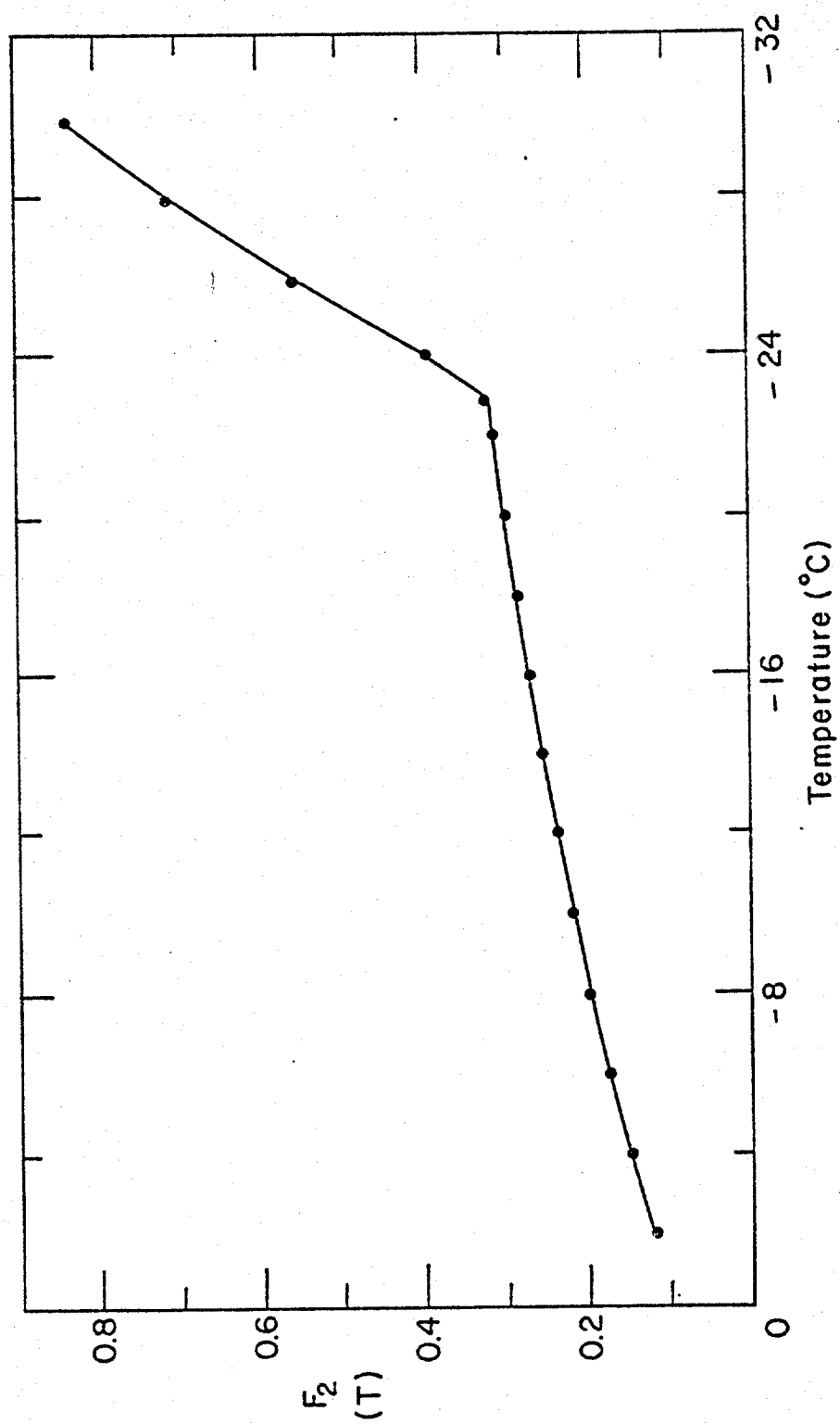


Figure 2: Function $F_2(T)$ versus temperature. Curve determined by method of least-squares.

Coefficients for these curves are given in Table 2. In determining the value of $F_2(T)$ at a given temperature, the pure ice density was calculated from (Pounder, 1965):

$$\rho_i (\text{g/cm}^3) = 0.918 - 1.403 \times 10^{-4} T (\text{°C})$$

Sea Ice Density

The sea ice density can be found from Equation (12) by solving for ρ :

$$\rho = \left(1 - \frac{V_a}{V} \right) \left(\frac{\rho_i F_1(T)}{F_1(T) - \rho_{is} F_2(T)} \right) \quad (15)$$

Unlike the calculated densities given in Schwerdtfeger (1963) and Anderson (1960), this equation considers the presence of both air and solid salts in the ice.

Air Volume at Another Temperature

The air volume and brine volume of sea ice are determined by measuring the volume and mass of the ice sample at a given temperature and the salinity of the melted sample. Since the air volume and brine volume are dependent upon the bulk ice density which varies with temperature, the air and brine volumes of a given sample will change with temperature. If tests are conducted at a temperature different than the temperature at which the bulk density was determined, the air and brine volumes must be recalculated.

Equations are now derived to calculate the air and brine volumes at a temperature which differs from the temperature at which the ice density was determined. Primed variables denote the initial value of the different variables, i.e., at $T = T_1$.

It is first assumed that the brine and air pockets are water connected. From Equation (4) we know that

$$V_b = \frac{M S_i}{F_1(T)}$$

Since the mass and salinity of the ice do not change with temperature

$$V_b = V_b^1 \frac{F_1^1(T)}{F_1(T)} \quad (16)$$

From Equation (11) we also know that

$$\frac{V_b}{V - V_a} = F_3(S_i, T) \quad (17)$$

where

$$F_3(S_i, T) = \frac{\rho_i S_i}{F_1(T) - \rho_i S_i F_2(T)} \quad (18)$$

Thus,

$$\frac{V_b}{V_b^1} = \frac{(V - V_a) F_3(S_i, T)}{(V^1 - V_a^1) F_3^1(S_i, T)} \quad (19)$$

Substituting Equation (16) into Equation (19) and solving for V_a/V we obtain

$$\frac{V_a}{V} = 1 - \left(1 - \frac{V_a^1}{V^1}\right) \frac{F_3^1(S_i, T) F_1^1(T)}{F_3(S_i, T) F_1(T)} \quad (20)$$

The brine volume is then determined from Equation (17):

$$\frac{V_b}{V} = \left(1 - \frac{V_a}{V}\right) F_3(S_i, T) \quad (21)$$

If the brine and air pockets are not connected, a change in air volume may also take place if the ice is warmed, that is, as less dense ice is melted to dilute the brine. In this case, the new air volume is equal to

$$\frac{V_a}{V} = \frac{V_a^1}{V^1} + 1 - \frac{F_3^1(S_i, T) F_1^1(T)}{F_3(S_i, T) F_1(T)} \quad (22)$$

If the brine and air pockets are not connected and the ice is cooled, the air volume will not change. However, due to phase changes, some brine will be lost from the sample as a result of brine expulsion. An estimate of the amount

of brine loss can be obtained from the brine expulsion equations given in Cox and Weeks (1975).

DISCUSSION

In addition to presenting a new set of equations to calculate the air volume of sea ice, it is instructive to determine whether or not it is important to consider the presence of solid salts in such calculations.

For sea ice above -8.2°C , Schwerdtfeger (1963) calculates the relative air volume of sea ice from

$$\frac{V_a}{V} = 1 - \frac{\rho}{1000} \left(\frac{1000 - S_i}{0.917} + \frac{4.98 S_i}{T} \right) \quad (23)$$

where ρ is in g/cm^3 , S_i in ‰ , and T in $^{\circ}\text{C}$. He neglects the presence of solid salts and assumes that the volume of brine in the ice is equal to the volume of pure water. If we neglect the presence of solid salts in our equations, Equation (12) simplifies to

$$\frac{V_a}{V} = \left(1 - \frac{\rho}{\rho_i} \right) + \frac{\rho S_i}{S_b} \left(\frac{1}{\rho_i} - \frac{1}{\rho_b} \right) \quad (24)$$

The results from Equations (23) and (24) are compared to the results from Equation (12) in Table 3. The air volume of sea ice of different salinities, densities, and temperatures are calculated using these three equations. Schwerdtfeger's results are given in Column 1, our results neglecting solid salts in Column 2, and our results considering solid salts in Column 3.

All the calculated values at a given salinity, density, and temperature are in close agreement. This indicates that even for sea ice below the $\text{NaCl} \cdot 2\text{H}_2\text{O}$ eutectic temperature, neglecting the presence of solid salts in air volume calculations is a reasonable assumption. For warm, high density sea ice (0.930 g/cm^3), Schwerdtfeger's value differs by 1.8 ‰ , or nearly 100%. However,

AIR VOLUME CALCULATIONS

$$S_i = 1 \text{ ‰}$$

T		$\rho \text{ (g/cm}^3\text{)}$								
<u>(°C)</u>		<u>0.890</u>			<u>0.910</u>			<u>0.930</u>		
		1	2	3	1	2	3	1	2	3
- 6	31.1	31.8	31.8		9.4	10.0	10.0	-	-	-
-10		32.0	32.1			10.2	10.4	-	-	-
-20		33.4	33.4			11.7	11.7	-	-	-
-30		34.8	34.6			13.1	12.9	-	-	-

$$S_i = 10 \text{ ‰}$$

T		$\rho \text{ (g/cm}^3\text{)}$								
<u>(°C)</u>		<u>0.890</u>			<u>0.910</u>			<u>0.930</u>		
		1	2	3	1	2	3	1	2	3
- 6	46.5	44.9	44.8		25.1	23.5	23.3	3.7	2.0	1.9
-10		42.7	42.7			21.2	21.2	-	-	-
-20		42.2	42.1			20.7	20.6	-	-	-
-30		43.1	41.0			21.6	19.4	-	-	-

Table 3: Air volume (‰) calculations from three methods for sea ice having different densities, salinities and temperatures (see text for explanation).

the brine volume of this ice is relatively much greater (85.1 ‰) and there is little difference in the total ice porosity.

CONCLUSIONS

Equations have been derived to quickly calculate the air volume of sea ice considering the presence and absence of solid salts. The results show that neglecting the presence of solid salts is a reasonable assumption. However, in this era of computers and sophisticated hand calculators, we recommend not neglecting the presence of solid salts and the use of Equation (12) to calculate the air volume of sea ice.

REFERENCES

- Anderson, D.L. (1960) The physical constants of sea ice. Research, Vol. 13, p. 310-318.
- Assur, A. (1960) Composition of sea ice and its tensile strength. CRREL Research Report 44, 49 p.
- Cox, G.F.N. and Weeks, W.F. (1975) Brine drainage and initial salt entrapment in sodium chloride ice. CRREL Research Report 345, 85 p.
- Frankenstein, G. and Garner, R. (1967) Equations for determining the brine volume of sea ice from -0.5 to -22.9°C. Journal of Glaciology, Vol. 6, No. 48, p. 943-944.
- Pounder, E.R. (1965) The physics of ice. New York, Pergamon Press.
- Schwerdtfeger, P. (1963) The thermal properties of sea ice. Journal of Glaciology, Vol. 4, p. 789-807.
- Weeks, W.F. (1968) Understanding the variations of the physical properties of sea ice. In SCAR/SCOR/LAPO/IUPS Symposium on Antarctic Oceanography (Santiago, Chile, 1966). Cambridge, England, Scott Polar Research Institute, p. 173-190.
- Weeks, W.F. and Assur, A. (1969) Fracture of lake and sea ice. CRREL Research Report 269, 79 p.
- Zubov, N.N. (1945) Arctic ice. Translation, U.S. Naval Electronics Laboratory, 1963.

Shell Development Company

A Division of Shell Oil Company



Bellaire Research Center
P. O. Box 481
Houston, Texas 77001

3737 Bellaire Boulevard
Houston, Texas 77025

March 3, 1982

LIST OF PARTICIPANTS

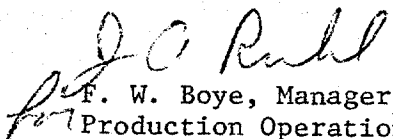
Gentlemen:

MECHANICAL PROPERTIES OF SEA ICE

Enclosed please find a copy of Progress Report No. 4 by CRREL for the Mechanical Properties of Sea Ice program. This is the progress report promised in Attachment I of my letter dated February 23.

We are looking forward to discussing the program with you at the participants' meeting on March 11.

Yours very truly,


F. W. Boye, Manager
Production Operations
Research Department

Enclosure

cc: G. F. N. Cox, Cold Regions Research and Engineering Laboratory

LIST OF PARTICIPANTS

MECHANICAL PROPERTIES OF SEA ICE STUDY

Amoco Production Company
ATTN: Mr. J. R. Olds
Amoco Building
Denver, Colorado 80202

Amoco Production Company
ATTN: Mr. Dan Gibson
Amoco Building
Denver, Colorado 80202

ARCO Oil and Gas Company
ATTN: Mr. Donald B. Reed
Plano Production Research Center
P. O. Box 2819
Dallas, Texas 75221

ARCO Oil and Gas Company
ATTN: Mr. John Currier
Plano Production Research Center
Dallas, Texas 75221

Chevron Oil Field Research Co.
ATTN: Mr. Gordon Strickland
P. O. Box 446
La Habra, California 90631

Exxon Production Research Company
ATTN: Mr. John Prince
P. O. Box 2189
Houston, Texas 77001

Exxon Production Research Company
ATTN: Mr. Tony Wang
P. O. Box 2189
Houston, Texas 77001

Gulf Research & Development Company
ATTN: Mr. Kaung J. Chang
P. O. Box 36506
Houston, Texas 77036

Gulf Research & Development Company
ATTN: Mr. Ram Sisodiya
P. O. Box 36506
Houston, Texas 77036

Mitsui Engineering & Shipbuilding Co., Ltd.
ATTN: Mr. M. Oshima
6-4 Tsukiji 5-Chome
Chuo-Ku, Tokyo 104
Japan

National Science Foundation
ATTN: Mr. Charles Babendreier
Geotechnical Energy Program
Washington, D. C. 20550

Sohio Petroleum Company
ATTN: Mr. Terry Walden
100 Pine Street
San Francisco, California 94111

Sohio Alaska Petroleum Company
ATTN: West Reg. Exploration Manager
100 Pine Street
San Francisco, California 94111

Texaco Inc.
ATTN: Mr. D. Rutherford
P. O. Box 60252
New Orleans, Louisiana 70160

Texaco Inc.
ATTN: Mr. G. E. Mott
P. O. Box 60252
New Orleans, Louisiana 70160

U. S. Geological Survey
ATTN: Mr. John B. Gregory
EGS - Mail Stop 620
12201 Sunrise Valley Drive
Reston, Virginia 22092

U. S. Geological Survey
ATTN: Dr. Paul Teleki
930 National Center
Reston, Virginia 22092

U. S. Department of Energy
ATTN: Mr. S. J. Canja
Mail Station FE-32 D107
Washington, D. C. 20545

U. S. Coast Guard Res. & Development Ctr.
ATTN: Mr. R. Quincy Robe
Avery Point
Groton, Connecticut 06340

MECHANICAL PROPERTIES OF MULTI-YEAR SEA ICE

PROGRESS REPORT 4

1 February 1982

by

G.F.N. Cox, M. Mellor and W.F. Weeks

U.S. Army Cold Regions Research and Engineering Laboratory

Prepared for

Shell Development Company

United States Geological Survey

INTRODUCTION

This progress report describes the work performed in the Mechanical Properties of Multi-year Sea Ice Study from 1 October 1981 to 1 February 1982. During this period about 90 uniaxial compression tests were performed and partially analyzed; work continued on the development of suitable uniaxial tension, constant load, and triaxial testing techniques; and we began preparing for the Phase II field sampling program.

Most of the uniaxial compression test results from Production Run 1 were presented at the December Participants Meeting in Houston. This report contains an up-to-date compilation of the test data and a preliminary analysis of the variation of ice strength within and between multi-year pressure ridges. Data are presented on the effect of porosity on ice strength. We also give an evaluation on the effect of sample squareness on our results.

At the conclusion of Production Run 1, we began to look at the ice structure from a representative number of ice samples. The status of this effort is reviewed.

With regard to testing techniques, we have completed a series of tests to determine the bond strength between the ice and our synthane end caps. This information is being used to size our tension specimens. The constant load test equipment has been designed and fabricated. We are now conducting "warm" room tests to check out the equipment. We have also completed a conceptual design of a triaxial cell for our test program.

Preparation for the Phase II field program is well underway. The 12-inch diameter core barrel has been fabricated. A commercial drilling

rig has been purchased to support and drive the auger. Once the drilling rig is modified, the large auger will be tested in our ice pit. As part of Phase II, we have built a jig to obtain horizontal 4.2-inch diameter samples from the 12-inch core and have put together some Brazil testing equipment. A series of Brazil tests will be conducted on pairs of ice samples in the field and laboratory to assess the effects of ice shipment and storage on ice strength.

PRODUCTION RUN 1 RESULTS

During Production Run 1, about 90 uniaxial compression tests were performed on multi-year ridge ice samples at two different temperatures and strain-rates. Before presenting the test results, it is helpful to consider how the compression samples are instrumented. A photograph of an instrumented test sample is shown in Figure 1. Two DCDTs are mounted on opposite sides of the sample to measure the axial strain of the specimen on the center portion (5.5 inches) of the specimen. An extensometer is also connected between two aluminium rings which are attached to the end caps. The extensometer provides a measurement of the axial strain over the entire sample length (10 inches) and is used to control the strain-rate on our closed-loop testing machine.

Data tables and force-displacement cruves from Production Run 1 were distributed at the December Participants Meeting in Houston. Up-to-date data tables are given in Tables 1 through 8. The data are grouped according to the sample position in the ridge, test strain-rate, and test temperature.

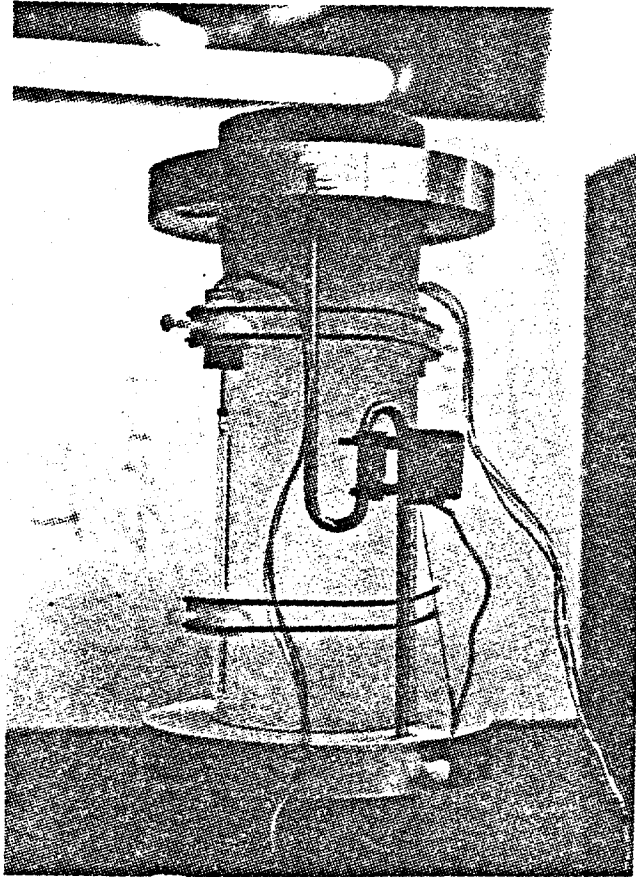


Figure 1: Instrumented uniaxial compression sample.

Table 1: $\dot{\epsilon} = 10^{-5}/\text{sec}$, $z = \text{above sea level}$, $T = -5^{\circ}\text{C}$ (23°F)

Sample No.	σ_m psi	ϵ_m (GL)%	ϵ_m (FS)%	t_m sec	σ_e psi	ϵ_e (FS)%	t_e sec	E_1 (GL)	E_0 (GL) psi($\times 10^6$)	E_0 (FS)	S_1 o/oo	ρ lb/ft ³	v_b o/oo	v_a o/oo	n o/oo	σ_e/σ_m	Squareness (in)		
																	ice	end cap	shim
R1A - 062/089	443	0.31	0.34	344	234	5.0	5000	1.66	0.143	0.130	1.8	55.05	17.1	41.9	59.0	0.528	0.080	0.028	
R1B - 062/089	128	0.11	0.37	365	214	5.0	5000	0.973	0.298	0.0886	0.3	54.54	2.8	48.4	51.3	0.652	0.022	0.044	0.038
R2A - 140/165	388	0.66	0.68	683	254	5.0	5000	0.804	0.0588	0.0571	0.1	56.77	1.0	9.1	10.1	0.655	0.010	0.007	0.006
R2B - 094/121	171	0.11	0.16	156	176	5.0	5000	0.563	0.155	0.107		49.42				1.029	0.005	0.004	0.004
R3A - 106/131	342	0.46	0.86	855	251	5.0	5000	0.654	0.0743	0.0398	0.6	55.61	5.8	30.1	35.9	0.734	0.007	0.006	0.006
R3B - 161/187	308	0.36	0.36	360	207	5.0	5000	0.598	0.0856	0.0856		57.01				0.672	0.010	0.007	0.006
R4A - 312/338	283	0.47	0.47	465	193	5.0	5000	0.703	0.0602	0.0602	1.6	53.92	14.9	61.2	76.1	0.682	0.006	0.019	0.018
R4B - 328/354	253	0.40	0.62	615	166	5.0	5000	0.411	0.0633	0.0480		56.20				0.656	0.011	0.003	0.010
R5A - 165/191	619	0.24	0.22	217	274	5.0	5000	1.50	0.258	0.281		56.67				0.443	0.007	0.003	0.002
R5B - 075/101	774	0.19	0.20	201	246	5.0	5000	1.18	0.407	0.387		54.35				0.318	0.006	0.001	None
R7A - 059/085	361	0.47	0.59	588	253	5.0	5000	0.804	0.0768	0.0612	1.7	54.37	15.9	53.6	69.5	0.701	0.003	0.001	None
R7B - 126/152	240	0.49	0.47	468	207	5.0	5000	0.603	0.0490	0.0511	0.4	51.90	3.6	94.6	98.2	0.863	0.014	0.002	
R8A - 133/159	245	0.34	0.33	333	208	5.0	5000	0.675	0.0721	0.0742	1.0	55.95	9.7	24.8	34.5	0.849	0.003	0.002	0.002
R8B - 162/189	336	0.37	0.47	473	235	5.0	5000	0.560	0.0908	0.0715		56.45				0.699	0.006	0.005	0.004

† Questionable

Table 2: $\dot{\epsilon} = 10^{-5}/\text{sec}$, $z = \text{below sea level}$, $T = -5^{\circ}\text{C}$ (23°F)

Sample No.	σ_m psi	ϵ_m (GL)%	ϵ_m (FS)%	t_m sec	σ_e psi	ϵ_e (FS)%	t_e sec	E_1 (GL)	E_0 (GL) psi($\times 10^6$)	E_0 (FS)	S_1 o/oo	ρ lb/ft ³	v_b o/oo	v_a o/oo	n o/oo	σ_e/σ_m	Squareness (in)		
																	ice	end cap	shim
R1A - 226/252	214	0.21	0.17	173	124	5.0	5000	0.916	0.101	0.126		57.09				0.579	0.061	0.035	0.032
R1A - 399/425	214	0.29	0.25	248	149	5.0	5000	0.751	0.0738	0.0856	2.4	56.62	23.4	15.4	38.9	0.696	0.007	0.014	0.012
R1B - 320/346	1090	0.30	0.25	253	189	5.0	5000	1.01	0.363	0.0436	1.9	57.08	18.7	6.6	25.3	0.173	0.015	0.005	0.004
R1B - 429/455	696	0.27	0.29	285	269	5.0	5000	1.15	0.258	0.240	1.8	57.11	17.7	5.9	23.7	0.386	0.004	0.008	0.008
R2A - 205/230	443	0.39	0.49	489	243†	2.98	2975	0.892	0.114	0.0904		55.40				0.549	0.021	0.015	0.012
R2A - 314/339	308	0.25	0.28	278	161	5.0	5000	0.667	0.123	0.110		56.88				0.523	0.018	0.004	0.004
R2B - 408/434	342	0.57	0.60	597	261	5.0	5000	0.662	0.0600	0.0570		55.90				0.763	0.009	0.005	0.004
R2B - 468/494	265	0.42	0.39	390	199	5.0	5000	1.07	0.0631	0.0679		55.99				0.751	0.006	0.007	0.006
R3A - 220/245	253	0.27	0.39	387	185	5.0	5000	0.350	0.0937	0.0649		57.15				0.731	0.006	0.005	0.004
R3A - 430/456	306	0.41	0.53	525	215	5.0	5000	0.782	0.0746	0.0577		56.30				0.703	0.009	0.017	0.012
R3B - 363/389	394	0.51	0.51	507	259	5.0	5000	0.787	0.0773	0.0773		57.08				0.657	0.010	0.002	0.002
R3B -	No sample																		
R4A - 426/452	322	0.27	0.33	330	183	5.0	5000	0.782	0.119	0.0976		55.87				0.568	0.014	0.005	None
R4A -	No sample																		
R4B - 391/417	290	0.30	0.31	308	185	5.0	5000	0.751	0.0967	0.0935		56.51				0.638	0.007	0.004	0.004
R4B - 449/475	243	0.42	0.37	368	175	5.0	5000	0.521	0.0579	0.0657		56.60				0.720	0.004	0.001	None
R5A - 397/423	314	0.36	0.56	558	227	5.0	5000	0.420	0.0872	0.0561		56.53				0.723	0.012	0.007	0.006
R5A - 442/468	462	0.29	0.28	279	218	5.0	5000	1.00	0.159	0.165		56.82				0.472	0.007	0.012	0.012
R5A - 504/530	327	0.45	0.56	555	227	5.0	5000	0.395	0.0727	0.0584		56.56				0.694	0.008	0.008	0.008
R5B - 341/367	368	0.61	0.61	608	264	5.0	5000	0.804	0.0603	0.0603		54.65				0.717	0.005	0.002	0.002
R5B - 398/423	300	0.40	0.53	525	231	5.0	5000	0.609	0.0750	0.0566		56.46				0.770	0.001	0.007	0.006
R7A - 263/289	68	0.06	0.10	96	61	5.0	5000	0.425	0.113	0.0680		50.30				0.897	0.008	0.001	None
R7A - 342/368	607	0.16	0.26	255	195	5.0	5000	0.908	0.379	0.233		56.66				0.321	0.009	0.004	0.004
R7B - 241/267	229	0.34	0.47	465	163	5.0	5000	0.523	0.0674	0.0487	1.3	53.63	12.0	65.8	77.8	0.712	0.007	0.003	0.002
R7B - 410/436	Sample lost on MTS set-up										1.0	56.73	9.8	11.2	21.0		0.007	0.003	
R8A - 164/190	261	0.11	0.29	285	175	5.0	5000	0.536	0.237	0.0900	1.2	56.45	11.7	16.4	28.1	0.670	0.007	0.010	0.010
R8A - 432/458	657	0.16	0.16	156	208	5.0	5000	1.07	0.411	0.411	1.8	57.06	17.7	6.8	24.5	0.317	0.004	0.007	0.006
R8B - 333/359	344	0.25	0.25	248	209	5.0	5000	0.479	0.138	0.138	1.5	57.04	14.8	6.7	21.4	0.608	0.009	0.006	0.004
R8B - 515/541	348	0.40				5.0	5000	0.592	0.0876		1.8	57.10	17.7	6.1	23.8		0.008		0.004

† Questionable

Table 3: $\dot{\epsilon} = 10^{-1}/\text{sec}$, $z = \text{above sea level}$, $T = -5^{\circ}\text{C}$ (23°F)

Sample No.	σ_m psi	ϵ_m (GL)%	ϵ_m (FS)%	t_m sec	σ_e psi	ϵ_e (FS)%	t_e sec	E_1 (GL)	E_o (GL)	E_o (FS)	S_1 o/oo	ρ lb/ft ³	v_b o/oo	v_a o/oo	n o/oo	σ_e/σ_m	Squareness (in)		
																	ice	end cap	shim
R1A - 175/201	1270	0.14	0.15	1.45	119	5.0	50.0	1.20	0.907	0.847	0.7	56.81	6.9	9.4	16.2	0.094	0.006	0.010	0.010
R1B - 131/157	1260	0.16	0.24	2.35	209	5.0	50.0	1.32	0.788	0.525		56.91				0.166	0.004	0.006	0.004
R2A - 110/135	408	0.05	0.04	0.44	408	0.04	0.44	0.868	0.816	1.02	0.2	52.43	1.8	85.0	86.9		0.010	0.009	0.004
R2B - 135/161	820	0.11	0.10	1.00	820	0.10	1.00	0.892	0.745	0.820	0.1	55.81	1.0	25.8	26.8		0.009	0.005	0.004
R3A - 188/213	970	0.16	0.16	1.64	199	5.0	50.0	1.06	0.606	0.606	1.4	56.85	13.7	9.8	23.5	0.205	0.007	0.007	
R3B - 130/155	900	0.14	0.15	1.50	255	5.0	50.0	1.17	0.643	0.600		56.37				0.283	0.008	0.008	0.004
R4A - 283/309	860	0.11	0.10	1.00	860	0.10	1.00	0.973	0.782	0.860	1.3	53.58	12.0	66.7	78.7		0.007	0.013	0.012
R4B - 299/325	910	0.14	0.15	1.50	99	5.0	50.0	0.973	0.650	0.607	1.3	54.89	12.3	43.9	56.2	0.109	0.012	0.004	0.004
R5A - 135/161	1090	0.10	0.09	0.85	1090	0.09	0.85	1.22	1.09	1.21	0.2	56.10	1.9	20.9			0.011	0.008	0.006
R5B - 141/167	1270	0.11	0.13	1.30	1270	0.13	1.30	1.28	1.15	0.977	0.2	56.20	1.9	19.2	21.1		0.011	0.003	0.002
R7A - 005/031	731	0.09	0.11	1.08	731	0.11	1.08	0.781	0.812	0.665	0.02	52.92	0.2	76.2	76.4		0.006	0.002	None
R7B - 072/098	487	0.06	0.14†	1.40†	487	0.14	1.40	2.03†	0.812	0.348†		54.61					0.011	0.007	0.006
R8A - 033/059	346	0.06	0.11	1.15	346	0.11	1.15	0.718	0.577	0.315	0.3	53.16	2.8	72.5	75.2		0.008	0.005	0.004
R8B - 011/037	811	0.09	0.08	0.80	811	0.08	0.80	0.997	0.901	1.10	0.1	52.48	0.9	84.0	84.9		0.007	0.021	0.020

† Questionable

Table 4: $\dot{\epsilon} = 10^{-2}/\text{sec}$, $z = \text{below sea level}$, $T = -5^{\circ}\text{C}$ (23°F)

Sample No.	σ_m psi	ϵ_m (GL)%	ϵ_m (FS)%	t_m sec	σ_e psi	ϵ_e (FS)%	t_e sec	E_1 (GL)	E_o (GL)	E_o (FS)	S_1 o/oo	ρ lb/ft ³	v_b o/oo	v_a o/oo	n o/oo	σ_e/σ_m	Squareness (in)		
																	ice	end cap	shim
R1A - 300/326	1580	0.12	0.14	1.38	1580	0.14	1.38	1.43	1.32	1.13	1.0	56.77	9.8	10.5	20.3		0.017	0.006	0.002
R1A -	No sample																		
R1B - 216/241	915	0.12	0.17	1.70	195	5.0	50.0	1.25	0.763	0.538	1.2	57.14	11.8	4.4	16.3	0.213	0.006	0.001	None
R1B - 243/268	1050	0.15	0.14	1.40	143	5.0	50.0	1.25	0.700	0.750		57.23				0.136	0.010	0.003	None
R2A - 285/310	1270	0.16	0.22	2.20	95	5.0	50.0	1.18	0.794	0.577	0.7	56.46	6.8	15.5	22.3	0.075	0.020	0.003	0.002
R2A - 383/408	1060	0.11	0.11	1.10	1060	0.11	1.10	1.30	0.964	0.964	2.0	56.81	19.6	11.5	31.1		0.005	0.010	0.016
R2B - 351/377	1130	0.14	0.13	1.26	1130	0.13	1.26	1.15	0.807	0.869		56.46							
R2B - 438/464	995	0.14	0.18	1.80	149	5.0	50.0	1.02	0.711	0.553	2.7	56.48	26.3	18.3	44.6	0.150	0.012	0.009	0.009
R3A - 348/373											1.9	57.08	18.7	6.6	25.3				
R3A - 401/427	925	0.16	0.15	1.52	164	5.0	50.0	1.05	0.578	0.617		57.12				0.177	0.010	0.008	0.004
R3B - 239/265	870	0.16	0.16	1.60	255	5.0	50.0	0.997	0.544	0.544	2.0	57.13	19.7	5.9	25.6	0.293	0.011	0.004	None
R3B - 331/357	971	0.16	0.18	1.75	211	5.0	50.0	1.05	0.607	0.539	2.0	57.79	19.6	11.8	31.4	0.217	0.009	0.005	0.002
R4A - 398/423	786	0.14	0.21	2.10	144	5.0	50.0	0.997	0.561	0.374	1.3	56.03	12.6	23.9	36.5	0.183	0.017	0.006	0.004
R4A -	No sample																		
R4B - 358/384	776	0.12	0.17	1.68	99	5.0	50.0	0.892	0.647	0.456		56.09				0.128	0.011	0.003	0.002
R4B - 420/446	910	0.15	0.19	1.85	910	0.19	1.85	1.06	0.607	0.479	3.3	56.39	32.2	20.8	53.0		0.014	0.004	0.004
R5A -	No sample																		
R5A - 473/499	875	0.14	0.17	1.68	169	5.0	50.0	0.949	0.625	0.515		55.83				0.193	0.005	0.006	0.006
R5B - 287/313	1040	0.10	0.10	1.05	1040	0.10	1.05	1.31	1.04	1.04	4.0	56.96	39.4	12.1	51.4		0.007	0.010	0.004
R5B - 370/396	816	0.12	0.14	1.40	149	5.0	50.0	0.989	0.683	0.583		55.17				0.183	0.017	0.004	None
R7A - 232/258	736	0.12	0.18	1.83	134	5.0	50.0	0.908	0.613	0.409	3.4	49.76	29.2	136.1	165.3	0.182	0.003	0.007	0.008
R7A - 295/321	612	0.11†	0.21	2.08	607	0.23	2.33	0.900	0.556	0.291		54.17					0.005	0.010	0.010
R7B - 175/201	557	0.06	0.04	0.43	557	0.04	0.43	0.876	0.928	1.39		56.12					0.010	0.013	0.012
R7B - 440/466	1540	0.17	0.23	2.30	1540	0.23	2.30	1.25	0.906	0.670		57.17					0.003	0.003	0.002
R8A - 305/331	589	0.11	0.11	1.05	243	5.0	50.0	0.728	0.535	0.535	1.5	56.70	14.7	12.6	27.2	0.413	0.008	0.007	0.006
R8A - 384/410	1297	0.15	0.17	1.69	1297	0.17	1.69	1.27	0.865	0.763	1.7	57.01	16.7	7.5	24.2		0.004	0.005	0.002
R8B - 300/326	587	0.17	0.29	2.93	247	5.0	50.0	1.17	0.345	0.202	0.3	56.61	2.9	12.2	15.1	0.421	0.006	0.004	0.004
R8B - 483/509	1440	0.20	0.38	3.78	1440	0.38	3.78	1.14	0.720	0.379	2.1	57.20	20.7	4.9	25.6		0.009	0.005	0.004

† Questionable

Table 5: $\dot{\epsilon} = 10^{-5}/\text{sec}$, $z = \text{above sea level}$, $T = -20^{\circ}\text{C}$ (-4°F)

Sample No.	σ_m psi	ϵ_m (GL)%	ϵ_m (FS)%	t_m sec	σ_e psi	ϵ_e (FS)%	t_e sec	E_1 (GL)	E_o (GL)	E_o (FS)	S_1 o/oo	ρ lb/ft ³	v_b o/oo	v_a o/oo	n o/oo	σ_e/σ_m	Squareness (in)		
																	ice	end cap	shim
R1C - 065/092	617	0.17	0.19	192	229	5.0	5000	1.52	0.363	0.325		55.90				0.371	0.007	0.008	0.006
R1D - 071/098	612	0.22	0.22	219	193	5.0	5000	1.00	0.278	0.278		56.57				0.315	0.013	0.004	

Table 6: $\dot{\epsilon} = 10^{-5}$ /sec, z = below sea level, T = -20°C (-4°F)

Sample No.	σ_m psi	ϵ_m (GL)%	ϵ_m (FS)%	t_m sec	σ_e psi	ϵ_e (FS)%	t_e sec	E_1 (GL)	E_o (GL)	E_o (FS)	S_1 o/oo	ρ lb/ft ³	v_b o/oo	v_a o/oo	n o/oo	σ_e/σ_m	Squareness (in)		
																	ice	end cap	shim
RIC - 210/236	403	0.22	0.28	282	239	5.0	5000	0.769	0.183	0.144		55.36				0.593	0.003	0.005	0.001
RIC - 240/266	443	0.25	0.25	246	247	5.0	5000	0.989	0.177	0.177		55.84				0.558	0.013	0.014	0.001
RID - 209/236	557	0.17	0.28	282	254	5.0	5000	0.876	0.328	0.199		55.97				0.456	0.015	0.010	0.010
RID - 315/342	264	0.22	0.29	285	181	5.0	5000	0.712	0.120	0.0910		56.49				0.686	0.008	0.010	0.001

Table 7: $\dot{\epsilon} = 10^{-3}$ /sec, z = above sea level, T = -20°C (-4°F)

Sample No.	σ_m psi	ϵ_m (GL)%	ϵ_m (FS)%	t_m sec	σ_e psi	ϵ_e (FS)%	t_e sec	E_1 (GL)	E_o (GL)	E_o (FS)	S_1 o/oo	ρ lb/ft ³	v_b o/oo	v_a o/oo	n o/oo	σ_e/σ_m	Squareness (in)		
																	ice	end cap	shim
RIC - 127/154	1520	0.15	0.17	1.66	1520	0.17	1.66	1.40	1.01	0.894		56.08					0.010	0.004	None
RID - 153/178	1270	0.10	0.08	0.84	1270	0.08	0.84	1.52	1.27	1.59		56.16					0.010	0.006	0.004

Table 8: $\dot{\epsilon} = 10^{-3}$ /sec, z = below sea level, T = -20°C (-4°F)

Sample No.	σ_m psi	ϵ_m (GL)%	ϵ_m (FS)%	t_m sec	σ_e psi	ϵ_e (FS)%	t_e sec	E_1 (GL)	E_o (GL)	E_o (FS)	S_1 o/oo	ρ lb/ft ³	v_b o/oo	v_a o/oo	n o/oo	σ_e/σ_m	Squareness (in)		
																	ice	end cap	shim
RIC - 349/375	1440	0.19	0.18	1.80	1440	0.18	1.80	1.31	0.758	0.800		56.67					0.004	0.008	0.006
RIC - 384/410	1020	0.11	0.10	1.02	1020	0.10	1.02	1.10	0.927	1.02		54.61					0.006	0.005	0.002
RID - 179/206	1640	0.14	0.18	1.84	1640	0.18	1.84	1.45	1.20	0.911		56.59					0.012	0.011	0.008
RID - 285/312	1650	0.11			1650			1.57	1.50			57.25					0.006	0.004	None

In these tables σ , ϵ and t are stress, strain, and time, respectively. The subscript m denotes the values of σ , ϵ , and t at the peak or maximum stress, σ_m , during the test. The subscript e denotes the values of σ , ϵ , and t at the end of the test, t_e . ϵ (GL) is the axial strain as determined from the average values of the two DCDTs for the gauge length of 5.5 inches. ϵ (FS) is the axial strain of the full sample as determined from the extensometer mounted between the end caps.

Elastic moduli are determined from the force and displacements. E_i (GL) and E_o (GL) are the apparent initial tangent modulus and overall secant modulus, respectively. These values are obtained from the force-displacement curves where the displacements are obtained from the average DCDT values (GL). The overall secant modulus, E_o (GL), is defined as

$$E_o \text{ (GL)} = \frac{\sigma_m}{\epsilon_m \text{ (GL)}}$$

E_o (FS) is the overall secant modulus as determined from the extensometer where

$$E_o \text{ (FS)} = \frac{\sigma_m}{\epsilon_m \text{ (FS)}}$$

Sample properties are also given. S_i is the sample salinity, and ρ , v_b , v_a , and n are the sample density, brine volume, air volume, and porosity at the test temperature.

Information is also given on sample squareness after the ends of the sample are milled (ice), and after the end caps are mounted (end caps). The squareness is determined by placing the sample on a comparator and mea-

asuring the difference between the high and low end of the specimen. The amount of steel shim stock inserted between the low end of the sample and actuator just before testing is also given.

It should be noted that these tables are incomplete. As samples are analyzed for their ice structure, data on grain size and crystal orientation will be provided. Once thin sections are made for structural analyses, sample salinities will be determined from the remaining ice. The ice brine volume, air volume, and porosity will then be calculated. Thin sections have already been prepared for many of the samples; however, we have not yet finalized our classification scheme for multi-year ridge sea ice structure. More will be said about this later in the progress report.

We should also point out that our air volume equations have been modified resulting in slight changes in the test density values. Sample densities are first determined at 5°F (-15°C) and then corrected to the test temperature. In these tables, the density values that are given with salinity values have been corrected. The density values given without salinities still need to be changed. For the 23°F tests, the uncorrected values in the tables need to be multiplied by 0.998. These density values will be corrected as we obtain our salinity.

DISCUSSION OF RESULTS

Uniaxial Compressive Strength

The compressive strength of the specimens, or peak stress endured during each of the tests, is plotted against strain-rate in Figures 2 and 3. Figure 2 contains the results from those tests conducted at 23°F and Figure 3 presents the results from those tests conducted at -4°F. Average

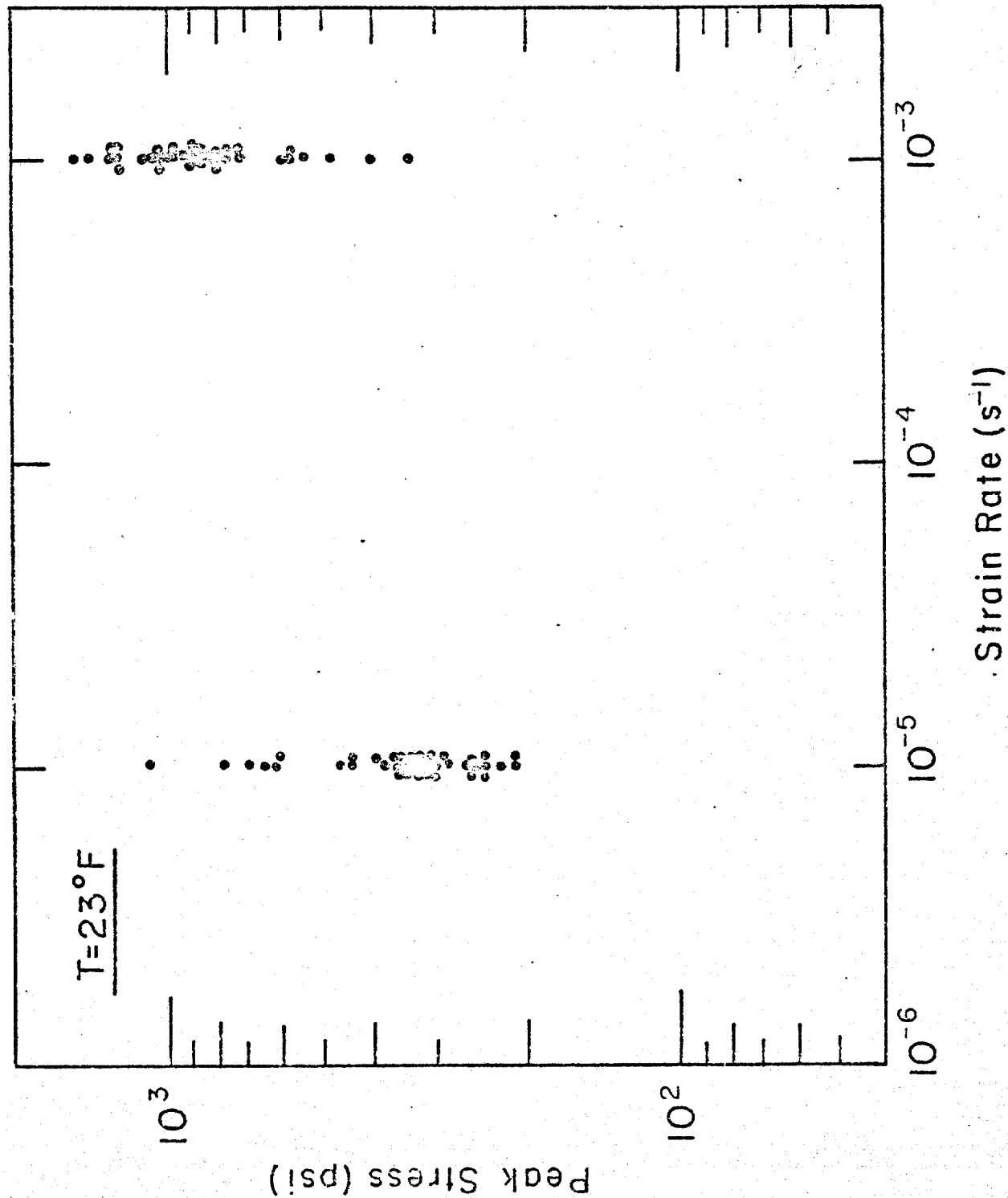


Figure 2: Uniaxial compressive strength at 23°F (-5°C) versus strain-rate for sea ice samples obtained from multi-year pressure ridges.

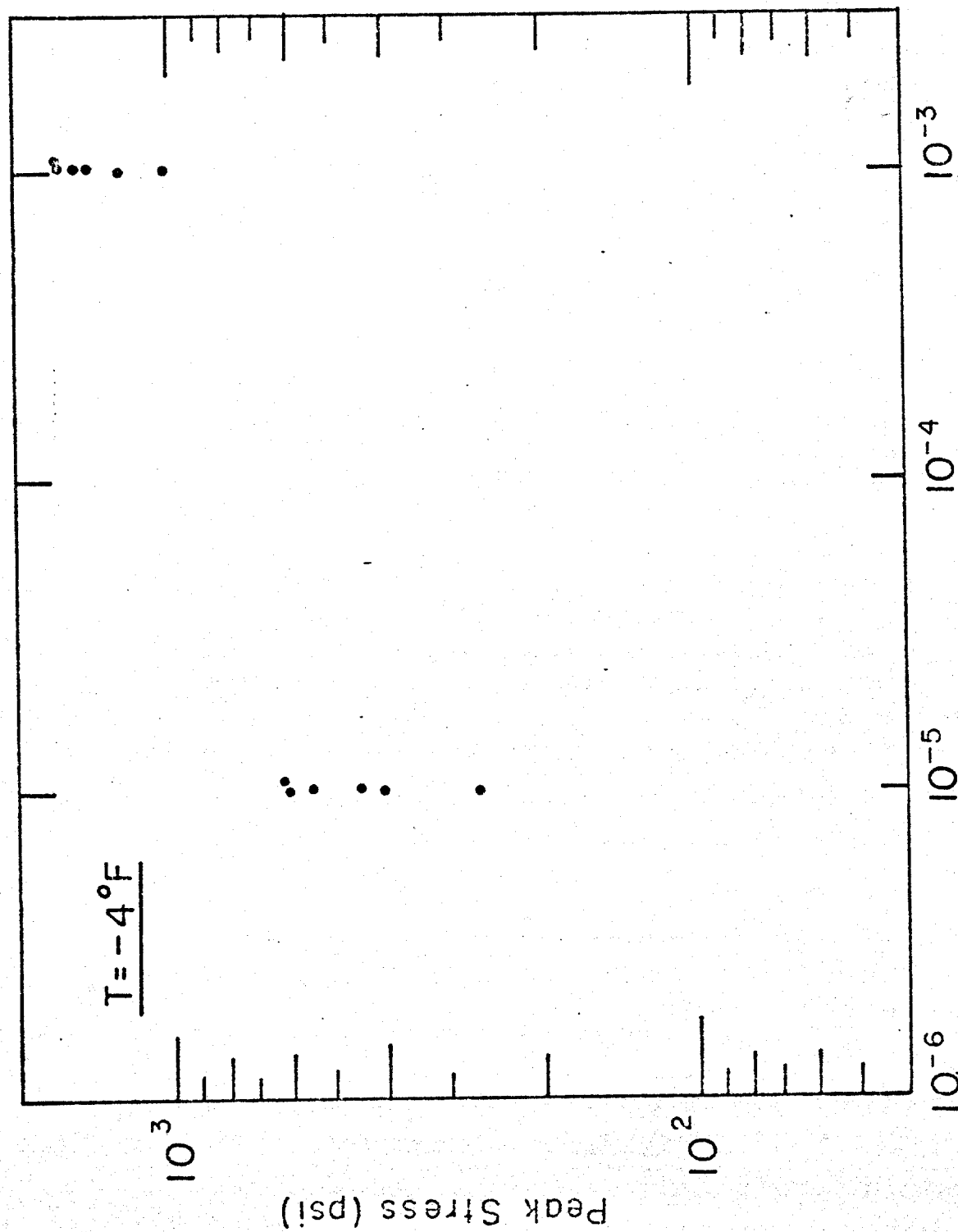


Figure 3: Uniaxial compressive strength at -4°F (-20°C) versus strain-rate for sea ice samples obtained from multi-year pressure ridges.

strength values are given in Table 9 and plotted against strain-rate in Figure 4. Figure 4 also compares our data to those obtained by other investigators.

The results indicate that the uniaxial compressive strength of sea ice obtained from multi-year pressure ridges increases with strain-rate and decreases with temperature. These trends are consistent with test data for first-year sea ice as reported by Wang (1979). The shaded area in Figure 4 represents the variation of ice strength of first-year columnar, oriented-columnar, and granular sea ice in different loading directions at 14°F (-10°C). Relative to first-year sea ice, the strength of the ridge ice is comparable to the strength of columnar, oriented first-year sea ice in the hard fail direction and granular first-year sea ice. Our data also agree with the multi-year sea ice strength values at -15°F obtained by Frederking and Timco (1980). The multi-year ridge ice samples also appear to be slightly weaker than the constant displacement rate samples obtained from the presumably undeformed multi-year floe which was samples in our study.

Based on the work of previous investigators, we would expect that the compressive strength of our samples would decrease with increasing brine volume or porosity. The compressive strength, or peak stress, of a number of our test samples is plotted against ice brine volume and porosity in Figures 5 through 8. These figures show no dependence of ice strength on brine volume. In retrospect this is not surprising in that the ice has a low salinity and high air content. The plots of ice strength versus porosity (brine plus air volume) do show a trend of decreasing ice strength with increasing porosity. However, more test results are needed to establish this relationship.

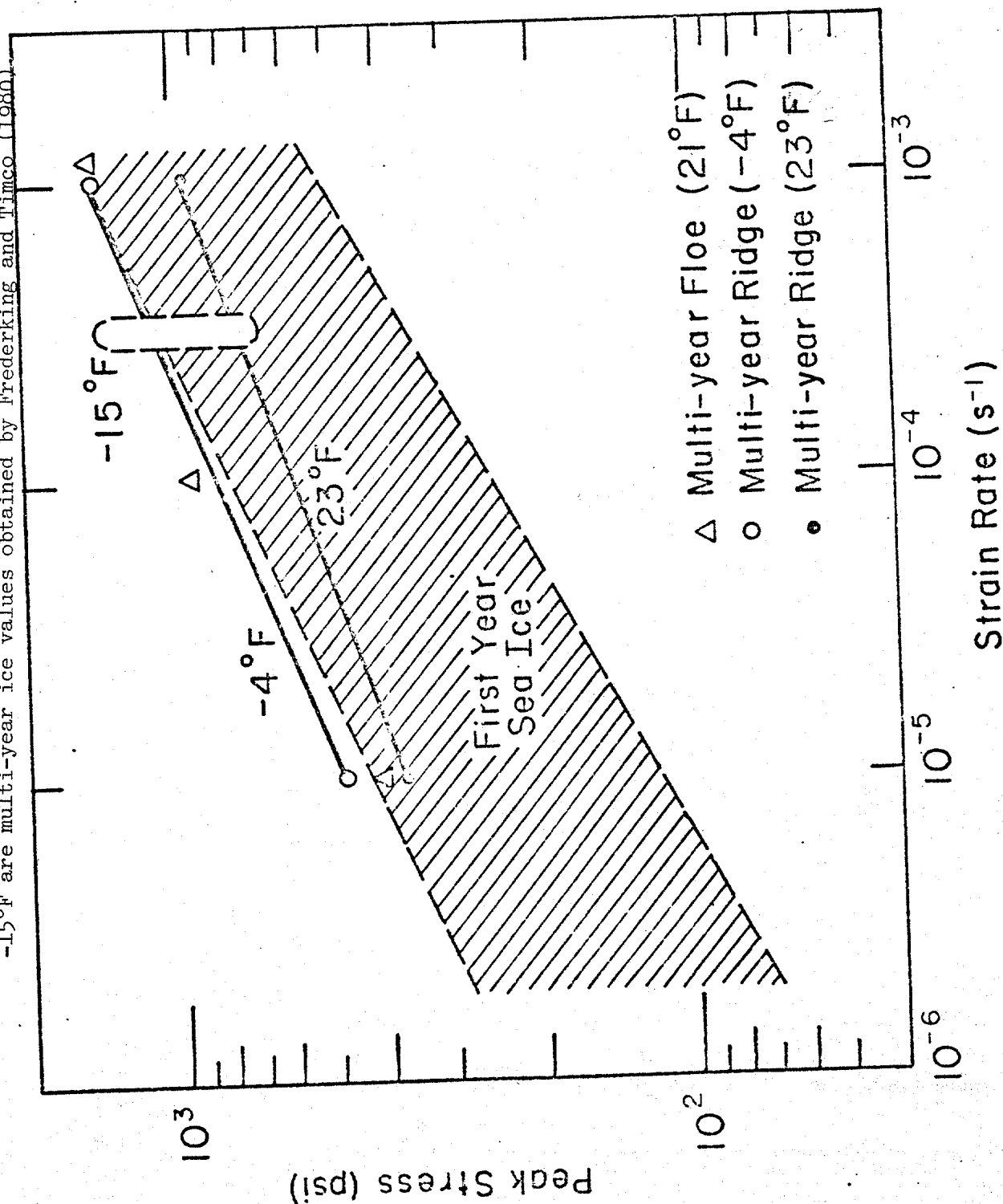
SUMMARY OF STRENGTH DATA

	$\bar{\sigma}_m$ (psi)	$\bar{\sigma}_e$ (psi)	$\bar{\sigma}_e/\bar{\sigma}_m$
<u>23°F (-5°C)</u>			
10 ⁻⁵ /sec	369±186	208±44	0.636±0.172
10 ⁻³ /sec	933±295	164±50*	0.176±0.059
<u>-4°F (-20°C)</u>			
10 ⁻⁵ /sec	483±139	244±30	0.496±0.141
10 ⁻³ /sec	1423±242	--	--

* 17 of 38 10⁻³/sec tests at -5°C (45%) failed in a ductile manner and went to 5% strain.

Table 9: Average uniaxial compression strength, σ_m , and residual strength (5% strain), σ_e , data from Production Run 1. Standard deviations also given.

Figure 4: Comparison of uniaxial compressive strength data of sea ice obtained from first-year ice sheets, multi-year floes, and multi-year pressure ridges. The first-year sea ice data (-14°F) is from Wang (1979) and the data at -15°F are multi-year ice values obtained by Frederking and Timco (1980).



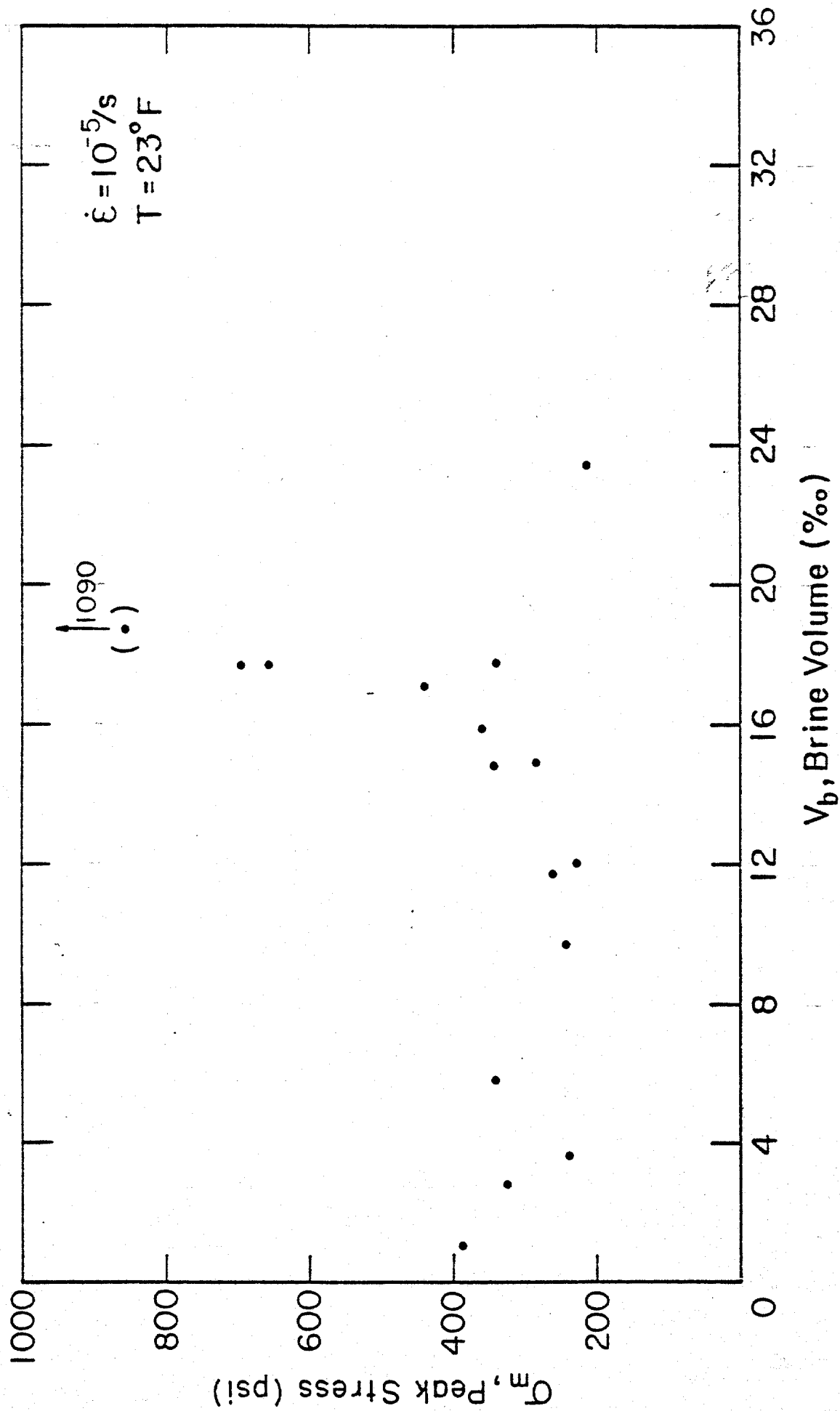


Figure 5: Unconfined compressive strength, or peak stress, versus brine volume for the $10^{-5}/\text{sec}$, $23^{\circ}F$ tests.

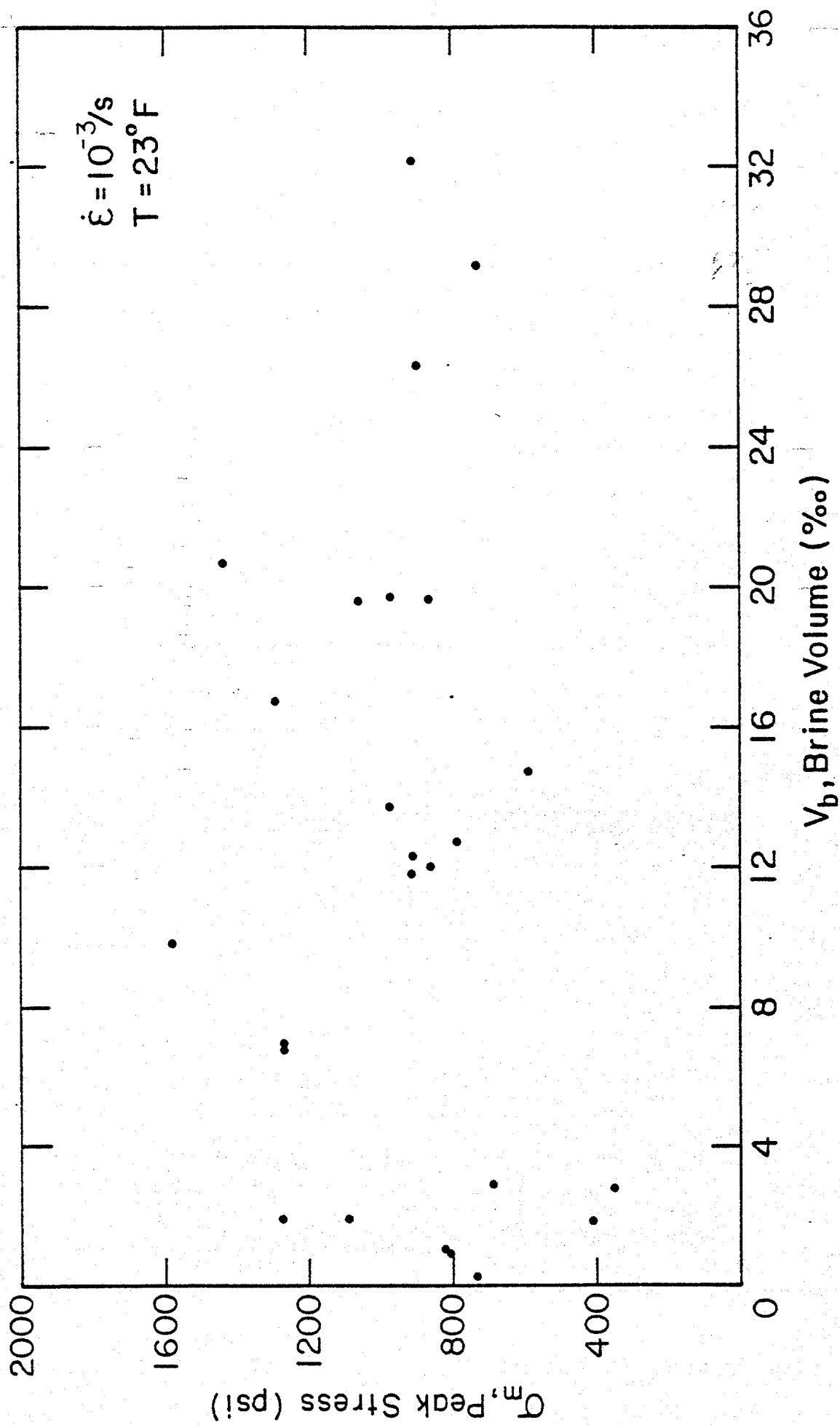
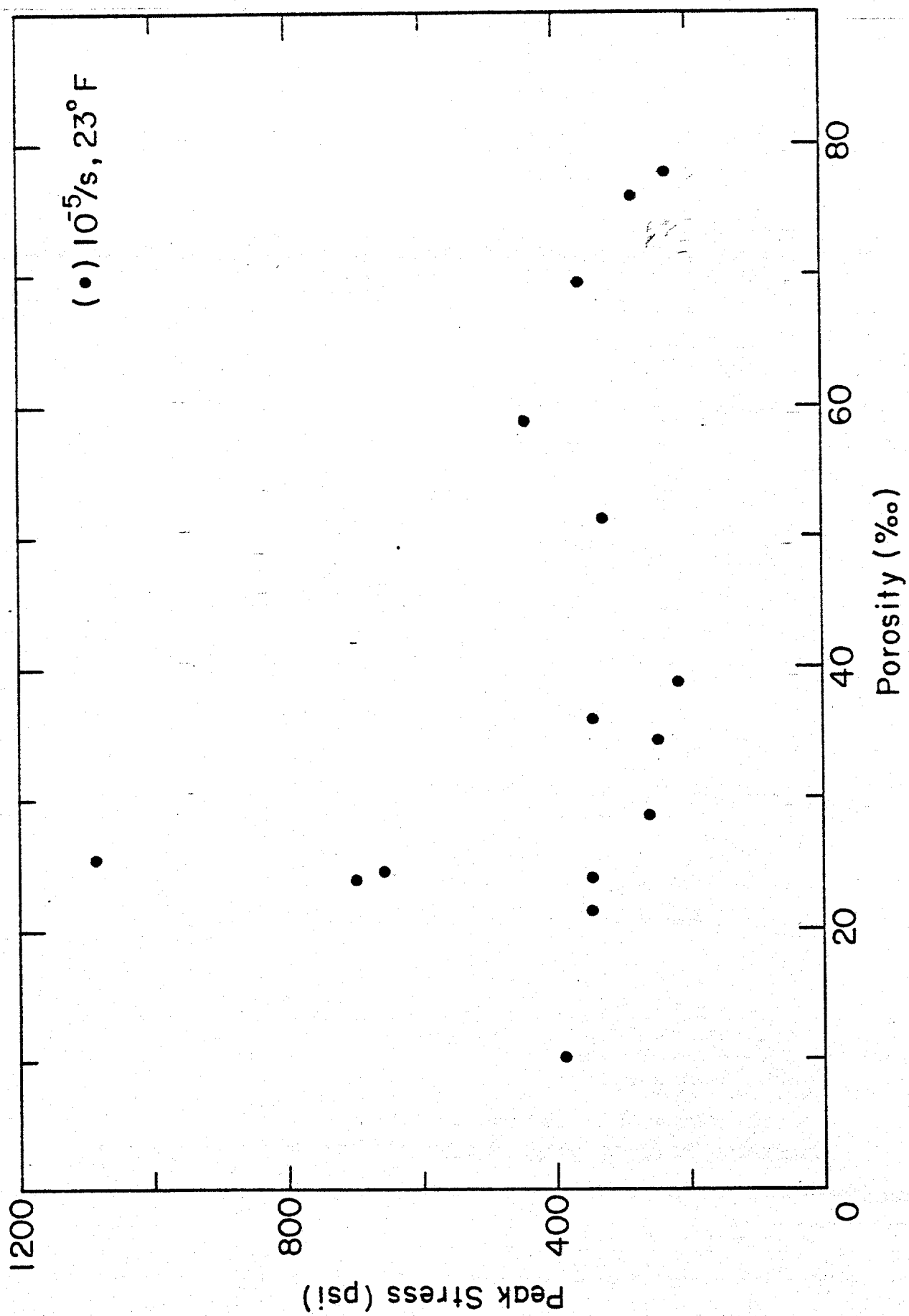


Figure 6: Unconfined compressive strength, or peak stress, versus brine volume for the $10^{-3}/\text{sec}$, $23^\circ F$ tests.

Figure 7: Unconfined compressive strength, or peak stress, versus porosity for the 10^{-5} /sec, 23°F tests.



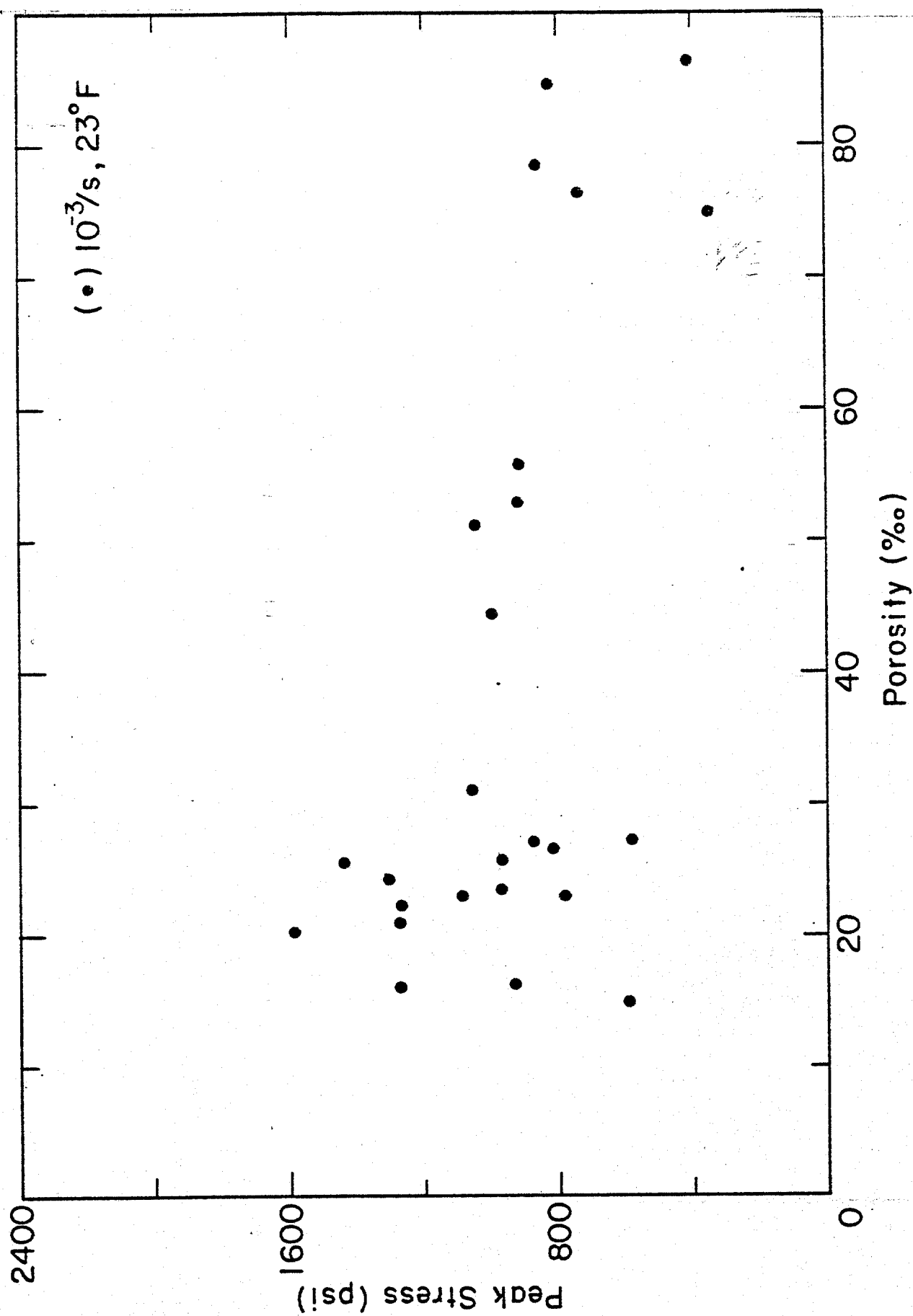


Figure 8: Unconfined compressive strength, or peak stress, versus porosity for the $10^{-3}/s$, $23^{\circ}F$ tests.

Residual Compressive Strength

Table 9 also gives the average residual compressive strength of the multi-year ridge ice samples under different loading conditions. The residual strength is defined here as the stress on the sample at 5% strain. A constant 4-inch diameter specimen is assumed in calculating the stress.

All of the tests conducted a strain-rate of 10^{-5} /sec continued to 5% strain. It is interesting to note that 17 of 38 tests conducted at 10^{-3} /sec at 23°F also continued to 5% strain whereas the 10^{-3} /sec tests at -4°F ruptured completely at very small strains. More tests at different strain-rates will be needed to define the ductile-brittle transition at each temperature of interest.

At a strain-rate of 10^{-5} /sec the residual strength of the ice is quite high: about two-thirds of the peak stress at 23°F and one-half of the peak stress at -4°F. For those tests which continued to 5% strain at 10^{-3} /sec and 23°F, the residual strength is about one-fifth of the peak stress. Further work on the non-simultaneous loading of wide structures may show that the residual strength is an important design parameter at low ice movement rates.

Failure Strains

Average sample failure strains, ϵ_m , at the peak or maximum stress for different test conditions are given in Table 10. The average strain to failure is found to decrease with increasing strain-rate and, for the 10^{-5} /sec tests, the average failure strain decreases as the temperature decreases. We would also expect to see a decrease in the average failure

SUMMARY OF FAILURE STRAIN DATA

<u>23°F (-5°C)</u>	<u>Average Failure Strain, $\bar{\epsilon}_m$ (%)</u>
10^{-5} /sec	0.34±0.14
10^{-3} /sec	0.13±0.03
<u>-4°F (-20°C)</u>	
10^{-5} /sec	0.21±0.03
10^{-3} /sec	0.13±0.03

Table 10: Mean and standard deviation of failure strain values, ϵ_m , under different test conditions.

strain with decreasing temperature in the 10^{-3} /sec tests; however, it is possible that the number of samples tested at 10^{-3} /sec and -4°F is insufficient to establish this trend.

Initial Tangent Modulus

The apparent initial tangent modulus of our test specimens is plotted against strain-rate in Figures 9 and 10. The modulus values were determined from the initial slope of the force-displacement curves obtained on the X-Y plotter. In those tests where seating of the actuator on the sample was a slight problem, the linear portion of the force-displacement curve immediately after seating was used to determine the modulus.

Figure 9 contains the results from those tests conducted at 23°F and Figure 10 presents the results from those tests conducted at -4°F . Average modulus values are given in Table 11 and plotted against strain-rate in Figure 11. The results show that the initial tangent modulus of sea ice obtained from multi-year pressure ridges increases with strain-rate and decreases with temperature. Similar observations have been made by Traetteberg and others (1975) for fresh water columnar and granular ice. In fact, for a given temperature and strain-rate, our values are in close agreement to those obtained by Traetteberg and others (1975). Our 10^{-3} /sec results are also comparable to dynamic, seismic determinations of Young's modulus (Schwarz and Weeks, 1975).

Previous investigators have reported that Young's modulus of sea ice decreases with increasing brine volume (Schwarz and Weeks, 1975). Young's modulus for a number of our tests is plotted against brine volume in Figures 12 and 13. In both the 10^{-5} /sec and 10^{-3} /sec tests there does not

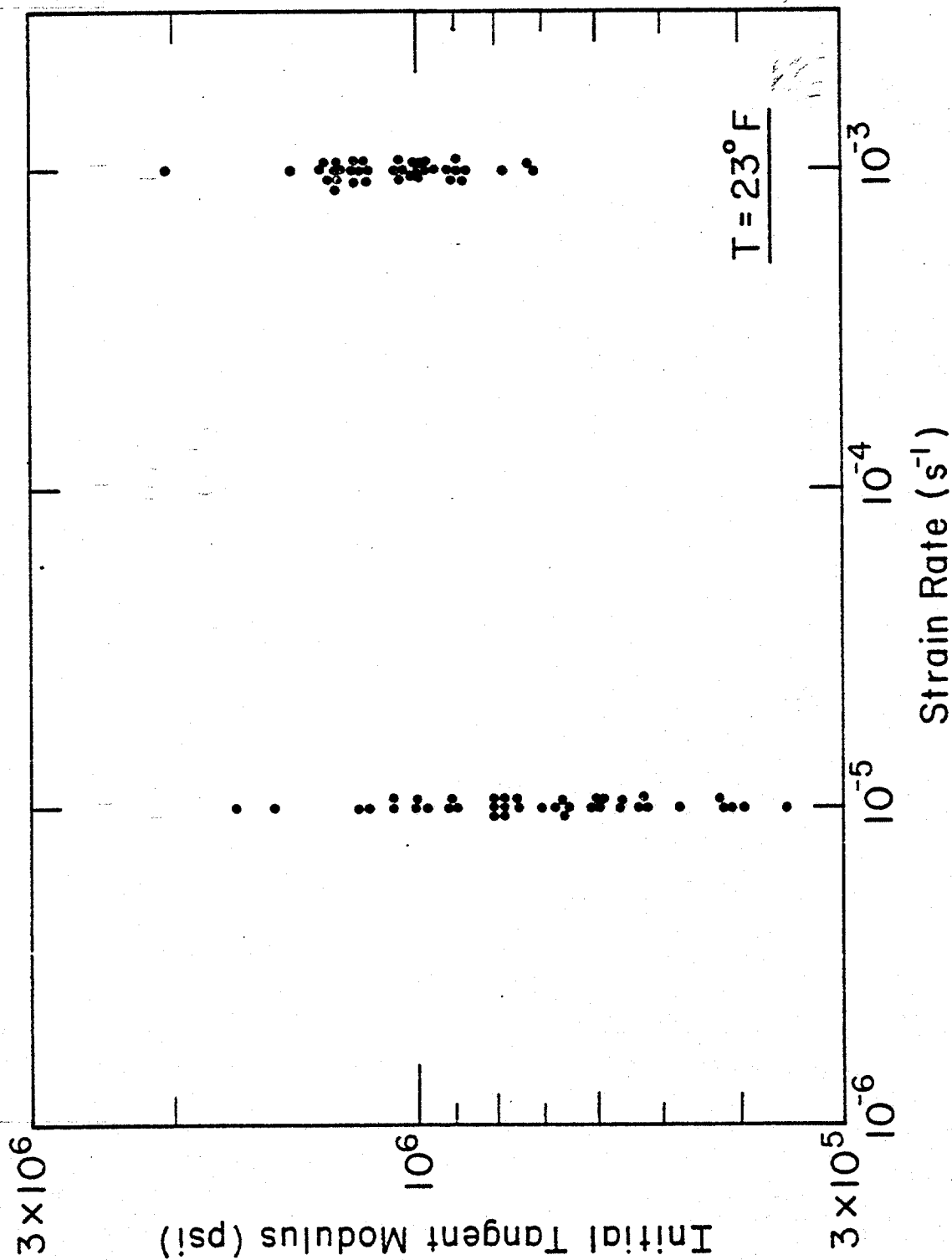


Figure 9: Initial tangent modulus versus strain-rate for the 23°F tests.

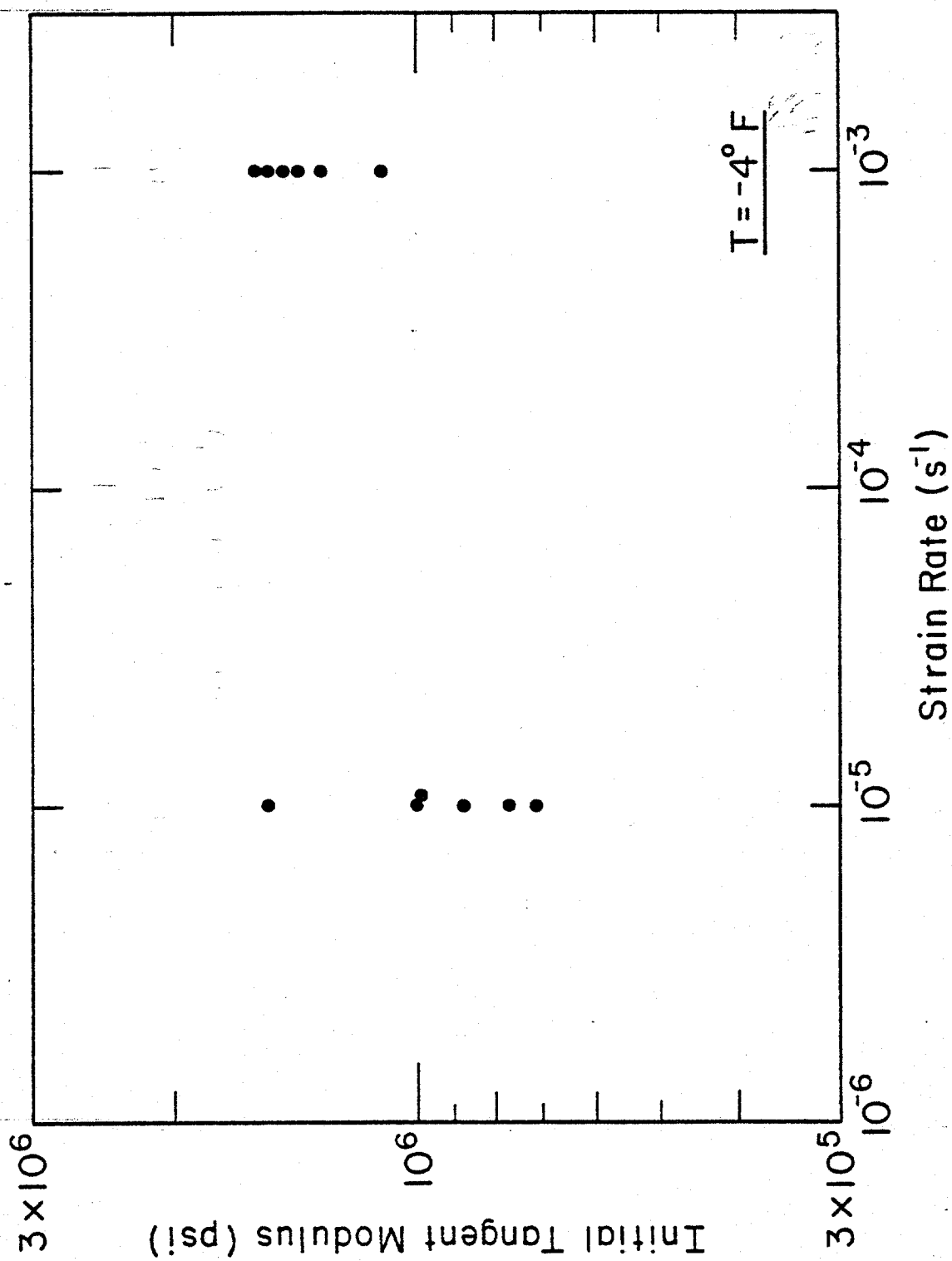


Figure 10: Initial tangent modulus versus strain-rate for the -4°F tests.

SUMMARY OF INITIAL TANGENT MODULUS DATA

<u>23°F (-5°C)</u>	<u>Average Initial Tangent Modulus, $\overline{E_i}$ (psi)</u>
$10^{-5}/\text{sec}$	$7.64 \times 10^5 \pm 2.88 \times 10^5$
$10^{-3}/\text{sec}$	$1.09 \times 10^6 \pm 0.24 \times 10^6$
<u>-4°F (-20°C)</u>	
$10^{-5}/\text{sec}$	$9.78 \times 10^5 \pm 2.90 \times 10^5$
$10^{-3}/\text{sec}$	$1.39 \times 10^6 \pm 0.17 \times 10^6$

Table 11: Average and standard deviation of initial tangent modulus data from Production Run 1.

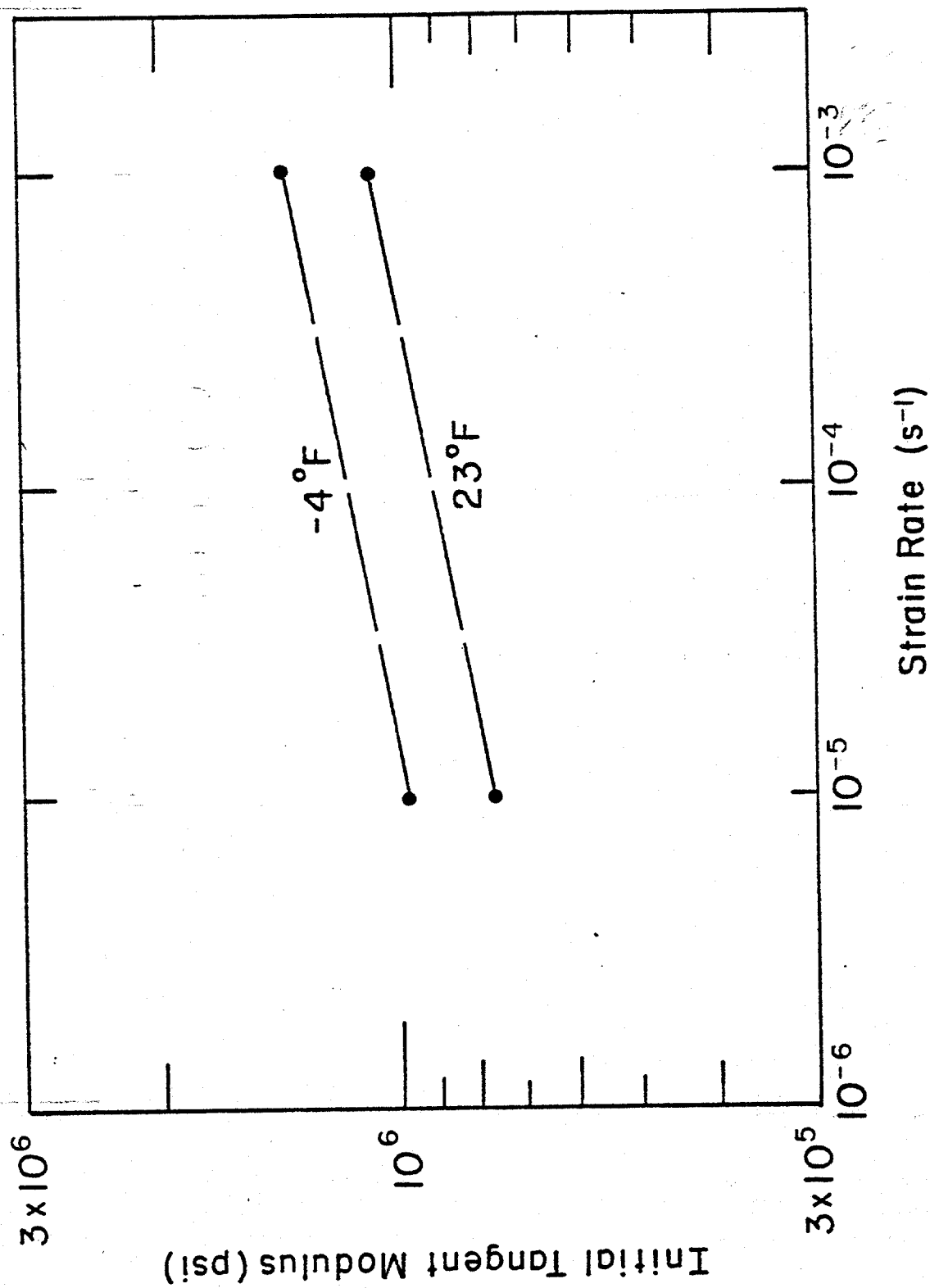


Figure 11: Average initial tangent modulus versus strain rate for the 23°F and 4°F tests.

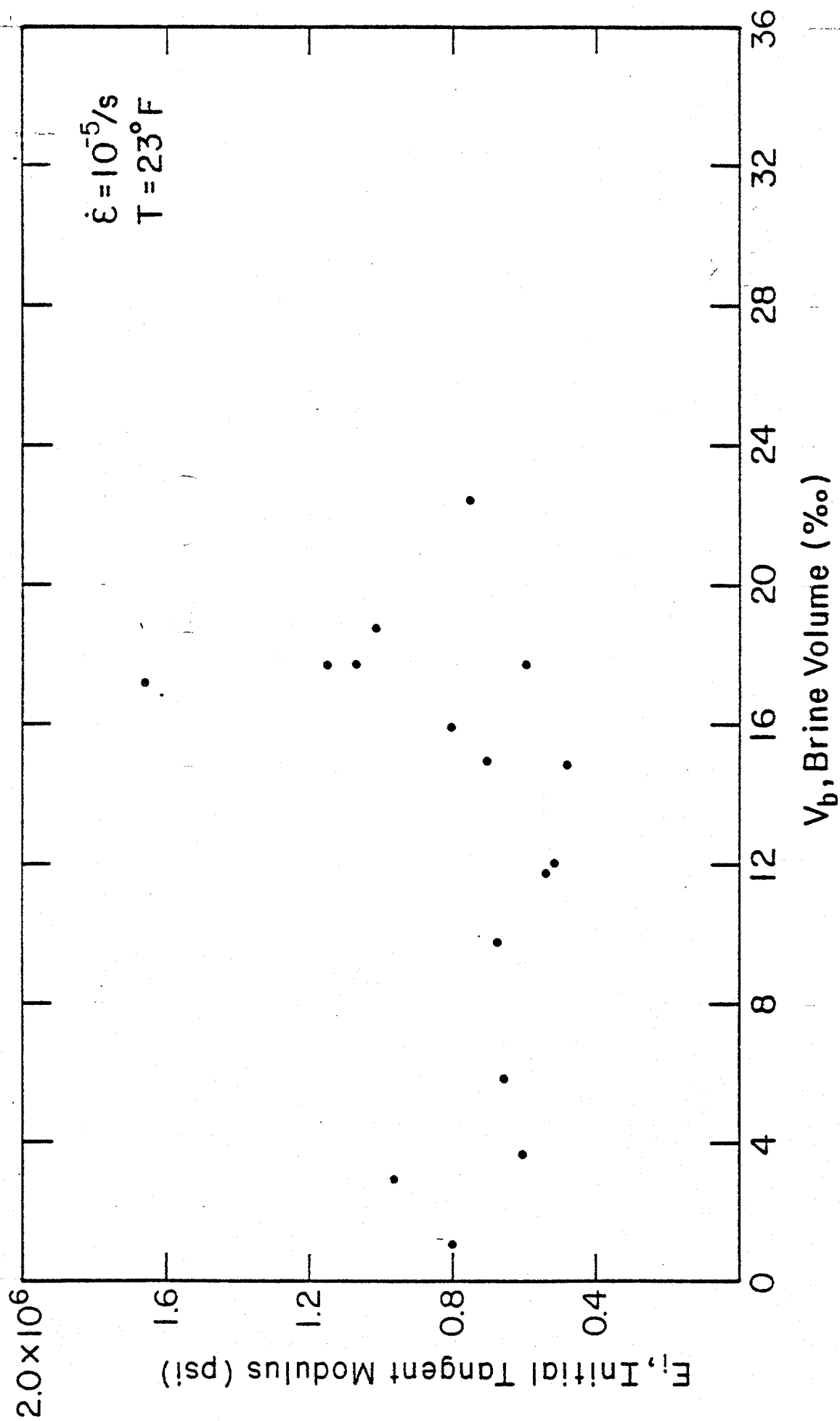


Figure 12: Young's modulus versus brine volume for the $10^{-5}/\text{sec}$, $23^\circ F$ tests.

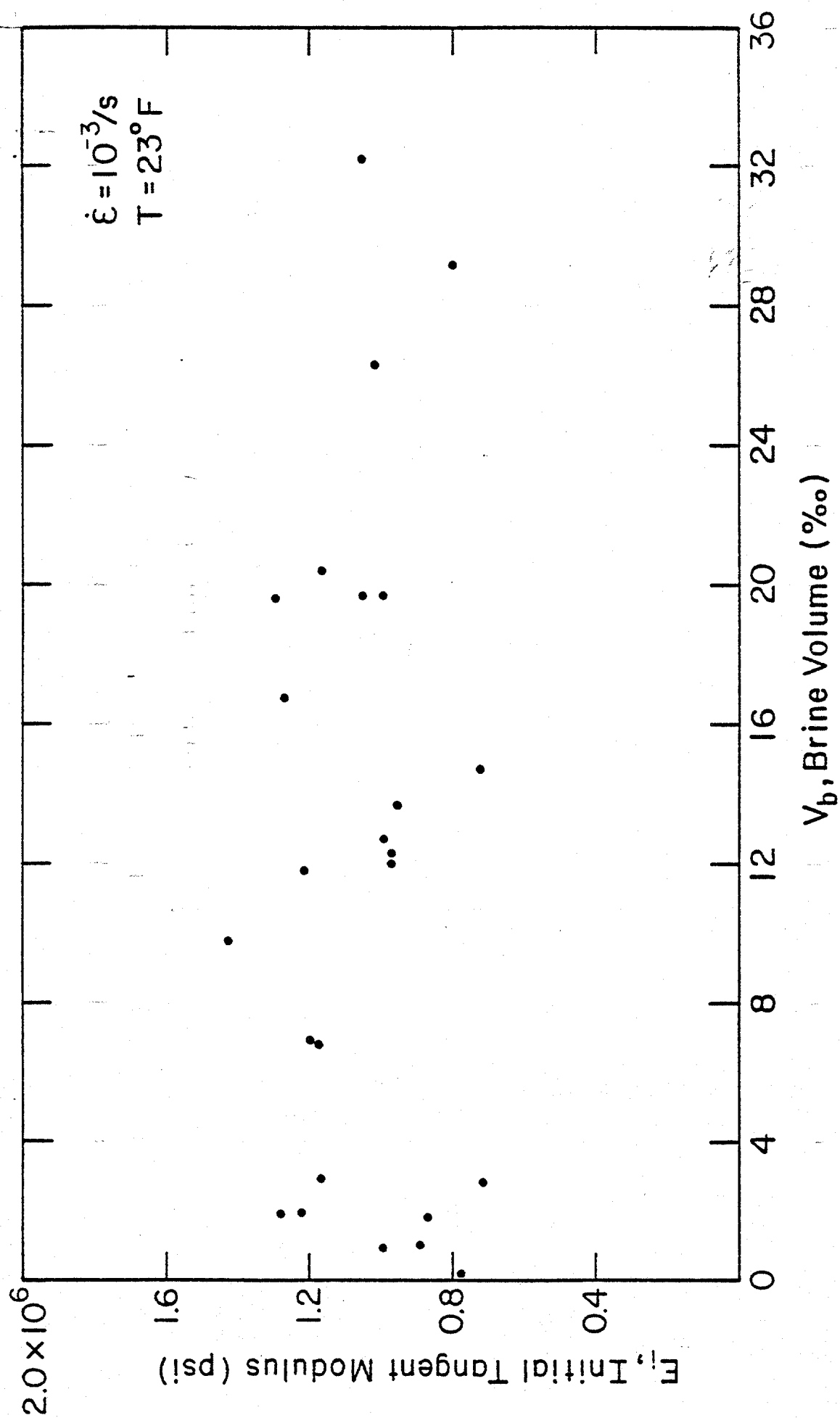


Figure 13: Young's modulus versus brine volume for the $10^{-3}/\text{sec}$, $23^\circ F$ tests.

appear to be any relation between the modulus and brine volume. However, our samples do have a relatively high air content. The Young's modulus is therefore plotted against porosity (brine plus air volume) in Figures 14 and 15 for the 10^{-5} /sec and 10^{-3} /sec tests, respectively. Again, the 10^{-5} /sec strain-rate tests show no relationship between modulus and porosity; but, the 10^{-3} /sec tests do show a slight decrease in modulus with increasing porosity. We expect that structural defects, such as cracks and cavities, play a more important role at high strain-rates where the ice exhibits elastic behaviour.

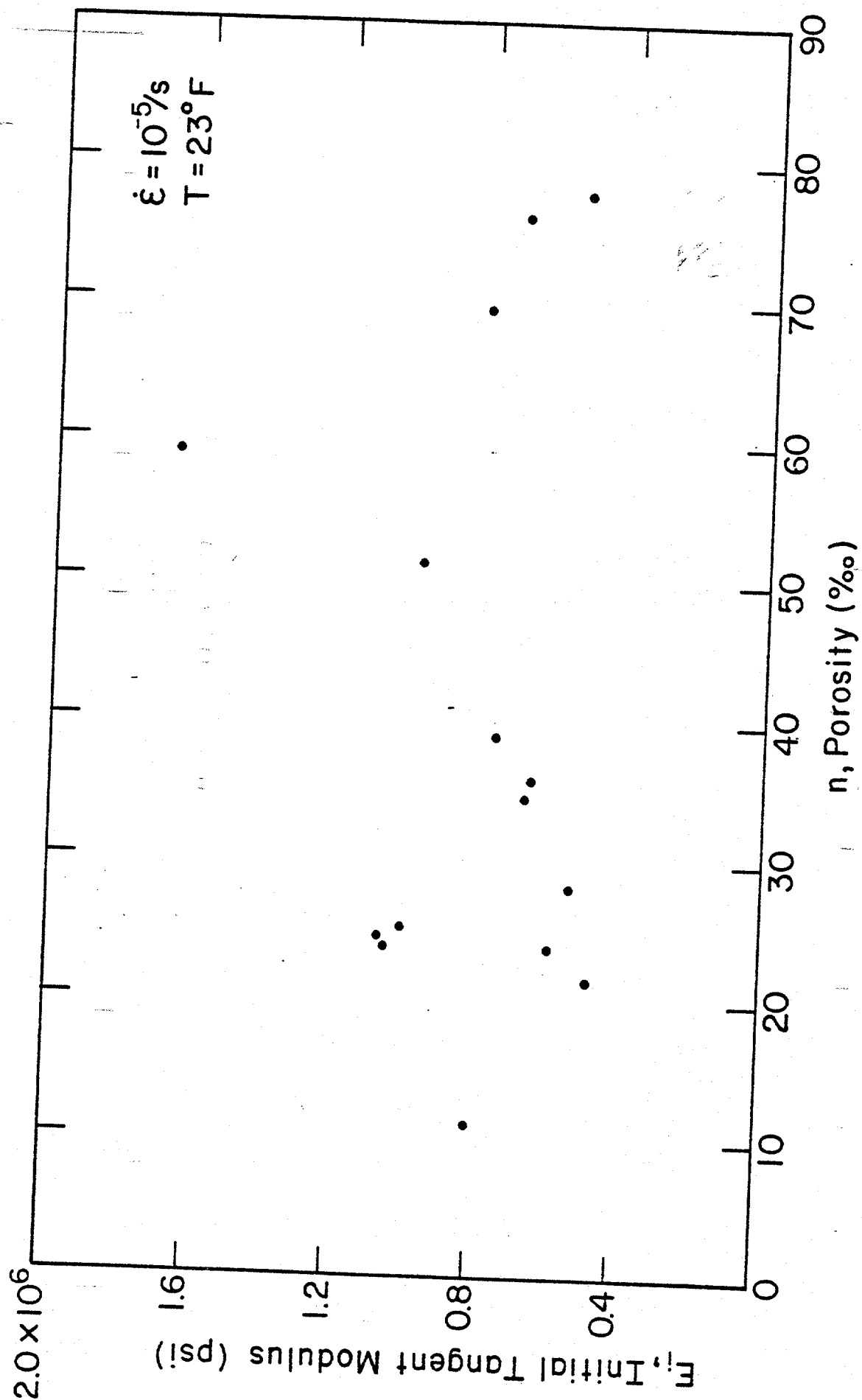
In addition to the ice porosity, we would expect that the modulus of the ice should also vary with density. The modulus of the ice is plotted against density in Figures 16 and 17. Both the 10^{-5} /sec and 10^{-3} /sec tests do show a slight increase in modulus with increasing density; however, the amount of scatter is too large to draw any definite conclusions.

ICE STRUCTURE ANALYSES

There are a number of variables that strongly affect the strength of sea ice. These include the salinity, temperature, porosity, and structure of the ice and the test strain-rate. If we look at the test results at a given strain-rate, temperature, and porosity (Figures 7 and 8), we still observe considerable scatter in the data. We attribute this scatter to large variations in the ice structure.

To analyze the structure of the test specimens, discs of ice are first cut from both ends of the sample prior to testing. If the samples were homogeneous throughout their length, thin sections from the sample end-planes would be sufficient to characterize the ice structure. Unfortu-

Figure 14: Young's modulus versus porosity for the $10^{-5}/\text{sec}$, 23°F tests.



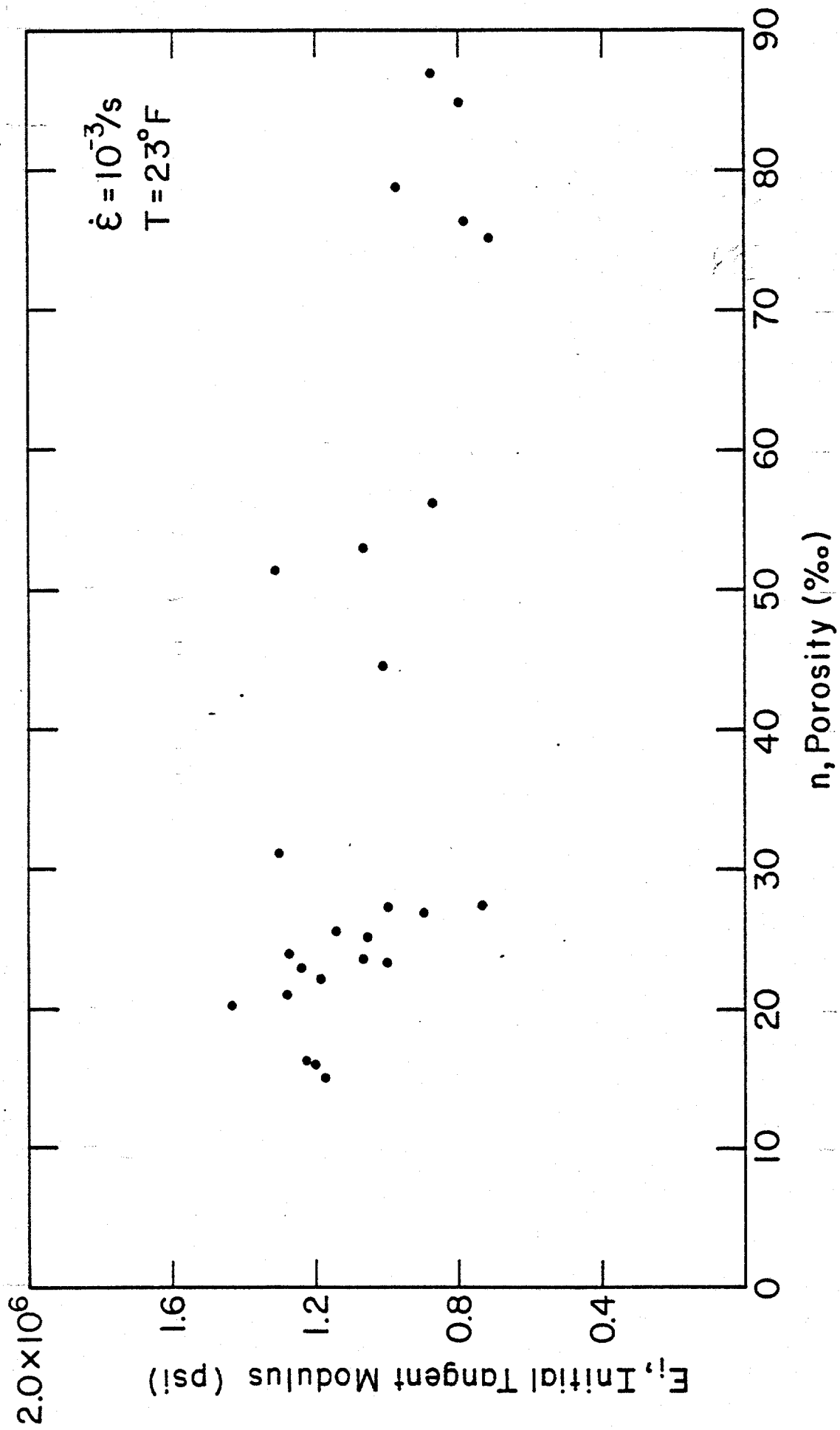


Figure 15: Young's modulus versus porosity for the $10^{-3}/\text{sec}$, $23^\circ F$ tests.

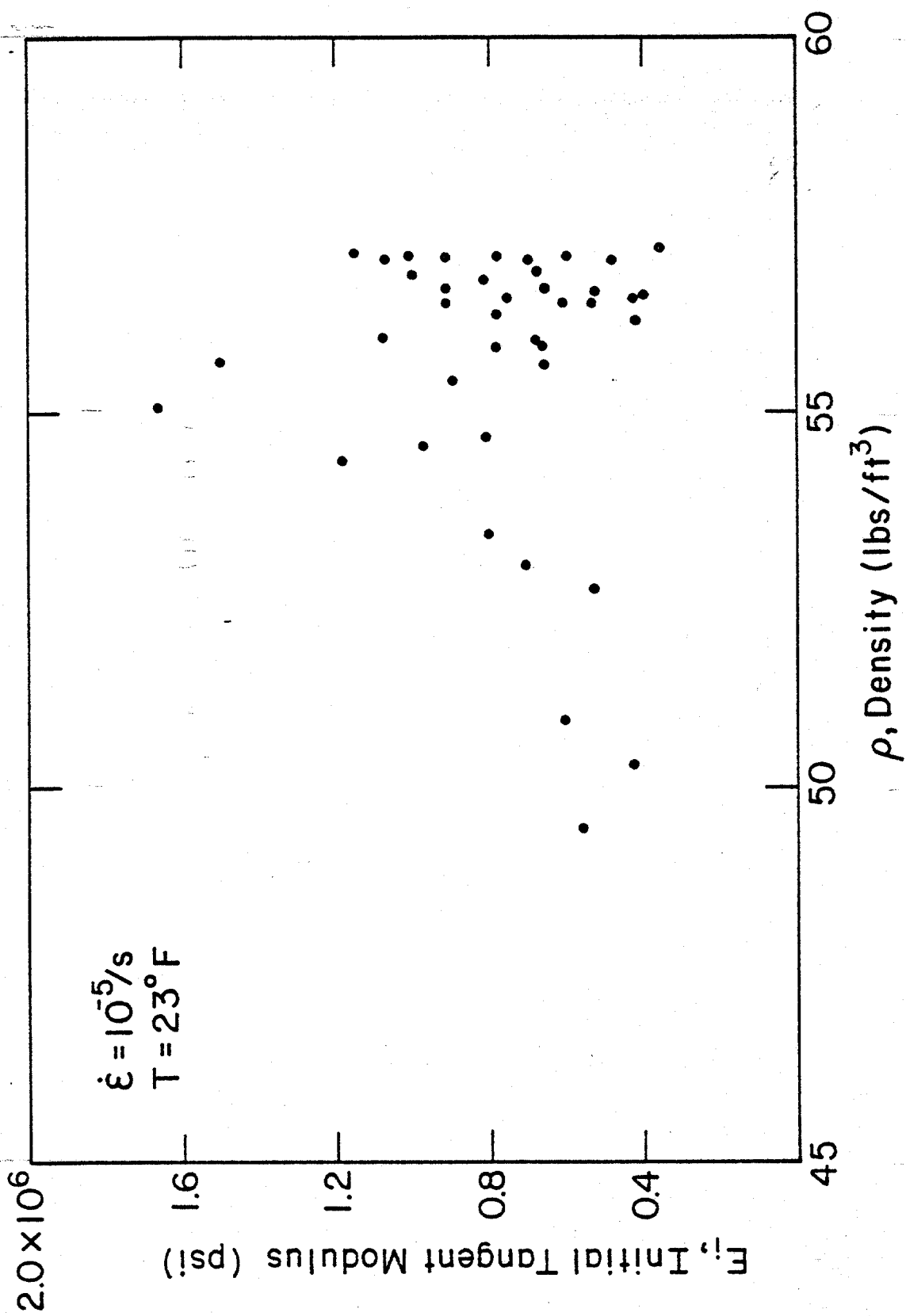


Figure 16: Young's modulus versus density for the $10^{-5}/\text{sec}$, $23^{\circ}F$ tests.

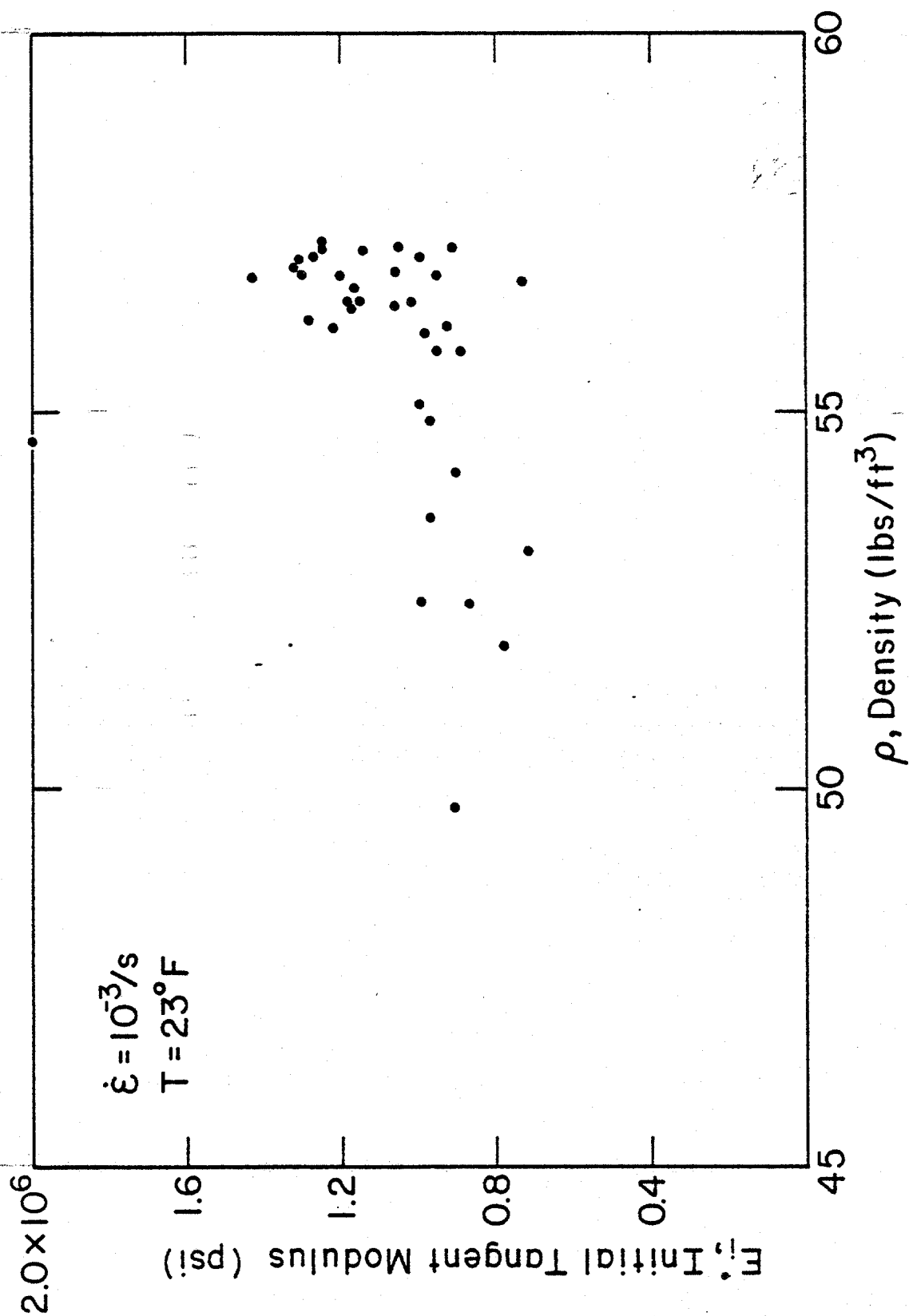


Figure 17: Young's modulus versus density for the $10^{-3}/s$, 23°F tests.

nately, many of the multiyear ridge sea ice samples appear to be inhomogeneous consisting of both columnar and granular crystals of varying grains size and orientation. Thus, in addition to studying the structure of the sample end-planes, it is also necessary to look at the structure of the failed specimen to properly describe the entire samples. This is accomplished by cutting vertical thick sections of the failed samples. It has been found that thick sections cut on a bandsaw, with no microtoming, are adequate to observe the ice structure.

At the conclusion of Production Run 1 we began to look at the ice structure from a representative number of high, medium, and low strength samples. Since we were interested in obtaining information on the sample salinity to determine its porosity, we concentrated on preparing vertical thick sections of the failed specimens. Besides obtaining the sample salinity, it was hoped that the vertical sections would be sufficient for providing a preliminary description of the structure of each sample.

To date we have looked at 28 samples. It is now apparent that vertical sections of the failed samples by themselves do not provide a clear picture of the original sample structure. It turns out that we do not know well enough the structure of untested multi-year ridge ice. Often it is difficult to differentiate between snow and slush ice and granular ice produced by sample shear.

In an effort to address these structure interpretation problems, we are now preparing horizontal and vertical sections of the continuous multi-year ridge core that was specifically obtained for structure and

salinity analyses. After the sections from this core have been analyzed we hope that we will be in a better position to interpret the structure of the test specimens. Data on ice structure from samples in Production Run 1 will be included in the next progress report.

STATISTICAL VARIATIONS IN ICE STRENGTH

Differences in the Above- and Below-Sea Level Yield Strengths

The above-sea level ice in pressure ridges is of lower salinity and presumably lower density due to a higher gas volume than the below-sea level ice. During most of the year it is also stronger as it is appreciably colder than the below-sea level ice. The strength data discussed in this report now make it possible to ask the question of whether there are intrinsic differences in the strengths at these two different levels above and beyond that resulting from the temperature differences.

There are, at present, two sets of data which can be tested for differences; the $\dot{\epsilon} = 10^{-3}$ and the $\dot{\epsilon} = 10^{-5}$ sets. Both test sets were determined at $T_i = -5^\circ\text{C}$. Each of these sets can then be sub-divided into above-sea level and below-sea level portions. These sub-sets can then be tested to see if there is reason to doubt the hypothesis that the above and below-sea level ice have the same population means (i.e. $H_0: \mu_a = \mu_u$ where μ is the population mean and the subscripts a and b indicate above and below sea level). These results are summarized in Table 12. At both strain rates it was found, using 2-tailed t-test that there was no reason at the 1% level to doubt that both the above-sea level and the below-sea level ice have the same population means. The physical interpretation of this result is presumably that in the above-sea level ice the decrease in

Table 12 . Statistical characteristics of the σ_m values for the above-sea level and the below-sea level ice. The test temperature is -50°C .

Set 1 Strain rate $\dot{\epsilon} = 10^{-5}$, uniaxial compression		
a) Above sea level $\bar{X}_a = 362.9$ $n = 14$ $s = 159.3$	b) below sea level $\bar{X}_b = 374.0$ $n = 25$ $s = 205.6$	
$\bar{X}_2 - \bar{X}_1 = 11.1$, $t = 0.17$ \therefore Accept $H_0: \mu_a = \mu_b$		
$t_{.025(37)} = 2.02$ $t_{.005(37)} = 2.70$		
c) all levels combined $\bar{X} = 370.1$ $s^2 = 35419$ $n = 39$ $s = 188.2$		
Set 2 Strain rate $\dot{\epsilon} = 10^{-3}$, uniaxial compression		
a) above sea level $\bar{X}_a = 866.6$ $n = 14$ $s = 302.9$	b) below sea level $\bar{X}_b = 972.0$ $n = 24$ $s = 290.0$	
$\bar{X}_2 - \bar{X}_1 = 105.3$, $t = 1.06$ \therefore Accept $H_0: \mu_a = \mu_b$		
$t_{.025(36)} = 2.03$ $t_{.005(36)} = 2.72$		
c) All levels combined $\bar{X} = 886.5$ $s^2 = 87016$ $n = 38$ $s = 295.0$		

salinity and increase in air content (relative to the below-sea level ice) tend to offset each other. This is an important result since we now have justification for combining both the above- and the below-sea level strength values into one population in succeeding analyses.

Sources of the Variation in the Yield Strengths

We initially planned to obtain test samples from exactly the same levels in co-located cores collected from each individual ridge. Because of problems with gouging on the sides of the cores and core breaks, this did not prove to be possible. Instead, samples from each core were chosen randomly in a vertical sense.

It is then possible to study the sources of the observed variation in yield strengths obtained under similar test conditions by using a 3 level tested Analysis of Variance (AOV) model. Using this model the total sample variance is partitioned into that contributed by differences

- a) between ridges,
- b) between cores co-located side by side on a given ridge, and
- c) between samples from the same core.

The linear AOV model assumed is

$$x_{ijk} = \mu + v_i + y_{ij} + z_{ijk}$$

with $i = 1 \dots r$

$j = 1 \dots t$ and

$k = 1 \dots n$

Here μ is the grand mean, v_i corresponds to the ridge effect, y_{ij} to the effect of co-located cores within the same ridge, and z_{ijk} to the

effect of samples within the same core. The parameters v_i , y_{ij} , and z_{ijk} are assumed to be independently normally distributed with zero means and variances ψ^2 , ω^2 and σ^2 . In our specific application $r = 7$, $t = 2$ and $n = 3$. Table 13 gives the AOV analysis for the above model. The results of the analysis for the $\epsilon = 10^{-3}$ and 10^{-5} data sets are given in Table 14 and show that in all cases there is at present no reason to doubt the hypothesis that ω^2 and ψ^2 are equal to zero (i.e. that there are no significant differences between ridges or between cores within ridges relative to the large variation observed between samples within the same core). If this is true this is a very important conclusion. However we prefer to reserve judgement on this matter until we have completed testing the remainder of the specimens. At that time we will also include a discussion of the problems associated with the fact that at some sites there are missing yield strength values.

The above tentative result does not mean that we believe that all multiyear pressure ridges have the same strength. As a first-year ridge gradually changes into a multiyear ridge over a period of at least 2 years (by definition multiyear ice has survived two or more summers), the voids in the ridge are slowly sealed with ice, increasing the overall strength of the ridge. In contrast, one of the ridges we sampled (Ridge 6) contained a large number of voids. The overall quality of the ice was also poor and resulted in limited core recovery. Perhaps this result should have been expected since the upper part of Ridge 6 still showed the semi-rounded outlines of ice blocks suggesting that we were sampling a 2 year old ridge. After this experience we always selected ridges that showed highly rounded

Table 13. Analysis for a 3-level nested AOV model.

Source of Variance	Sums of Squares	Degrees of Freedom	Mean Squares	E[Mean Squares]
Between Ridges	$nt \sum_i (\bar{x}_{i..} - \bar{x}_{...})^2$	$r-1$	s_r^2	$\sigma^2 + n\omega^2 + nt\psi^2$
Between co-located cores within ridges	$n \sum_j \sum_i (\bar{x}_{ij.} - \bar{x}_{j..})^2$	$r(t-1)$	s_t^2	$\sigma^2 + n\omega^2$
Between samples within co-located cores	$rtn \sum_{ijk} (x_{ijk} - \bar{x}_{ij.})^2$	$rt(n-1)$	s_n^2	σ^2
TOTAL	$rtn \sum_{ijk} (x_{ijk} - \bar{x}_{...})^2$	$rtn-1$		

TABLE 14. Results of 3-level nested AOV analysis of the variation in maximum yield strengths σ_m .

Source of Variance	Sum of Squares	d.f.	Mean Squares	Expected Mean Squares
A. $\dot{\epsilon} = 10^{-5}$				
Between ridges	271909	6	45318	$\sigma^2 + 3\omega^2 + 6\psi^2$
Between cores within ridges	311432	7	44490	$\sigma^2 + 3\omega^2$
Between samples within cores	784781	28	28028	σ^2
$H_0: \omega^2 = 0$	$F = 1.59$	$F_{.99}(7, 28) = 3.36$		
$H_0: \psi^2 = 0$	$F = 1.02$	$F_{.99}(6, 7) = 7.19$		
$\hat{\sigma}^2 = 28028$	$\hat{\omega}^2 = 5487$	$\hat{\psi}^2 = 1138$		
$\hat{\sigma} = 167$	$\hat{\omega} = 74$	$\hat{\psi} = 11.7$		
B. $\dot{\epsilon} = 10^{-3}$				
Between ridges	882609	6	147102	$\sigma^2 + 3\omega^2 + 6\psi^2$
Between cores within ridges	307388	7	43913	$\sigma^2 + 3\omega^2$
Between samples within cores	2315585	28	82699	σ^2
$H_0: \omega^2 = 0$	$F = 0.53$	$F_{.99}(7, 28) = 3.36$		
$H_0: \psi^2 = 0$	$F = 3.35$	$F_{.99}(6, 7) = 7.19$		
$\hat{\sigma}^2 = 82699$	$\hat{\omega}^2 = (-) 12929$	$\hat{\psi}^2 = 17198$		
$\hat{\sigma} = 287$	$\hat{\omega} = 114$	$\hat{\psi} = 131$		

surface profiles suggesting ridges that were 3 or more years old. One conclusion that can definitely be drawn from the present results is that within such ridges there is a large variation in the yield strengths obtained on ice from the same core hole. Considering the processes that form pressure ridges, this result is hardly surprising.

If histograms are prepared of the frequency distributions of the yield strengths at $\dot{\epsilon} = 10^{-3}$ and 10^{-5} respectively, Figures 18 and 19 result. The samples, although too small as yet for definite conclusions, are interesting in that the higher strain rates (10^{-3}) give a reasonably symmetrical, uni-modal distribution while the lower strain rates (10^{-5}) give a distribution that although uni-modal, has a pronounced positive skew. More data will be collected before we attempt to explain the difference in these distributions.

Finally, strength profiles of each of the tested cores are given in Figure 20 for the 10^{-5} /sec and 10^{-3} /sec tests. It is evident that the variation in ice strength at each core site is quite high and comparable to the variation between the different sites.

Sample End Squareness and its Effects

Figure 21 shows a histogram giving the frequency of different squareness values for the alignment of the synthane end caps. As can be seen the modal value for squareness is in the 0.002-0.004 in. class interval and the great majority (85%) of the samples showed squarenesses of less than 0.010. Considering the difficulty in maintaining axiality while mounting the end caps, we feel that this performance is quite satisfactory. However since EXXON discarded test samples with squareness values of greater than

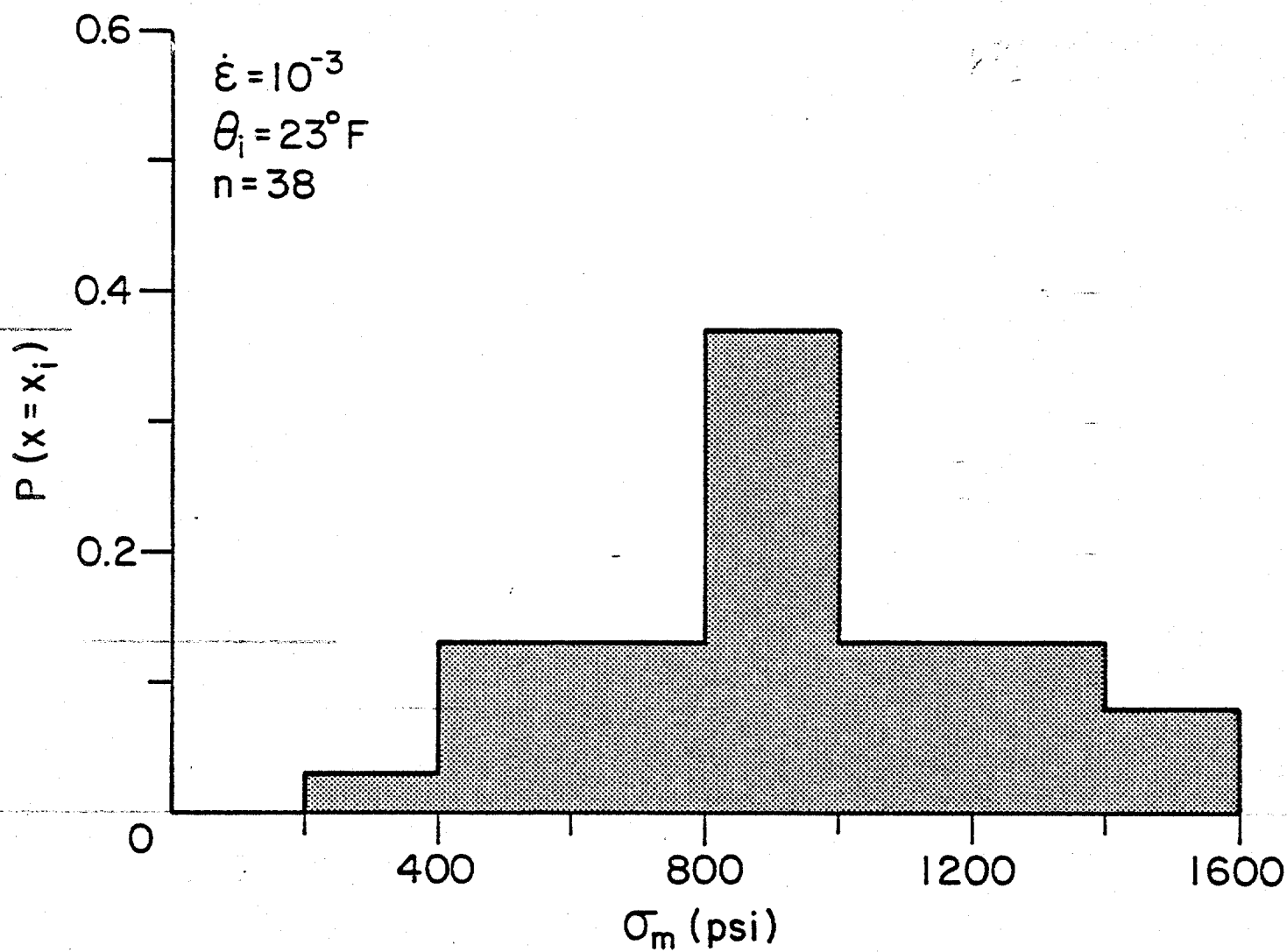


Figure 18: Histogram of the frequency distributions of yield strengths for the 10^{-3} , 23°F tests.

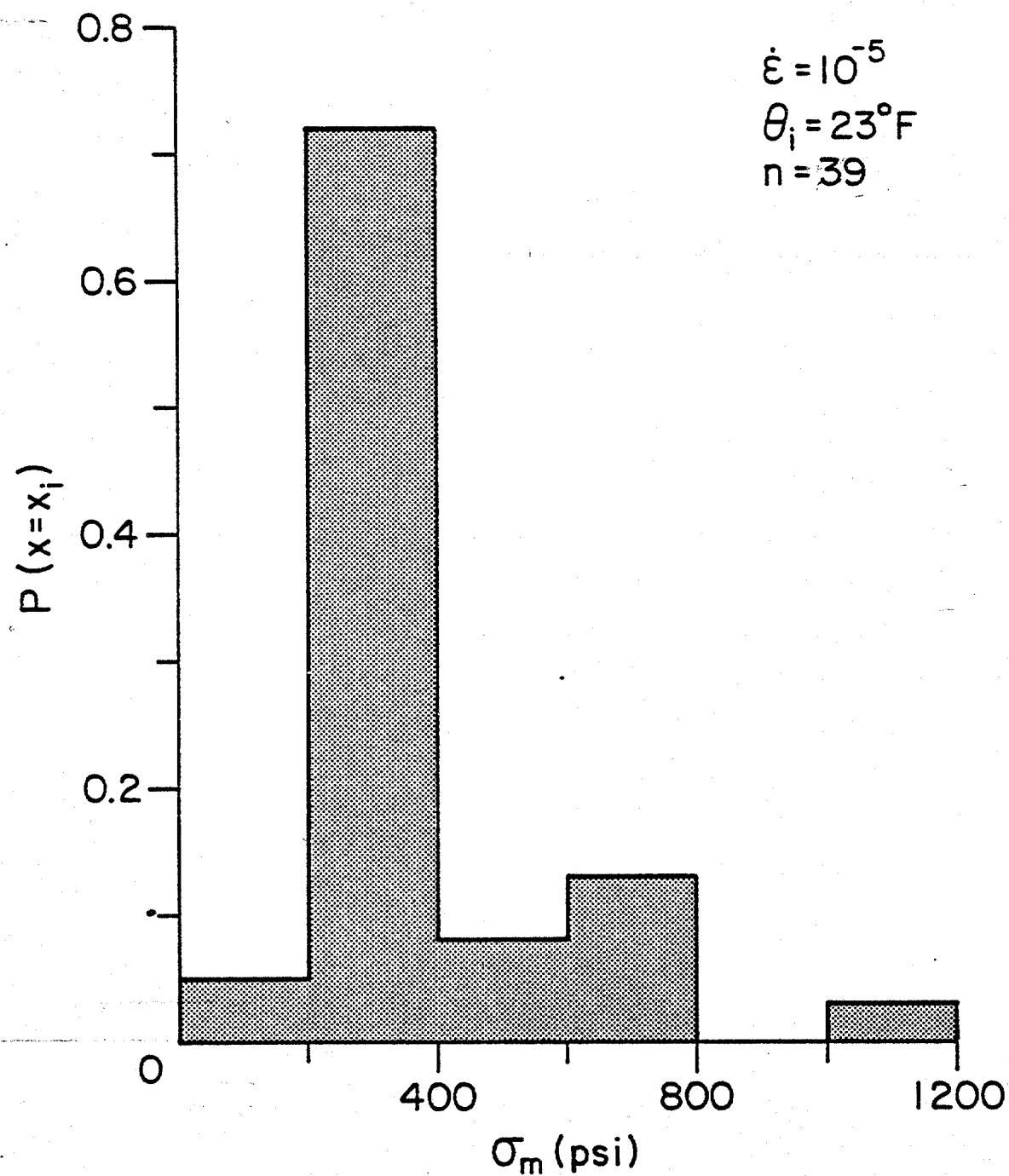


Figure 19: Histogram of the frequency distribution of yield strength for the 10^{-5} /sec, 23°F tests.

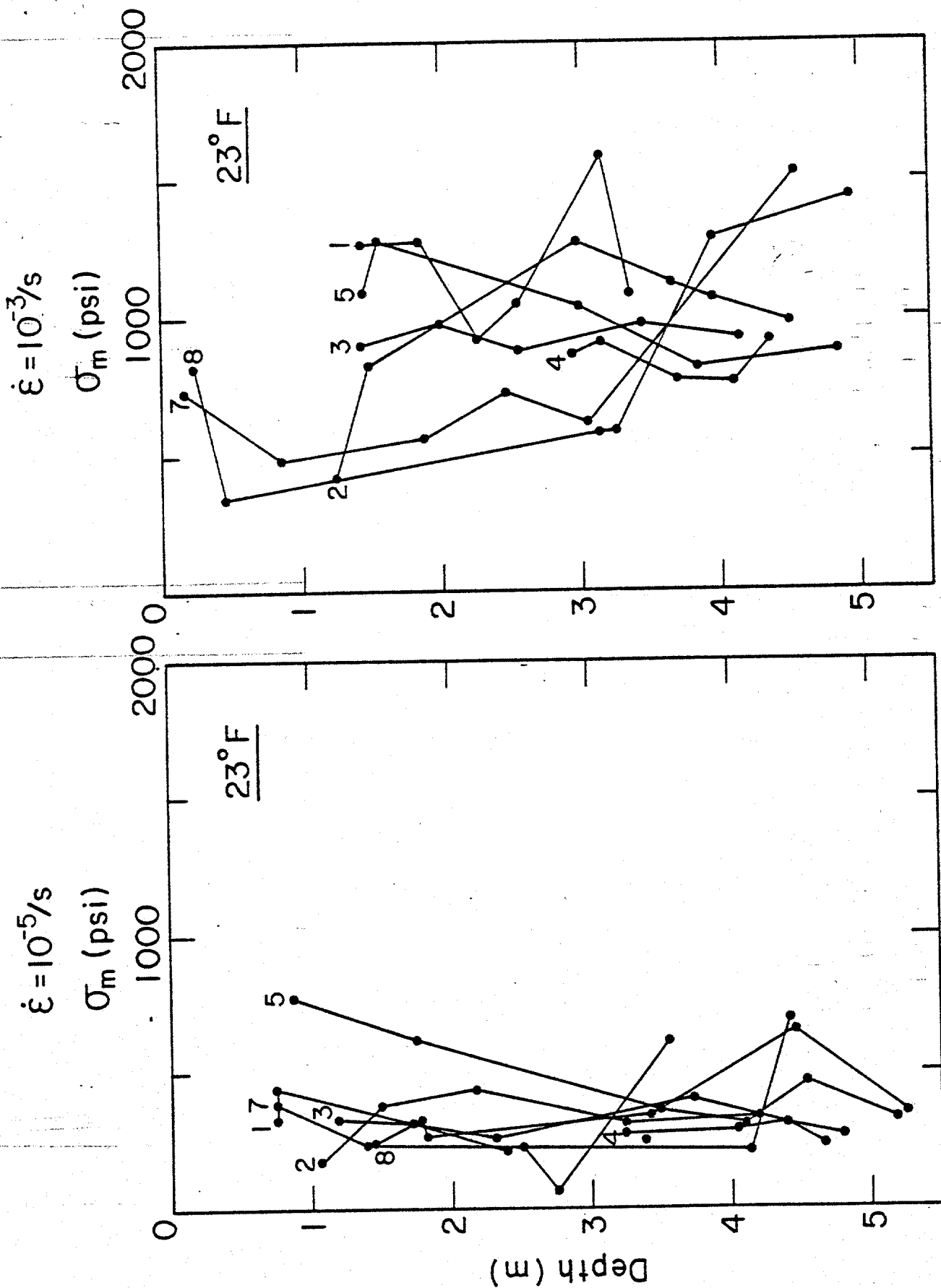


Figure 20: Plot of ice strength versus depth. The numbers at the top of each profile give the ridge number from which the samples were obtained.

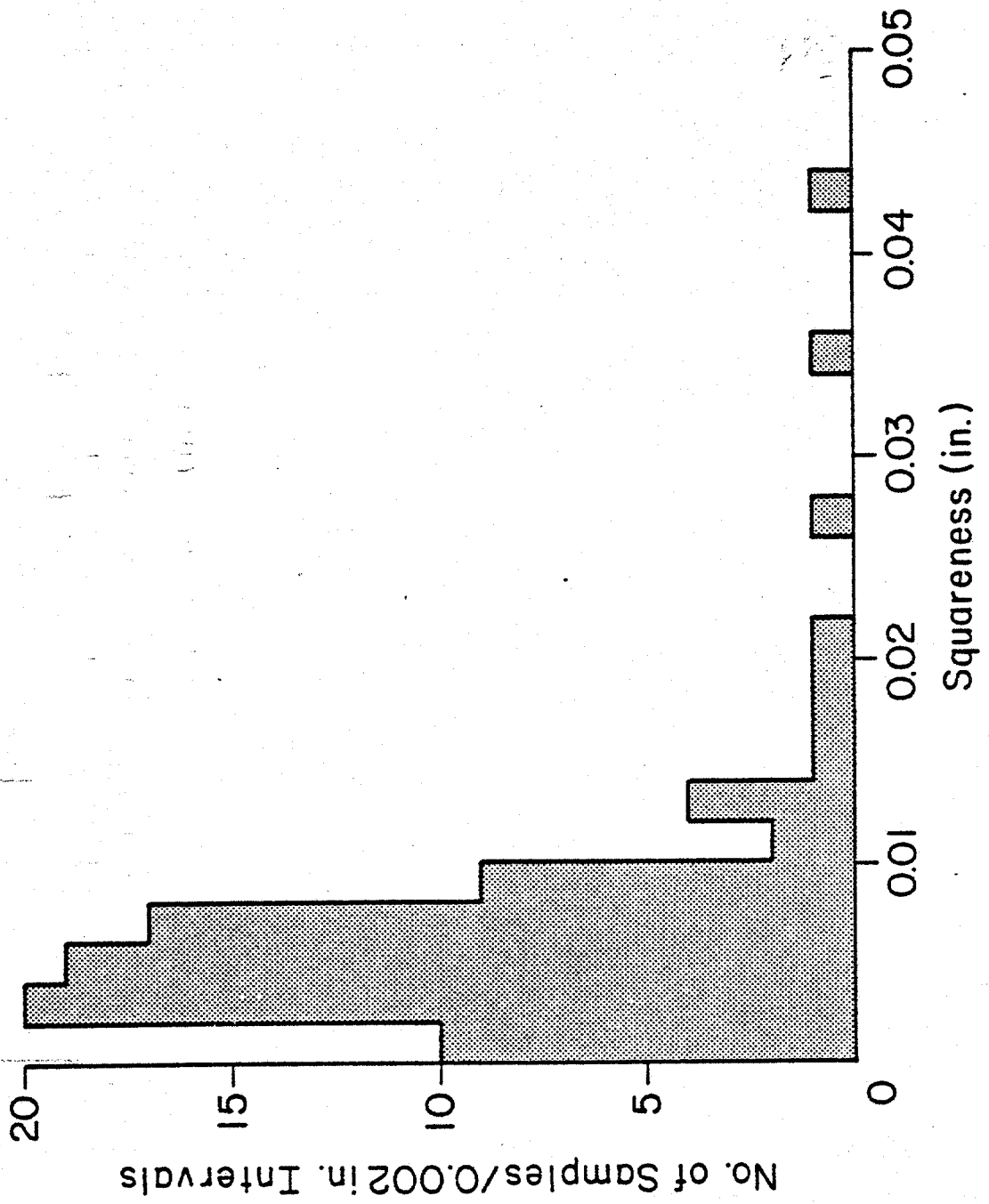


Figure 21: Histogram of sample squareness after end caps have been attached to ice sample.

0.005, it is interesting to see if, in our test series there is any evidence of a correlation between squareness and yield strength values for tests performed under identical conditions. Figures 22 and 23 show σ_m plotted against end cap squareness for $\dot{\epsilon} = 10^{-3}$ and 10^{-5} respectively (both sets of tests were performed at 23°F). Both plots show a significant scatter and no clear trends. In fact the respective correlation coefficients (ρ) are 0.19 ($\dot{\epsilon} = 10^{-3}$) and 0.08 ($\dot{\epsilon} = 10^{-5}$) indicating that linear regression lines would only account for 3.6% and 0.6% of the observed scatter. As the 95% confidence limits on the ρ estimates are ± 0.35 and ± 0.34 respectively there is clearly no reason to believe, at present, that the ρ values are significantly different from zero. Therefore, on the basis of our data we currently see no reason to reject tests on the basis of squareness. Shimming the low side of the sample on the MTS machine appears to be an effective means of correcting for any lack of sample squareness.

DEVELOPMENT OF TESTING TECHNIQUES

Uniaxial tension, constant load, and triaxial testing techniques still need to be developed in this year's study. Our progress on each of these three types of test is described below.

Uniaxial Tension Tests

Earlier in the study it was decided to bond endcaps to our specimens to provide radial constraint on the sample end-planes in compression and a means of applying a load to the core sample in tension. In the tension tests a sufficiently high bond strength between the ice and endcap is essential to obtaining failure in the middle of the specimen away from the end-planes.

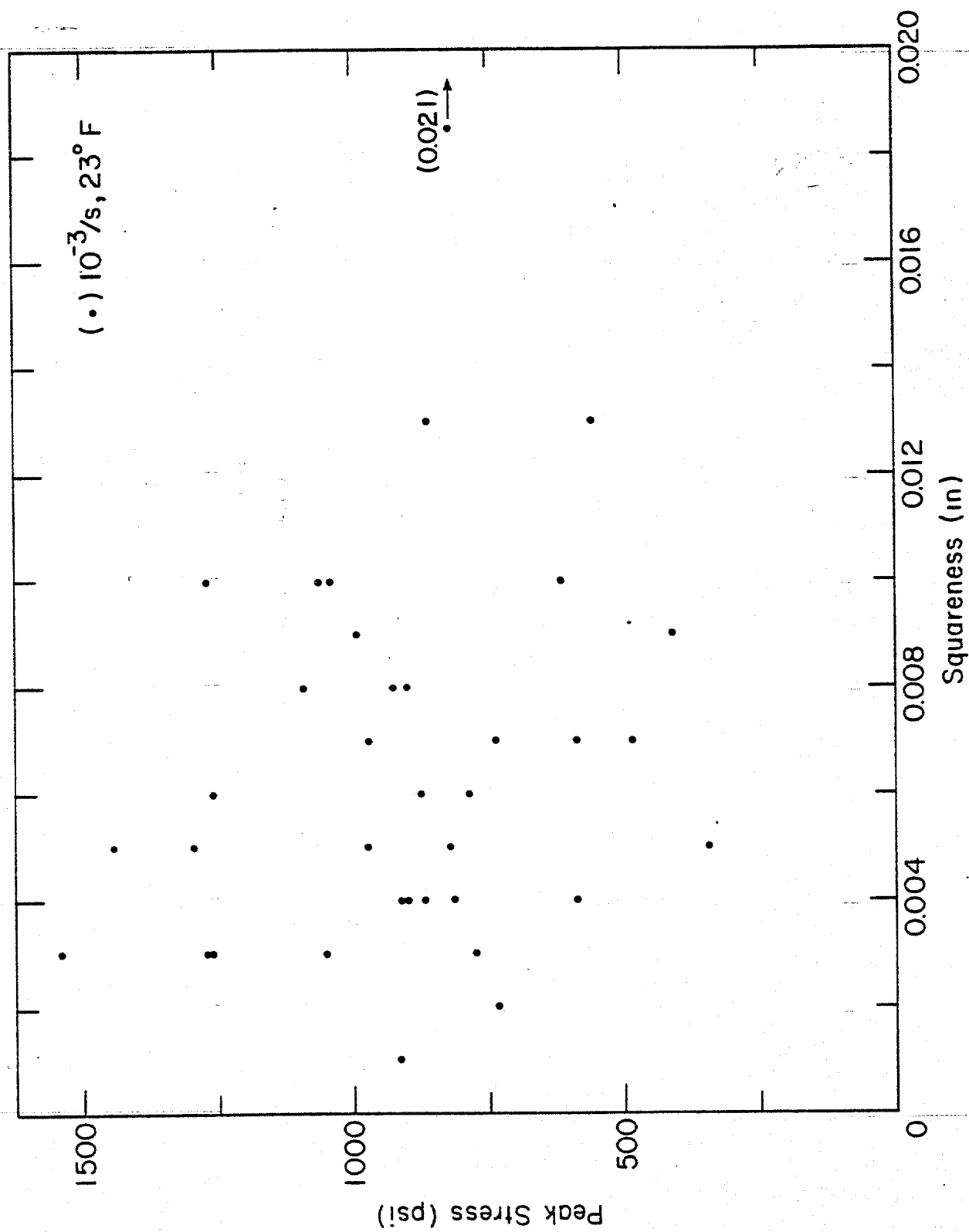


Figure 22: Unconfined compressive strength versus sample squareness for tests conducted at $10^{-3}/s$ and $23^{\circ}F$.

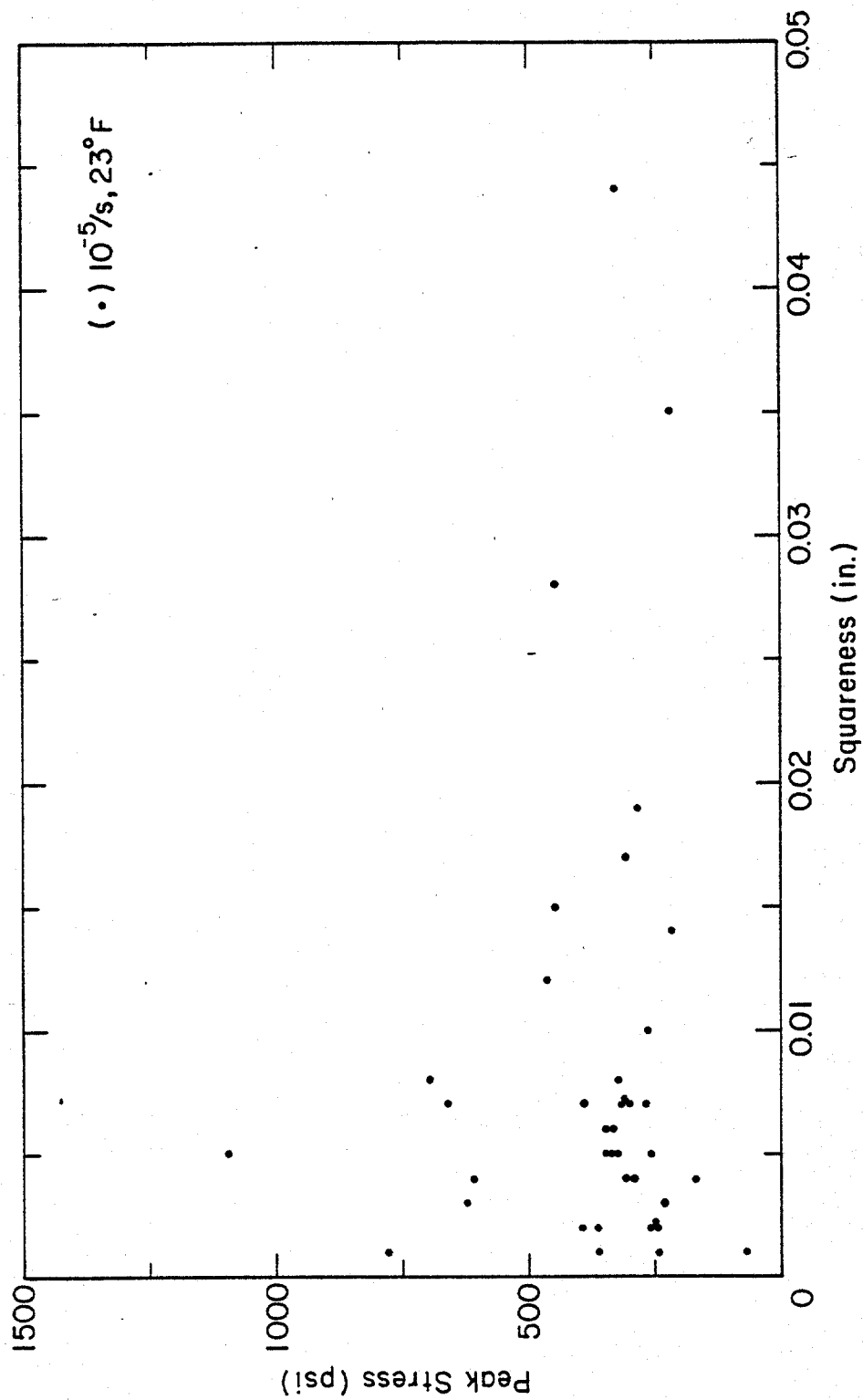


Figure 23: Unconfined compressive strength versus sample squareness for tests conducted at 10^{-5} /sec and 23°F .

A series of uniaxial tension tests were performed on 4.2-inch diameter, 10-inch long, right circular cylinders of ice to evaluate the bond strength between the ice and endcaps. The samples were obtained from the undeformed multi-year ice cores collected in the field last April. In all but one of the tests, the endcaps were bonded to the specimen using the same techniques as in the preparation of the compression samples. In one test, warm endcaps were melted onto the specimen and allowed to freeze. To save time, none of the samples were turned down on the lathe.

The endcapped specimens were held in position, aligned, and loaded on the MTS machine with spherical ball-joints attached to both endcaps. These ball-joints have been successfully used by Currier (1981) to determine the tensile strength of polycrystalline ice.

The test results are given in Table 15. Tests were conducted at two temperatures and two strain-rates. In two of the tests the ice failed away from the endcaps. These specimens had tensile strengths of 92 and 96 psi. The specimen with the melted endcaps had a relatively low bond strength of 38 psi indicating that this method of bonding is inferior to our original technique. The remaining tests had a mean bond strength of 174 ± 26 psi and showed little variation with temperature and strain-rate. This is not surprising as the tensile strength of fresh-water polycrystalline ice shows little variation with temperature and strain-rate.

In most of the tests the sample failed 0 to 1/4-inches from either the lower or upper endcap at a full sample strain of $0.018 \pm 0.003\%$. As the ends of the sample are square and radially constrained, there is a stress riser near the end-planes causing failure in this zone. If the samples had a

BOND STRENGTH TEST RESULTS

Sample No.	$\dot{\epsilon}$ (sec^{-1})	T ($^{\circ}\text{C}$)	σ_m (psi)	ϵ_m (%)	t_m (sec)	Nature of Break
C9-084/111	10^{-3}	- 5	171	0.018	0.18	Failed 0-1/8" from lower endcap
C9-235/261	10^{-3}	- 5	170	0.018	0.26	Failed 0-1/8" from upper endcap
C11-169/195	10^{-3}	- 5	125	0.015	0.15	Failed 0-1/8" from lower endcap
C9-266/292	10^{-5}	- 5	92	0.018	16	Failed 1/3 of the length up from lower endcap
C11-041/068	10^{-5}	- 5	96	0.018	18	Failed 1-1 1/2" from lower endcap
C11-075/101	10^{-5}	- 5	161	0.016	15	Failed 0-1/8" from upper endcap
C11-132/159	$>10^{-3}$	-20	204	0.016	--	
C11-258/285*	10^{-3}	-20	38	0.002	0.02	Failed 0-1/8" from upper endcap and 0-1/4" from lower endcap
C8-077/103	10^{-5}	-20	218	0.018	17	Failed 0-1/8" from upper endcap
C8-237/263	10^{-5}	-20	159	0.024	23	Failed 0-1/8" from lower endcap
C9-163/189	10^{-5}	-20	164	0.016	14	Failed 0-1/8" from lower endcap
C9-131/157	10^{-5}	-20	173	--	13.3	Failed 0-1/8" from lower endcap
C8-166/192	$>10^{-3}$	-20	193	0.019	--	Failed 0-1/4" from upper endcap

* melted endcap

Table 15: Bond strength test results.

slight fillet at both ends, as on our compression test samples, conceivably larger bond strengths would have been obtained.

Based on the above test results and our understanding of the tensile strength of fresh-water and first-year sea ice, it appears that a 3-inch, reduced diameter dumbbell specimen should conservatively meet our requirements. If we assume that the bond strength of the endcaps is 174 psi, or 2410 lbs over the 4.2-inch diameter endcap, we should be able to sustain a stress of about 340 psi over a reduced, 3-inch diameter section. Tensile strength values of polycrystalline fresh water ice go up to 300 psi, and up to 250 psi for first-year low salinity sea ice.

To minimize stress concentrations near the ends, the specimen should have fillets with a radius of curvature of two diameters, or in our case 6 inches. For a 10-inch long sample, this geometry gives a straight 5.1 inch gauge length and an L/D ratio of 1.7 on the reduced section. Photoelastic studies by Hawkes and Mellor (1972) have shown that for this geometry there are no significant stress concentrations and there is a gradual change in stress from the central neck to the flared end sections, with no stress discontinuities. Since a three-inch diameter reduced section appears to be conservative, we will first try some larger diameter specimens. Ideally, we would like to maintain geometric similarity between our tension and compression specimens and keep a high diameter/grain size ratio. Should these larger diameter specimens fail near the end-planes, progressively smaller necked specimens will be tested.

Constant Load Tests

A loading apparatus has been designed and fabricated to perform uniaxial compression constant load tests. The loading frame consists of

two 14 x 14 x 1 inch thick aluminium plates which are separated 17.5 inches by four 3/4-inch diameter steel tie rods. A load is applied to the endcapped ice sample by a 3500 lb capacity Bellofram pneumatic piston fastened to the upper aluminium plate. The loading train includes a ball seat which is attached to the piston, 3/4-inch ground steel platens, and pins to properly center the sample in the loading frame.

The pneumatic cylinder has been calibrated and we have constructed an environmental chamber to house the unit in a cold room. Constant load tests will be shortly underway once the strain transducers and recording equipment are assembled. We plan to record gauge length (GL) and full sample (FS) strains on the sample under an applied load of 1256 lbs (100 psi). Test at higher constant loads will be performed on the MTS machine.

Triaxial Tests

After numerous inquiries to soil and rock mechanics testing equipment companies, we have decided to design and fabricate our own triaxial cell. Commercially available cells are too small for our specimens and do not provide a direct means of increasing the confining pressure with the axial load. As of this time we have completed a conceptual design of a 1000 psi hydraulic cell and are working on the design details (seals, etc.). A discussion of the apparatus will be provided in the next progress report.

FIELD SAMPLING PROGRAM PREPARATION

Equipment is now being assembled and checked out for the Phase II field program. The 4 1/4-inch diameter core barrels have been refurbished and improved. We have strengthened the upper portion of the auger flights and designed new core dogs to minimize scouring on the sides of the core.

The 12-inch diameter core barrel has been fabricated. We are now modifying a small commercial drilling rig to support and drive the auger. Once the rig is modified, the large auger will be tested in our ice pit.

As part of Phase II, we have built a jig to obtain horizontal 4 1/4-inch diameter samples from the 12-inch core. The jig consists of a drill press with a 14-inch long, 4 1/4-inch diameter core barrel, and a cradle to firmly hold the core. The jig should eliminate "wobble" in the coring procedure and produce uniform test samples. The jig will be tested on a 12-inch core taken from the CRREL ice pit prior to going into the field.

A tentative objective of Phase II is to determine the effects of shipment and storage on ice strength. This can be accomplished by conducting Brazil tests on 25 pairs of ice samples in the field and laboratory. The Brazil test is attractive in that it does provide a good strength index (not tensile strength) on samples requiring a minimum amount of preparation. We are now assembling the equipment which includes a 10,000 lb Soil Test compression machine and a specially designed jig to hold and load 2-inch thick ice samples. An environmental chamber will also be made to test the samples in the field at a controlled temperature, slightly above ambient.

The remaining equipment that is being assembled is similar to that used in the Phase I field sampling program.

AIR VOLUME EQUATIONS

Progress Report 3 contained a set of equations to calculate the air and brine volume of sea ice samples. These equations have been reviewed and an error was found in the set of equations describing the change in air

volume with sample temperature; that is the air volume at a temperature other than that at which the sample density was determined. A revised discussion of the air volume calculations is attached. This paper has been submitted for review as a CRREL Research Report.

REFERENCES

- Currier, J.H. (1981) The brittle to ductile transition in polycrystalline ice under tension. Dartmouth College, Thayer School of Engineering, M.S. thesis, 112 p.
- Frederking, R.M.W. and Timco, G.W. (1980) NRC ice property measurements during the Canmar Kigoriak trials in the Beaufort Sea. National Research Council, Canada, DBR Paper No. 947.
- Hawkes, I. and Mellor, M. (1972) Deformation and fracture of ice under uniaxial stress. Journal of Glaciology, Vol. 11, No. 61, p. 103-131.
- Schwarz, J. and Weeks, W.F. (1975) Engineering properties of sea ice. Journal of Glaciology, Vol. 19, No. 81, p. 499-531.
- Traetteberg, A.; Gold, L.W.; and Frederking, R. (1975) The strain rate and temperature dependence of Young's modulus of ice. IAHR Ice Problem Symposium, 1975, p. 479-486.
- Wang, Y.S. (1979) Sea ice properties. Technical seminar on Alaskan Beaufort Sea Gravel Island Design. Exxon Company, U.S.A.

Equations for Determining the Gas and Brine Volumes in Sea Ice Samples

by

G.F.N. Cox and W.F. Weeks

U.S. Army Cold Regions Research and Engineering Laboratory
72 Lyme Road
Hanover, NH 03755, USA

ABSTRACT

Equations are developed that can be used to determine the amount of gas present in sea ice from measurements of the bulk ice density, salinity and temperature in the temperature range of -2 to -30°C . Conversely these relations can be used to give the density of sea ice as a function of its temperature and salinity considering both the presence of gas and of solid salts in the ice. Equations are also given that allow the calculation of the gas and brine volumes in the ice at temperatures other than that at which the bulk density was determined.

INTRODUCTION

A knowledge of the total porosity of sea ice is important in interpreting its physical properties. It has been shown, both theoretically and experimentally, that the mechanical, thermal, and electrical properties of sea ice vary with the relative volume of brine existing in the ice (Weeks and Assur, 1967; Schwarz and Weeks, 1977). However, not only is the ice brine volume important, but also its air or gas volume. This is particularly true for low salinity sea ice, such as multiyear ice, where the gas volume may make up a major portion of its total porosity.

3

The gas volume of sea ice can be calculated given the density, salinity, and temperature of the ice. Generally, Assur's (1958) phase diagram table (Table III, p. 124) is used to perform such calculations. This table gives the relative masses of the different components in standard sea ice at two degree temperature intervals based on the experimental determinations of Nelson and Thompson (1954) and Ringer (1928). Here the expression standard sea ice is used to refer to sea ice of such a composition that the relative concentrations of ions in its melt water are the same as in normal sea water. From the density of the various components, the theoretical, or gas-free density of the sea ice can then be calculated and compared to the measured density to determine the actual gas volume present in the ice. However, since the table is based on standard sea ice having a salinity of 34.325 o/oo, it is first necessary to reduce the data to the appropriate ice salinity. This is done by dividing the masses of all the components, except pure ice, by $S_i/34.325$ where S_i is the ice salinity in parts per thousand. The mass of pure ice is then 1000g minus the total mass of brine and precipitated salts. Even though these calculations are straightforward, they are both time consuming and prone to arithmetic errors. In fact they are rarely performed and estimates of the amount of gas present in sea ice and of the total void volume of the ice are rarely obtained.

In the present paper equations are derived from which the gas volume and brine volume can be directly calculated given the ice salinity, temperature, and density. The equations cover the temperature range from -2°C to -30°C and consider the presence of solid salts. Equations are also given to calculate sea ice density and the variation of gas and brine

volume of a sea ice sample, if the temperature of the sample is changed from the temperature at which the ice density was originally obtained.

PREVIOUS WORK

Only a few investigators have advanced methods for calculating the density and gas volume in sea ice. Zubov (1945) calculated the density of gas-free sea ice providing a table of values that could be used at temperatures of -23°C and warmer. However, his work was done prior to Nelson and Thompson's (1954) studies of the phase relations for sea ice. Zubov also does not take the presence of solid salts into account. In (1960) Anderson published a table giving the density of gas-free sea ice at 14 selected temperatures in the temperature range between 0 and -50°C . This work was based on the Nelson and Thompson phase relations. As the exact method of calculation is not given, it is not clear whether or not Anderson considered the presence of solid salts in the ice. The only relation available that calculates the gas volume of sea ice directly was developed by Schwerdtfeger (1963). However, it is only valid at temperatures warmer than -8.2°C , the $\text{Na}_2\text{SO}_4 \cdot 10 \text{ H}_2\text{O}$ crystallization temperature. He also neglected the presence of solid salts and assumed that the volume of brine was equal to that of pure water. For warm sea ice these are reasonable approximations. At the conclusion of this paper comparisons are made between the results of these previous authors and the present results.

It should also be noted here that Assur's (1958) brine volume table and the brine volume equations based on this table derived by Frankenstein and Garner (1967) assume a constant ice density of 0.926 Mg/m^3 . Consequently, these reports should be used with caution in gas volume calculations. The brine volume obtained from these sources should be multiplied

by $\rho/0.926$, where ρ is the measured ice density in Mg/m^3 , to determine the brine volume for a given sea ice density.

DERIVATION OF EQUATIONS

A sample of sea ice is composed of pure ice, brine, solid salts, and gas. In determining the gas volume of sea ice we are interested in the relative masses and volumes of the different components at a given ice salinity, temperature, and bulk density.

In the derivations to follow, m_l , ρ_l and V_l are the mass, density, and volume of component l where the subscripts a, b, i, s, and ss denote the component air, brine, pure ice, salt, and solid salts, respectively. M is the bulk mass and ρ the bulk density. The terms m_s^b and m_s^{ss} denote the mass of salt in the brine and mass of salt in the solid salts, respectively.

Brine Volume

The salinity of the ice, S_i , is defined as

$$S_i = \frac{m_s}{M} = \frac{m_s^b + m_s^{ss}}{m_b + m_{ss} + m_i} \quad (1)$$

The mass of gas in the ice is assumed to be negligible. The salinity of the brine, S_b , is defined as

$$S_b = \frac{m_s^b}{m_b} \quad (2)$$

From these two relations an equation for the brine volume of sea ice can be derived. It should be noted that the brine salinity and the rela-

tive amounts of salt in the brine and solid salts are unique functions of ice temperature via phase relations.

From equation (1)

$$MS_i = m_s^{ss} + m_s^b$$

and

$$m_s^b = MS_i - m_s^{ss}$$

or

$$m_s^b = MS_i - km_s^b \quad (3)$$

where

$$k = \frac{m_s^{ss}}{m_s^b}$$

Solving for m_s^b from equation (3) and noting from equation (2) that

$$m_s^b = \rho_b V_b S_b$$

we obtain

$$V_b = \frac{MS_i}{\rho_b S_b} \left(\frac{1}{1+k} \right)$$

which because $M = \rho V$, can also be written as

$$\frac{V_b}{V} = \frac{\rho S_i}{\rho_b S_b} \left(\frac{1}{1+k} \right) \quad (4)$$

where V_b/V is the relative brine volume. If we neglect the salt present as solid salt, $k=0$, and equation (4) reduces to

$$\frac{V_b}{V} = \frac{\rho S_i}{\rho_b S_b}$$

a relation utilized earlier by Weeks and Lofgren (1967).

Because the brine density can be approximated by (Zubov, 1945; and Cox and Weeks, 1975):

$$\rho_b (\text{Mg/m}^3) = 1 + 0.0008 S_b (\text{o/oo})$$

and because S_b and k are unique functions of temperature, the relative brine volume can be expressed as

$$\frac{V_b}{V} = \frac{\rho S_i}{F_1(T)} \quad (5)$$

where S_i is in o/oo, ρ is in Mg/m^3 , and

$$F_1(T) = \rho_b S_b (1+k) \quad (6)$$

Values for $F_1(T)$ are given in Table 1 and plotted against temperature in Figure 1. The lines through the data in Figure 1 are least-squares curves of the form

$$F_1(T) = \alpha_0 + \alpha_1 T + \alpha_2 T^2 + \alpha_3 T^3 \quad (7)$$

where T is the ice temperature ($^{\circ}\text{C}$). Coefficients for the curves are given in Table 2.

Solid Salts Volume

Also, via the phase relations, at any given temperature the mass of solid salts (if solid salts are present) is proportional to the mass of brine. That is

$$m_{ss} = C m_b \quad (8)$$

where C is a function of T . The relative volume of solid salts, V_{ss}/V , is then equal to

$$\frac{V_{ss}}{V} = C \frac{\rho_b}{\rho_{ss}} \frac{V_b}{V} \quad (9)$$

where ρ_{ss} is the average solid salt density assumed to be constant at 1.5 Mg/m³.

Pure Ice Volume

The mass of pure ice is equal to

$$m_i = M - m_b - m_{ss}$$

or from equation (8)

$$m_i = M - (1+C)m_b$$

Since

$$m_i = \rho_i V_i$$

$$M = \rho V$$

$$m_b = \rho_b V_b$$

we have

Table 1. Values for S_b , k , C , $F_1(T)$,
and $F_2(T)$ at different temperatures.

T	S_b	$k \times 10^3$	$C \times 10^3$	$F_1(T)$	$F_2(T)$
(°C)	(o/oo)			(Mg/m ³)	(Mg/m ³)
- 2	37.6	0	0	38.731	0.123
- 4	70.6	0.554	0.148	74.662	0.151
- 6	99.8	1.050	0.387	107.876	0.177
- 8	126.5	1.400	0.660	139.441	0.199
-10	142.8	55.277	18.256	167.865	0.222
-12	157.6	84.141	30.493	192.378	0.240
-14	171.5	97.627	38.421	214.143	0.256
-16	184.4	106.330	44.952	234.033	0.271
-18	197.0	112.570	50.808	253.588	0.284
-20	209.9	118.078	56.851	274.074	0.298
-22	222.6	123.090	63.015	294.496	0.312
-24	230.5	509.787	217.168	412.236	0.394
-26	232.7	1312.694	537.697	638.433	0.556
-28	234.1	2065.827	842.341	852.171	0.708
-30	235.6	2685.708	1098.887	1032.102	0.836

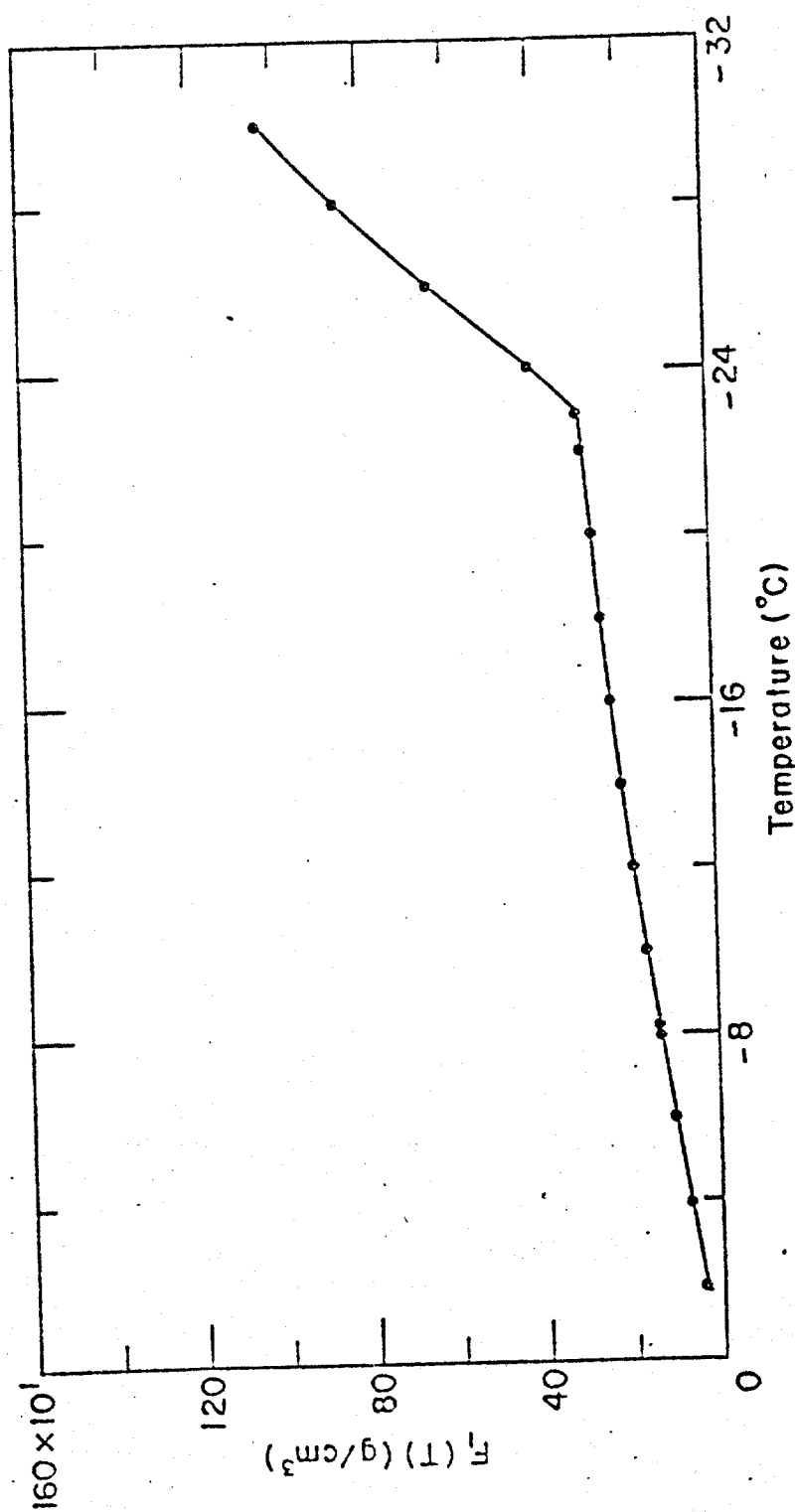


Figure 1. Function $F_1(T)$ versus temperature. Curve determined by method of least-squares.

Table 2. Coefficients for functions $F_1(T)$ and $F_2(T)$ determined by method of least-squares.

$T(^{\circ}\text{C})$	$F_1(T)$				Correlation Coefficient
	α_0	α_1	α_2	α_3	
$-2 \geq T \geq -22.9$	-4.732	-2.245×10^1	-6.397×10^{-1}	-1.074×10^{-2}	0.9999
$-22.9 \geq T \geq -30$	9.899×10^3	1.309×10^3	5.527×10^1	7.160×10^{-1}	0.9999
$F_2(T)$					
$-2 \geq T \geq -22.9$	8.903×10^{-2}	-1.763×10^{-2}	-5.330×10^{-4}	-8.801×10^{-6}	0.9999
$-22.9 \geq T \geq -30$	8.547	1.089	4.518×10^{-2}	5.819×10^{-4}	0.9999

$$\rho_i V_i = \rho V - (1+C) \rho_b V_b$$

Solving for the relative pure ice volume, V_i/V , we obtain:

$$\frac{V_i}{V} = \frac{\rho}{\rho_i} - (1 + C) \frac{\rho_b}{\rho_i} \frac{V_b}{V} \quad (10)$$

Air Volume

The relative air volume, V_a/V , is equal to

$$\frac{V_a}{V} = 1 - \frac{V_b}{V} - \frac{V_i}{V} - \frac{V_{ss}}{V} \quad (11)$$

Substituting equations (9), and (10) into equation (11) we obtain

$$\frac{V_a}{V} = 1 - \frac{\rho}{\rho_i} + \frac{V_b}{V} \left((1 + C) \frac{\rho_b}{\rho_i} - C \frac{\rho_b}{\rho_{ss}} - 1 \right) \quad (12)$$

Equation (12) can be simplified by defining

$$F_2(T) \equiv \left((1 + C) \frac{\rho_b}{\rho_i} - \frac{C \rho_b}{\rho_{ss}} - 1 \right), \quad (13)$$

substituting for (V_b/V) from equation (4), and recalling the definition of $F_1(T)$ given in equation (6). The resulting relation is

$$\frac{V_a}{V} = 1 - \frac{\rho}{\rho_i} + \frac{\rho S_1}{\rho_i} \frac{F_2(T)}{F_1(T)} \quad (14)$$

Values for $F_2(T)$ are given in Table 1 and plotted against temperature in Figure 2. The lines through the data in Figure 2 are also least-squares curves of the same form as equation (7).

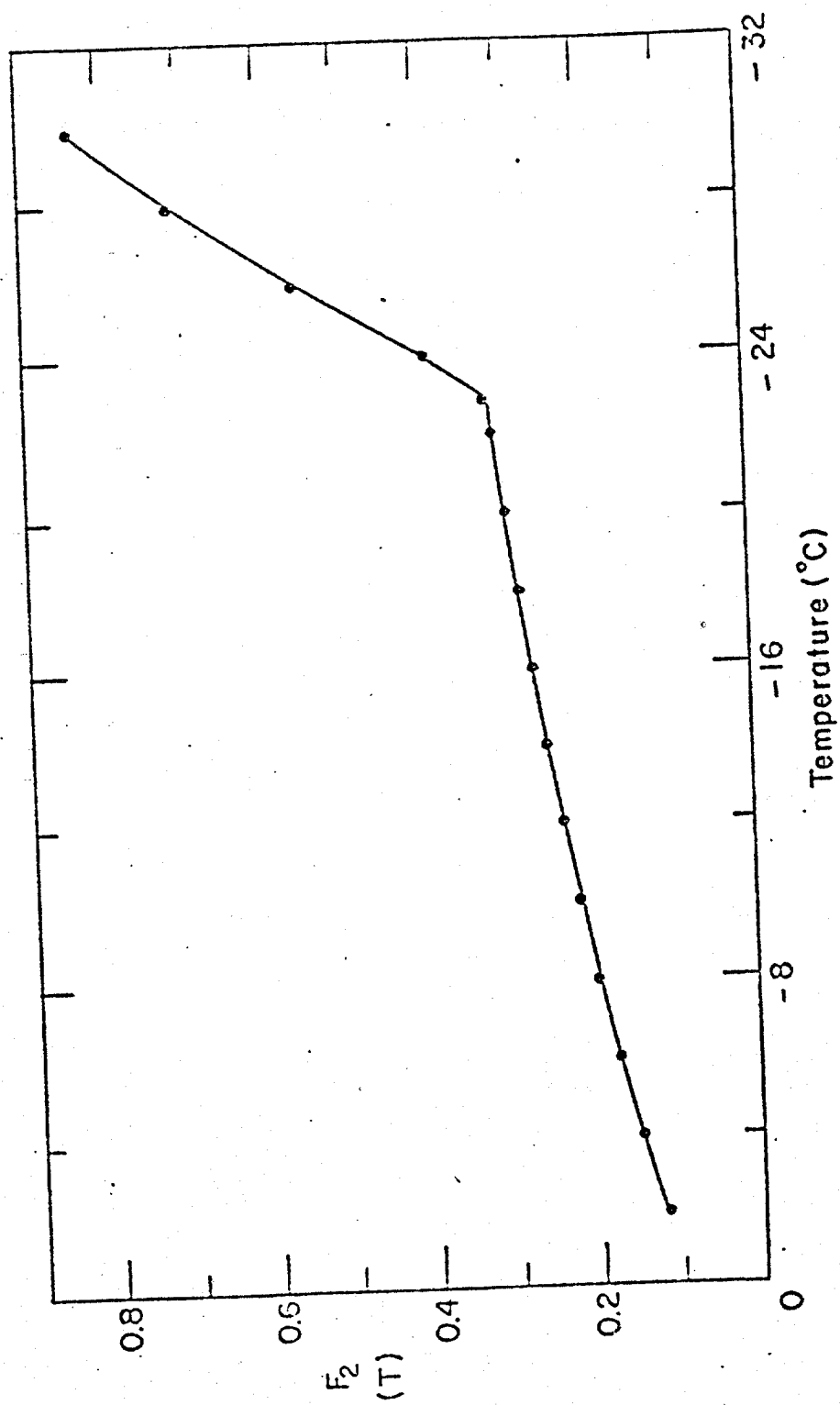


Figure 2: Function $F_2(T)$ versus temperature. Curve determined by method of least-squares.

Coefficients for these curves are given in Table 2. In determining the value of $F_2(T)$ at a given temperature, the pure ice density was calculated from (Pounder, 1965):

$$\rho_i (\text{Mg/m}^3) = 0.917 - 1.403 \times 10^{-4} T(^{\circ}\text{C})$$

Sea Ice Density

The sea ice density can be found from equation (14) by solving for ρ :

$$\rho = \left(1 - \frac{V_a}{V}\right) \frac{\rho_i F_1(T)}{F_1(T) - \rho_i S_i F_2(T)} \quad (15)$$

Unlike the calculated densities given in Schwerdtfeger (1963) and Anderson (1960), this equation considers the presence of both air and solid salts in the ice. A comparison between the different density estimates is given later in this paper.

Gas Volume at Another Temperature

The gas volume and brine volume of sea ice are determined by measuring the volume and mass of the ice sample at a given temperature and the salinity of the melted sample. If tests are conducted at a temperature different than the temperature at which the bulk density was determined, the air and brine volumes must be recalculated.

Equations are now derived to calculate the air and brine volumes at a temperature which differs from the temperature at which the ice density was determined. Primed variables denote the initial value of the different variables.

It is initially assumed that the brine and air pockets are interconnected. From equation (5) we know that

$$V_b = \frac{M S_1}{F_1(T)}$$

Because the mass and bulk salinity of the ice do not change with temperature

$$V_b = V'_b \frac{F'_1(T)}{F_1(T)} \quad (16)$$

By rearranging equation (14), substituting for ρ based on equation (5) and defining

$$F_3(S_i, T) \equiv \frac{\rho_i S_i}{F_1(T) - \rho_i S_i F_2(T)} \quad (17)$$

it can be shown that

$$V_b = (V - V_a) F_3(S_i, T) \quad (18)$$

Also dividing both sides of equation (1) by V and noting that

$$V = \frac{\rho' V'}{\rho}$$

we obtain for the new brine volume

$$\frac{V_b}{V} = \frac{\rho}{\rho'} \frac{V'_b}{V'} \frac{F'_1(T)}{F_1(T)} \quad (19)$$

From equation (18) we can also conclude that

$$\frac{V_b}{V'_b} = \frac{(V - V_a) F_3(S_i, T)}{(V' - V'_a) F'_3(S_i, T)} \quad (20)$$

Substituting equation (19) into (20) and solving for V_a/V we obtain for the new air volume

$$\frac{V_a}{V} = 1 - \left(1 - \frac{V'_a}{V'}\right) \left(\frac{\rho}{\rho'}\right) \left(\frac{F'_3(S_i, T) F'_1(T)}{F_3(S_i, T) F_1(T)}\right) \quad (21)$$

If the volume of the sample is not known at the new temperature, one can assume that the change in the external dimensions of the sample is due to the volumetric change in the ice matrix, that is

$$\frac{\rho}{\rho'} \approx \frac{\rho_i}{\rho'_i}$$

In the temperature range where many investigations are carried out

$$\frac{\rho_i}{\rho'_i} \approx 1$$

If the brine and gas pockets are not connected, a change in gas volume may also take place if the ice is warmed, that is, as less dense ice is melted to dilute the brine. In this case the new air volume is equal to

$$\frac{V_a}{V} = \frac{V'_a}{V'} + 1 - \frac{\rho}{\rho'} \frac{F'_3(S_i, T) F'_1(T)}{F_3(S_i, T) F_1(T)} \quad (22)$$

and in many applications

$$\frac{\rho}{\rho'} \approx \frac{\rho_i}{\rho'_i} \approx 1$$

DISCUSSION

As methods for calculating the gas content of sea ice invariably contain a calculation of the density of gas-free sea ice, it is interesting to compare the density estimates developed in this paper with previously published estimates. Table 3 gives such a comparison. As can be seen, the agreement between the present results and those of Anderson (1960) is very

Table 3. The calculated densities of gas-free sea ice at different temperatures and salinities as given by different authors.

T = -2C	1	3	5	10	20 o/oo
Zubov (1945)	.922	.926	.930	.939	
Anderson (1960)	.9198	.9252	.9307	.9447	.9739
Schwerdtfeger (1963)	.9191	.9233	.9275	.9379	.9588
This paper (CW)	.9200	.9254	.9308	.9448	.9740
T = -8C					
Zubov (1945)	.920	.923	.925	.932	.944
Anderson (1960)	.9192	.9216	.9240	.9301	.9426
Schwerdtfeger (1963)	.9175	.9186	.9196	.9222	.9275
This paper (CW)	.9193	.9218	.9242	.9303	.9429
T = -10C					
Zubov (1945)	.920	.922	.925	.929	
Anderson (1960)	.9194	.9216	.9239	.9296	.9412
This paper (CW)	.9195	.9218	.9240	.9297	.9413
T = -30C					
Anderson (1960)	.9216	.9230	.9245	.9281	.9354
This paper (CW)	.9219	.9233	.9247	.9281	.9352

good (the present values are at most $+0.0003 \text{ Mg/m}^3$ higher with a modal difference of only $+0.0001 \text{ Mg/m}^3$). This agreement is, however, not surprising in that both Anderson's and our calculations are based on Assur's phase equilibrium tables. The agreement essentially verifies both sets of calculations. When comparisons are made with Schwerdtfeger's (1963) results for sea ice warmer than -8.2°C , much larger differences are found. Within this temperature range these differences vary from $+0.0009$ at warm temperatures (-2°C) and low salinities (1 o/oo) to $+0.0154$ at -8°C and 20 o/oo . The agreement with the earlier values of Zubov (1945) is better than with Schwerdtfeger with the largest difference being $+0.0058 \text{ Mg/m}^3$.

It is also interesting to use the relations that have been developed to examine the importance of considering the presence of solid salts in making gas volume calculations. For sea ice warmer than -8.2°C , Schwerdtfeger (1963) calculated the relative air volume from

$$\frac{V_a}{V} = 1 - \frac{\rho}{1000} \left(\frac{1000 - S_i}{0.917} + \frac{4.98 S_i}{T} \right) \quad (23)$$

where ρ is in Mg/m^3 , S_i in o/oo , and T in $^\circ\text{C}$. As mentioned earlier he neglected the presence of solid salts and assumes that the volume of brine in the ice is equal to the volume of pure water. If we neglect the presence of solid salts in our equations, equation (12) simplifies to

$$\frac{V_a}{V} = \left(1 - \frac{\rho}{\rho_i} \right) + \frac{\rho S_i}{S_b} \left(\frac{1}{\rho_i} - \frac{1}{\rho_b} \right) \quad (24)$$

The results from equations (23) and (24) are compared to the results from equation (12) in Table 4. The air volume of sea ice of different assumed

Table 4. Air volume (o/oo) calculations from three methods for sea ice having different densities, salinities and temperatures (see text for explanation).

$S_i = 1$ o/oo

T (°C)	$\rho(\text{g/cm}^3)$								
	<u>0.890</u>			<u>0.910</u>			<u>0.930</u>		
	1	2	3	1	2	3	1	2	3
- 6	31.1	31.8	31.8	9.4	10.0	10.0	-	-	-
-10		32.0	32.1		10.2	10.4	-	-	-
-20		33.4	33.4		11.7	11.7	-	-	-
-30		34.8	34.6		13.1	12.9	-	-	-

$S_i = 10$ o/oo

T (°C)	$\rho(\text{g/cm}^3)$								
	<u>0.890</u>			<u>0.910</u>			<u>0.930</u>		
	1	2	3	1	2	3	1	2	3
- 6	46.5	44.9	44.8	25.1	23.5	23.3	3.7	2.0	1.9
-10		42.7	42.7		21.2	21.2	-	-	-
-20		42.2	42.1		20.7	20.6	-	-	-
-30		43.1	41.0		21.6	19.4	-	-	-

salinities, densities, and temperatures are calculated using these three equations. Schwerdtfeger's results are given in Column 1, our results neglecting solid salts in Column 2, and our results considering solid salts in Column 3.

All the calculated values at a given salinity, density, and temperature are in close agreement. This indicates that even for sea ice below the $\text{NaCl} \cdot 2\text{H}_2\text{O}$ eutectic temperature, neglecting the presence of solid salts in air volume calculations is a reasonable assumption. For warm, high density, high salinity sea ice (0.930 Mg/m^3), Schwerdtfeger's value differs by 1.8 o/oo, or nearly 100%. However, the brine volume of this ice is relatively much greater (85.1 o/oo) and there is little difference in the total ice porosity.

CONCLUSIONS

Equations have been derived to quickly calculate the air volume of sea ice considering the presence and absence of solid salts. The results show that neglecting the presence of solid salts is a reasonable assumption. However, in this era of computers and sophisticated hand calculators, we recommend considering the presence of solid salts and the use of equation (12) to calculate the air volume of sea ice. A program for making such calculations on a Hewlett-Packard 41C calculator is available from the authors.

REFERENCES

- Anderson, D.L. (1960) The physical constants of sea ice. Research, Vol. 13, p. 310-318.
- Assur, A. (1958) Composition of sea ice and its tensile strength. In "Arctic Sea Ice." U.S. National Academy of Sciences - National Research Council Pub. 598, 106-138.
- Cox, G.F.N. and Weeks, W.F. (1975) Brine drainage and initial salt entrapment in sodium chloride ice. CRREL Research Report 345, 85 p.
- Frankenstein, G. and Garner, R. (1967) Equations for determining the brine volume of sea ice from -0.5 to -22.9°C. Journal of Glaciology, Vol. 6, No. 48, p. 943-944.
- Nelson, K.H. and Thompson, T.G. (1954) Deposition of salt from sea water by frigid concentration. University of Washington, Department of Oceanography, Tech. Rept. 29.
- Pounder, E.R. (1965) The Physics of Ice. New York, Pergamon Press.
- Ringer, W.E. (1928) Über die Veränderungen in der Zusammensetzung des Meereswassersalzes beim Ausfrieren. Conseil permanent intern. exploration mer, Rapp. 47, p. 226-32.
- Schwarz, J. and Weeks, W.F. (1977) Engineering properties of sea ice. Journal of Glaciology, Vol. 19, No. 81, p. 499-531.
- Schwerdtfeger, P. (1963) The thermal properties of sea ice. Journal of Glaciology, Vol. 4, No. 36, p. 789-807.
- Weeks, W.F. and Assur, A. (1969) Fracture of lake and sea ice. CRREL Research Report 269, 79 p.
- Weeks, W.F. and Lofgren, G. (1967) The effective solute distribution coefficient during the freezing of NaCl solutions. In "Physics of Snow and Ice," Proceed. Internat. Conference on Low Temperature Science, Hokkaido University, Sapporo, Vol. I, Part 1, p. 579-597.
- Zubov, N.N. (1945) Arctic ice. Translation, U.S. Naval Electronics Laboratory, 1963.